The intention of this work is twofold:
On the one hand, we explore the controlability of GaAs nanowire growth concerning orientation, shape and crystal structure. These are necessary steps, since the growth of GaAs nanowires proceeds not necessarily uniformly, and in GaAs nanowires the in bulk unstable wurtzite phase, and the usual observed zinc-blende crystal phase may coexist in one and the same nanowire.
On the other hand, we include ferromagnetic materials into GaAs nanowires. To do that, we produce either "core/shell" structures, where the GaAs nanowire is coated with a ferromagnetic "shell" material, or grow ferromagnetic nanoscale segments in GaAs nanowires.

Universitätsverlag Regensburg

ISBN 978-3-86845-132-0
gefördert von: Alumni der physikalischen Fakultät der Universität Regensburg e.V.

Universität Regensburg

Dissertationsreihe Physik - Band 48

Joachim Hubmann

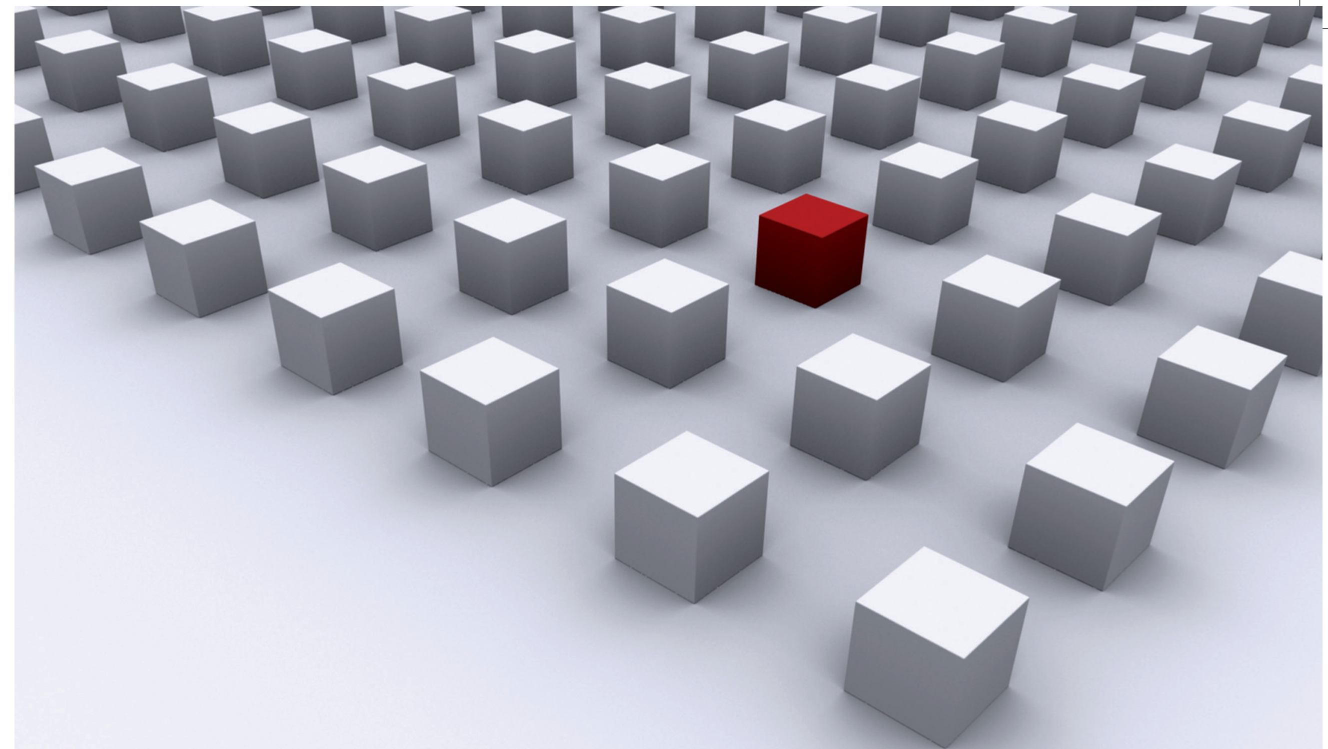

Joachim Hubmann

GaAs nanowires: Epitaxy, crystal structure-related properties and magnetic heterostructures

Universitätsverlag Regensburg

48 Dissertationsreihe Physik

Joachim Hubmann

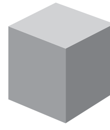

GaAs nanowires: Epitaxy, crystal structure-related properties and magnetic heterostructures

GaAs nanowires: Epitaxy, crystal structure-related properties and magnetic heterostructures

Dissertation zur Erlangung des Doktorgrades der Naturwissenschaften (Dr. rer. nat.)
der Fakultät für Physik der Universität Regensburg
vorgelegt von

Joachim Hubmann

aus Neustadt an der Waldnaab
im Jahr 2015

Die Arbeit wurde von Prof. Dr. Dominique Bougeard angeleitet.
Das Promotionsgesuch wurde am 30.6.2015 eingereicht.
Das Kolloquium fand am 22.12.2015 statt.

Prüfungsausschuss:	Vorsitzender:	Prof. Dr. John Schliemann
	1. Gutachter:	Prof. Dr. Dominique Bougeard
	2. Gutachter:	Prof. Dr. Josef Zweck
	weiterer Prüfer:	Prof. Dr. Christian Back

Dissertationsreihe der Fakultät für Physik der Universität Regensburg, Band 48

Herausgegeben vom Präsidium des Alumnivereins der Physikalischen Fakultät:
Klaus Richter, Andreas Schäfer, Werner Wegscheider

Joachim Hubmann

GaAs nanowires: Epitaxy, crystal structure-related properties and magnetic heterostructures

Universitätsverlag Regensburg

Bibliografische Informationen der Deutschen Bibliothek.
Die Deutsche Bibliothek verzeichnet diese Publikation
in der Deutschen Nationalbibliografie. Detailierte bibliografische Daten
sind im Internet über http://dnb.ddb.de abrufbar.

1. Auflage 2016
© 2016 Universitätsverlag, Regensburg
Leibnizstraße 13, 93055 Regensburg

Konzeption: Thomas Geiger
Umschlagentwurf: Franz Stadler, Designcooperative Nittenau eG
Layout: Joachim Hubmann
Druck: Docupoint, Magdeburg
ISBN: 978-3-86845-132-0

Alle Rechte vorbehalten. Ohne ausdrückliche Genehmigung des Verlags ist es nicht gestattet, dieses Buch oder Teile daraus auf fototechnischem oder elektronischem Weg zu vervielfältigen.

Weitere Informationen zum Verlagsprogramm erhalten Sie unter:
www.univerlag-regensburg.de

Contents

1. Introduction **1**

2. GaAs nanowires: Fundamental principles **3**

2.1. VLS growth mechanism: Growth kinetics . . . 3
2.1.1. Modelling nanowire growth . . . 4
2.1.2. Chemical potentials of atomic states . . . 5
2.1.3. Transition state theory . . . 7
2.1.4. Flow of matter towards the catalyst . . . 8
2.1.5. Diffusion of adatoms in general . . . 9
2.1.6. Diffusion of Ga and As adatoms . . . 11
2.1.7. Ga adatom diffusion towards the liquid catalyst . . . 12
2.1.8. The liquid-solid transition . . . 15
2.1.9. Summary . . . 17
2.2. GaAs nanowires: Growth of zinc-blende and wurtzite phase . . . 18
2.2.1. Site-dependent nucleation . . . 19
2.2.2. Wetting area dependent nucleation . . . 22
2.2.3. Impact of liquid surface tension and contact angles . . . 24
2.2.4. The supersaturation of the liquid phase . . . 26
2.2.5. Summary . . . 28
2.3. Properties of GaAs in nanowires . . . 29
2.3.1. Zinc-blende and wurtzite crystal structure . . . 29
2.3.2. WZ phase: Symmetry breaking and spontaneous polarization . . . 31
2.3.3. Band structures and optical selection rules . . . 33
2.3.4. Surface states and passivation . . . 36

3. Mn containing ferromagnetic materials **39**

3.1. Ferromagnetism and Curie temperature . . . 39
3.2. Diluted magnetic semiconductor (Ga,Mn)As . . . 41
3.2.1. Structural properties of (Ga,Mn)As . . . 42
3.2.2. Origin of ferromagnetism in (Ga,Mn)As . . . 44
3.2.3. (Ga,Mn)As in GaAs/(Ga,Mn)As core/shell nanowires . . . 46
3.2.4. Annealing of (Ga,Mn)As . . . 50
3.3. Manganese Arsenide (MnAs) . . . 51
3.3.1. Structural properties . . . 51
3.3.2. MnAs thin films on GaAs substrates . . . 52

3.3.3. Magnetic anisotropy of MnAs thin films . . . 53

4. GaAs nanowire growth 55
4.1. Nucleation and vertical nanowire growth on Si(111) . . . 56
4.1.1. Optimization of nucleation on native oxide . . . 56
4.1.2. Site-selective growth . . . 58
4.1.3. Conclusion . . . 59
4.2. Epitaxy of GaAs nanowires on Si(111) . . . 61
4.2.1. Temperature dependence . . . 62
4.2.2. Dependence on the arsenic pressure . . . 64
4.2.3. Dependence on the Ga rate . . . 66
4.2.4. Conclusion . . . 68
4.3. Crystal structure optimization of GaAs nanowires . . . 69
4.3.1. Optimizing the wurtzite phase . . . 69
4.3.2. Optimizing the zinc-blende phase . . . 73
4.3.3. Conclusion . . . 77

5. Optical properties of GaAs nanowires 79
5.1. Radiative recombination: Enhancing nanowire passivation . . . 80
5.1.1. AlGaAs/GaAs shell growth . . . 80
5.1.2. Radiative recombination strength and AlGaAs shell thickness . . . 82
5.1.3. Radiative recombination strength and AlGaAs shell composition . 83
5.2. PL: Correlation with nanowire crystal structure . . . 84
5.2.1. PL: Stacking-fault-free wurtzite GaAs nanowires . . . 84
5.2.2. PL: Zinc-blende nanowires . . . 86
5.3. GaAs lasing nanowires . . . 89
5.3.1. Nanowire growth . . . 89
5.3.2. PL: Lasing operation . . . 90
5.4. Conclusion . . . 92

6. Spontaneous polarization in WZ GaAs 95

7. GaAs/(Ga,Mn)As core/shell nanowires 99
7.1. Strain and (Ga,Mn)As shell thickness . . . 100
7.2. WZ and ZB (Ga,Mn)As shells in comparison . . . 101
7.2.1. Lattice relaxation: Reciprocal space mapping . . . 102
7.2.2. Magnetic properties . . . 104
7.2.3. Conclusion . . . 107
7.3. WZ (Ga,Mn)As shells: Different Mn concentrations . . . 108
7.3.1. Growth . . . 108
7.3.2. Curie temperature determination . . . 109
7.3.3. Magnetotransport measurements . . . 110
7.3.4. Conclusion . . . 112

8. MnAs segments in GaAs nanowires **113**
8.1. GaAs:Mn nanowire growth . . . 113
8.2. Ferromagnetic MnAs segments in GaAs nanowires . . . 117
8.2.1. Growth of single ferromagnetic MnAs segments . . . 117
8.2.2. Growth of multiple MnAs segments . . . 121
8.3. Conclusion . . . 122

9. Conclusion and Outlook **125**

A. Experimental techniques **129**
A.1. Molecular beam epitaxy (MBE) of GaAs nanowires . . . 129
A.1.1. Cell calibration . . . 129
A.1.2. Nanowire growth . . . 130
A.1.3. Temperature measurement . . . 130
A.1.4. Reflection high-energy electron diffraction (RHEED) . . . 131
A.2. Transmission electron microscopy (TEM) . . . 133
A.2.1. Energy-dispersive X-ray spectroscopy (EDX) . . . 133
A.2.2. Differential phase contrast microscopy (DPC) . . . 133
A.3. Reciprocal space mapping (RSM) . . . 135
A.4. Micro-photoluminescence (µPL) spectroscopy . . . 136
A.5. Superconducting quantum interferometry (SQUID) . . . 136
A.6. Magnetic force microscopy (MFM) . . . 136
A.7. Magnetotransport measurements . . . 137
A.8. Wet chemical etching of Si oxides . . . 137

B. Binary phase-diagrams **139**

C. Publications **143**

D. Abbreviations **145**

Bibliography **147**

Acknowledgments **165**

1. Introduction

Semiconductor nanowires have been extensively studied for the past twenty years [1] in order to unveil their novel properties, stemming from the wire-like geometry. Thus, nanowires may offer promising perspectives for multiple applications in the electronic and optoelectronic realm. For instance, nanowires can be used as field effect transistors [2], light emitting devices [3], lasers [4, 5] and solar cells [6]. Furthermore, nanowires may be used in future nanoscale spintronic devices [7]. However, to optimize these applications, or to fulfill the requirements for new applications, special prerequisites are demanded, like the growth of well-defined nanowire heterostructures, and the usage of specific substrates. In order to fulfill these prerequisites, some major challenges in nanowire growth have to be overcome.

A first task is the growth of uniform nanowires with a well-defined and reproducible size and shape. Commonly, nanowires grow through the formation of self-organized liquid catalyst particles, whose sizes and positions are randomly distributed, and can be controlled to a certain extent only. A precisely controllable growth method would involve the usage of structured masks [8, 9, 10, 11], which passivate most of the surface of the substrate. However, this method is technically difficult, and its success has been limited for different nanowire and substrate materials. Thus, this growth technique is an active field of investigation.

Due to the nanowire geometry and the consequential large surface to volume ratio, in III-V semiconductor nanowires the cubic zinc-blende and the hexagonal wurtzite crystal structure are stable [12]. This zinc-blende/wurtzite polytypism leads to the coexistence of both crystal structures in single nanowires. Thus, the main challenge in compound semiconductor nanowire growth is the control of the crystal structure [13, 14]. Especially in the GaAs system, the growth of phase pure structures without inclusions of the other crystal structure are rarely seen. As the wurtzite band structure differs from the zinc-blende one, GaAs nanowires may provide new opportunities. Also, the combination of wurtzite and zinc-blende GaAs crystals in form of heterostructures may be desirable. Thus, the controlled growth of either zinc-blende or wurtzite crystal structure is important. However, this has proven to be challenging, and requires optimization in epitaxy.

When incorporating ferromagnets in nanowire semiconductor devices, spin-dependent functionalities can be introduced in these quasi one-dimensional structures. Due to the nanowire geometry, thereby two different approaches can be performed [15]. The nanowire can be either coated with a ferromagnetic material, i.e. a radial core/shell structure is grown, or ferromagnetic segments can be incorporated axially into the semiconductor nanowire in the form of segments. In both approaches, the epitaxial growth

of ferromagnet/semiconductor nanowire heterostructures with a large lattice mismatch may allow higher qualities compared to planar 2D growth, as nanowires easily absorb strain via a relaxation of the lattice in radial direction [16, 17].

In the GaAs system, for the growth of ferromagnetic core/shell structures, the diluted magnetic semiconductor (Ga,Mn)As [18] can easily be used, as here only additionally magnetic Mn atoms are introduced in the GaAs lattice. Here, the shell grows pseudomorph onto the GaAs core, i.e. adopts the crystal structure of the GaAs core nanowire [19]. This behavior enables the growth of wurtzite (Ga,Mn)As exclusively in GaAs/(Ga,Mn)As core/shell structures. Compared to (Ga,Mn)As films on GaAs substrates, however, the up to now produced core/shell structures possess a reduced quality, reflected in the maximum Curie temperatures of 20 K [19, 20] compared to 190 K [21] in 2D (Ga,Mn)As films.

In case of the axial integration of ferromagnets into III-V semiconductor nanowires, very few progress is done. Only recently, MnAs segments in InAs nanowires were realized [22]. The lack of axial ferromagnet/semiconductor heterostructures can be attributed to the complex realization of axial segments of a foreign material within a semiconductor nanowire in epitaxy.

The aim of this work is twofold: On the one hand, we explore the controlability of the GaAs nanowire growth concerning orientation, shape and crystal structure. These are necessary steps, since the growth of GaAs nanowires proceeds not necessarily uniformly, and in GaAs nanowires the in bulk unstable wurtzite phase, and the usual observed zinc-blende crystal phase may coexist in one and the same nanowire. On the other hand, we include ferromagnetic materials into GaAs nanowires. To do that, we produce either GaAs/(Ga,Mn)As core/shell structures, or grow ferromagnetic nanoscale MnAs segments in GaAs nanowires.

This thesis is structured as follows: In chapter 2, the fundamental principles of GaAs nanowire growth are summarized concerning growth kinetics and crystal structure. Furthermore, it covers the properties of GaAs nanowires in general. Chapter 3 treats the characteristics of the ferromagnetic materials used in this work. The integration of GaAs nanowires on Si substrates is examined in chapter 4. Here, also the methods to obtain phase pure GaAs nanowire crystal phases are described. Photoluminescence experiments on phase pure wurtzite and zinc-blende GaAs nanowires are performed in chapter 5. Additionally, the stimulation of GaAs nanowires to lasing operation is shown. In chapter 6 spontaneous polarization in WZ GaAs is uncovered. The growth of radial and axial magnetic heterostructures, as well as the evaluation of the magnetic properties of these structures is described in chapters 7 and 8. Finally, all results of this thesis are summarized in chapter 9.

2. GaAs nanowires: Fundamental principles

In this chapter, the fundamental principles of GaAs nanowire growth, as well as the general characteristics of GaAs nanowires are described.

GaAs nanowires grow on substrates in a bottom-up process, when Ga atoms and As atoms are simultaneously supplied, and suitable growth conditions are chosen. This process is usually either performed with molecular beam epitaxy (MBE) under ultra-high vacuum, or with molecular vapor phase epitaxy (MOVPE) using carrier gasses. In this work, the nanowires are grown with MBE only, so for this kind of epitaxy the kinetics of the growth process is described in the first part of this chapter (section 2.1).

GaAs nanowires usually possess a mixed crystal structure. It consists of the GaAs bulk phase, which is zinc-blende (ZB), and the, in bulk crystals unstable, wurtzite (WZ) phase. The occurrence of WZ GaAs in nanowires enables to study the physical properties of this unconventional GaAs phase, once a WZ GaAs nanowire crystal of sufficient quality can be produced. In section 2.2, models explaining the preferential nucleation of either ZB or WZ crystal structure in GaAs nanowires are introduced. By interpreting these models, ideal conditions for the growth of phase pure ZB and WZ GaAs nanowires are deduced. On the basis of the derived conditions, the growth of GaAs nanowires will be optimized towards phase pure crystal phases in a later section (section 4.3).

The general properties of GaAs nanowires are summarized in section 2.3. Here, the structural differences between the ZB and the WZ phase are shown. As both crystal phases exhibit a direct band gap, the application of GaAs nanowires for optical spectroscopy is evaluated. Furthermore, the occurrence of spontaneous polarization in the WZ crystal phase is introduced.

2.1. VLS growth mechanism: Growth kinetics

In this section we start with a historical evolution of the description of nanowire growth (section 2.1.1). Then, following the latest models, the kinetics of the transitions between the different atomic states, which are adopted by the Ga and As atoms during nanowire growth, is described. The transition rates are derived as a function of intrinsic parameters, which describe the states as well as the surrounding environment.

Since the kinetic of transitions is accompanied by the exchange of particles, in section 2.1.2 the chemical potentials of all states are introduced. Using transition state theory (section 2.1.3), the current of matter towards a liquid state, which catalyzes nanowire growth, is described in section 2.1.4. After introducing the principle of adatom diffusion in section 2.1.5, quantitative estimations of the current of matter are given in section

2.1.6. Additionally, Ga adatom diffusion during nanowire growth is considered in section 2.1.7. The transition of atoms from the catalyst to the solid phase, i.e. the nanowire growth, is kinetically described in section 2.1.8. Eventually, a summary is given in section 2.1.9.

2.1.1. Modelling nanowire growth

The growth of "nanowires" or "nanowhiskers" was first described by Wagner and Ellis in 1964 [23], who used Au particles on a Si substrate to grow Si whiskers: by thermal heating, small droplets of a liquid Au-Si alloy form on the substrate. When additionally providing silicon, the alloy acts as a sink for the arriving atoms, which nucleate at the liquid/solid interface and form a Si nanocrystal with the liquid droplets "riding" atop. Wagner and Ellis determine the growth directions of those whiskers to be $\langle 111 \rangle$ directions, while their side facets consist of $\{11\overline{2}\}$ or $\{110\}$ planes. The growth mode, which they call "Vapor-Liquid-Solid (VLS) mechanism", is named after the subsequently adopted phases of the used material. This VLS mechanism proceeds as long as the liquid droplets remain atop the whiskers, or the growth conditions are changed drastically. Later, Wagner and Ellis found that the VLS mechanism works not only for the catalysis of Si-whiskers from a liquid Au-Si alloy, but also from other metals forming an alloy with Si [24].

First kinetic descriptions of the VLS growth of GaAs nanowhiskers from an Au-Ga alloy were done by Givargizov in 1975 [25]. He derived the vertical nanowhisker growth rate from the difference in chemical potentials of the materials in the vapor, the liquid and the solid phase. In 2004, Dubrovskii et al. [26] generalized the theory of Givargizov, and derived the growth rates for nanowhiskers by applying the Kolmogorov, Johnson, Mehl and Avrami (KJMA) model, which gives a mean crystallization rate for phase transitions.

In 2005, Dubrovskii et al. proposed a model for the diffusion induced growth of GaAs nanowhiskers in MBE [27], since the direct impinging flux of atoms onto the liquid droplet cannot account for the large growth rate of the nanowires. Thus, the nanowire growth rate was estimated using Fick's diffusion equations for Ga adatom motion on the nanowire side facets [27]. This model was consecutively improved by considering the adsorption and desorption of adatoms in the liquid droplet, and the radial growth of the nanowire side facets [28].

The theory concerning the nucleation of solid GaAs from the liquid droplet was developed by Glas et al. in 2007 [13], who explained for the first time the occurrence of the hexagonal wurtzite (WZ) crystal structure in nanowires besides the bulk zinc-blende (ZB) phase. In 2008, Dubrovskii and Glas together developed a model to describe the growth kinetics in semiconductor nanowire growth and the precipitating crystal structure simultaneously [29]. After adding surface adatom diffusion and a change in the chemical potential in the liquid due to the Gibbs-Thomson effect in 2009 [30], the description of the GaAs nanowire growth seemed to be sufficient.

But in 2008, Colombo et al. [31] explored a growth mechanism for GaAs nanowires

without any foreign catalyst material. Here, liquid Ga droplets form at the substrate, which promote the growth of GaAs nanowires underneath. So the nucleation model had to be slightly altered. The conditions for the nucleation of WZ or ZB crystal structure were first adopted from the Au-catalyzed regime [32]. The transition from the Au-catalyzed to the Ga-catalyzed growth mode, together with the nucleating crystal structure was addressed by Soda et al. [33]. Krogstrup et al. [34] gave the shape of the liquid droplet a crucial impact on the precipitating crystal structure, and finally published a summary of III-V nanowire growth dynamics in general in 2013 [35].

In the following sections, based on the latest publication [35], the kinetics of nanowire growth is derived from thermodynamics and transition state theory. To do that, first the chemical potentials of all atomic states contributing to nanowire growth are evaluated.

2.1.2. Chemical potentials of atomic states

When an exchange of particles between different states is determined, it is convenient to characterize the states via their chemical potentials. The chemical potential μ of a phase P with N atoms of kind i can be derived from the differential of the Gibbs free energy G of a system, which has the common form [36]

$$dG = -SdT + Vdp + \sum_{P,i} \mu_{P,i} dN_{P,i} + \sum_{k} \gamma_k dA_k + \sum_{k} X_k dx_k. \tag{2.1}$$

Here, S denominates the entropy, T the temperature, V the volume, p the pressure and dA the area of an interface k with the interfacial energy γ_k. In general, all these terms describe forces X_k acting against a variation of the corresponding extension variable x_k.

To compare chemical potentials of different states among each other, one commonly calculates the difference to an arbitrary reference potential or "equilibrium reference state" (ERS). For that, Krogstrup et al. [35], use the chemical potential of the infinite solid GaAs phase $\mu^{\infty}_{s,GaAs}$. It is a function of the temperature only, since its stoichiometry is fixed to 1:1.

To determine the chemical potential of the ERS of a single phase i, μ_i^{ERS}, we consider a system consisting of a liquid alloy of Ga+As and solid GaAs only. This system describes exemplarily a part of the Ga-catalyzed nanowire growth system. Here, μ_i^{ERS} is given by the chemical potential of the liquid phase when solid and liquid are in equilibrium. For $i = Ga$, this reads [35]

$$\mu_{Ga}^{ERS} \equiv \mu^{\infty}_{l,Ga}(x_{Ga}^{ERS}, x_{As}^{ERS}) = \mu^{\infty}_{s,GaAs} - \mu^{\infty}_{l,As}(x_{Ga}^{ERS}, x_{As}^{ERS}). \tag{2.2}$$

∞ means large phases without size effects like the Gibbs-Thomson effect, and $x_{Ga/As}^{ERS}$ denominates the ERS mole fraction of Ga or As in the liquid phase, $x_{Ga} + x_{As} = 1$.

The parameters determining the chemical potential of the liquid in eq. 2.2 are the temperature, x_{Ga}^{ERS} and x_{As}^{ERS}. However, the mole fractions in the liquid are also a function of the temperature only and set by the GaAs binary phase diagram. Therefore, in this system both μ_i^{ERS} are set by the temperature. This dependency does not change

when the Ga-catalyzed nanowire growth system is described in full extension, i.e. when other equilibrium states participate [35]. Thus, in the case of Ga-catalyzed nanowire growth, only one parameter (the temperature) determines the chemical potential of the equilibrium reference states of Ga and As.

If growth is catalyzed by a foreign element like gold, one needs to include a second parameter, like the concentration of one element in the liquid, to define the ERS in the liquid [35]. Since the thermodynamic properties of the ternary As-Au-Ga liquid system have already been calculated [37], one can relate the thermodynamic properties of the ternary liquid system to those of the binary liquid system. Thus, for general considerations, $x_{Au} = 0$ and the same ERS as for Ga-catalyzed nanowire growth can be chosen.

The states, that need to be considered for each element in nanowire growth are depicted in fig. 2.1a: The beam (b) and the vapor (v) states, which sum up the supplied material from the gaseous phase including re-emitted and evaporated atoms from any surfaces in the growth chamber. The adatom (a) state, which can be adopted by the supplied species and supports the flow of matter to the liquid (l) state. The liquid state catalyzes the incorporation of matter into the solid (s) state, leading to nanowire growth.

The chemical potentials $\mu_{p,i}$ of an atom i in the state p with respect to the ERS [35],

$$\delta\mu_{p-ERS,i} = \mu_{p,i} - \mu_i^{ERS}, \tag{2.3}$$

are evaluated in equations 2.4 to 2.7 for the four states accounting for the equilibrium in the whole system (v, a, l and s) [35]:

$$\delta\mu_{v-ERS,i}\left(p_i, T\right) = k_B T \cdot \ln\left(\frac{p_i}{p_i^{ERS}}\right) \tag{2.4}$$

$$\delta\mu_{a_j-ERS,i}\left(\rho_{j,i}, T\right) = k_B T \cdot \ln\left(\frac{\rho_{j,i}}{\rho_{j,i}^{ERS}}\right) \tag{2.5}$$

$$\delta\mu_{l-ERS,i}\left(x_{Ga}, x_{As}, T\right) = \mu_{l,i}^{\infty}\left(x_{Ga}, x_{As}, T\right) + \gamma_{vl}\frac{\partial A_{vl}}{\partial N_{l,i}} - \mu_i^{ERS} \tag{2.6}$$

$$\delta\mu_{s-ERS,GaAs}^{X} = \sum_j \gamma_j \frac{\partial A_j}{\partial X}\frac{\partial X}{\partial N_{s,GaAs}} + \Delta\epsilon_s \tag{2.7}$$

Equation 2.4 describes the chemical potential of the vapor phase, calculated for an ideal gas with respect to the ERS. Equation 2.5 depicts the chemical potential of the adatom phase with respect to the ERS, assuming low adatom concentrations $\rho_{j,i}$ on the j-th facet and low adatom binding energies [35]. Equation 2.6 determines the chemical potential of an atom in the liquid phase with respect to the ERS. Here, an infinite liquid is considered together with the Gibbs-Thomson effect of a small liquid phase of N_l atoms possessing a vapor/liquid interface area A_{vl} and surface energy of γ_{vl} [35]. In equation 2.7, the chemical potential of a GaAs pair in the solid with respect to the ERS of an infinite GaAs crystal is calculated. Since adding matter to a finite sized crystal results in the

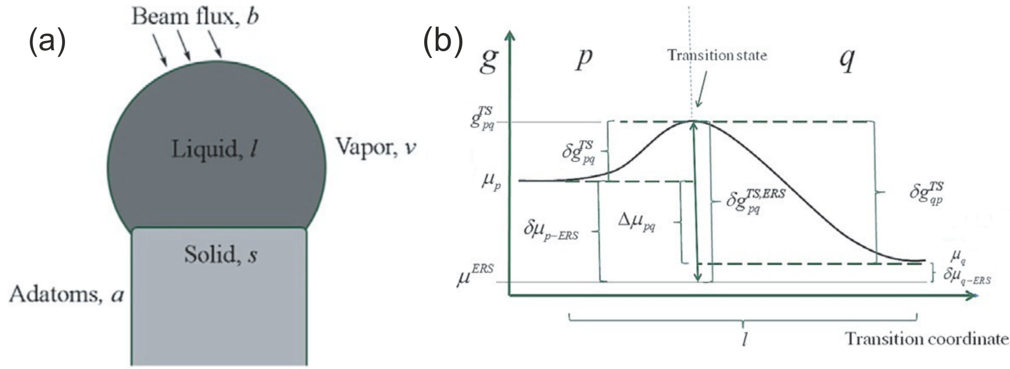

Figure 2.1.: (a) Sketch of a nanowire tip: the phases contributing to the growth of nanowires via the VLS mechanism are depicted. (b) Chemical potentials for a phase transition from state p to state q via a transition state (TS). The potential of an state used as reference value is labeled μ^{ERS}. For further details, see text. Adopted from [35].

change of its shape and its volume, a set of parameters X, like lengths and angles, is necessary to describe the crystal completely [35, 36]. This is summed up in the first term. The second term corresponds to the difference in bulk cohesive energy between the ERS and the actually forming structure s, taking into account the GaAs nanowire related zinc-blende/wurtzite polytypism [35]. It is zero when the ERS and the actual forming state possess the same crystalline structure.

2.1.3. Transition state theory

The transition rate between two atomic states can be deduced from transition state theory [38]. Here, a potential for a transition state (TS) is introduced, summing up the Gibbs free energy necessary for the activation of the transition. The relations of the chemical potentials involved in the transition from a state p to a state q via a TS are sketched in fig. 2.1b. In the following, the effective flux of matter for this kind of transition is evaluated.

The flux of atoms i from a state p to a state q depends on the difference in chemical potential between the TS and the initial state p, $\delta g_{pq,i}^{TS}$ [35]. Additionally, the chemical potentials of the initial state and the TS, μ_p and $g_{pq,i}^{TS}$, can be expressed with respect to the chemical potential of the ERS, μ^{ERS}: $\delta\mu_{p-ERS,i} = \mu_{p,i} - \mu_i^{ERS}$ (eq. 2.3) and $\delta g_{pq,i}^{TS,ERS} = g_{pq,i}^{TS} - \mu^{ERS}$. Then, the mean flux of atoms $\Gamma_{pq,i}$ from state p to state q equals [35]

$$\Gamma_{pq,i} = \Xi_{pq,i}\bar{c}_{p,i} \exp\left(-\frac{\delta g_{pq,i}^{TS}}{k_B T}\right), \text{ if } \delta g_{pq,i}^{TS,ERS} \geq \delta\mu_{p-ERS,i}, \text{ and} \tag{2.8}$$

$$\Gamma_{pq,i} = \Xi_{pq,i}\bar{c}_{p,i}, \text{ if } \delta g_{pq,i}^{TS,ERS} \leq \delta\mu_{p-ERS,i} \text{ (barrier free transition).} \tag{2.9}$$

Here, $\Xi_{pq,i}$ accounts for the number of attempts per atom to pass from state p to the TS per unit time and unit area, whereas $\overline{c}_{p,i}$ is the probability of meeting an atom i in the state p. The form of $\Xi_{pq,i}$ depends on the considered state [35]. For a condensed state (a, l or s), $\Xi_{pq,i}$ has the form $\Xi_{pq,i} = Z_{pq,i}\nu_{p,i}$, with $Z_{pq,i}$ being the steric factor of the p to q transition per unit area, and $\nu_{p,i}$ being the vibration frequency of the atom in state p. For the gas states (b or v) $\Xi_{pq,i} = S_{b(v)q,i} f^{\perp}_{b(v)}/\overline{c}_{b(v),i}$. Here, $S_{b(v)q,i}$ is the sticking coefficient for the b or v atoms and $f^{\perp}_{b(v)}$ the effective flux of atoms from the b or v states impinging normal to the interface.

To calculate the effective flux $\Delta\Gamma_{pq,i}$ from state p to state q across a TS, the backward flux has to be taken into account as well [35]:

$$\Delta\Gamma_{pq,i} = \Gamma_{pq,i} - \Gamma_{qp,i}. \tag{2.10}$$

By assuming zero net flux across the barrier ($\Delta\Gamma^{ERS}_{pq,i} = 0$) at ERS conditions ($\delta\mu_{p-ERS} = \delta\mu_{q-ERS} = 0$), a relation between the prefactors $\Xi_{pq,i}$ and $\Xi_{qp,i}$ can be deduced. With this relation, and by taking into account transition state barriers for both directions, the effective flux reads [35]

$$\begin{aligned}\Delta\Gamma_{pq,i} = \Xi_{pq,i} \exp\left(-\frac{\delta g^{TS,ERS}_{pq,i}}{k_B T}\right) \cdot \Bigg[\overline{c}_{p,i} \exp\left(\frac{\delta\mu_{p-ERS,i}}{k_B T}\right) \\ - \frac{\overline{c}^{ERS}_{p,i}}{\overline{c}^{ERS}_{q,i}} \overline{c}_{q,i} \exp\left(\frac{\delta\mu_{q-ERS,i}}{k_B T}\right)\Bigg].\end{aligned} \tag{2.11}$$

This expression describes the exchange of matter between all atomic states.

In the following, with equation 2.11 the terms for the transition of atoms to the liquid phase state are derived, which acts as a catalyst for GaAs nanowire growth.

2.1.4. Flow of matter towards the catalyst

Due to mass conservation, the atomic flow to and from the liquid phase can be written as [39]

$$\frac{d}{dt} N_l = I_{Ga} + I_{As} - I_{inc}. \tag{2.12}$$

Here, N_l is the number of atoms in the liquid, and I_i describe the effective sorption currents of group i atoms from the adatom and from the gas phase to the liquid phase [35],

$$I_i = \int \Delta\Gamma_{al,i} dl_{TL} + \int \Delta\Gamma_{(vb)l,i} dA_{vl}. \tag{2.13}$$

I_{inc} is the effective atomic incorporation current from the liquid to the solid, which will be addressed in section 2.1.8. dl_{TL} describes an infinitesimal part of the triple phase line length L_{TL} [35], i.e. the line where vapor, liquid and solid meet, and that is crossed by adatoms reaching the droplet (compare fig. 2.1a). A_{vl} denominates the projected liquid-vapor surface area [37], which is exposed to the respective gaseous phases.

To relate the state of the liquid phase with the beam and vapor phase, no transition state barrier for sorption in the liquid droplet is assumed [35]. At equilibrium vapor pressure p_i^{eq}, the rate of emitted atoms from the liquid equals the rate of adsorbed atoms from the vapor and the beam phase, and is given by $\Gamma_{lv} = p_i^{eq}/\sqrt{2\pi m_i k_B T}$ [36]. Knowing that any state in the vapor or beam phase is occupied, $\overline{c}_{vb,i}^{ERS} = 1$, equation 2.11 reads for the $(vb) \rightarrow l$ state transition [35]

$$\Delta\Gamma_{(vb)l,i} \cong f_{i,\perp} - \frac{x_i}{x_i^{ERS}} \frac{p_i^{ERS}}{\sqrt{2\pi m_i k_B T}} \exp\left(\frac{\delta\mu_{l-ERS,i}}{k_B T}\right). \tag{2.14}$$

Here, $f_{i,\perp} = f_{b,i,\perp} + f_{v,i,\perp}$ is the effective impinging flux of group i atoms. At typical growth conditions with $f_{As} > f_{Ga}$, the As vapor flux is proportional to the As beam flux, $f_{v,As} \propto f_{b,As}$, since a large contribution of As atoms stems from secondary adsorption [40]. Secondary adsorption of Ga can be neglected since adatom diffusion plays a more dominant role for Ga (see section 2.1.6). Introducing $A_{vl}^{'}$ as the projection of the liquid surface A_{vl} exposed to the incident beam flux $f_{b,i}$ [37], the sorption current from the vapor or beam phase reads [35]

$$\int \Delta\Gamma_{(vb)l,i} dA_{vl} \cong A_{vl} \left[f_{v,\perp} - \frac{x_i}{x_i^{ERS}} \frac{p_i^{ERS}}{\sqrt{2\pi m_i k_B T}} \exp\left(\frac{\delta\mu_{l-ERS,i}}{k_B T}\right)\right] + A_{vl}^{'} f_{b,i}. \tag{2.15}$$

The net flux from the adatom to the liquid phase can be evaluated assuming no transition state barrier for sorption from the adatom state. For adatoms, not every state is occupied, $\overline{\rho}_i^{ERS} \neq 1$, so $\Delta\Gamma_{al,i}$ reads [35]

$$\Delta\Gamma_{al,i} \cong \Xi_{al} \left[\overline{\rho}_i - \overline{\rho}_i^{ERS} \frac{x_i}{x_i^{ERS}} \exp\left(-\frac{\delta\mu_{a-ERS,i} - \delta\mu_{l-ERS,i}}{k_B T}\right)\right]. \tag{2.16}$$

Then, the atomic flow from the adatom to the liquid state is determined to [35]

$$\int \Delta\Gamma_{al,i} dl_{TL} \cong L_{TL} \Xi_{al} \left[\overline{\rho}_i - \overline{\rho}_i^{ERS} \frac{x_i}{x_i^{ERS}} \exp\left(-\frac{\delta\mu_{a-ERS,i} - \delta\mu_{l-ERS,i}}{k_B T}\right)\right]. \tag{2.17}$$

With this, the atomic flow of matter towards the liquid catalyst droplet is fully described by thermodynamics and transition state theory. However, this description of the dynamics between the states contributing to the nanowire growth is not very intuitive. To assess the amount of adatoms reaching the liquid droplet in dependence on the chemical potentials and the temperature qualitatively, in the next section the principle of diffusing adatoms is introduced.

2.1.5. Diffusion of adatoms in general

To obtain a better understanding of the adatom kinetics in the transition state approach, a description for adatom migration on a large homogenous surface is introduced. Here, no net diffusion exists, and all parameters are invariant on translation [35]. Consequently,

one needs to consider three main transition paths for an adatom only: surface diffusion ($a \rightarrow a$), desorption ($a \rightarrow v$) and incorporation ($a \rightarrow s$) at a favorable crystal site [35]. The mean distance for an atom i to travel on an interface j between adsorption from the vapor or beam state to the adatom state, and desorption or incorporation in the crystal, is called diffusion length [35]

$$\lambda_{j,i} = \sqrt{D_{j,i}\tau_{j,i}}. \tag{2.18}$$

Here,

$$D_{j,i} = \overline{Z}_{aa,i}\nu_{a,i}l_j^2\left(1-\overline{\rho}_{j,i}\right)\exp\left(-\frac{\delta g_{aa,i}^{TS}}{k_BT}\right) \tag{2.19}$$

is the mean adatom diffusivity on the j-th surface and

$$\tau_{j,i} = \left(\frac{1}{\tau_{j,i,as}} + \frac{1}{\tau_{j,i,av}}\right)^{-1} \tag{2.20}$$

is the average adatom lifetime [35]. $\overline{Z}_{aa,i}$ denotes the mean steric factor for a transition between two adjacent adatom sites with spacing l_j along the lowest energy path with an activation free energy of $\delta g_{aa,i}^{TS}$. $\nu_{p,i}$ is the vibration frequency of the adatoms and $\overline{\rho}_{j,i}$ the normalized adatom density, which gives the probability of an adatom to hop on a free site $\left(1-\overline{\rho}_{j,i}\right)$. The lifetimes of an adatom, until an $a \rightarrow s$ or an $a \rightarrow v$ state transition takes place, are inversely proportional to the respective transition rates [35],

$$\tau_{j,i,as} = \frac{1}{\overline{Z}_{as,i}\overline{c}_{inc,i}\nu_{a,i}}\exp\left(\frac{\delta g_{as,i}^{TS}}{k_BT}\right), \text{ and} \tag{2.21}$$

$$\tau_{j,i,av} = \frac{1}{\overline{Z}_{av,i}\nu_{a,i}}\exp\left(\frac{\delta g_{av,i}^{TS}}{k_BT}\right). \tag{2.22}$$

Here, $\overline{c}_{inc,i}$ describes the normalized density of incorporation sites. The difference between both transitions is, that desorption can take place everywhere, whereas incorporation into the solid is considered to happen only at favored sites like kinks and steps.

With equations 2.18 to 2.22, the adatom diffusion length on a homogenous interface is described by

$$\lambda_{j,i} = \sqrt{\frac{\overline{Z}_{aa,i}l_j^2\left(1-\overline{\rho}_{j,i}\right)\exp\left(-\frac{\delta g_{aa,i}^{TS,ERS}}{k_BT}\right)}{\overline{Z}_{as,i}\overline{c}_{inc,i}\exp\left(-\frac{\delta g_{as,i}^{TS,ERS}}{k_BT}\right)+\overline{Z}_{av,i}\exp\left(-\frac{\delta g_{av,i}^{TS,ERS}}{k_BT}\right)}}, \tag{2.23}$$

which is independent on the chemical potential $\mu_{a,i}$ and the vibration frequency $\nu_{a,i}$ of the adatoms [35]. However, the number of incorporation sites $\overline{c}_{inc,i}$ depends on the local adatom densities of both atomic components and on the facet orientation [35]. Therefore, this value is dependent on the chemical potential of the local adatom state.

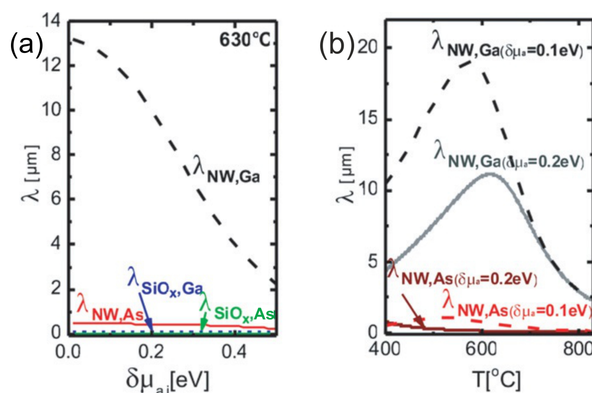

Figure 2.2.: (a) Diffusion lengths for Ga and As adatoms on GaAs nanowire side facets and on a SiO_x passivated substrate in dependence on the chemical potential of the adatom state $\mu_{a,i}$: At $T = 630°C$, the diffusion lengths for Ga and As on SiO_x as well as for As on the side facets are negligibly low. However, the diffusion length of Ga on the side facets is substantial. In the case of Ga, the behavior on the side facets is attributed to a low activation energy for adatom-adatom state transitions and a high one for desorption. Instead for As, it is vice versa. (b) For $\mu_{a,i} = 0.1$ eV and 0.2 eV, the diffusion lengths on the side facets are calculated in dependence on the temperature: Since desorption prevails at high temperatures and crystal growth on the substrate at low temperatures, the diffusion length of Ga is highest for intermediate temperatures. As adatoms reside at these temperatures in the desorption limited regime with negligibly low diffusion lengths. Adopted from [35].

2.1.6. Diffusion of Ga and As adatoms

To determine the diffusion lengths of Ga and As adatoms explicitly, Krogstrup et al. assume no barrier for $a \rightarrow s$ transitions [35]. Additionally, they transform equation 2.23 slightly, to be able to use calculated activation enthalpies for the different TS activation energies [41]. They further assume a low density of adatoms, $\left(1 - \overline{\rho}_{j,i}\right) \approx 1$, and a density of incorporation sites $\overline{c}_{inc,i}$, which depends strongly on the chemical potential of the adatom state ($\propto \exp\left(\delta\mu_{a,i}/k_B T\right)$) [35].

In figs. 2.2 the calculated diffusion lengths for Ga and As on GaAs nanowire sidewalls ($\{1\bar{1}0\}$ side facets), and on a with silicon oxide (SiO_x) passivated substrate are shown [35]. The diffusion lengths are depicted in fig. 2.2a as a function of the chemical potential of the adatom state $\delta\mu_{a,i}$, and in fig. 2.2b as a function of the growth temperature T.

For a typical nanowire growth temperature of 630°C the diffusion lengths of As and Ga of adatoms on the passivated substrate ($\lambda_{SiO_x,i}$) are negligible, independent on the chemical potential $\delta\mu_{a,i}$ (fig. 2.2a). Obviously, both kinds of atoms reside in a regime, where desorption prevails [35]. However, the diffusion length of Ga adatoms on the nanowire side facets ($\lambda_{NW,Ga}$) is by far higher than the one of As adatoms ($\lambda_{NW,As}$): the minimum activation energy for an adatom-adatom transition on the side facets is roughly twice as high for As adatoms than for Ga adatoms, and the activation energy for

desorption is less for As adatoms than for Ga adatoms [41]. Additionally, we see, that the diffusion lengths generally decrease with $\delta\mu_{a,i}$. This is reasonable, since an elevated chemical potential of the adatom state goes along with an elevated adatom density (equation 2.5). An elevated adatom density reduces the probability for an adatom to hop on a free adatom-site, and therefore reduces adatom diffusion.

Considering the temperature-dependence of the diffusion lengths on nanowire side facets in fig. 2.2b, one observes a clear peak-behavior for Ga adatoms, whereas the diffusion length of As adatoms is negligibly low. These behaviors are independent on different chemical potentials of the adatom state, while an elevated $\delta\mu_{a,i}$ generally decreases the diffusion length, see above. The peak behavior of Ga adatoms is explained by a prevailing incorporation of adatoms into the GaAs crystal at low temperatures, whereas at high temperatures one resides in the desorption limited regime. Both mechanisms, desorption and crystal growth, decrease the diffusion length. Consequently, the diffusion length, and coincidentally, the amount of adatoms diffusing towards the liquid droplet, is highest for intermediate temperatures, with a maximum at approximately 600°C. Instead, the diffusion length of As remains very low in the whole temperature range, indicating prevailing desorption.

Thus, in models describing the kinetics of nanowire growth, Ga adatoms are considered to contribute to the formation of the liquid catalyst at the wire tip. Instead, As is considered as immobile on the side facets, and reaches the droplet exclusively via the beam or vapor phase. The effective sorption current of As atoms, I_{As}, to the liquid phase is therefore determined by equation 2.15. The value of this term is not dependent on the growth time, i.e. the length of the nanowires and the corresponding change of the nanowire surrounding. This finding is attributed to the As-limited growth rate (see section 2.1.8), which remains constant during the whole growth of nanowires for constant As beam fluxes [40, 42]. In contrast, the effective flux of Ga atoms to the liquid catalyst is additionally determined by surface and side facet diffusion, and changes with the length of the nanowires.

2.1.7. Ga adatom diffusion towards the liquid catalyst

To determine the net flux of Ga atoms reaching the droplet via diffusion, the adatom concentrations on the nanowire side facets ρ_{NW} and on the planar substrate ρ_{sub}, are considered in a classical Fickian diffusion regime [30]. Assuming stationary adatom concentrations ρ_j and an isotropic diffusion constant D_j on each interface j, the second Fickian equation holds,

$$\frac{\partial \rho_j}{\partial t} = D_j \vec{\nabla}^2 \rho_j. \tag{2.24}$$

For adatom diffusion on the nanowire side facets, this equation reads

$$D_{NW} \frac{\rho_{NW}(z)}{\lambda_{NW}^2} - f_{NW,\perp} - \Gamma_{sa(NW)} - \Gamma_{va(NW)} = D_{NW} \frac{d^2}{dz^2} \rho_{NW}(z), \tag{2.25}$$

with z being the vertical coordinate along the nanowire [35]. D_{NW} is set by equation 2.19, λ_{NW} by equation 2.23, and $f_{NW,\perp} = \frac{1}{2} \cdot f \sin\varphi$ is the average incoming Ga flux. The factor $\frac{1}{2}$ takes into account the fraction of the nanowire side facets exposed to the beam, while φ is the angle of the Ga beam with respect to the substrate normal. $\Gamma_{sa(NW)}$ and $\Gamma_{va(NW)}$ describe the effective fluxes from the solid and the vapor state to the adatom state on the nanowire side facet [35].

For adatom diffusion on the substrate, equation 2.24 reads

$$D_{sub}\frac{\rho_{sub}(r)}{\lambda_{sub}^2} - f_{sub,\perp} - \Gamma_{sa(sub)} - \Gamma_{va(sub)} = D_{sub}\frac{1}{r}\frac{d}{dr}\left(r\frac{d}{dr}\rho_{sub}(r)\right), \tag{2.26}$$

assuming a radial symmetry of the atomic flux towards the nanowire [35]. In this case $f_{sub,\perp} = f\cos\varphi$, while all other parameters possess the same shape as in equation 2.25.

Both diffusion equations (equation 2.25 and equation 2.26) have to satisfy three boundary conditions [30], namely, that the adatom concentration at the side facet/substrate interface is equal,

$$\rho_{NW}\big|_{z=0} = \rho_{sub}\big|_{r=\frac{d_{NW}}{2}}, \tag{2.27}$$

and that the adatom density is continuous at the very same spot

$$D_{NW}\left.\frac{d\rho_{NW}}{dz}\right|_{z=0} = -D_{sub}\left.\frac{d\rho_{sub}}{dr}\right|_{r=\frac{d_{NW}}{2}}. \tag{2.28}$$

Additionally, the adatom density at the substrate surface far away from the nanowire is assumed to be constant,

$$\left.\frac{d\rho_{sub}}{dr}\right|_{r\to\infty} = 0, \tag{2.29}$$

ignoring effects from other nanowires.

The exact solutions for the adatom densities ρ_{NW} and ρ_{sub} can be obtained, which are page-filling [35] and hardly computable, and therefore not shown here. Instead, a result for the net flux of Ga adatoms to the liquid droplet for a simplified model is shown, assuming no effective flux from the solid to the adatom state and from the vapor to the adatom state ($\Gamma_{sa} = 0$ and $\Gamma_{va} = 0$). The latter simplification implies that all matter is supplied by an incoming effective Ga flux f. The solution can be estimated by first solving the coupled diffusion equations taking into account the boundary conditions, so expressions for ρ_i are found. The net flux of Ga adatoms into the liquid droplet, $\Delta\Gamma_{al}$, can then be determined by solving the first Fickian equation at the nanowire top ($z = L_{NW}$) [43],

$$\Delta\Gamma_{al} = -D_{NW}\left.\frac{d\rho_{NW}}{dz}\right|_{z=L_{NW}}. \tag{2.30}$$

Then, the diffusion induced flux towards the liquid catalyst reads [43]

$$\Delta\Gamma_{al} = d_{NW}\pi f\left[\frac{\sin\varphi}{2}\lambda_{NW}\tanh\left(\frac{L_{NW}}{\lambda_{NW}}\right) + \frac{\cos\varphi\lambda_{sub}}{\cosh\left(\frac{L_{NW}}{\lambda_{NW}}\right)}\frac{K_1\left(\frac{d_{NW}}{2\lambda_{sub}}\right)}{K_0\left(\frac{d_{NW}}{2\lambda_{sub}}\right)}\right]. \tag{2.31}$$

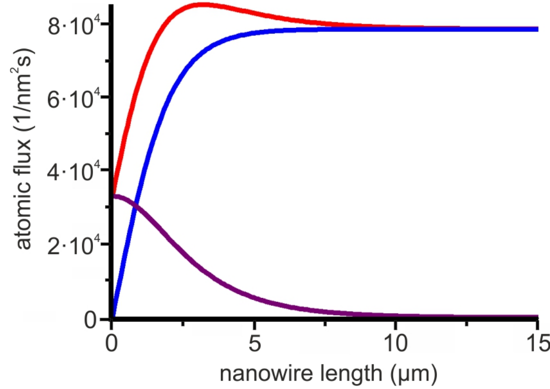

Figure 2.3.: Diffusion induced flux of Ga adatoms towards the liquid catalyst and its dependence on the nanowire length L_{NW} (equation 2.31): The flux of Ga adatoms adsorbing on the substrate and diffusing to the droplet (purple) decreases with increasing nanowire length due to the increasing distance to travel on the wire side facets. The flux of Ga atoms adsorbing on the side facets and diffusing to the liquid (blue) initially increases with the nanowire length. This is dedicated to the increasing side facet surfaces. Finally, this atomic flux gets constant, caused by the diffusion length limited reservoir of adatoms on the side facets. The sum, i.e. the total Ga adatom flux to the liquid catalyst $\Delta\Gamma_{al}$, is depicted in red. The parameters were set as: $d_{NW} = 50$ nm, $\varphi = 30°$, $\lambda_{NW} = 2$ µm, $\lambda_{sub} = 0.1$ µm and $f = 1/\text{nm}^2\text{s}$.

Here, $K_i(x)$ describes the modified Bessel function of the second kind and order i. The first and the second term in equation 2.31 account for Ga atoms adsorbing on the nanowire side facets and the substrate, respectively [43].

Fig. 2.3 graphically illustrates $\Delta\Gamma_{al}$ and its two separate contributions in dependence on the nanowire length. The amount of Ga adatoms reaching the droplet from the substrate (purple) clearly drops with increasing nanowire length, since the distance, which these adatoms have to travel on the side facets, is equal to the nanowire length. Thus, their probability to reach the nanowire tip strongly reduces with increasing nanowire length.

In contrast, the amount of adatoms, which only diffuse from the side facets to the droplet (blue), increases with nanowire length and then saturates. The increase is explained by an increase of the side facet surface with the elongating nanowire, on which more Ga atoms adsorb. When the nanowire length exceeds the side facet diffusion length by far, the amount of adatoms reaching the droplet gets constant, since then the adatom reservoir on the side facets is limited by the diffusion length.

Thus, the total flux of Ga adatoms towards the droplet (red) is lowest at the beginning of the nanowire growth, then increases to a absolute maximum, and decreases again to a constant level. Note that in case of negligible substrate diffusion ($\lambda_{sub} \ll \lambda_{NW}$), the maximum in-between vanishes.

With this, the amount of Ga adatoms feeding the liquid catalyst is derived in dependence on the nanowire length. So, the overall currents of Ga atoms and As atoms

towards the liquid droplet during nanowire growth are determined by equation 2.31 (Ga adatom diffusion) and equation 2.15 (As and Ga flux from the vapor or beam phase). However, to describe the kinetics of the VLS mechanism completely (equation 2.12), the transition from the liquid to the solid state needs to be considered.

2.1.8. The liquid-solid transition

The transition from the liquid phase to the solid phase is usually described under the assumption, that diffusion in the liquid is fast on timescales of nanowire growth, and that the liquid phase is homogenous [35]. Additionally, the VLS growth of GaAs nanowires is considered to happen at the liquid/solid interface only. Here, one distinguishes between growth with the necessity of forming a small nucleus (nucleation limited growth) for the initiation of a new monolayer, and growth without the necessity of forming a small nucleus (nucleation free growth) for the completion of this monolayer [35].

Nucleation free growth

In nucleation free growth, the growth or the rearrangement of facets is only limited by the transfer of single Ga-As atom pairs to the growth front. The transition rate into the solid can be described by equation 2.11, which transforms to [35]

$$\begin{aligned}\Delta\Gamma^{X}_{ls,Ga-As} = {} & \Xi_{ls,Ga-As} \exp\left(-\frac{\delta g^{TS,ERS}_{ls,Ga-As}}{k_B T}\right) \\ & \cdot \left[x_{As} \exp\left(\frac{\delta\mu_{l-ERS,Ga-As}}{k_B T}\right) - x^{ERS}_{As} \exp\left(\frac{\delta\mu^{X}_{s-ERS,Ga-As}}{k_B T}\right)\right] .\end{aligned} \tag{2.32}$$

Here, an activation energy $\delta g^{TS,ERS}_{ls,Ga-As}$ for the $l \rightarrow s$ transition of a Ga-As atom pair is assumed. Also, the concentration of Ga-As pairs in the liquid and the As concentration in the liquid are set equal, $\bar{c}_{Ga-As} = x_{As}$. This is justified, as in the VLS growth of GaAs nanowires, As is the less abundant species in the liquid catalyst [35, 37].

Nucleation limited growth

The dominating growth type for the nucleation of a new monolayer at the nanowire top facet, i.e. the (111)B facet, is the nucleation limited case [12, 37, 44]. Here, an additional energy barrier has to be introduced, accounting for the formation of a stable nucleus on the corresponding facet, which has a size larger than one Ga-As atom pair. To overcome this nucleation barrier, the liquid has to reach a critical level of supersaturation [37]. Meanwhile, other facets, which are not nucleation limited, will reshape according to equation 2.32. Thus, the top facet is stabilized as long as the difference in chemical potential between the liquid and the top facet is smaller than the critical value. When this critical value is overcome, a new nucleus is formed, and thereafter a whole monolayer nucleates by nucleation free growth. In nanowire growth one assumes that first a

complete monolayer forms at the top facet before a second nucleus originates. This is justified by the small liquid phase, whose supersaturation drops far below the critical value after the nucleation event [29, 35, 45].

The nucleation probability can be derived assuming steady-state nucleation rate conditions, which is the typical assumption in NW growth theory [13, 29, 46, 47]. This means, that the attachment and detachment of atoms from clusters, which are smaller than the critical nucleus, is assumed to take place on much shorter timescales than between two separate nucleation events. Furthermore, the attachment or detachment frequency of GaAs pairs to and from the clusters is assumed to be limited by As atoms, since As atoms are less abundant in the catalyst, and As atoms stabilize the (111) interface [35]. If the interface is Ga-terminated, i.e. a (111)A surface, the Ga atoms are bound with only one covalent bond and three covalent bonds are left free, whereas if the interface is As-ended, i.e. a (111)B surface, the As atoms are bound with three covalent bonds, and only one covalent bond per pair is left free. Additionally, the chemical potential of the solid depends on the stacking type of the crystal structure (compare equation 2.7). Thus, the energies necessary for the nucleation of the WZ and ZB phase need to be distinguished. Then, the mean nucleation rate at the top facet can be written as [35]

$$j_s = A_n Z_s c_1 \Xi_{ls,Ga-As} x_V \exp\left(-\frac{\delta g_{ls,int}^{TS,ERS}}{k_B T}\right) \exp\left(-\frac{\Delta G_{n,s}}{k_B T}\right). \tag{2.33}$$

A_n is the area covered by the critical nucleus of n GaAs pairs, $Z_s = \frac{1}{n}\sqrt{\Delta G_{n,s}/4\pi k_B T}$ the 2D Zeldovich factor, and $\Delta G_{n,s} = -\sum_{i=2}^{n} \delta\mu_{l-ERS,Ga-As} - \delta\mu_{s-ERS,Ga-As}^{i}$ the formation free energy of the nucleus [35]. Furthermore, $\delta\mu_{s-ERS,Ga-As}^{i}$ is the chemical potential of a cluster of i GaAs pairs, while s describes the solid structure by its stacking type (ZB or WZ). $\delta g_{ls,int}^{TS,ERS}$ is the transition state barrier for the attachment of a single pair to the interface, and c_1, the concentration of single GaAs pairs at the interface, can be assumed to be equal to the As concentration in the liquid, x_V [35].

With this, the nucleation limited growth rate at the liquid/solid interface at the top facet is defined, which is followed by the completion of the whole monolayer via the nucleation free rate given by equation 2.32. After these nucleation events, the supersaturation of the liquid builds up again until the next nucleation limited event takes place. This behavior is sketched in fig. 2.4. Here, the time evolution of x_{As} in a liquid Ga droplet is simulated for different local As/Ga ratios [35]. After the initial increase of the As concentration in the droplet, the formation of a stable nucleus takes place at the assumed critical value of 2.6 %, which is followed by the completion of the whole monolayer. This procedure goes along with the instantaneous decrease of the As concentration, which thereafter increases again. Reasonably, this layer-by-layer growth happens faster at larger As/Ga ratios. Note that no nanowire growth is obtained for As/Ga ratios below a certain threshold value, since here the critical As concentration, and correspondingly the necessary supersaturation of the liquid, cannot be obtained.

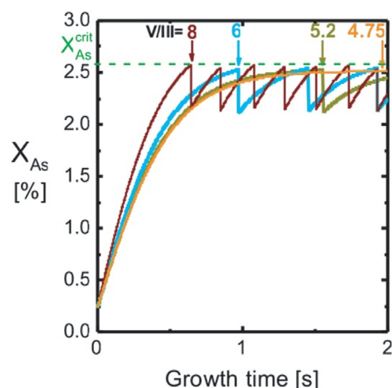

Figure 2.4: Time evolution of the As concentration x_{As} in a liquid Ga droplet for different local As/Ga ratios: With increasing local V/III ratios, x_{As} refills faster and the nucleation of a complete monolayer takes place with a higher rate. Here, a value of 2.6 % is assumed for the formation of a critical nucleus. Adopted from [35].

2.1.9. Summary

In this section, the growth of nanowires via the VLS mechanism was introduced. When providing As and Ga fluxes in MBE, the As and Ga atoms pass through different atomic states due to the minimization of energy in the system. Therefore, the chemical potentials of the liquid, the solid, the adatom, and the vapor phase were deduced from thermodynamics [35]. Using transition state theory, a general expression for the exchange of matter between two arbitrary states was derived (eq. 2.11) [35]. Applying this equation and the deduced chemical potentials, the for nanowire growth relevant transition rates were described.

To assess the sorption of Ga and As adatoms towards the liquid state, their diffusion lengths on the nanowire side facets and the substrate were evaluated. It turned out, that the adatom diffusion length of As is negligible, i.e. As reaches the droplet solely via adsorption from the vapor or beam phase. Instead, the diffusion length of Ga adatoms is substantial, and depends on the growth temperature (see fig. 2.2b) [35]. The quantity of Ga adatoms that reaches the liquid catalyst droplet at the nanowire tip also depends on the nanowire length (see fig. 2.3), as deduced from a Fickian diffusion regime [35, 43].

Furthermore, the general nucleation model for nanowire growth from a supersaturated catalyst was summarized. At the nanowire top facet, the nucleation of a new monolayer is initiated by the formation of a nucleus of distinct size, which is only accessible when the supersaturation reaches a critical value [12, 37, 44]. The monolayer is completed by the attachment of GaAs pairs to the nucleus without the necessity to exceed this critical value [35]. The whole process (initiation+completion) is assumed to be ended before a new nucleus is formed again initiating the growth of the next monolayer. The frequency of this mechanism, i.e. the growth rate of the wires, is limited by the As concentration in the liquid droplet, which can be affected by the applied As flux [35, 37].

However, the kind of the preferentially forming critical nucleus (wurtzite or zinc-blende) was not specified. The requirements to form GaAs nuclei of either wurtzite or zinc-blende type at the nanowire top facet are derived in the next section.

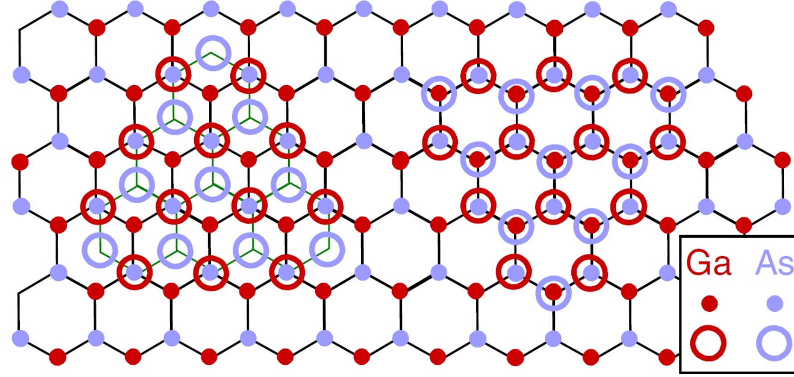

Figure 2.5.: Positions for ZB (left) and WZ nucleation (right) on a GaAs(111) surface: the circles indicate the positions of the Ga and As atoms of the new forming nucleus on the underlying GaAs(111) lattice (dots). Adopted from [13].

2.2. GaAs nanowires: Growth of zinc-blende and wurtzite phase

GaAs nanowires grow in the zinc-blende (ZB) phase, which is the crystal structure of bulk GaAs, but also in the wurtzite (WZ) crystal structure, which can be only obtained in bulk with a special temperature and pressure treatment [48]. Both lattices differ solely in the stacking sequence in cubic [111] direction, which is equivalent to the hexagonal [0001] direction. For ZB, the stacking sequence is ABCABC, while for WZ it is ABABAB. For further details about the properties of the WZ and ZB GaAs phases, see section 2.3. This section covers the growth of both phases in nanowires with the VLS mechanism, which was explained for the first time by Glas et al. [13].

First of all, we define a nucleus, which is a set of atoms of monolayer height with fixed relative positions. However, these relative positions are equal for ZB and WZ crystal structure. This is illustrated in fig. 2.5, where the blue and red circles on the left and on the right depict nuclei in ZB and WZ position, respectively. Thus, to distinguish between ZB and WZ crystal structure, one has to take into account the orientational positioning of the nucleus on a (111) plane with respect to the previous monolayer. In ZB position (left in fig. 2.5), the tetrahedra of the nucleus have the same orientation as the previous monolayer, whereas in WZ position (right in fig. 2.5), the tetrahedra are rotated by 180° [12]. Consequently, to determine whether a crystal consists of zinc-blende or wurtzite crystal structure, one has to consider at least a stack of two subsequent monolayers of GaAs(111). Pure WZ or ZB crystal structure originates, if each monolayer nucleates in WZ or ZB position.

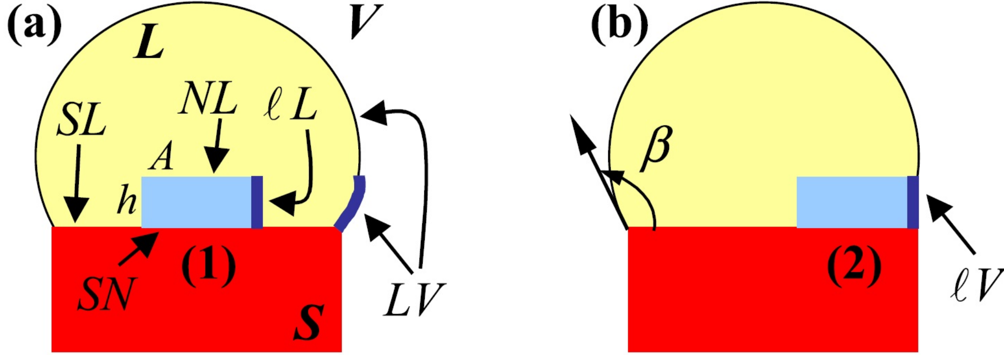

Figure 2.6.: Originating and disappearing interfaces of a nucleus forming at the liquid/solid interface at the nanowire top facet: (a) The nucleus is completely covered by the liquid. (b) The nucleus forms at the triple phase line (TPL), where liquid, vapor and solid meet. For the specific labeling, see text. Adopted from [13].

2.2.1. Site-dependent nucleation

In their model, Glas et al. [13] consider the formation of a nucleus at the plain liquid/solid interface. This is sketched in figs. 2.6: the liquid catalyst droplet (yellow) covers the top facet of the nanowire (red), where the nucleus (blue) forms. Glas et al. compare the energy that has to be raised, when introducing either a WZ or ZB nucleus at different nucleation sites. In the geometry when a droplet completely covers the plain surface, only two different nucleation sites exist: either in the center of the droplet (fig. 2.6a), with all surfaces of the nucleus covered by the liquid, or at the edge (fig. 2.6b), with one lateral surface exposed.

Nucleation in the nanowire center

If a nucleus of monolayer height h and a perimeter P, which covers a lateral area A of the underlying crystal, forms at the interface, and itself is totally covered by the liquid as shown in fig. 2.6a, the free energy of the system changes by [13]

$$\Delta G_{center} = -Ah\Delta\mu + Ph\gamma_{lL} + A\left(\gamma_{NL} - \gamma_{SL} + \gamma_{SN}\right). \qquad (2.34)$$

Here, $\Delta\mu = \delta\mu_{l-ERS,Ga-As} - \delta\mu_{s-ERS,Ga-As}$ is the difference in chemical potential per unit volume of a Ga-As pair between the liquid and the solid phase, and γ_{xy} are the energies for the interfaces between phases x and y. The subscript S denominates the substrate, N the upper and l the lateral surface of the nucleus, and L the liquid.

To calculate the difference in energy for WZ and ZB nuclei in center position, Glas et al. [13] conduct the following considerations. The solid/liquid interface and the upper nucleus/liquid interface have the same atomic configuration, irrespective of the nucleus position, so both interface energies are equal, $\gamma_{SL} = \gamma_{NL}$. Since the considered nucleus is the same for ZB and WZ nucleation, i.e. has the same edges, γ_{lL} is the same for both

phases. The interfacial energy between a ZB substrate and nucleus in ZB position is zero $\gamma_{SN}^{ZB} = 0$ (compare equation 2.7). For WZ nucleation on a ZB substrate, which can be associated with the introduction of a twin plane in a ZB crystal (see section 2.3.1), some energy has to be raised, $\gamma_{SN}^{WZ} = \gamma_F$. Consequently, equation 2.34 writes

$$\Delta G_{center}^{ZB,WZ} = -Ah\Delta\mu + Ph\gamma_{lL} + A\gamma_{SN}^{ZB,WZ} \tag{2.35}$$

for WZ and ZB positions, respectively [13]. The difference in free energy between WZ and ZB nucleation in center position then reads

$$\Delta G_{center}^{WZ} - \Delta G_{center}^{ZB} = A\gamma_F. \tag{2.36}$$

Since γ_F adopts positive values only, in center position nucleation is energetically favored in ZB position. Therefore, ZB is the predominating crystal structure in nanowires, if the nuclei of subsequent GaAs layers form in the center of the liquid catalyst.

Nucleation at the triple phase line

The circumstances change, when the nucleus is not entirely covered by the liquid, depicted in fig. 2.6b. If the nucleus forms at the edge of the top facet, i.e. at the triple phase line (TPL), where solid, liquid and vapor meet, one has to take into account other surfaces, that are displaced by the originating nucleus, compared to center position. It is not sufficient any longer to consider an equivalent lateral interface energy γ_{lL} for WZ and ZB, since a fraction of the nucleus replaces the liquid/vapor interface [13].

Assuming, that the formation of an area s of the nucleus/vapor interface displaces an area τs of the liquid/vapor interface, and the fraction of the perimeter in contact with the vapor denominates α, the free energy for the formation of a nucleus at the TPL reads [13]

$$\Delta G_{TPL}^{ZB,WZ} = -Ah\Delta\mu + Ph\left[(1-\alpha)\gamma_{lL} + \alpha\left(\gamma_{lV}^{ZB,WZ} - \tau\gamma_{LV}\right)\right] + A\gamma_{SN}^{ZB,WZ}. \tag{2.37}$$

For simplification, usually an axisymmetric nucleus is assumed. Then, τ is set by the contact angle β between the droplet and the wire, i.e. $\tau = \sin\beta$ [13, 32].

Now, the question is which crystal structure nucleates predominantly at the TPL. Again, the crystal phase is favored in TPL position, whose free energy for the formation of a nucleus is smaller than the other. Thus, the condition for preferential WZ nucleation reads

$$\Delta G_{TPL}^{ZB} - \Delta G_{TPL}^{WZ} > 0. \tag{2.38}$$

The only relevant terms depending on the precipitating crystal structure in equation 2.37 are those containing the energy of the lateral side facet of the nucleus to the vapor, γ_{lV}, and the substrate dependent interface energy γ_{SN}. All other terms are equal and cancel each other. Thus, equation 2.38 reads

$$Ph\alpha\left(\gamma_{lV}^{ZB} - \gamma_{lV}^{WZ}\right) - A\gamma_F > 0. \tag{2.39}$$

Assuming a nucleus shaped as a equilateral triangle with the side length D, with one side lying at the TPL ($\alpha = 1/3$), a critical nucleus size can be determined, below which WZ nuclei are preferred instead of ZB ones [13]. The thereby deduced condition is

$$D < \frac{4\sqrt{3}}{3} h \frac{\gamma_{lV}^{ZB} - \gamma_{lV}^{WZ}}{\gamma_F}. \tag{2.40}$$

With the values of interface energies for commonly observed nanowire side facets, determined by density functional theory stability calculations, the critical side length of a triangle GaAs nucleus can be evaluated. The difference in surface energy between the side facets of ZB nanowires, the $\{1\bar{1}0\}$ facets, and WZ nanowires, the $\{1\bar{1}00\}$ or the $\{11\bar{2}0\}$ facets, $\gamma_{lV}^{ZB} - \gamma_{lV}^{WZ}$, is at least 0.096 J/m^2 [29, 49, 50]. This means that in any case WZ side facets have a lower surface energy than ZB ones. The twin plane energy γ_F can be assumed to be half the stacking fault energy in ZB GaAs [46], which is $4.5 \cdot 10^{-4}$ J/m^2 [51]. Finally, with the height of a monolayer GaAs, $h = 3.26$ Å, the critical diameter is evaluated to be 321 nm. This value shows that in GaAs nanowires, whose diameter is usually less than 100 nm, nucleation at the TPL always takes place in WZ position.

Note, that equation 2.37 is only valid for vertical side facets growing from a vertical stack. For non-vertical side facets, γ_{lV} has to be replaced by another term, since additional facets form and the surface tension of the liquid is affected in a larger extent [13, 52]. This is not explicitly shown here, since the surface energies calculated for corresponding reconstruction-free low index ZB and WZ surfaces are by far higher than the ones mentioned above [49], and therefore improbable to form in GaAs nanowire growth. Indeed, other side facets than the aforementioned vertical ones are not observed in GaAs nanowire growth.

Thus, in contrast to nucleation in center position, which preferentially occurs in ZB position, the nuclei forming at the TPL predominantly adopt WZ position. With this, the question arises, when nucleation takes place at the TPL or in center position, and which parameters affect this.

Nucleation at the TPL or in center position

The condition for preferential nucleation at the TPL is fulfilled, when the free energy for the formation of a nucleus at the TPL is less than for the formation of an equivalent nucleus in center position, $\Delta\gamma = \Delta G_{TPL} - \Delta G_{center} < 0$. With equation 2.35 and equation 2.37, $\Delta\gamma$ reads [13, 32]

$$\Delta\gamma = \gamma_{lV} - \gamma_{lL} - \gamma_{LV} \sin\beta < 0. \tag{2.41}$$

Thus, the energetically favored position for the nuclei is highly sensitive on the interfacial energies of the liquid. These interfacial energies allow predominantly TPL nucleation only if $\gamma_{lV} < \gamma_{lL} + \gamma_{LV}$. Assuming that TPL nucleation (and thereby WZ nucleation) is accessible, which is the case in GaAs nanowire growth, the contact angle β can be

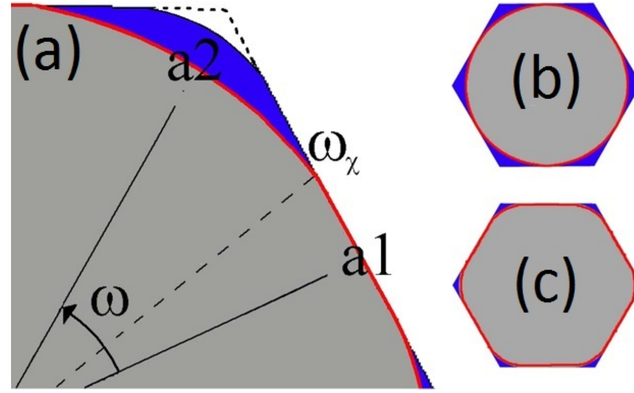

Figure 2.7.: Sketches of the wetting of a nanowire top facet by a liquid droplet (grey) with its TPL (red) and the areas left blank (blue): (a) To describe the wetting area at the top facet a polar description is introduced: a1 denominates the position at the TPL with respect to the middle of the side facet ($\omega = 0$), a2 is the position of the TPL in direction to the edge of the side facet ($\omega = 30°$), and ω_χ is the maximum angle when the TPL leaves the edge of the top facet. (b) A small droplet wets solely the top facet, so the TPL does not touch the edges of the top facet. (c) For elevated droplet volumes, the TPL partially follows the edges of the top facet. Adopted from [34].

used to choose the respective site for nucleation. For contact angles β close to 90°, the probability to form a nucleus at the TPL is highest. Instead, nucleation in center position predominates, when $\beta \ll 90°$ or $\beta \gg 90°$. The contact angle of the droplet on the nanowire top facet is reasonably affected by the size of the droplet and by the surface tension of the liquid.

However, the droplet size also determines the wetting area of the liquid catalyst droplet on the top facet, which is not included in the model of Glas et al. [13]. How the wetting area and the droplet size determine the position of nucleation is considered in the next section. The dependence of nucleation on the liquid surface tension and the contact angle is described in the section thereafter.

2.2.2. Wetting area dependent nucleation

The size of the liquid droplet determines, whether the whole nanowire top facet or only parts of it are wetted. However, this affects the free energy for the formation of a nucleus at the TPL, which is not included in equation 2.37.

To add this dependence to the calculations, Krogstrup et al. introduce a polar description of the wetting of the top facet [34]. In fig. 2.7a the top view of a quarter of a nanowire is sketched, which is covered by a liquid droplet (grey). The red line indicates the TPL, and blue color the uncovered top facet. Since the nanowire side facets are six-fold symmetric, it is sufficient to consider a region of 30°. The limits of this region extend from the nanowire center to the middle of the side facet (position a1, $\omega = 0°$) and towards one edge of the corresponding side facet (position a2, $\omega = 30°$). ω_χ describes

the maximum angle, where the TPL leaves the edge of the top facet, and χ the fraction of the TPL in contact with the edge of the top facet.

The free energy for the formation of a nucleus at the TPL, equation 2.37, then can be rewritten in dependence on the wetting of the top facet [34],

$$\Delta G_{TPL}^{ZB,WZ} = -Ah\Delta\mu + Ph\Gamma_{TPL}^{ZB,WZ}(\omega) + A\gamma_{SN}^{ZB,WZ}, \tag{2.42}$$

with

$$\begin{aligned} \Gamma_{TPL}^{ZB,WZ}(\omega) = & \left[1 - \alpha(\omega) - \kappa(\omega)\right]\gamma_{lL} + \alpha(\omega)\left[\gamma_{lV}^{ZB,WZ} - \gamma_{LV}\sin\left[\beta(\omega)\right]\right] \\ & + \kappa(\omega)\left[\gamma_{lV_{TF}} - \gamma_{LV}\sin\left[\beta(\omega)\right]\right]. \end{aligned} \tag{2.43}$$

Here, $\alpha(\omega)$ and $\kappa(\omega)$ denote the fraction of the nucleus perimeter in contact with the TPL *at the edge* of the top facet and *on* the top facet, respectively. Dependent on the precipitating crystal structure is only $\gamma_{lV}^{ZB,WZ}$. The lateral surface energies of the nucleus in contact with the liquid, γ_{lL}, and with the top facet, $\gamma_{lV_{TF}}$, are each the same for ZB and WZ positions of the nucleus, since both nuclei have equivalent edges on the top facet [34]. All other parameters are equal to those introduced in section 2.2.1.

In the following, the crystal structure precipitating at the TPL is derived from equation 2.42 and equation 2.43 for different sizes of the liquid droplet. Since WZ nuclei can only form at the TPL (compare section 2.2.1), it is sufficient to derive in which configuration WZ nuclei predominantly originate at the TPL. In all other cases, ZB crystal structure will be preferentially adopted.

The first case we consider is when a droplet wets solely the top surface without touching its edges ($\chi = 0$), depicted in fig. 2.7b. This state corresponds to position a2 in fig. 2.7a all along the TPL. Here, $\kappa = 1$ and $\alpha = 0$, so $\Gamma_{TPL}^{ZB,WZ}(\omega)$ (equation 2.43) is crystal structure independent. Then, equation 2.42 is minimized for $\gamma_{SN}^{ZB,WZ} = 0$. This implies, that nucleation occurs preferentially in ZB position for the same reason as in the center of the liquid droplet: $\gamma_{SN}^{ZB} = 0$, whereas $\gamma_{SN}^{WZ} = \gamma_F > 0$. This means, that the predominantly precipitating crystal structure from a catalyst droplet, which wets solely the top facet without touching the edges of the top facet, is in any case ZB, for both TPL and center nucleation.

When the droplet size is larger, the TPL wets parts of the edges of the top facet ($0 < \chi < 1$), depicted in fig. 2.7c. Then, equation 2.43 cannot be neglected any more, since it becomes crystal structure dependent as $\alpha \neq 0$. In this case, $\Gamma_{TPL}^{ZB,WZ}(\omega)$ is strongly dependent on the sine of the contact angle $\beta(\omega)$, so in the following we distinguish the cases $\beta(\omega) < 90°$ and $\beta(\omega) > 90°$.

For $\beta(\omega) < 90°$, the contact angle is lowest at $\omega = 30°$ (position a2 in fig. 2.7a). It increases continuously with ω to its maximum value at $\omega = 0°$ (position a1) due to the limitation by the edge of the top facet. Since $\sin(\beta(0°)) > \sin(\beta(\omega \neq 0°))$ and consequently $\Gamma_{TPL}^{ZB,WZ}(0°) < \Gamma_{TPL}^{ZB,WZ}(\omega \neq 0°)$, the nucleation barrier is lowered to a higher extent at $\omega = 0°$ than for all other $\omega \neq 0°$. Therefore, when the droplet partially wets the edge of the top facet with $\beta(\omega) < 90°$, nucleation at the TPL can take place

preferentially at the edge of the top facet. This is possible only, if the critical value of the contact angle $\beta < 90°$ at $\omega = 0°$ is overcome, so that equation 2.41 is fulfilled. Only then WZ nucleation is accessible, while otherwise ZB nucleation in center position prevails.

An increase in droplet volume increases the fraction of the droplet touching the edge of the side facets χ, but at some point coincidentally increases $\beta(\omega) > 90°$. Both phenomena have a reverse effect on the nucleation probability of WZ nuclei. An increase in χ increases the probability for nucleation taking place at the TPL in contact with the edge of the top facet, simply due to a larger interface. Instead, the elevation of $\beta(\omega)$ beyond 90° increases the nucleation barrier again, due to its angular dependence. This is most pronounced for $\omega = 0°$, where the contact angle is largest. Thus, for large droplet volumes with $\beta(\omega) > 90°$, a critical value exists beyond which the nucleation barrier near position a2 ($\omega = 30°$) at the top facet becomes less than for any position at the TPL in contact with the edge of the side facet ($\omega < \omega_\chi$). This corresponds to a favored formation of nuclei in ZB position over those in WZ position.

When $\beta(\omega)$ increases further, corresponding to a further increase of the droplet size, the TPL starts to move onto the side facets, and the fraction of the TPL on the top facet approaches zero. Additionally to the effects already described for $\beta(\omega) > 90°$ beyond the critical value, the decreasing χ reduces the probability to form a WZ nucleus at the TPL in contact with the edge of the top facet. If furthermore $\sin(\beta(\omega))$ becomes too low to fulfill the condition for nucleation at the TPL (equation 2.41), the formation of nuclei moves from the TPL in contact with the top facet to the center of the liquid. Nevertheless, the predominantly precipitating crystal structure remains ZB.

If the droplet size increases further, and the TPL resides completely on the side facets, nucleation can only take place in center configuration favoring ZB nuclei, since no TPL on the edge of the top facet exists.

The overall behavior of the precipitating crystal structure in dependence on the wetting area is summarized in figs. 2.8a, 2.8b and 2.8c. For a droplet, which only wets the top facet without touching its edges (fig. 2.8a), the predominantly forming crystal structure is ZB. When the TPL covers the edge of the top facet with a contact angle close to 90° (fig. 2.8b), nucleation takes place here, preferring the WZ phase. In the case of a large droplet wetting exclusively the nanowire side facets (fig. 2.8c), only nucleation in center position is accessible, favoring the ZB phase. The crystal, which grows at the same time on the side facets, adopts the crystal structure of the already existing layers of the GaAs core wire.

2.2.3. Impact of liquid surface tension and contact angles

Additionally to the wetting area, the liquid surface tension γ_{LV} and the corresponding contact angles of the liquid on the respective surfaces have a critical impact on the precipitating crystal structure (compare equation 2.41). In this work, catalyst droplets of liquid Ga and a liquid Au-Ga alloy are used, so in the following their surface tensions and contact angles are estimated, and correspondingly their application to grow phase

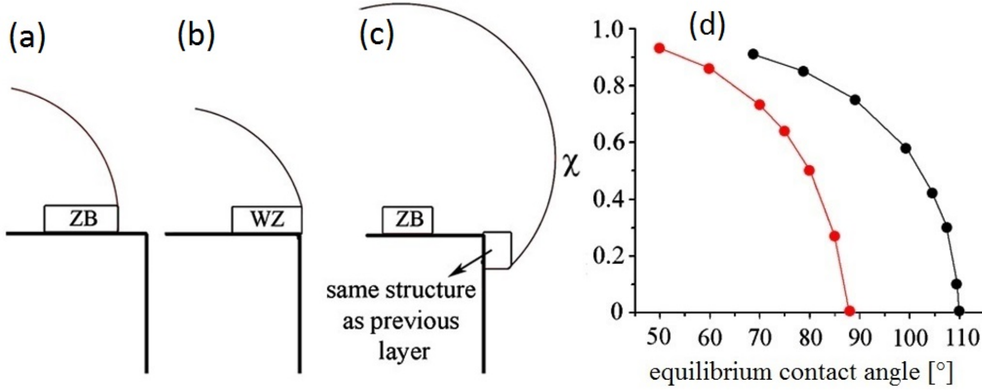

Figure 2.8.: (a) - (c) Sketch of the predominantly forming kind of nuclei (ZB or WZ) in dependence on different wetting areas of the catalyst droplet. For further specifications, see text. (d) Fraction of the TPL in contact with the edge of the top facet χ in dependence on the equilibrium contact angle of the liquid droplet: for large equilibrium contact angles and low droplet volumes V ($V_{black} = 1.24 \cdot V_{red}$), χ is reduced. Adopted from [34].

pure crystal structures.

For pure liquid Ga droplets, the equilibrium contact angle on the GaAs(111) surface is in the range of $40° - 70°$ [53], and the liquid surface tension at a typical nanowire growth temperature of 600°C is $\gamma_{LV_{Ga}} = 0.67$ J/m^2 [32, 54]. For Au, the surface tension at 600°C, interpolated from liquid Au above 1065°C using Eötvös's rule [55], is roughly twice as high as for Ga, $\gamma_{LV_{Au}} = 1.24$ J/m^2 [32, 56]. Thus, the equilibrium contact angle for a liquid Au-Ga alloy is expected to be significantly higher than for pure liquid Ga.

Note, that the equilibrium contact angle is not equal the maximum contact angle, i.e. the angle when the TPL moves on the side facet. The maximum contact angle indeed depends mainly on the equilibrium contact angle, but also and the vapor and beam pressure onto the liquid droplet [53]. Nevertheless, if one assumes a Ga and Au-Ga droplet of the same size exposed to low vapor or beam pressures, the equilibrium contact angle gives a measure for the maximum possible contact angle.

Fig. 2.8d shows, for two different droplet sizes on the nanowire top facet, the effect of different equilibrium contact angles on the fraction of the TPL in contact with the edges of the top facets χ [34]. Here, the droplet volume corresponding to the black curve is 1.24 times larger than the one corresponding to the red curve. Reasonably, for lower equilibrium contact angles and larger droplet volumes, the full coverage of the edges of the top facet, $\chi \rightarrow 1$, is reached faster. Instead, for large equilibrium contact angles, $\chi \rightarrow 0$. If one relates this to pure liquid Ga and an Au-Ga alloy, due to the higher surface tension and consequently the higher equilibrium contact angle of Au-Ga, the condition $\chi = 1$ applies for much smaller pure Ga droplet volumes than for Au-Ga ones.

Since the maximum contact angle of liquid Ga on the GaAs(111) top facet is very likely less than 90° [53], the maximum value of $\sin\beta$ seems in this case rather low. Thus,

for pure Ga droplets, nucleation at the edge of the top facet is not as likely as for a Au-Ga alloy. Here, the maximum contact angle, and correspondingly $\sin\beta$, is larger. Therefore, conditions for preferential TPL-nucleation with large contact angles at the edge of the top facet are rather accessible with an Au-Ga alloy.

This behavior can also be understood introducing Young's equation for the wetting of a side facet by a droplet with an equilibrium contact angle ϕ, $\cos\phi = (\gamma_{lV} - \gamma_{lL})/\gamma_{LV}$ [57]. Assuming β to be the equilibrium contact angle on the top facet, the condition for preferential TPL nucleation (equation 2.41) reads:

$$\Delta\gamma = \cos\phi - \sin\beta < 0. \tag{2.44}$$

$\Delta\gamma$ is utmost negative, and consequently the probability for TPL nucleation is highest, when ϕ is as large as possible and β is 90°. This is rather the case when an Au-Ga alloy is used as a catalyst instead of pure Ga, as the elevated surface tension of Au also allows larger equilibrium contact angles on the nanowire side facets, $\phi_{Ga} < \phi_{Au-Ga}$.

Therefore, the necessary conditions for the growth of a WZ crystal, i.e. the TPL resides at the edge of the top facet with a large contact angle, is more likely, when growing GaAs nanowires with a catalyst droplet consisting of an Au-Ga alloy. Instead, the probability to attain ZB crystal structure is highest, when both equilibrium contact angles in equation 2.44 are low, i.e. this regime should be accessible more easily with pure Ga catalyst droplets.

Following Eötvös's rule [55], the surface tension of a liquid decreases almost linearly with an increase in temperature. Consequently, the maximum contact angle is maximized for lower temperatures. So from this point of view, for the growth of WZ GaAs nanowire crystals rather low temperatures should be used due to the necessity of TPL nucleation at the edge of the top facet. Instead, high temperatures reduce the equilibrium contact angles, and thus give more easily access to the growth of ZB GaAs nanowire crystals via center nucleation.

2.2.4. The supersaturation of the liquid phase

In the last two sections, it was described how one obtains preferential WZ or ZB crystal structure by lowering the nucleation barrier at the TPL or in the center of the droplet under the respective contrary level. In doing so, $\Delta\gamma$ was maximized in equation 2.41 or equation 2.44 towards negative or positive values. This can be done by changing the droplet size and choosing the composition of the liquid droplet, i.e. pure Ga or an Au-Ga alloy, which both have effects on the wetting area and the maximum contact angle.

Considering the chemical potentials involved in the transition of a Ga-As pair from the liquid to the solid phase in fig. 2.9, we observe, that not only the difference in chemical potential between the transitions states ($\Delta\gamma$) is of importance for the nucleation of a pure crystal. Also the supersaturation of a Ga-As pair in the liquid with respect to the solid, $\Delta\mu$ (compare equations 2.35, 2.37 and 2.42), highly affects the crystal growth: $\Delta\mu$ should be rather high, corresponding to an elevation of the chemical potential of a Ga-As pair in the liquid (left in fig. 2.9). Then, the fraction of energy, which is necessary

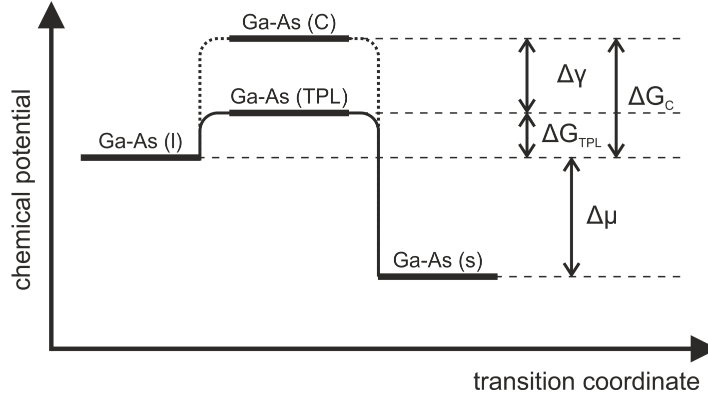

Figure 2.9.: Sketch of the chemical potentials for the transition of a Ga-As pair from the liquid (left) to the solid state (right): Ga-As (C) and Ga-As (TPL) are the transition states taking into account the formation of a nucleus in center position or at the TPL. The difference $\Delta\gamma$ between both barriers (here assumed $\Delta\gamma < 0$), and the absolute values for the nucleation barriers, ΔG_{TPL} or ΔG_C, which depend on the chemical potential of the liquid with respect to the solid $\Delta\mu$, determine the probability for nucleation in center or TPL position.

for nucleation at one site with respect to the other site, $\Delta G_{TPL/C}/\Delta G_{C/TPL}$, is reduced and leads to the preference of one crystal phase.

The dependence of $\Delta\mu$ on different growth parameters, like the growth temperature and the (Au-)Ga-As composition of the droplet, was calculated by Glas et al. for pure Ga droplets [42] and liquid Au-Ga alloys [37]. They calculate $\Delta\mu$ for an infinite liquid without size effects like the Gibbs-Thomson effect, and assume a GaAs crystal of the ZB phase. Nevertheless, the Gibbs-Thomson effect or WZ crystal structure can be easily added by introducing the corresponding extra chemical potential to the liquid or the solid chemical potential [37] (compare equations 2.6 and 2.7).

The concentration of As atoms, which dissolve within a pure Ga droplet at a temperature of 610°C is shown in fig. 2.10a in the second panel in dependence on the applied As flux or As_4 beam equivalent pressure (BEP). Clearly, the As concentration in the liquid increases with the As_4 BEP and so does the supersaturation $\Delta\mu$ (first panel).

In fig. 2.10b, the dependence of these quantities is shown for an increase in growth temperature at a constant As_4 BEP of $4.5 \cdot 10^{-6}$ Torr. For an increase in temperature, the Ga-As phase diagram (compare appendix B fig. B.1) allows a higher solubility of As in liquid Ga (second panel). Contrary to the case of an increasing supersaturation with increasing As_4 BEP, $\Delta\mu$ decreases for elevated temperatures (first panel). This can be explained with a superior impact of the growth temperature over the As concentration determining the liquid chemical potential [37].

The increase of the supersaturation of the liquid with the As concentration and its decrease with elevating temperature are also valid for an Au-Ga alloy [37]. These trends are shown in fig. 2.10c for three different Ga concentrations $c_{\mathrm{Ga}} = 0.2, 0.35, 0.7$ and

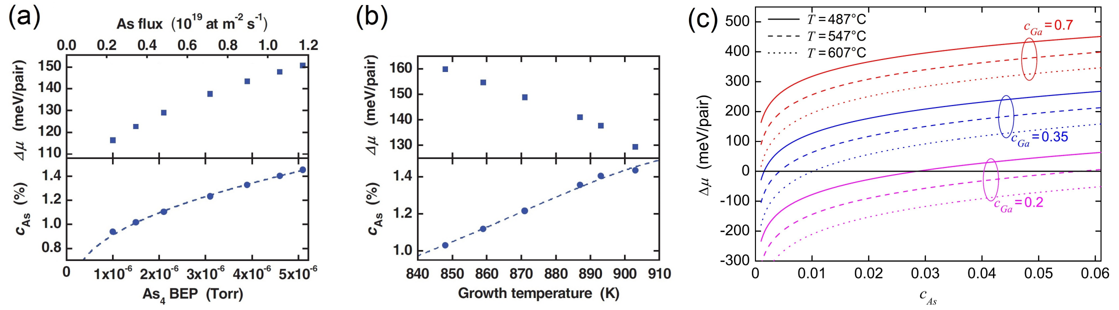

Figure 2.10.: (a) Dependence of the supersaturation and the As concentration in a liquid Ga droplet on the applied As_4 BEP for a constant temperature of 610°C. (b) Temperature-dependence of the same parameters. (c) Chemical potentials of a liquid Au-Ga alloys supersaturated with As, calculated for different compositions and temperatures. In any case, the supersaturation increases with the As-concentration and with a reduction of the growth temperature. Adopted from [37] and [42].

three different temperatures (T = 487°C, 547°C and 607°C). From these dependencies, one may get the impression that the highest supersaturation is reached, when c_{Ga} is maximum, i.e. 1. However, this is not the case. From the As-Au-Ga ternary phase-diagram (compare appendix B fig. B.5), one can deduce the solubility of As in the Au-Ga alloy in dependence of c_{Ga}: the solubility of in the liquid alloy is lowest for $c_{Ga} \approx 0.7$, i.e. here the supersaturation is highest, whereas towards $c_{Ga} \to 1$ the solubility increases as well as for $c_{Ga} \to 0.2$, and consequently the supersaturation reduces in both cases.

Thus, to increase the supersaturation of a Ga-As pair in the liquid droplet with respect to the solid, c_{Ga}, c_{As} and the growth temperature should be optimized. The derived conditions are (a) a large As concentration in the droplet mediated by a large As BEP, (b) a low growth temperature, and (c) the usage of an Au-Ga alloy as catalyst, in optimum case with $c_{Ga} \approx 0.7$.

2.2.5. Summary

In this section, the preferential sites for the nucleation of WZ and ZB GaAs in the liquid catalyst at the nanowire top facet were derived. Additionally, conditions for nanowire growth with a pure crystal structure were indicated.

It was shown that the prevailing nucleus, forming at the interface between the liquid droplet and the GaAs(111) top facet, depends on the site where nucleation takes place. In center position, ZB nuclei are energetically favored, whereas WZ nuclei are favored at the edge of the top facet, due to its lower surface energy compared to ZB. The site where nucleation predominantly takes place is mainly determined by the sine of the contact angle of the liquid catalyst droplet on the top facet (equation 2.41). For large values of the sine, nucleation at the edge of the top facet (WZ) is favored over center nucleation (ZB), whereas for low values it is vice versa.

The maximum contact angle is determined by the surface tension of the liquid. Due to the high surface tension of Au, contact angles of 90° are more likely accessible for Au-Ga droplets than for pure Ga droplets. Consequently, WZ crystal structure should be more easily attainable with a liquid Au-Ga alloy as catalyst than for pure Ga droplets. Since for the growth of nanowires with preferential ZB crystal structure the shape of the droplet is crucial, i.e. the TPL should fully reside either on the top facet or on the side facets to avoid nucleation at the edges of the top facet, both catalysts should be applicable.

Finally, to maximize the difference in energy, which is necessary for the nucleation of a monolayer WZ and ZB, respectively, the conditions for a large supersaturation of the liquid with respect to the solid were derived. These are a large As concentration in the droplet mediated by a large As BEP, a low growth temperature, and the usage of a Au-Ga alloy as catalyst, in optimum case with $c_{Ga} \approx 0.7$. As also the maximum contact angle increases with decreasing temperature, the growth of the WZ GaAs crystal structure is set to low temperatures. However, for ZB crystal structure, due to the necessity of a droplet with a small or large volume, the temperature dependencies of the contact angle and the supersaturation do not seem to be that significant.

The structural differences and the physical properties of the two GaAs crystal phases are summarized in the next section.

2.3. Properties of GaAs in nanowires

The growth of nanowires gives access to the wurtzite (WZ) GaAs phase, which cannot be obtained in bulk GaAs under common circumstances. Since both GaAs crystal phases appear in GaAs nanowires, in section 2.3.1 the atomic configurations of ZB and WZ crystal structure are described. The symmetry breaking in WZ crystals leads to spontaneous polarization, which is introduced in section 2.3.2. Thereafter, the band structures and optical selection rules for GaAs in the ZB and WZ phase are depicted in section 2.3.3. Since optical transitions are quenched in bare GaAs nanowires due to the high non-radiative recombination velocity of surface states, the passivation of GaAs nanowire surfaces is introduced in section 2.3.4.

2.3.1. Zinc-blende and wurtzite crystal structure

The bulk crystal structure of GaAs is the zinc-blende (ZB) phase. It is a face centered cubic (fcc) lattice with a lattice constant of $a_{\mathrm{ZB}} = 5.65$ Å, containing two sub-lattices at (0, 0, 0) and $(\frac{1}{4}, \frac{1}{4}, \frac{1}{4})a_{\mathrm{ZB}}$, occupied by Ga and As atoms, respectively. The unit cell of ZB GaAs is depicted in fig. 2.11a.

Viewing along the diagonal of the cubic unit cell in ZB GaAs, which coincides with the nanowire growth direction, the [111] direction, polar planes are monitored, i.e. planes, which only consist of one kind of atoms. Therefore, a GaAs crystal with (111) surfaces can be either Ga-terminated, labeled GaAs(111)A, or As-terminated (GaAs(111)B). In nanowire growth, the latter case is the usual one. The inter-distance between two

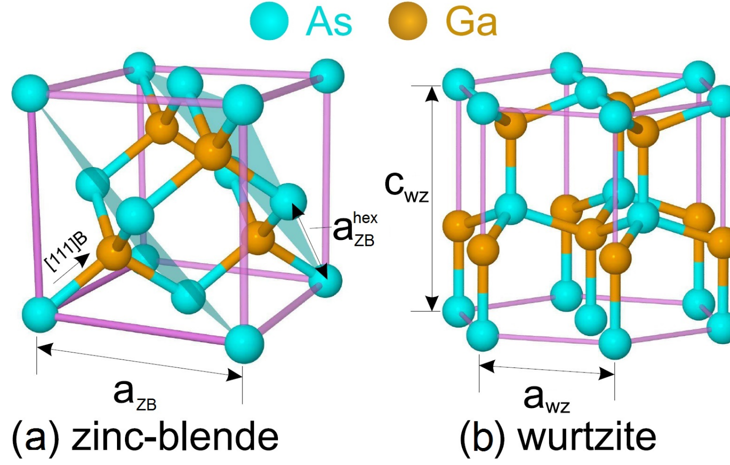

Figure 2.11.: (a) The zinc-blende (ZB) lattice consists of two fcc lattices displaced by $(\frac{1}{4}, \frac{1}{4}, \frac{1}{4})a_{\text{ZB}}$. These lattices are either occupied by Ga or As atoms. Along the [111] direction, subsequent bilayers are stacked in an ABCABC sequence. (b) The wurtzite (WZ) phase is a hexagonal close packed crystal with a stacking sequence of ABABAB. Concerning the stacking sequences, see also fig. 2.12. Adopted from [58].

subsequent GaAs(111)A or GaAs(111)B planes is $\frac{1}{\sqrt{3}}a_{\text{ZB}} = 3.26$ Å, while the inter-distance between two neighboring atoms in a (111) plane, which possess a hexagonal arrangement, is $a_{\text{ZB}}^{\text{hex}} = \frac{1}{\sqrt{2}}a_{\text{ZB}} = 4.00$ Å. To form a close packed structure, subsequent bilayers of GaAs(111)A and GaAs(111)B orientate differently with respect to the first bilayer. In ZB crystal structure, the stacking sequence repeats every third bilayer, i.e. the stacking sequence is "ABCABC".

However, a second close packed structure exists, known as hexagonal close packed (hcp). It has an "ABABAB" stacking sequence and shows a hexagonal lattice configuration. In fig. 2.11b, this lattice is sketched for GaAs, with the hexagonal lattice constants a_{WZ} along $\langle 1\bar{1}00 \rangle$ directions and c_{WZ} along the [0001] direction. For binary compounds, this hcp lattice is also called wurtzite (WZ) structure. The lattice constants of WZ GaAs, deduced from a WZ bulk phase produced by a thermal and pressure treatment are $a_{\text{WZ}} = 3.99$ Å and $c_{\text{WZ}} = 6.56$ Å [48]. These values deviate slightly from the equivalent ZB ones of $a_{\text{ZB}}^{\text{hex}} = 4.00$ Å and $\frac{2}{\sqrt{3}}a_{\text{ZB}} = 6.52$ Å (see also section 2.3.2).

Zinc-blende/wurtzite polytypism

In nanowires the ZB GaAs phase as well as the WZ GaAs phase is accessible [13, 59, 60]. Nanowires differ from the bulk phase only due to their large surface to volume ratio. The large surface accounts for the stability of the WZ phase in nanowires, as WZ possesses a lower number of dangling bonds on the nanowire side facets than the ZB phase [61, 62]. This manifests in a reduced surface energy for WZ side facets [49], which can compensate the small difference in cohesive energy of 24 meV between a WZ Ga-As atomic pair and

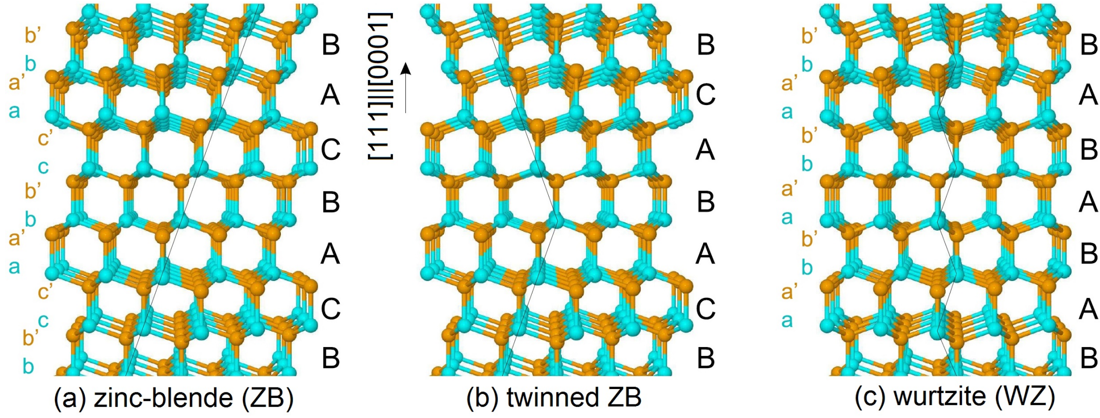

Figure 2.12.: (a) Zinc-blende (ZB), (b) twinned ZB and (c) wurtzite (WZ) crystal structure along $\langle 1\bar{1}0 \rangle \,||\, \langle 11\bar{2}0 \rangle$ viewing directions. The corresponding stacking sequences are marked with capital letters. Adopted from [58].

a ZB one [12].

Viewing both GaAs phases along a cubic $\langle 1\bar{1}0 \rangle$, or its hexagonal equivalent, a $\langle 11\bar{2}0 \rangle$ direction in figs. 2.12, the different stacking sequences of the ZB phase "ABCABC" (fig. 2.12a) and of the WZ phase "ABABAB" (fig. 2.12c) can be detected. The capitals denominate the column coordinates of a Ga-As pair along the cubic [111] direction, which is parallel to the hexagonal [0001] direction, differing the rows (a) and (a'), (b) and (b'), and (c) and (c'). Due to the layer-by-layer growth of GaAs nanowires along the [111]||[0001] direction (compare section 2.1.8), often stacking faults and rotational twins are observed. A rotational twin inverts the ZB stacking sequence from "ABC" to "CBA", which corresponds to a rotation of the "ABC" stacked ZB lattice by 180° around the [111] axis. This kind of stacking fault is depicted in fig. 2.12b in the form "(ABC)[AB|A](CBA)", whereby "|" denominates the twin boundary. Therefore, the rotational twin forms one monolayer of the WZ phase with "ABA" stacking sequence. Thus, ZB crystal structure is transformed to WZ crystal structure by introducing a rotational twin after each monolayer.

2.3.2. WZ phase: Symmetry breaking and spontaneous polarization

Considering the atomic configuration in the WZ phase along the [0001] direction in fig. 2.13a, the third-nearest neighbor of an atom (3) directly sits above the zeroth atom (0), while in the ZB phase along the [111] direction (fig. 2.13b), the upper tetrahedron is rotated by 180°. The successive stacking of these differently oriented tetrahedrons leads to the "ABCABC" stacking of the ZB crystal and the "ABABAB" stacking of the WZ crystal. In ZB configuration, the distance of zeroth atom and third nearest neighbor, and also the distance of the covalent bonds between zeroth atom and first neighbor (1) and between second (2) and third neighbor is largest. Instead, in WZ crystal structure

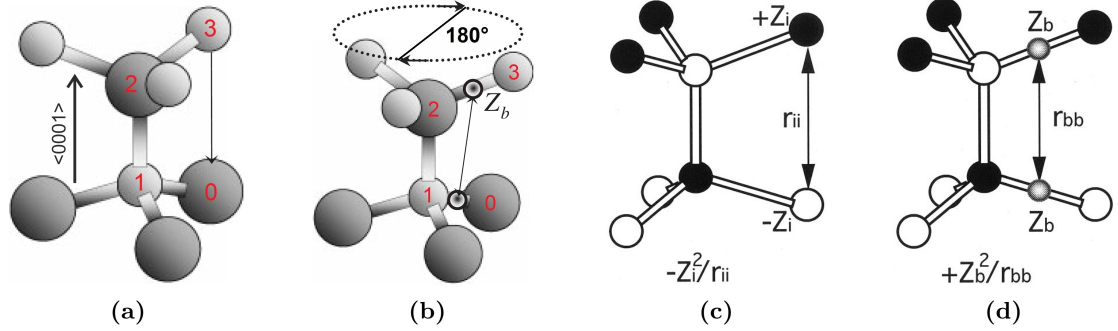

Figure 2.13.: Octet configuration in the WZ and ZB phase along the [111]||[0001] direction: In WZ (a,c,d), the third nearest neighbor (3) resides directly atop the zeroth atom. In ZB (b), the upper tetrahedron is rotated by 180°, so (3) resides above empty space. (c) Attractive interaction between between zeroth atom and third nearest neighbor with charges $\pm Z_i$ at an inter-distance r_{ii}. (d) Repulsive interaction between the corresponding bond electrons with charges Z_b at an inter-distance r_{bb}. Adopted from [63, 64].

both distances are shortest.

Considering the bonds as partially ionic and partially covalent, the energy E of a bond can be estimated via the sum of the energies of a fully covalent bond E_c and a fully ionic bond E_i [65],

$$E = (1 - f_i)\, E_c + f_i E_i, \tag{2.45}$$

introducing the ionicity $f_i \, \epsilon \, [0, 1]$ of the considered bond. In the octet configuration shown in fig. 2.13c and fig. 2.13d, E_i can be described as the attractive interaction $-Z_i^2/r_{ii}$ of the ions with charges Z_i at the respective lattice sites separated by r_{ii} ($Z_i = 3$ for III-V semiconductors) [64]. E_c can be interpreted as the Coulomb repulsion Z_b^2/r_{bb} between the electrons of the covalent bonds ($Z_b = -2$), residing between the atoms at a distance r_{bb} [64]. The difference in energy between WZ and ZB crystal structure, $\Delta E_{\text{WZ-ZB}}$, can then be estimated by

$$\Delta E_{\text{WZ-ZB}} = c \left[\frac{3}{2} (1 - f_i) \frac{Z_b^2}{r_{bb}} - f_i \frac{Z_i^2}{r_{ii}} \right], \tag{2.46}$$

with c being a constant coefficient [64]. Consequently, a high ionicity f_i of the bond stabilizes the WZ phase, whereas a predominantly covalent bond characteristic stabilizes the ZB phase. Thus, for a high electronegativity of the group V bond partner, e.g. nitrogen, the crystal structure of a III-V semiconductor is WZ, while for atoms with a low electronegativity like arsenic the ZB crystal is favored.

An interesting consequence of the elevated interaction between the third nearest neighbors in a WZ crystal is, that the inter-distance of subsequent bilayers in [0001] direction is slightly altered with respect to the ideal tetrahedral ZB crystal. The corresponding measure for this symmetry breaking is the relation between the lattice parameters c and a, which is for an ideal tetrahedron (ZB crystal) $c/a = \sqrt{8/3} = 1.6333$. For a stable

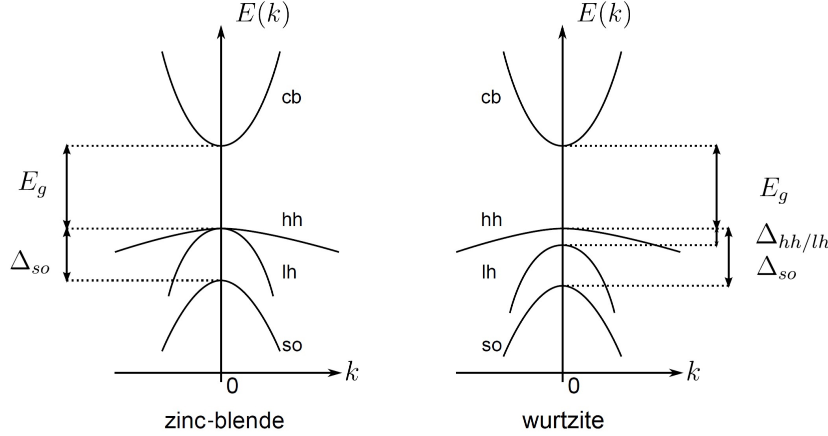

Figure 2.14.: Energy dispersion for ZB and WZ GaAs at the Γ point: In ZB GaAs, the heavy hole (hh) and the light hole (lh) bands are degenerate at k = 0, the split-off band is separated by $\Delta_{so} = 0.34$ eV. In WZ GaAs, the hh band is separated from the lh band, as well as the split-off band. Adopted from [70].

WZ bulk crystal $c/a < \sqrt{8/3}$ applies, while $c/a > \sqrt{8/3}$ indicates unstable WZ bulk crystals [12, 63, 66]. For instance, calculated values for WZ GaN and GaAs are 1.6293 and 1.6456, respectively [66], corresponding to a reduced distance between (0001) planes in WZ GaN, whereas in WZ GaAs the distance is increased.

Furthermore, this symmetry breaking in the WZ phase leads to a separation of the centers of charge along the [0001] direction, called spontaneous polarization. This is a well known issue in GaN, and was recently experimentally quantified [67]. In WZ GaAs, the strength of spontaneous polarization is predicted to be one order of magnitude lower than in GaN [66], and has not been experimentally observed. The observation and quantification of spontaneous polarization in WZ GaAs in nanowires is described in chapter 6.

2.3.3. Band structures and optical selection rules

Since the properties of GaAs in the ZB bulk phase are well known, with its direct band gap residing at the Γ point, it is reasonable to determine the physics of bulk GaAs optically. The direct band gap persists in WZ GaAs [59, 68], but the reduced symmetry in WZ crystals has different effects on the band structure [69]. Thus, in the following, the dispersion relations of both GaAs phases at the Γ point, the band structure for nanowire typical ZB/WZ transitions, and the optical selection rules in both phases are shown, according to the latest observations or theoretical predictions.

Band structures at the Γ point

In fig. 2.14, the energy dispersions $E(k)$ at the Γ point for ZB and WZ GaAs are shown.

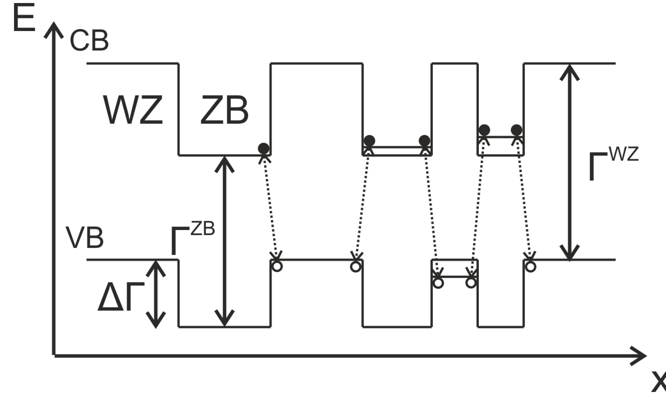

Figure 2.15.: Sketch of the band structure for ZB/WZ phase transitions with different widths of each segment: A staggered band alignment leads to the separation of carriers in the respective crystal structure. Confinement in ZB or WZ parts with a width of some nanometers reduces the band gap. Γ^{ZB} and Γ^{WZ} denote the band gap in ZB and WZ GaAs, respectively, and $\Delta\Gamma$ the valence band offset of WZ GaAs.

In ZB GaAs, the s-like conduction band has its minimum at k = 0, as well as the maximum of the p-like valence bands. At the valence band maximum, the heavy hole (hh) and the light hole (lh) band are degenerate, while due to spin-orbit interaction, the split-off band is separated by an energy Δ_{so} of 0.34 eV at 0 K [71]. The band gap energy E_g between conduction band minimum and the valence band maximum follows the empiric Varshni formula [72], with the values of 1.52 eV at 0 K and 1.42 eV at room temperature [73].

In WZ GaAs, the direct band gap persists at the Γ point, as experimentally verified by Spirkoska et al. [59]. However, direct measurements of the WZ exciton energy were not possible, since for this purpose, a very pure WZ GaAs crystal structure is necessary, as WZ/ZB interfaces sophisticate the measured band gap, see below. Some theoretical calculated band gaps of WZ GaAs are by some meV larger than the ZB one [74, 75, 76], but also a slightly reduced band gap was calculated [77]. The degeneracy at the valence band maximum is lifted in WZ GaAs by crystal field splitting and spin-orbit interaction into a heavy hole, light hole and a split-off band.

Wurtzite/zinc-blende GaAs interfaces

At WZ/ZB GaAs interfaces, which commonly occur in nanowires in large numbers, a staggered type II band alignment is predicted, with a positive valence band offset of the WZ crystal structure [75, 77]. This band alignment is sketched in fig. 2.15. Here, the electrons are confined in ZB segments, whereas holes are bound to WZ segments. Due to the overlap of the wave functions at ZB/WZ interfaces, optical transitions between the localized states can be observed. The energy of the corresponding transitions depends on the valence band offset ΔΓ, and, as ZB and WZ segments of monolayer widths are commonly observed, on the confinement of the wave functions.

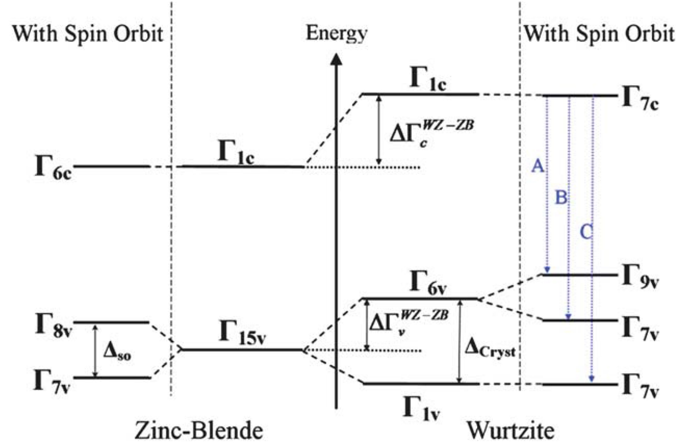

Figure 2.16.: Sketch of the energy level splitting at the Γ point in WZ and ZB GaAs: Considering solely the crystal field, in ZB GaAs the valence band maximum is degenerate (Γ_{15v}), whereas in WZ the degeneracy is lifted (Γ_{6v}, Γ_{1v}). With spin-orbit interaction, in ZB GaAs a split-off band separates (Γ_{7v}) from the degenerate topmost Γ_{8v} valence band. In WZ GaAs, the degeneracy of the topmost valence band (Γ_{6v}) is lifted, and a heavy hole (Γ_{9v}) and a light hole Γ_{7v} band forms. All possible transitions in ZB GaAs are unpolarized, whereas in WZ, the Γ_{1c}-Γ_{6v} and the "A" transition is strongly polarized perpendicular to the WZ $\hat{c}$-axis ("B" and "C" are unpolarized). Adopted from [78].

At 0 K, the valence band offset $\Delta\Gamma$ of WZ GaAs is estimated to reside between 63 meV and 84 meV [75, 77], while the well-known ZB exciton is located at 1.515 eV. This explains emission from GaAs nanowires with mixed crystal structure at energies between the ZB exciton energy and the exciton energy minus the valence band offset $\Delta\Gamma$, i.e. from 1.515 eV to maximum 1.431 eV [59]. Instead, nanowires with a quite pure crystal structure, i.e. when crystal defects are separated at least by the diffusion length the electrons in the crystal, should emit photons at the exciton energy of the respective crystal phase.

Optical selection rules

The selection rules for the optical transitions at the Γ point in ZB and WZ GaAs were recently evaluated by Wilhelm et al. [78] in dipole approximation. In fig. 2.16 the discrete energy levels at the Γ point are sketched for both crystal structures, using the Bouckaert, Smoluchowski and Wigner (BSW) notation for the respective bands [79].

In ZB crystal structure, the transition from the lowest conduction band (Γ_{1c}) to the topmost valence band (Γ_{15v}) is unpolarized due to crystal symmetry (the subscript c and v label the conduction and valence band, respectively). Taking into account spin-orbit interaction, the degenerate Γ_{15v} valence band splits into a degenerate (hh and lh) Γ_{8v} band, and a split-off Γ_{7v} valence band, whereas the conduction band changes to Γ_{6c}. However, the $\Gamma_{6c} - \Gamma_{8v}$ and $\Gamma_{6c} - \Gamma_{7v}$ transitions maintain unpolarized. Thus, when

exciting ZB GaAs optically with an energy close to the band gap, neither absorption nor emission is expected to be polarization dependent.

In WZ GaAs this behavior is expected to be different. Due to the symmetry breaking in [0001] direction, i.e. along the WZ $\hat{c}$-axis, the Γ_{15v} valence band splits into a Γ_{6v} and a Γ_{1v} valence band, while the conduction band remains Γ_{1c}. Both possible interband transitions are highly polarized. The oscillator strength for the $\Gamma_{1c} - \Gamma_{6v}$ transition is 10^{16}-times higher when the absorbed/emitted electric field $\vec{E}$ is perpendicular to the $\hat{c}$-axis compared to $\vec{E}||\hat{c}$, while the $\Gamma_{1c} - \Gamma_{1v}$ transition seems to be polarized parallel to the $\hat{c}$-axis [68, 69]. Considering additionally spin-orbit interaction, the degeneracy of the Γ_{6v} band is lifted and splits into a heavy hole (Γ_{9v}) and a light hole (Γ_{7v}) band, whereas the Γ_1 bands transform to Γ_7 bands. The $\Gamma_{7c} - \Gamma_{9v}$ transition "A" maintains the polarization perpendicular to the $\hat{c}$-axis from the $\Gamma_{1c} - \Gamma_{6v}$ transition, whereas the other two $\Gamma_{7c} - \Gamma_{7v}$ transitions ("B","C") are unpolarized. Consequently, absorption and emission from WZ GaAs at the band edge is expected to be strongly polarized perpendicular to the $\hat{c}$-axis. Note, that the symmetry of the lowest conduction band is still controversial discussed (either Γ_7 or Γ_8). Nevertheless, the selection rules for WZ GaAs are not affected by this debate.

However, in bare GaAs nanowires, optical transitions from excited carriers are hardly detectable, since they preferential recombine non-radiatively via surface states [80, 81, 82]. Therefore, the large nanowire surface has to be passivated.

2.3.4. Surface states and passivation

Due to the high surface to volume ratio of nanowires, on the one hand WZ crystal structure in the GaAs system is accessible and its electronic properties can be studied. On the other hand, the side facets provide a lot of unsaturated bonds, which oxidize at ambient air and lead to the formation of an extraordinary high amount of states in the middle of the band gap, commonly called surface states.

These states trap carriers, which are added to the crystal by background doping or by optical or electrical injection. This induces an electric field, and consequently leads to the formation of a hollow-cylindrical-shaped depletion region at the nanowire side facets [80, 82]. Depending on the diameter of the nanowire, a conducting channel in the center of the nanowire remains, or the depletion region extends over the whole nanowire capturing a huge amount of free carriers [80, 82]. The latter case applies for nanowires with a diameter less than 100 nm and a doping level less than 10^{17} cm^{-3} [81], which holds for most wires presented in this work. Consequently, when exciting carriers in nanowires, one obtains hardly radiative recombination. In GaAs, this effect is very pronounced since the surface recombination velocity is much higher than for other semiconductors [78, 83].

To circumvent this problem, GaAs nanowires are commonly coated with the larger band gap material AlGaAs [80, 82, 83], resulting in a so called "core/shell" nanowire. Since the bulk crystal structures and lattice constants of AlAs and GaAs are quite the same (zinc-blende type with a = 5.66 Å and 5.65 Å, respectively), the shell simply adopts the crystal structure of the core nanowire with the interface being atomically

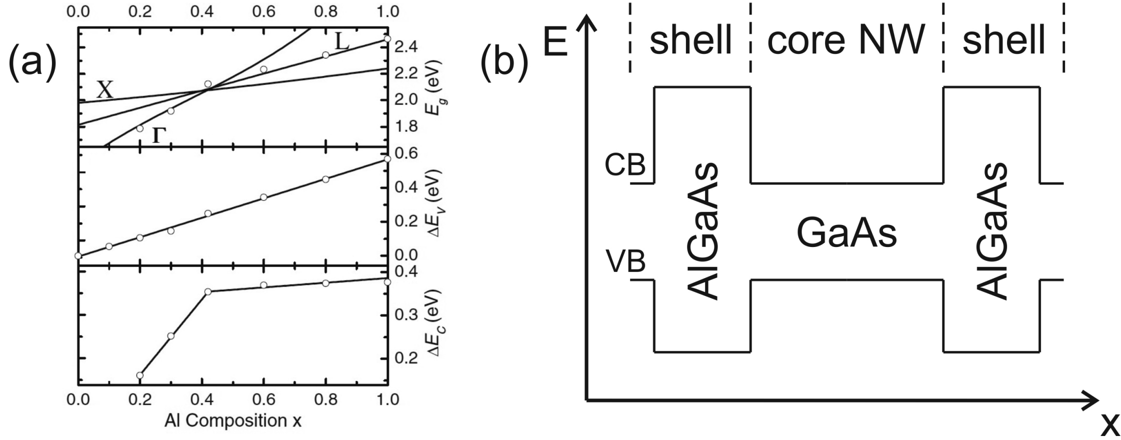

Figure 2.17.: (a) Upper panel: behavior of the band gap E_g in $Al_xGa_{1-x}As$ in dependence on the Al concentration x at the X, L and Γ points. Middle panel: dependence of the valence band offset ΔE_V on x. Bottom panel: dependence of the conduction band offset ΔE_C on x. Adopted from [85]. (b) Sketch of the energy levels of the lowest conduction band and the topmost valence band in GaAs/AlGaAs/GaAs core/shell nanowires.

flat [84]. Here, hardly any carriers accumulate, and the formation of a depletion region in its vicinity is suppressed. Additionally, the GaAs/AlGaAs interfacial recombination velocity is three orders of magnitude lower than the one for bare GaAs [83]. These properties lead to an enhanced radiative recombination strength in the lower band gap material GaAs.

The band gap of AlGaAs strongly depends on the Al concentration x. For $x < 38$ %, $Al_xGa_{1-x}As$ has a direct band gap at the Γ point. For $x > 38$ %, the band gap is indirect with the conduction band minimum at the X point [86], whereas the valence band maximum remains at the Γ point. At 4.2 K, the value of the band gaps $E_g^i(x)$ at position i in reciprocal space can be evaluated via

$$E_g^\Gamma(x) = 1.519 + 1.155x + 0.3x^2 \text{ and } E_g^X(x) = 1.988 + 0.207x + 0.055x^2, \qquad (2.47)$$

for the direct and indirect band gap, respectively [87]. The dependencies of $E_g^i(x)$ at the Γ, L and X point are shown in fig. 2.17a in the upper panel. For any reciprocal lattice point, $E_g^i(x)$ increases nearly linearly with x and the band gaps meet at $x \approx 40$ %, which was later reduced to $x = 38$ % [86]. For a GaAs/AlGaAs heterostructure, the ratio between conduction band offset (third panel in fig. 2.17a) and valence band offset (second panel in fig. 2.17a) is roughly 60:40 for the direct band gap region [73, 85]. In the indirect region, the conduction band offset increases only slowly, and the valence band offset evolution remains linear. Thus, the GaAs/AlGaAs band alignment is in any case type I (straddling gap).

For the investigation of the optical properties of the GaAs nanowires with photoluminescence, the GaAs/AlGaAs core/shell structure is extended by a GaAs shell to

passivate the highly oxidizing AlGaAs surface. The resulting energy levels of the lowest conduction bands and the topmost valence bands are shown qualitatively in fig. 2.17b, depicting clearly the barrier function of AlGaAs for carriers in the GaAs core nanowire. The growth of these GaAs/AlGaAs/GaAs core/shell heterostructures, as well as the optical measurements on nanowires are summarized in chapter 5.

3. Mn containing ferromagnetic materials

With molecular beam epitaxy (MBE) the growth of a variety of heterostructures is possible. To introduce the spin degree of freedom into a semiconductor, usually the growth of ferromagnet/semiconductor heterostructures is performed. The ferromagnets applied for spin-injection experiments into GaAs are typically Fe [88, 89], or Fe containing compounds [90, 91], but also Mn containing compounds like ZnMnSe [92], (Ga,Mn)As [93] and MnAs [94] are used. To detect the spin polarized currents, mostly an light-emitting diode (LED) [95] structure is applied.

In this work, GaAs/(Ga,Mn)As and GaAs/MnAs nanowire heterostructures are grown (see chapter 7 and chapter 8, respectively). Thus, the properties of the ferromagnets (Ga,Mn)As and MnAs are introduced in section 3.2 and section 3.3. Additionally, the epitaxy of these compounds onto GaAs substrates and/or nanowires is summarized. However, to start this chapter, the principles of ferromagnetism are described shortly.

3.1. Ferromagnetism and Curie temperature

In ferromagnetic systems, due to the interaction between the spins, a magnetization is measurable without applying an external magnetic field. In the following, the dependence of the magnetization of a ferromagnetic system on the temperature and the external magnetic field is derived. To do that, the mean field approximation is used to solve the Heisenberg model. Here, the existence of magnetic domains and magnetic anisotropies, as observed in real ferromagnets, is neglected.

The Hamilton operator of a spin system, which couples via exchange interaction and is exposed to an external magnetic field $\vec{B}$, is given by the Heisenberg exchange energy (first term) and the Zeeman energy (second term) [96]:

$$\hat{\vec{H}} = -J_{ij} \sum_{i,j} \hat{\vec{s}}_i \cdot \hat{\vec{s}}_j + g_J \sum_j \mu_B \hat{\vec{s}}_j \cdot \vec{B}. \tag{3.1}$$

J_{ij} is the exchange integral, $\hat{\vec{s}}_i$ and $\hat{\vec{s}}_j$ the spin operators, μ_B the Bohr magneton and g_J the gyromagnetic factor for a particle with total angular momentum of J. In the following, we assume that the system possesses no orbital momentum ($L = 0$), so that $J = S$.

The Heisenberg model of spin exchange interaction can be solved in mean field approximation. This means that the sum of all spin operators $\hat{\vec{s}}_j$ acting on a single spin $\vec{s}_i$ is replaced by an average spin operator summing up the interactions with all neighboring

spins. Then, the interactions of the particles with a single one can be replaced by an effective magnetic field, the molecular field [96]

$$\vec{B}_{\mathrm{mf}} = -\frac{2}{g_J \mu_B} \sum_j J_{ij} \hat{\vec{s}}_j. \tag{3.2}$$

The effective Hamiltonian of a ferromagnetic coupling system then reads

$$\hat{\vec{H}}_{\mathrm{eff}} = g_J \mu_B \sum_i \hat{\vec{s}}_i \cdot \left(\vec{B} + \vec{B}_{\mathrm{mf}} \right), \tag{3.3}$$

which is equivalent to the Hamiltonian of a paramagnet in an external magnetic field $\vec{B} + \vec{B}_{\mathrm{mf}}$ [96]. Since the molecular field measures the effect of the ordering of the system [96], one assumes that

$$\vec{B}_{\mathrm{mf}} = \lambda \vec{M}. \tag{3.4}$$

Here, λ is a constant relating the molecular field with the magnetization of the system $\vec{M}$.

At low temperatures, the magnetic moments can be aligned by the internal molecular field, even when no external magnetic field is present. As the temperature is raised, thermal fluctuations begin to progressively destroy the magnetization, and at a critical temperature, the magnetic order will be eliminated.

Treating the system like a paramagnet in the magnetic field $\vec{B} + \vec{B}_{\mathrm{mf}}$, the recursive relation between $|\vec{M}| = M$ and $|\vec{B}| = B$ reads [96]

$$\frac{M}{M_S} = B_J(y). \tag{3.5}$$

Here, M_S is the saturation magnetization, B_J the Brillouin function for particles with a total angular momentum J and

$$y = \frac{g_J \mu_B J (B + \lambda M)}{k_B T}. \tag{3.6}$$

The system of equations set by equation 3.5 and equation 3.6 is commonly solved graphically.

Assuming no external magnetic field (B = 0), y is linearly dependent on M for a constant temperature. By sketching M/M_S in dependence of y in fig. 3.1a, the intersect of the resulting straight and the Brillouin function gives the magnetization for the system at the respective temperatures. Due to the zero offset of equation 3.6, $M = 0$ is a solution for any temperature. If the slope of the straight at the origin is less steep than the one of the Brillouin function at the very same place, which is the case for small enough temperatures, two additional intersects emerge. It turns out, that in the latter case the non-zero solutions are stable and the zero solution is unstable. This means, that below a transition temperature T_C, known as the Curie temperature, and determined by the equivalency of the slope of straight and Brillouin function at $y = 0$, the system shows

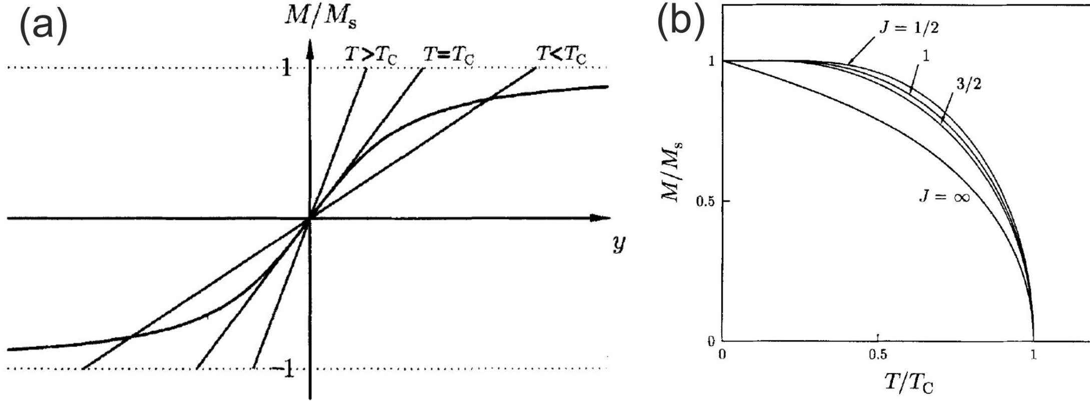

Figure 3.1.: (a) Graphical solution of equation 3.5 and equation 3.6 for B = 0. (b) Mean field magnetization as a function of temperature, deduced for different values of J. Adopted from [96].

a spontaneous magnetization, whereas for temperatures above, no net magnetization is observed.

The temperature dependence of the magnetization can be estimated by iteratively determining the intersects. In fig. 3.1b, $M(T)$ is depicted for some values of J, showing a continuous reduction of the magnetization from $M = M_S$ at $T = 0$ to $M = 0$ at $T = T_C$. The magnetization changes continuously at $T = T_C$, but not its derivative. This behavior sets the transition from ferromagnetic to non-magnetic to a second order state transition.

In an external magnetic field, the phase transition from ferromagnetic to non-magnetic is removed. This can be easily seen from equation 3.6, which then forbids the solution at the origin. The intersect of the straight and $M = 0$ shifts to positive y-values, depicted in fig. 3.2a. Therefore, ferromagnets align even for $T > T_C$ along the direction of the magnetic field, giving a non-zero magnetization. This is sketched in fig. 3.2b for different values of B. Here, larger external fields induce a higher magnetic ordering in the system, also above T_C.

In this work, $M(T)$ curves are obtained by SQUID measurements, which are conducted with a small magnetic field applied to align the probed ferromagnet in a certain direction. To extract the Curie temperature of the ferromagnet from these measurements, the characteristic of the second order phase transition is used. The second derivative of a $M(T)$ curve is set to zero, determining the turning point of the $M(T)$ curve.

3.2. Diluted magnetic semiconductor (Ga,Mn)As

(Ga,Mn)As, which is the most prominent example of a diluted magnetic semiconductor (DMS), was explored 1996 in a pioneering experiment by Ohno et al. [18]. Using

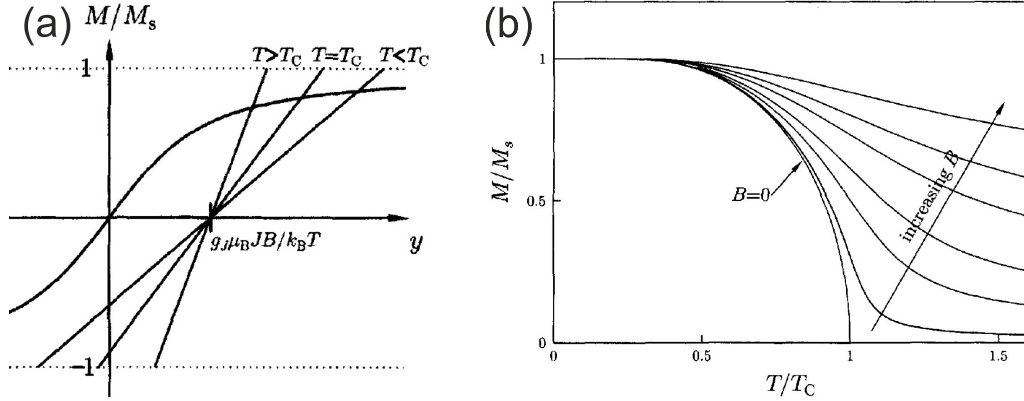

Figure 3.2.: (a) Graphical solution for equation 3.5 and equation 3.6 for B $\neq$ 0. (b) Mean field magnetization as a function of temperature for different magnetic field strengths. Here, $J = 1/2$ is assumed. A ferromagnetic/non-magnetic phase transition exists only for B = 0. Adopted from [96].

DMS, the growth of lattice matched ferromagnetic metals onto the respective semiconductor is possible, introducing the spin degree of freedom into semiconductor physics. In (Ga,Mn)As, the ferromagnetic interaction between Mn atoms is induced by itinerant holes. However, ferromagnetic coupling is only possible when the effective Mn concentration exceeds 1 % [97]. By optimizing the growth of (Ga,Mn)As films, the Curie temperature was maximized until nowadays to 190 K [21].

In section 3.2.1 the structural properties and the main crystal defects introduced during the growth of (Ga,Mn)As are presented, followed by the models explaining ferromagnetism in (Ga,Mn)As in section 3.2.2. Section 3.2.3 approaches the already explored findings of covering GaAs nanowires with a (Ga,Mn)As shell, while in section 3.2.4 crystal defect healing in (Ga,Mn)As by annealing is described.

3.2.1. Structural properties of (Ga,Mn)As

Since (Ga,Mn)As uses GaAs as a host, the crystal structure of (Ga,Mn)As is the same as the GaAs crystal structure, i.e. in a bulk crystal the zinc-blende (ZB) lattice. The equilibrium solubility of Mn atoms in solid GaAs is about 0.1 % [98]. Therefore, the formation of ferromagnetic (Ga,Mn)As can only be obtained far from the thermodynamic equilibrium. In molecular beam epitaxy (MBE), this is realized by the reduction of the growth temperature ("low temperature" (LT) growth). Here, the diffusion lengths and desorption probabilities of Mn adatoms are reduced, and the precipitation of secondary Mn containing compounds is avoided. But LT growth implicates also the incorporation of a large number of crystal defects, which deteriorate the performance of (Ga,Mn)As. In the following, the preferentially occupied lattice sites in ZB GaAs for Mn atoms and the main impurities occurring in LT-(Ga,Mn)As growth, are summarized.

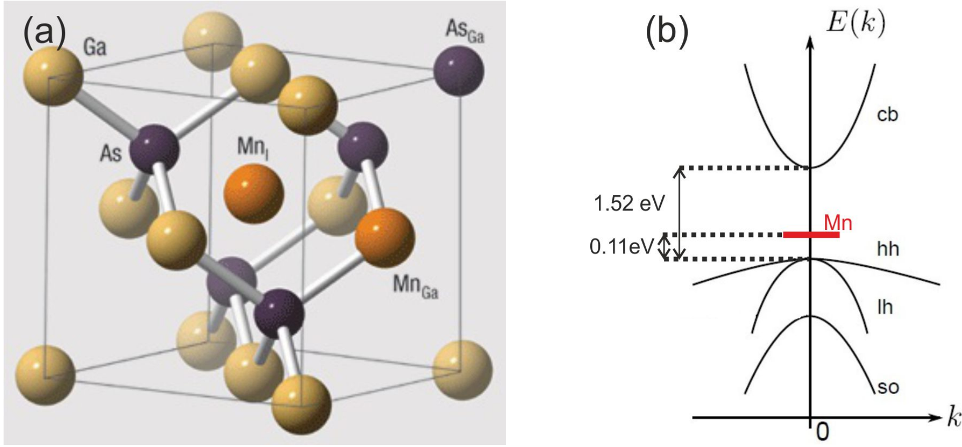

Figure 3.3.: (a) Unit cell of (Ga,Mn)As: Mn atoms reside typically at Ga lattice sites in the GaAs fcc host lattice. Also crystal defects, like Mn interstitials at tetrahedral positions and As anti-sites are depicted. Adopted from [100]. (b) Band structure of GaAs at the Γ point with the Mn impurity level 113 meV above the valence band (at T = 0 K).

In the ZB GaAs crystal, Mn atoms, which introduce a spin-moment of 5/2, preferentially occupy two different lattice sites. They either substitute Ga atoms (Mn_{Ga}) or reside at tetrahedral interstitial sites (Mn_I), depicted in the unit cell of GaAs in fig. 3.3a. Mn_{Ga} provide a hole each and account for the hole-mediated ferromagnetism in (Ga,Mn)As. Instead, Mn_I comprise two electrons, and interact anti-ferromagnetically with Mn_{Ga}. Therefore, they deteriorate the properties of (Ga,Mn)As electrically and magnetically.

The distribution of Mn_{Ga} and Mn_I can be evaluated by minimizing the formation energies of Mn_{Ga} and Mn_I impurities, which are strongly dependent on the partial concentrations of both impurity types [97]. It turns out, that for an overall Mn doping concentration $c_{Mn} < 1.5$ %, Mn_{Ga} have a lower formation energy than Mn_I. Instead, for $c_{Mn} \geq 1.5\%$ both impurities are formed with similar probability. This dependence can be understood considering the electric doping behavior of Mn atoms. The electrostatic attraction between Mn_{Ga} acceptors and Mn_I donors stabilizes the interstitial tetrahedral sites, forming a Mn_{Ga}-Mn_I pair [99]. If no Mn_{Ga} is in the vicinity of a Mn_I, which is rather the case for a low c_{Mn}, Mn_I are highly mobile and therefore unstable.

Other frequent impurities, introduced by LT growth into (Ga,Mn)As, are As atoms residing at Ga sites, called As anti-sites (As_{Ga}, see fig. 3.3a). They also comprise two electrons, and therefore reduce the electric conductance. The incorporation of As_{Ga} depends strongly on the growth parameters, and is supported by low growth temperatures and high As fluxes [101].

Since the atomic radii of Mn and As are larger than the one of Ga, the three main impurities Mn_{Ga}, Mn_I and As_{Ga} widen the GaAs host lattice. The equilibrium lattice

constant of (Ga,Mn)As, $a_{\mathrm{(Ga,Mn)As}}$, can be approximated via [102]

$$a_{\mathrm{(Ga,Mn)As}} = a_{\mathrm{GaAs}} + 0.02 \cdot c_{\mathrm{Mn_{Ga}}} + 0.69 \cdot c_{\mathrm{Mn_I}} + 1.05 \cdot c_{\mathrm{As_{Ga}}}. \qquad (3.7)$$

Here, $c_{\mathrm{Mn_{Ga}}}$, $c_{\mathrm{Mn_I}}$ and $c_{\mathrm{As_{Ga}}}$ denote the concentrations of $\mathrm{Mn_{Ga}}$, $\mathrm{Mn_I}$ and $\mathrm{As_{Ga}}$ impurities, respectively, and a_{GaAs} the lattice constant of GaAs.

If a too high growth temperature is applied, no smooth (Ga,Mn)As crystal is obtained any more, but MnAs clusters in a (Ga,Mn)As matrix are observed [18]. The occurrence of MnAs can be attributed to the low equilibrium solubility of Mn in GaAs, and the circumstance of an As overpressure in LT MBE. The As-rich conditions make MnAs the only stable solid Mn-As compound, compare the Mn-As phase diagram in appendix B fig. B.4. The properties of the ferromagnet MnAs are summarized in section 3.3.

3.2.2. Origin of ferromagnetism in (Ga,Mn)As

Mn atoms possess the electron configuration $[\mathrm{Ar}]3\mathrm{d}^5 4\mathrm{s}^2$, with a half filled 3d shell. The five 3d electrons all possess the same spin orientation, and thus comprise a pure spin moment of 5/2. This very stable d shell configuration is not touched, when a Mn atom substitutes a Ga atom at its lattice site. Here, the two 4s Mn valence electrons participate in the sp^3 hybridized bonds, which account for the tetrahedral zinc-blende lattice, just as the three Ga valence electrons ($[\mathrm{Ar}]4\mathrm{s}^2\mathrm{p}^1$ configuration). Due to the missing electron, one sp orbital remains only half occupied and provides a hole. The corresponding energy level lies 113 meV above the valence band edge [103] (see fig. 3.3b).

The hole and the $3\mathrm{d}^5$ electrons of a $\mathrm{Mn_{Ga}}$ couple anti-ferromagnetically with each other. This behavior can be explained by taking into account different mechanisms, which split the respective energy states, depicted in fig. 3.4a [104]. The Mn $3\mathrm{d}^5$ states all have the same spin orientation and hybridize hardly with the tetrahedral sp orbitals. Due to exchange coupling, the spin degeneracy of the 3d states is lifted (red), whereas the p-like hole state (blue) remains degenerate. Assuming some compensating carriers in the crystal, the Fermi energy E_F resides at the p state. The occupied 3d states reside deep in the valence band, whereas the states with reversed spin configuration are high in the conduction band. Due to the tetrahedral crystal symmetry, each $3\mathrm{d}^5$ level splits into three degenerate t_2 and two degenerate e states. Nevertheless, they comprise a local spin moment of 5/2, while the hole state remains degenerate. However, p-d hybridization splits the p-like hole state. Compared to the occupied $3\mathrm{d}^5$ states, the state with the same spin orientation is pushed above the Fermi energy, whereas the state with odd spin orientation lies below the Fermi energy. Thus, the $3\mathrm{d}^5$ electrons couple anti-ferromagnetically to the hole, which is introduced by the same atom.

By increasing the Mn doping level in the GaAs host crystal, a semiconductor-metal transition takes place. The implications on the valence band structure and the Fermi energy during this transition are not easily accessible, and still under debate. In the following we use a generally accepted picture of the semiconductor-metal transition by Jungwirth et al. [105], based on observations from transport and optical studies on 2D

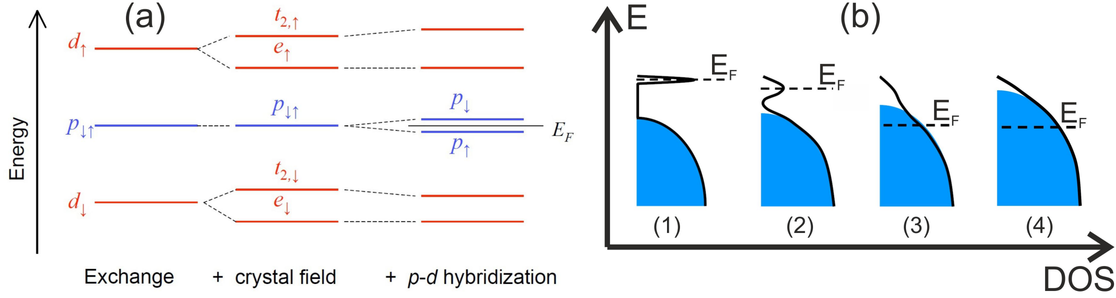

Figure 3.4.: (a) Splitting of the states of the Mn_{Ga} near the Fermi energy: Exchange interaction lifts the spin degeneracy of the 3d states, while the crystal field accounts for the splitting in 3 t_2 and 2 e states. Finally p-d hybridization splits the p-like state at the Fermi energy. (b) Density of states and Fermi energy in (Ga,Mn)As for an increasing doping concentration from 1 to 4: Low doped (Ga,Mn)As (1, 2) is insulating, the impurity band is detached from the valence band. With increasing doping (3, 4), the impurity band merges with the valence band and the Fermi energy resides within delocalized states: metallic behavior originates. Blue areas indicate delocalized states. Adopted from [104] and [105].

(Ga,Mn)As with different Mn doping levels. The implications of an increasing doping level on the valence band structure are sketched in figs. 3.4b.

At weak doping (1 and 2 in fig. 3.4b), the isolated impurities form a narrow band of localized states, separated from the valence band by the energy of the impurity level. Assuming some compensation, the Fermi level resides inside the impurity band. For increased Mn doping, the impurity band widens and finally merges with the valence band (3 and 4 in fig. 3.4b). This can be understood when going from a host crystal with some local impurities to an imperfect crystal with broadened and shifted Bloch bands. The merging happens for a Mn concentration of 1 % to 2 % and is accompanied with the drop of the Fermi level to delocalized states in the valence band, while the tail of the valence band still may consist of localized states. Then, a metallic state is reached and spin communication between local Mn 3d states via hole conductance is possible, leading to a ferromagnetic coupling DMS.

The ferromagnetic coupling via itinerant holes was described qualitatively by Dietl et al. [106] using a mean field Zener model. Generally, an indirect exchange coupling between states can be described using the RKKY exchange coupling [107, 108, 109]. Here, an exchange integral is introduced for the indirect coupling of spins between two impurities, which oscillates in dependence of the product of their distance r_{ij} and the Fermi wave vector k_F. Thus, either a ferromagnetic or anti-ferromagnetic coupling can be obtained. The corresponding Hamiltonian writes

$$H = -2 \sum_{i \neq j} \frac{\sin(2r_{ij}k_F) - 2r_{ij}k_F \cos(2r_{ij}k_F)}{(2r_{ij}k_F)^4} \vec{S}_i \cdot \vec{S}_j. \tag{3.8}$$

In (Ga,Mn)As, the mean field Zener model and the RKKY exchange coupling both predict a hole-mediated ferromagnetic interaction [106, 110]. Due to the low doping

of (Ga,Mn)As, the average distance between carriers is much larger than the distance between the localized spins [111]. Thus, in (Ga,Mn)As the exchange integral (first term in equation 3.8) is positive, yielding a ferromagnetic coupling of the Mn spins. Both models also predict equivalent Curie temperatures T_C for (Ga,Mn)As [111]. It turns out, that T_C is proportional to the product of the effective Mn concentration c_{eff} and the cube root of the hole density p,

$$T_C \propto c_{\text{eff}} \cdot \sqrt[3]{p}. \tag{3.9}$$

3.2.3. (Ga,Mn)As in GaAs/(Ga,Mn)As core/shell nanowires

In 2009, Rudolph et al. [19] introduced the growth of ferromagnetic (Ga,Mn)As on GaAs nanowire side facets, yielding a GaAs/(Ga,Mn)As core/shell structure. Like in the growth of (Ga,Mn)As thin films, shell growth is performed with LT MBE at temperatures below 245°C [112]. Also the (Ga,Mn)As shell adopts the crystal structure of the underlying substrate, i.e. the GaAs core nanowire.

The main differences between thin film and core/shell growth are the growth direction and the overgrown surfaces. Since the growth direction is usually vertical to the exposed surfaces, thin film growth proceeds perpendicularly to the substrate plane. However, shell growth takes place radial on the core, i.e. parallel to the substrate plane. The substrates used for 2D (Ga,Mn)As thin film growth possess usually a GaAs(001) surface, while in core/shell structures the overgrown surfaces depend on the crystal structure of the GaAs core wire. These are commonly $\{1\bar{1}0\}$ and $\{11\bar{2}0\}$ faces for zinc-blende and wurtzite nanowires, respectively.

When covering these faces with a (Ga,Mn)As shell, the formation of additional side facets with $\{11\bar{2}\}$ or $\{1\bar{1}00\}$ orientation is observed [19] (see fig. 3.5a). Along the corresponding directions, Mn atoms are predominantly incorporated forming stripes, whereas in $\{1\bar{1}0\}$ or $\{11\bar{2}0\}$ directions, i.e. on the maintained side facets of the core, a reduced Mn density is detected [113]. This is indicated in the nanowire cross section in fig. 3.5b by the red and blue points, respectively. A similar behavior was observed for Al atoms in the growth of AlGaAs shells around GaAs core nanowires, which was explained with the formation of a narrow corner facet as the result of self-limited growth via capillary diffusion in non-planar nanostructures [84]. The enhanced incorporation of Mn atoms in the stripes leads also to an elevated Mn_I concentration and results, together with the reduced Mn concentration in (Ga,Mn)As on the core side facets, in a reduced Curie temperature compared to (Ga,Mn)As thin films [114].

Magnetization in (Ga,Mn)As shells

The maximum Curie temperature of as-grown (Ga,Mn)As shells, extracted from SQUID measurements, is 20 K [19]. The corresponding M(T) curve is shown in the inset of fig. 3.6a. This is far below the 75 K observed in (Ga,Mn)As thin film growth on GaAs$(1\bar{1}0)$ [115]. The large discrepancy was explained on the one hand with the Mn segregation into the stripes, and therefore an elevated Mn_I incorporation and a reduced

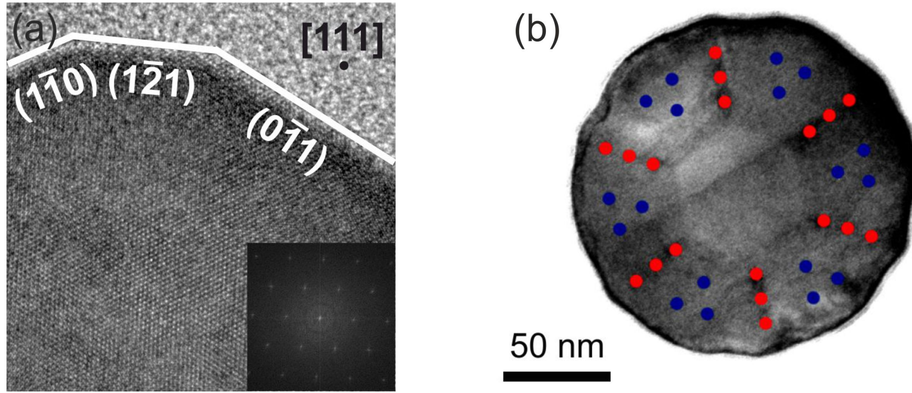

Figure 3.5.: GaAs/(Ga,Mn)As core/shell cross sections in TEM: (a) During (Ga,Mn)As shell growth additional side facets with $\{11\bar{2}\}$ or $\{1\bar{1}00\}$ orientation emerge (inset: corresponding FFT). Here, the labeling is cubic. (b) In (Ga,Mn)As shell growth, Mn atoms accumulate along $\langle 11\bar{2}\rangle$ or $\langle 1\bar{1}00\rangle$ directions (red points), whereas the concentration of Mn atoms is reduced in the residual parts (blue points). Adopted from [113].

density of ferromagnetic coupling Mn_{Ga}. On the other hand, a poor crystal structure of the shell was thought to deteriorate the (Ga,Mn)As performance as well [19], as the GaAs core wires contained lots of crystal defects [114].

Additionally, an uniaxial magnetic anisotropy of the (Ga,Mn)As shell was detected in SQUID (see fig. 3.6a) [19]. When an external magnetic field was applied parallel the nanowire axis, a hysteretic behavior was observed, indicating a magnetic easy axis. Applying the external magnetic field perpendicular to the wire axis, a magnetic hard axis behavior was monitored. At first sight, this behavior might be attributed to shape anisotropy, induced by the wire-like geometry. However, by assuming a wire-like geometry, the anisotropy field calculated from the measured saturation magnetization should be by far smaller than measured in magnetotransport [116]. Thus, another explanation for the detected anisotropy was proposed.

In the growth of (Ga,Mn)As thin films, the magnetic anisotropies in (Ga,Mn)As are additionally affected by strain [117, 118, 119], mediated by the pseudomorphic growth of (Ga,Mn)As on the substrate. Here, compressive strain along one crystal direction accounts for a magnetic easy axis in the same direction, whereas tensile strained (Ga,Mn)As in the growth plane leads to a out-of-plane magnetic easy axis. Thus, the observed magnetic easy axis in the core/shell nanowires was rather attributed to the compressively strained growth of the (Ga,Mn)As shell onto the GaAs core in axial direction, while in radial direction lattice relaxation can take place [19, 20]. To ensure whether the (Ga,Mn)As shell grows compressively strained onto the GaAs core, or relaxes and tensilely strains the core, is examined in section 7.2.1.

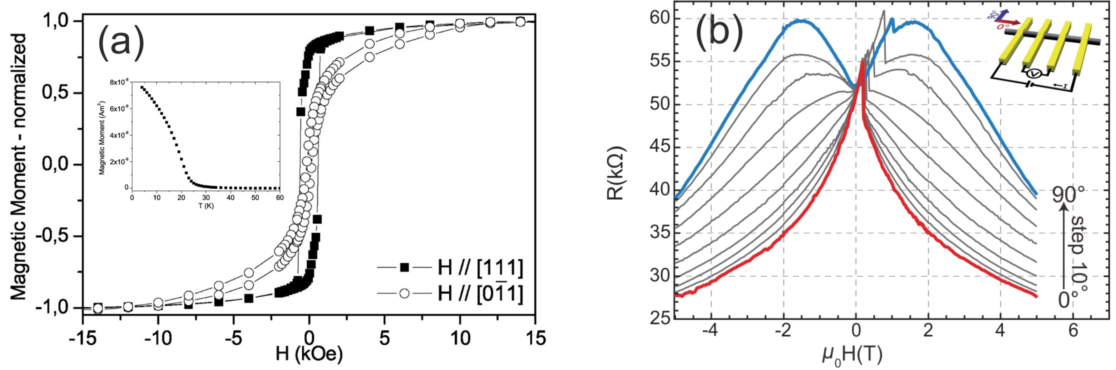

Figure 3.6.: (a) M(H) and M(T) curves (inset) of GaAs/(Ga,Mn)As core/shell nanowires: The magnetic easy axis lies along the wire axis ([111] direction), while the magnetic hard axis is perpendicular to the wire axis (exempl. [0$\bar{1}$1] direction). The derived Curie temperature is 20 K. Adopted from [19]. (b) Magnetoresistance curves of a GaAs/(Ga,Mn)As core/shell nanowire measured for different in-plane magnetic field directions. The sample was rotated from 0° to 90° by 10° steps. Orientation see inset. Adopted from [20].

Magnetotransport characteristics

The uniaxial magnetic anisotropy is confirmed in magnetotransport measurements [20]. In these experiments, the wires reveal a linear transport behavior, so metallic conduction prevails. In the resistance curves, shown in fig. 3.6b, a transition from a magnetic easy axis behavior, when the external magnetic field is applied parallel to the nanowire axis, to a magnetic hard axis behavior, when the external magnetic field applied perpendicular to the wire axis, is detected. These behaviors are superimposed by a strong negative magnetoresistance (NMR), which results from an elevated ordering of the spins with an increasing magnetic field. However, the observed NMR cannot only be attributed to an enhanced magnetic ordering in dependence on the external magnetic field. The resistance also increases with the external magnetic field, e.g. for low values of the magnetic field when it is applied perpendicular to the wire axis (blue curve in fig. 3.6b).

To explain the observed shapes of the curves, Butschkow et al. [20] introduce an effective magnetic field H_{eff}. The precession of spins, or in general, of a magnetization vector $\vec{M}$ around an effective magnetic field, can be described by

$$\frac{\partial \vec{M}}{\partial t} = -\gamma \left(\vec{M} \times \vec{H}_{\text{eff}} \right), \tag{3.10}$$

with γ being the gyromagnetic factor. The strength of H_{eff} strongly depends on the strength of the external magnetic field H_0 and the anisotropy field H_A, as well as the angles of the magnetization and the external magnetic field with respect to the magnetic easy axis, φ_M and φ_H [20],

$$H_{\text{eff}} \propto H_0 \cos\left(\varphi_M - \varphi_H\right) + H_A \cos\left(2\varphi_M\right). \tag{3.11}$$

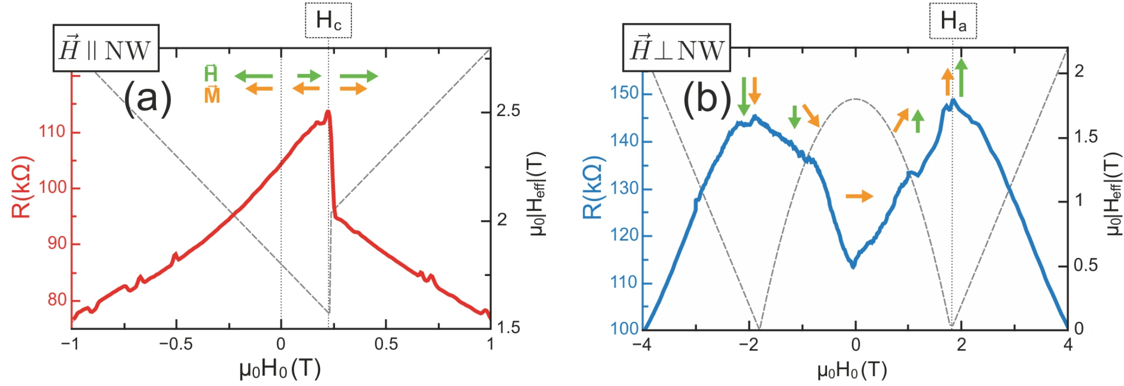

Figure 3.7.: Magnetotransport curves for the magnetic field applied parallel (a) and perpendicular (b) to the wire axis: A magnetic easy and magnetic hard axis behavior is identified, induced by a strong NMR behavior. The arrows denominate the orientation of the magnetization and the external magnetic field, whereas the dashed lines depict the effective magnetic field. Adopted from [20].

In parallel configuration ($\vec{H}_0||NW$, i.e. $\varphi_M \wedge \varphi_H \in \{0°, 180°\}$), H_{eff} is proportional to either $H_0 + H_A$ or $-H_0 + H_A$, due to the parallel or anti-parallel alignment of $\vec{H}$ and $\vec{M}$. Considering the behavior of the NMR for low external magnetic fields in fig. 3.7a, the NMR is nearly linearly dependent on H_{eff} (dashed curve). Additionally, a discontinuity at a coercive field strength H_C is observed, ascribed to the reversal of the magnetization direction. Here, H_{eff} leaps by $2H_C$.

In perpendicular configuration ($\vec{H}_0 \perp NW$), no discontinuity is observed in the magnetoresistance (fig. 3.7b). As the effective magnetic field (dashed curve) possesses a minimum at the anisotropy field strength H_A, in the vicinity of H_A the spins are not well aligned due to the low effective field. This leads to the rounded shape of the magnetoresistance for low values of H_{eff}. The orientation of the magnetization changes from an alignment with the magnetic easy axis for low external fields to an alignment with the external field for large effective fields $H_{\text{eff}} \gg H_A$. Additionally, for large effective fields, a nearly linearly dependence of the NMR with H_{eff} is monitored, just as in parallel configuration.

This dependency of the NMR on the effective magnetic field is similar to a magnon magnetoresistance effect observed in permalloy nanowires [120], and indicates that spin disorder scattering is the dominating effect for the large NMR in GaAs/(Ga,Mn)As core/shell structures.

Note that for structured 2D (Ga,Mn)As thin films the values of the magnetoresistance and the anisotropy field strength are roughly one order of magnitude lower than in the case of (Ga,Mn)As shells [20]. Here, the anisotropic magnetoresistance (AMR) governs the transport behavior, while the NMR plays a minor role. In addition to the reduced Curie temperature, the strong NMR behavior indicates a lower crystalline quality in (Ga,Mn)As shells than in 2D (Ga,Mn)As thin films.

The quality of the (Ga,Mn)As shell can be improved by optimizing the crystal structure of the GaAs core nanowire and the (Ga,Mn)As shell growth. These optimization processes are performed in sections 4.3.1 and 7.3 concerning the unusual WZ GaAs and WZ (Ga,Mn)As crystal structure.

3.2.4. Annealing of (Ga,Mn)As

The quality of as-grown (Ga,Mn)As films or shells can be improved using an annealing procedure [121], which is usually performed separately from growth. Here, crystal defects, introduced by low temperature MBE growth, are removed by thermal annealing.

Considering the most common impurities in (Ga,Mn)As, i.e. Mn_I, Mn_{Ga} and As_{Ga}, Mn_I are the least stable impurities, since they are not covalently bound into the crystal lattice. Thus, initially Mn_I, which deteriorate the (Ga,Mn)As crystal electronically and magnetically, are activated when the sample temperature is increased. This happens at temperatures above 160°C [122], so Mn_I are able to diffuse within the (Ga,Mn)As crystal between interstitial sites. Since at the sample surface lots of unsaturated bonds exist, the diffusing Mn atoms get bound there and loose its double-donor character due to oxidation. The most effective passivation of Mn_I at the crystal surface was observed under oxygen atmosphere [123], while nitrogen is less efficient [124], and an As-cap on top of the (Ga,Mn)As leads to the formation of MnAs [125].

With increasing annealing temperature, the out-diffusion of Mn_I becomes faster, but also processes with a higher activation energy get more probable, like removing Mn_{Ga} and the formation of MnAs clusters within the crystal. This would, of course, deteriorate the quality of the (Ga,Mn)As layer and therefore must be avoided. A degradation of the (Ga,Mn)As layer due to the activation of Mn_{Ga} is also observed for too long annealing times at low temperatures, so ideally annealing of (Ga,Mn)As layers is performed at temperatures < 190°C for times shorter than 200 h [97, 122].

The introduction of As_{Ga} is set by the applied conditions during the (Ga,Mn)As growth and cannot be altered by annealing, since for their activation temperatures above 500°C are necessary [126]. Such elevated temperatures would also lead to the out-diffusion of Mn_{Ga} and to the formation of MnAs clusters, which deteriorates the quality of the (Ga,Mn)As layer.

The effect of annealing on the properties of GaAs/(Ga,Mn)As core/shell nanowires was investigated by Eckrot [127]. As in (Ga,Mn)As thin films, the out-diffusion of Mn_I leads to an improvement of the conductance and ferromagnetic coupling. The maximum Curie temperature obtained hereby was 60 K [114], which is roughly half the value of annealed films grown on equivalent substrate surfaces [115]. However, this relatively high Curie temperature for (Ga,Mn)As shells could not be reproduced, so this value should be treated with caution. Common Curie temperatures after annealing are values below 25 K [127], which probably result from the reduced quality of the as-grown wires. After annealing, the strength of the NMR reasonably decreases due to the elevated magnetic ordering in the crystal. Surprisingly, another phenomenon is detected concerning the as-grown uniaxial anisotropy. While the magnetic easy axis behavior along the wire

axis maintains after annealing, the magnetic hard axis behavior perpendicular to the nanowire axis vanishes and is replaced by a magnetic easy axis behavior comparable to the one along the nanowire axis. Since strain is in (Ga,Mn)As one of the influences on the magnetic anisotropy, this change was attributed to the reduction of strain anisotropy in the GaAs/(Ga,Mn)As core/shell system by the out-diffusion of Mn_I to the surface [127].

3.3. Manganese Arsenide (MnAs)

MnAs is a metallic compound, whose ferromagnetism was discovered by Hilpert and Dieckmann in 1911 [128]. They produced MnAs by the direct reaction of the elements in a furnace. When cooling down the obtained small MnAs crystallites to room temperature, two polymorphic transformations were observed, which affect crucially the magnetic properties of MnAs, see below.

Later, with the possibility to realize ferromagnet/semiconductor hybrid structures in molecular beam epitaxy, MnAs became one of the candidates for spin injection at room temperatures [129]. So MnAs films directly grown on GaAs are an intensively studied material system. The growth and interface formation of GaAs/MnAs heterostructures [130], the usage of MnAs as spin injectors into GaAs, proven in a spin LED geometry [94], as well as the spin valve effect in a MnAs/GaAs/MnAs trilayer were explored [131].

In section 3.3.1, the structural properties of MnAs are described in general. The heteroepitaxy of MnAs on GaAs is exemplarily shown for the GaAs(111) interface in section 3.3.2, which is relevant for the growth of MnAs segments in GaAs nanowires (see section 8.2). The magnetic anisotropy behavior of MnAs thin films on GaAs substrates is presented in section 3.3.3.

3.3.1. Structural properties

The solid crystal structure of stoichiometric MnAs adopts three different phases, depending on the lattice temperature. Below 40°C, the ferromagnetic α-MnAs phase of the hexagonal wurtzite type is observed. At 40°C, a first order phase transition takes place. Here, the ferromagnetic coupling vanishes, giving the Curie temperature of MnAs. Additionally, the hexagonal lattice parameter a decreases abruptly by 1 % with rising temperature, while the lattice parameter c remains unchanged. The values of a and c are shown in fig. 3.8 in dependence on the temperature. The first order transition possesses a thermal hysteresis of about 10°C, so when cooling down the between 40°C and 126°C stable orthorhombic β-MnAs phase to RT, usually not only α-MnAs is observed, but also the orthorhombic phase. The distortions of the orthorhombic from the hexagonal lattice are small and vanish at a temperature of 126°C again, reversing the crystal structure to the hexagonal wurtzite type in a second order phase transition, without a volume change. The magnetic behavior of β-MnAs is still under discussion, since it neither shows a long-range anti-ferromagnetic order nor a Curie-Weiss magnetic susceptibility, but it is usually assumed to be paramagnetic [132]. The wurtzite γ-MnAs phase above 126°C is also paramagnetic.

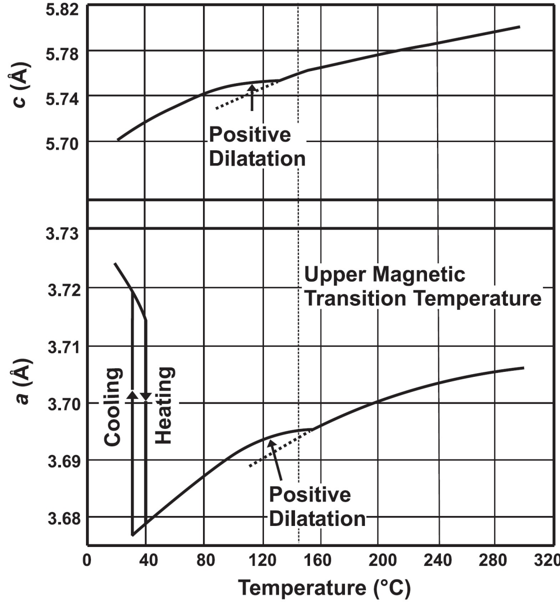

Figure 3.8: Temperature-dependent change of the MnAs lattice constants a and c: The first order phase transition at 40°C induces an abrupt change of a, which shows a hysteretic behavior. The lattice constant c along the [0001] direction shifts continuously. The second order phase transition at 126°C shows no volume change of the MnAs unit cell. Adopted from [132].

3.3.2. MnAs thin films on GaAs substrates

The heteroepitaxial growth of MnAs on GaAs with MBE proceeds rather in Volmer-Weber (3D island) or Stranski-Krastanov growth mode (layer plus island), than in the desirable Frank-van der Merwe growth mode (layer-by-layer). To improve the quality of the MnAs films, usually a growth temperature between 200°C and 250°C is used [132], so γ-MnAs is epitaxied on GaAs. The properties of the ferromagnetic α-MnAs phase are then studied after cooling down to RT.

The observed epitaxial relations between MnAs layers and GaAs substrates, resulting from the minimization of the interface energy, are known as M-plane and C-plane orientations for hexagonal materials. The orientation of MnAs on GaAs(001) and GaAs(110) is $[1\bar{1}00]$ (M-plane), while on GaAs(111) it is [0001] (C-plane). In the following, the fully epitaxial relationships and the mismatch accommodation mechanism for MnAs-layers on GaAs(111) are described only, since this is the observed MnAs/GaAs interface when growing MnAs segments in GaAs nanowires (see section 8.2).

For this interface, the commonly observed relations of the crystal lattices are sketched in fig. 3.9a: the MnAs $\hat{c}$-axis is oriented out-of-plane, i.e. [0001]MnAs||[111]GaAs, while the $\langle 11\bar{2}0\rangle$ directions are parallel to $\langle 1\bar{1}0\rangle$ orientations of GaAs and lie in-plane, just as the $\langle 1\bar{1}00\rangle$MnAs|| $\langle 11\bar{2}\rangle$GaAs orientations.

The MnAs(0001) facets on GaAs(111) possess a terrace-like structure, which can be visualized in STM (see fig. 3.9b). As already mentioned, at RT usually α-MnAs and β-MnAs coexist. In MnAs(0001) layers grown on GaAs(111), α-MnAs forms quasi-hexagons, while β-MnAs gives a honeycomb lattice around. This can be visualized with X-ray magnetic circular dichroism photoemission electron microscopy (XMCDPEEM) [135], which gives a contrast in dependence on the domain orientation (see fig. 3.9c).

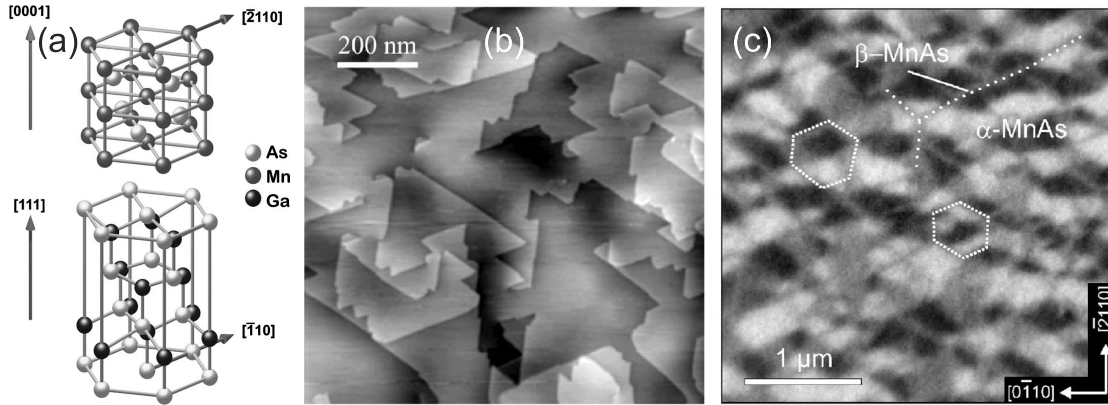

Figure 3.9.: (a) Sketch of the crystal orientations for the growth of wurtzite MnAs (above) on the (111) surface of a zinc-blende GaAs crystal (below). The epitaxial relations are [0001]MnAs||[111]GaAs, $\langle 11\bar{2}0\rangle$MnAs|| $\langle 1\bar{1}0\rangle$GaAs and $\langle 1\bar{1}00\rangle$MnAs|| $\langle 11\bar{2}\rangle$GaAs. (b) STM image of a MnAs(0001) surface: the growth of large terraces is visible. (c) XMCD-PEEM image of a MnAs(0001) film at room temperature: The distribution of β-MnAs (grey) within the matrix of quasi-hexagonal α-MnAs is honeycomb-like. α-MnAs can be identified by the white and black areas, which monitor the opposed orientation of the magnetization. Adopted from [133, 134, 135]

The different lattice constants between the hexagonal WZ MnAs (a = 3.725 Å and c = 5.713 Å [136]) and cubic ZB GaAs (a = 5.65 Å) introduce strain in the MnAs layer, which gets released in the two in-plane MnAs crystal directions differently. The lattice mismatch of approximately 7 % along $\langle 11\bar{2}0\rangle$MnAs|| $\langle 1\bar{1}0\rangle$GaAs is released through the introduction of periodic dislocations at the interface [137]. According to Mattoso et al. [134], a coincident super-lattice with only 0.16 % mismatch accounts for a dislocation-free heteroepitaxy along the $\langle 1\bar{1}00\rangle$MnAs|| $\langle 11\bar{2}\rangle$GaAs directions.

3.3.3. Magnetic anisotropy of MnAs thin films

In M-plane MnAs thin films grown on GaAs substrates, a uniaxial magnetic anisotropy with magnetic anisotropy constants close to the bulk MnAs values is detected [138, 139]. The magnetization shows an almost perfectly squared loop hysteresis characteristic when the magnetic field is applied along the in-plane [11$\bar{2}$0] direction giving the magnetic easy axis. Instead, the in-plane [0001] direction possesses no hysteretic behavior [136], typical for a magnetic hard axis.

In the case of C-plane MnAs films, as observed for the epitaxy of MnAs on GaAs(111), the magnetic hard axis is perpendicular to the surface plane, whereas the growth plane is a magnetic easy plane being nearly magnetic isotropic [135]. Here, measurements of the magnetization in dependence on the applied magnetic field reveal a rounded loop hysteresis (see fig. 3.10a), which is correlated with the topographic structure of the MnAs film [135]. The forming quasi-hexagonal α-MnAs structures of hundreds of

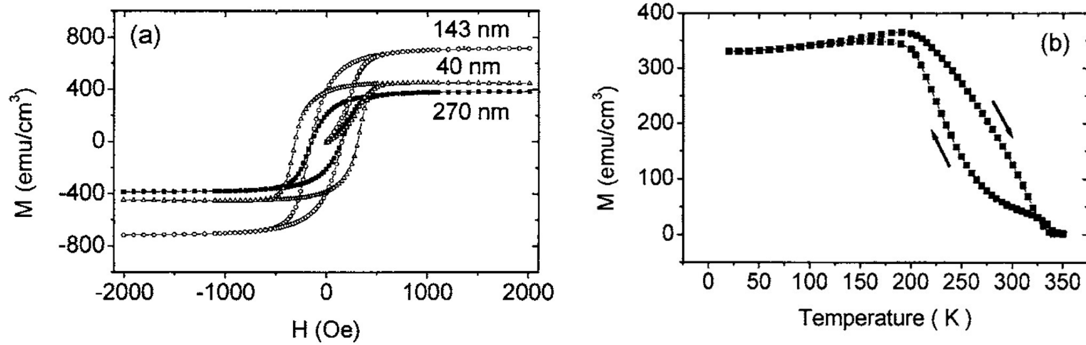

Figure 3.10.: (a) Room temperature hysteresis loops (M(H) curves) for different film thicknesses of MnAs(0001) epitaxied on GaAs(111). (b) The typical zero field M(T) curve of MnAs(0001) on GaAs(111) shows a hysteretic behavior for cooling and defrosting, indicating the coexistence of α- and β-MnAs over a large temperature range. Adopted from [140].

nm in diameter, surrounded by the non-magnetic β-MnAs honeycomb lattice (compare fig. 3.9c), possess mainly a vortex-like domain pattern.

Temperature-dependent measurements of the magnetization (see fig. 3.10b) also reveal the coexistence of α- and β-MnAs over a wide temperature range [140]. A hysteretic behavior of the magnetization below the Curie temperature of α-MnAs is observed for cooling and defrosting, when no magnetic field is applied. In the temperature range, when β-MnAs separates single α-MnAs areas, these areas easily lose their magnetic relation, reducing the observed total magnetic moment. If a magnetic field is applied during cooling/defrosting, no hysteresis is observed, since the magnetic domains all orientate along the same direction [140].

4. GaAs nanowire growth

This chapter addresses macroscopic and microscopic features of GaAs nanowire growth. In molecular beam epitaxy (MBE), the nanowires were grown with the Vapor-Liquid-Solid (VLS) mechanism using either pure Ga or an Au-Ga alloy as the catalyst. In the case of Ga-catalyzed nanowire growth, the used substrates were Si(111) wafers, which can be easily used to nucleate GaAs nanowire growth. In the Au-catalyzed case, GaAs(111)B wafers covered with a thin Au layer of sub-nm height were applied.

At the start of this thesis, it was known, that GaAs nanowire growth on Si(111) is possible, whereas the initial stages during nucleation of this heteroepitaxial growth were unknown. This resulted in nanowire growth along multiple $\langle 111 \rangle$ directions, not only vertical to the substrate plane. However, vertical growth is necessary for the usage of nanowires for further applications, e.g. for the growth of a radial-symmetric shell. The conditions for vertical nanowire growth on Si(111) are deduced in section 4.1 from the growth of nanowires on Si(111) substrates, whose surfaces were prepared in different ways. The basics of Au-catalyzed growth on GaAs(111)B in the MBE system in Regensburg were already investigated by Rudolph [114], and are therefore not further elucidated here.

After finding a reliable preparation method to obtain only vertical GaAs nanowire growth on Si(111) substrates, the effect of different growth parameters on macroscopic properties of the forming wires are investigated in section 4.2. Here, the temperature range, in which the Ga-catalyzed growth of the GaAs nanowires on Si(111) is possible, as well as the areal nanowire density and the nanowire shape are determined. The behaviors of these properties are explained via the models of growth kinetics, which were introduced in section 2.1.

Furthermore, in section 4.3, the crystal structure of the nanowires is optimized towards stacking-fault-free wurtzite (WZ) and twin-plane-free zinc-blende (ZB) GaAs. This is a necessary step, since the occurrence of a mixed crystal structure in the wire leads to the observation of different physical properties, which cannot be easily attributed to either the WZ or ZB GaAs phase. For crystal structure optimization, the growth parameters corresponding to the conditions derived by thermodynamical considerations, introduced in section 2.2, are applied. Thereby, Au- or Ga-catalyzed nanowire growth at different conditions and crystal structure determination of the nanowires in transmission electron microscopy (TEM) is performed.

4.1. Nucleation and vertical nanowire growth on Si(111)

First growth studies of GaAs nanowires in the III-Arsenic MBE system in Regensburg using the Ga-catalyzed growth technique were performed on GaAs and Si substrates covered with different kinds of passivating silicon oxides [114]. In this thesis, we focus on the growth of GaAs nanowires on Si(111) substrates, which are covered with a passivating native oxide layer, that originates from the wafer production process. As the GaAs nanowires grow in ⟨111⟩ direction, we chose the substrate orientation to be (111), so exclusively vertical growth can be obtained. This is important for the growth of nanowires with a radially symmetric shell, see sections 5.1.1 and 7.

But also for the growth on passivated Si(111) substrates, we observe a non-vertical growth of nanowires. This observation is attributed to the thickness and roughness of the oxide layer, which leads to a randomly loss of the epitaxial contact of the wires. In order to avoid the growth of non-vertical wires, we introduce a wafer treatment method before growth. The kind of the oxide is further analyzed using Fourier transform infrared spectroscopy (FTIR).

4.1.1. Optimization of nucleation on native oxide

When applying suitable growth parameters for the VLS growth of GaAs nanowires in MBE, e.g. a Ga rate of 2.8 Å/s, an As_4 BEP of $6.5 \cdot 10^{-6}$ Torr and a growth temperature of 600°C, the nanowires usually grow higgledy-piggledy, as can be seen in the top view of a nanowire sample in fig. 4.1a. If we takes a closer look, some vertical grown wires can be identified (some are provided with green circles). Also, some wires grown along three ⟨111⟩ directions, which have a rotational symmetry in the surface plane of 120° (solid red arrows) and an inclination angle of 19° towards the substrate, are present. Additionally, nanowires growing along the red dashed directions are monitored, which indicate ⟨111⟩ directions that appear due to a second order twinning phenomenon of the initial crystalline GaAs nucleus [141], called hereafter "seed". Eventually, nanowires are observed, which grow in arbitrary directions, i.e. they lost the epitaxial contact to the substrate due to a too thick oxide layer between wire and substrate. Thus, the low percentage of vertical nanowires is attributed to the thickness and roughness of the native silicon oxide on the substrate, which both seem too high to provide a proper epitaxial contact for the GaAs wires on the Si substrate, and also lead to a twinning of the GaAs seed.

The sort of the native oxide on the Si surface can be estimated using Fourier transform infrared spectroscopy (FTIR) [142]. From interstitial Si-O-Si bonds absorption bands arise at 810 cm^{-1} and 1107 cm^{-1}, whereas a prominent feature of stoichiometric SiO_2, the longitudinal optical phonon, emerges at 1250 cm^{-1}. Reflexion FTIR measurements of the native oxide on the Si substrate (red curve in fig. 4.1b) reveal only the bands at approximately 810 cm^{-1} and 1107 cm^{-1}, indicating that the native oxide consists mainly of interstitial bonds. As the oxygen content in the bond increases with the silicon oxide layer thickness [142], a dominating interstitial oxide in thin native oxide layers (< 2 nm)

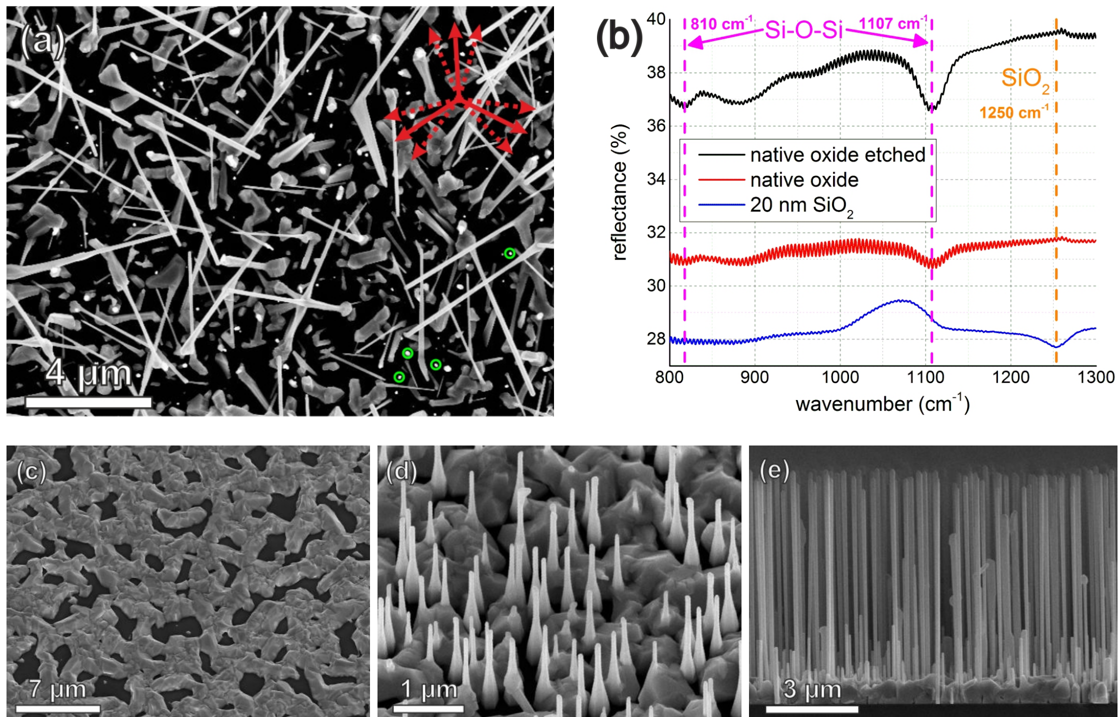

Figure 4.1.: (a) Scanning electron microscopy (SEM) top view of GaAs nanowires grown on a Si(111) wafer with untreated native oxide: the nanowires grow higgledy-piggledy. Red arrows: ⟨111⟩ directions with 19° inclination angle towards the substrate. Dashed arrows: ⟨111⟩ directions occurring due to second order twinning phenomena of the GaAs seed. Green circles: some vertical grown nanowires. (b) Reflectance FTIR reveals the sort of oxide used for nanowire growth: it is sub-stoichiometric interstitial Si-O-Si and no SiO_2. For comparison, a wafer with 20 nm thermal SiO_2 was measured. (c) After etching the native oxide with NH_4F for 10 s no nanowires grow, but coalescing GaAs clusters. (d) Highly tapered nanowires start growing from single clusters when etching the oxide less than 5 s. (e) Optimum conditions for the growth of vertical nanowires are obtained for a short NH_4F dip of 1 s.

is reasonable. The longitudinal optical phonon of SiO_2 was only detected in Si substrates covered with an oxide layer of 20 nm thickness (blue curve in fig. 4.1b).

Since the initially forming GaAs seed particles seem to loose the epitaxial relation easily on an untreated native oxide, the oxide thickness was diminished via wet chemical etching in an ammonium fluoride (NH_4F) containing etchant. The etching does not affect the sort of oxide, as proven by reflexion FTIR measurements (black curve in fig. 4.1b): again, interstitial Si-O-Si bonds dominate.

The results of nanowire growth on Si(111) substrates covered with native oxide, which was etched for 10 s, 5 s and 1 s, respectively, are shown in figs. 4.1c, 4.1d and 4.1e. When growing on a substrate, which was etched for 10 s (fig. 4.1c), no nanowires are observed, but coalescing traces of horizontal GaAs crystallites. The entire suppression of nanowire growth may be attributed to the dissolution of the whole passivating oxide, leaving only the bare Si(111) surface. Here, the growth of GaAs traces in the substrate plane seems preferred. For a diminished etching time of 5 s (fig. 4.1d), the growth of highly tapered nanowires is monitored, emerging from non-coalescing clusters. Seemingly, here also unpassivated areas dominate, which are covered by GaAs clusters. Nanowires are only observed atop these clusters, whose lateral growth is apparently limited by the remaining passivating oxide. When reducing the etching time further to 1 s (fig. 4.1e), a nearly untapered growth of nanowires with a high areal density is observed. Since here more of the passivating oxide remained on the substrate, the horizontal GaAs trace or cluster growth seems to be suppressed during the early stage of growth, and the formation of perpendicular wires is supported.

Therefore, in the case of etching the native oxide for 1 s, which obviously corresponds to small unpassivated areas, the amount of untapered vertical wires is best. Instead, for longer etching times, meaning larger unpassivated areas, highly tapered or even no nanowire growth, but lateral growth is observed. The reasons for this behavior will be discussed in section 4.1.3 after introducing the site-selective growth of GaAs nanowires in the next section.

4.1.2. Site-selective growth

Another task, besides the growth of exclusively vertical nanowires, is the growth of uniform nanowires, each possessing the same length and the same diameter. This should be possible when growing wires from equivalent seeds, and providing the same local growth conditions. However, this is not the case for the growth on silicon substrates covered with native oxide, although the wires in fig. 4.1e look quite promising. Here, the seed size depends primarily on the roughness of the passivating oxide, and can only be affected to a certain extent (compare section 4.2). Even equivalent growth conditions for all wires on the sample are not ensured by applying constant molecular fluxes. When the wires grow too dense, shadowing effects of the molecular fluxes occur due to the nanowires in the vicinity [143], which affect the local growth conditions and lead to differently shaped nanowires. To avoid this, in the following we preset uniform openings far apart from each other in a fully passivated surface, where uniform nuclei can form

and nanowires can grow at the same local growth conditions [9].

For these experiments, Si(111) substrates covered with 32 nm passivating thermal SiO_2 were used. Applying electron beam lithography and wet chemical etching (see [114, 144, 145] for detail), periodic openings with different spacings were predefined in the SiO_2. These openings provide nucleation sites for the GaAs seeds on the Si substrate. They typically have a diameter of 200 nm, as can be seen by the dark islands in the SEM top view in fig. 4.2a, and were designed so that there was no silicon oxide remaining inside. The round particles inside the openings are Ga droplets, occurring due to a "Ga predeposition" step, see below.

Conditions suitable for nanowire growth were explored by varying the As_4 BEP while the growth temperature and the Ga rate were held constant at 600°C and 0.4 Å/s, respectively. In order to ensure the formation of catalyzing liquid Ga droplets in each opening, the growth was initiated by solely opening the Ga cell for 90 s, called "Ga predeposition" [8]. This step was followed by the additional opening of the As cell, which results in the growth of the GaAs crystals.

The typical growth dependence on the As_4 flux or As_4 beam equivalent pressure (BEP) is exemplarily shown in figs. 4.2b, 4.2c and 4.2d for a 2 µm spacing. At a low As_4 BEP of $1.8 \cdot 10^{-7}$ Torr, large droplets form (fig. 4.2b), which cover the whole area of the opening and indicate a huge local Ga excess. Above As_4 BEPs of $3.7 \cdot 10^{-6}$ Torr, the local As/Ga ratio seems to change to highly As-rich. The predeposited Ga droplets are consumed and GaAs crystallites grow (fig. 4.2c). They mostly exhibit a threefold symmetric pyramidal form, dedicated to the low growing GaAs {110} crystal facets [146]. Only for intermediate As_4 fluxes the growth of wires is observed, as exemplarily shown in fig. 4.2d for an As_4 BEP of $3.7 \cdot 10^{-7}$ Torr. Surprisingly, not a single wire grows perpendicularly to the substrate. They all emerge from a large GaAs crystal, which covers the whole Si(111) surface of the opening, and then crawl on the passivated substrate, or grow in a $\langle 111 \rangle$ direction different from the perpendicular one.

This indicates that, even if a liquid Ga droplet is already present on the Si(111) surface, the growth of a nanowire is not necessarily preferred. Apparently, first GaAs cluster growth takes place in the substrate plane until the bare Si(111) surface is covered, and only thereafter nanowire growth can occur.

4.1.3. Conclusion

From the experiments in sections 4.1.1 and 4.1.2, we detect a completely horizontal coverage of the bare Si(111) surface before the growth of vertical nanowires is observed. Seemingly, first a GaAs crystal grows on unpassivated Si(111) laterally, as long as the liquid Ga droplet has a remaining contact to the substrate, as already indicated for Au-assisted growth on Si(111) [147, 148]. At a later stage of growth, when the interface to the passivating oxide is reached, the Ga droplet appears to move fully atop the GaAs crystal. Depending on which facet(s) is/are wetted and how many twin defects already occurred in the lateral growth, then the specific $\langle 111 \rangle$ growth direction is set. However, as the growth of GaAs on Si(111) is not lattice matched (mismatch of ≈ 4.1 %), crystal defects

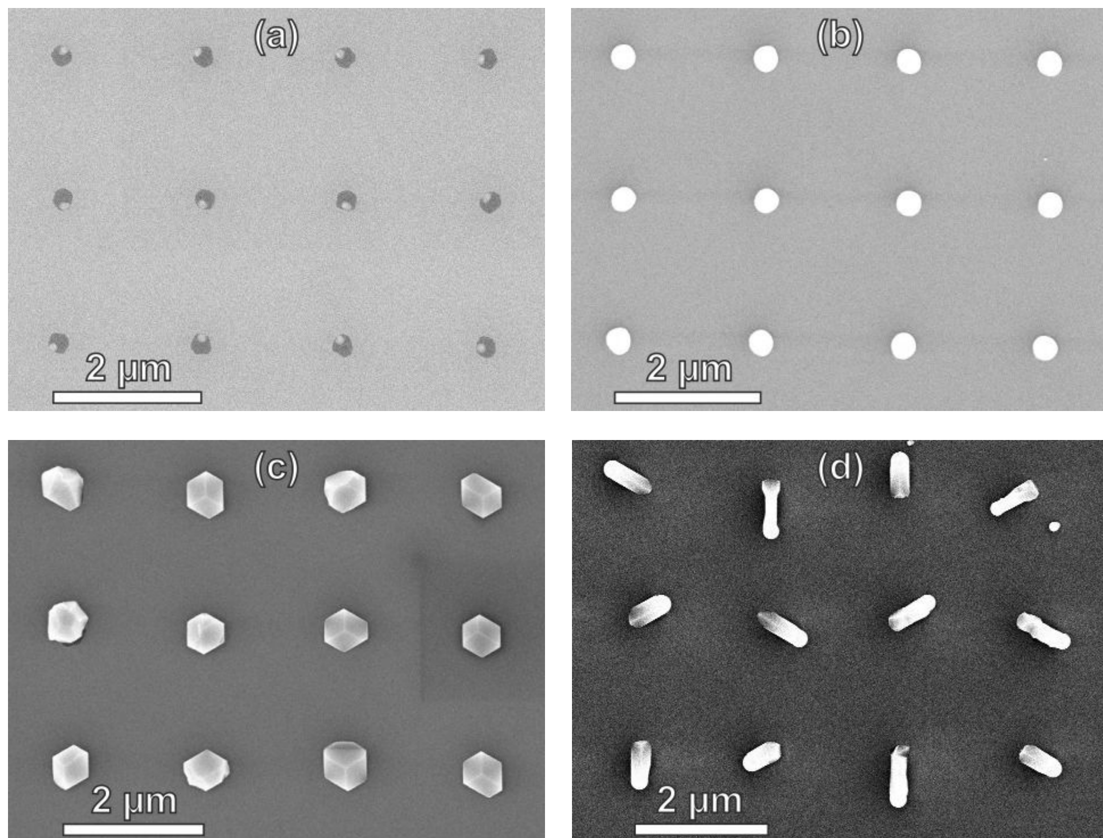

Figure 4.2.: SEM top views of site-selectively grown samples with a spacing of the openings of 2 µm: (a) Ga droplets (bright, ∅ = 80 nm) form in the openings (dark, ∅ = 200 nm) in a "Ga predeposition" step. (b) Growth with As_4 BEPs below $1.8 \cdot 10^{-7}$ Torr leads to the formation of huge Ga droplets, which cover the whole opening, indicating a local Ga excess. (c) Local As excess leads to the consumption of the catalyst droplet and to the formation of pyramidal shaped GaAs crystals for As_4 BEPs above $3.7 \cdot 10^{-6}$ Torr. (d) Nanowire growth is observed for intermediate As_4 BEPs only.

during lateral growth are easily introduced in the seed. This is more likely for large openings or unpassivated Si(111) areas than for small ones, where lateral relaxation may take place more easily. Thus, the size of the free Si(111) surface appears to be directly linked to the amount of twin defects occurring in the GaAs seed crystal, which has to be avoided for the growth of nanowires in vertical direction.

This dependence coincides with a behavior derived from different accessible GaAs seed shapes [149, 150]. For large droplets, the GaAs seed has more likely an octahedral shape due to the formation of the lowest energy surfaces, i.e. {111}B facets. This seed makes eight different growth directions possible, depending on which facet the droplet finally moves to. Instead, in small droplets, the forming of a flat seed is preferred, when the growth of a monolayer GaAs on Si(111) is completed before the next monolayer nucleates (compare section 2.1.8). Then, the droplet wets solely the (111) top facet, and nanowire growth proceeds vertical.

Both findings, the formation of a flat seed instead of an octahedral one, and the suppression of crystal defects within the seed, indicate the necessity of a small unpassivated Si surface for the growth of vertical GaAs nanowires on Si(111). With this, the high amount of vertical nanowires, obtained with the slight etching of the native oxide (section 4.1.1), which obviously leads to small openings, can be explained. The impossibility to grow vertical nanowires site-selectively in large openings of a fully passivated substrates (section 4.1.2) can also be attributed to these reasons.

However, the structuring of fully passivated substrates with small openings for site-selective growth is not easily attainable with electron beam lithography and wet chemical etching. Also, the growth of GaAs nanowires on those substrates is not straightforward [10, 143], and even when an attempt succeeded [8], it was not reproducible. The reasons behind this are currently under investigation and not easily accessible, so in this thesis, the site-selective growth of GaAs nanowires is not pursued further. Instead, to be able to grow suitable wires for further applications, the growth of GaAs nanowires on Si(111) covered with native oxide is studied concerning the effects of different growth parameters.

4.2. Epitaxy of GaAs nanowires on Si(111)

In the last section the impact of the substrate surface on the nanowire growth was investigated and a reproducible procedure for the preparation of substrates covered with native oxide for optimum vertical nanowire growth was found. This section focuses on the effects of different parameters on the growth of GaAs nanowires on the optimized substrate. Here, different Ga rates, As_4 BEPs and growth temperatures are applied, and macroscopic characteristics of the grown nanowires, like the nanowire length, areal nanowire density and nanowire diameters are determined. To separate the effect of one parameter from the others, two parameters were held constant, while the third was varied for a row of samples. For all growth runs the growth duration was set to 25 min. The macroscopic nanowire characteristics were deduced from multiple SEM images of at least twenty single nanowires from each sample.

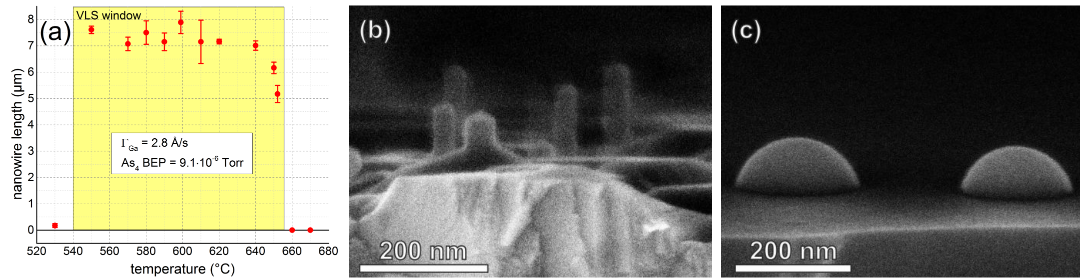

Figure 4.3.: (a) Temperature dependence of the nanowire length L for a fixed Ga rate (Γ_{Ga}) of 2.8 Å/s and an As_4 BEP of $9.1 \cdot 10^{-6}$ Torr: the nanowire length in the VLS growth regime is nearly independent on the temperature. Error bars mark the standard deviation due to the averaging over at least twenty nanowires. (b) At temperatures below 540°C, small GaAs stubs without a liquid catalyst and mainly layer growth is obtained. (c) Above 650°C solely liquid Ga droplets form on the substrate.

4.2.1. Temperature dependence

First, the effect of the growth temperature on GaAs nanowire growth was examined. For all samples the Ga rate and the As_4 BEP were set to 2.8 Å/s and $9.1 \cdot 10^{-6}$ Torr, respectively, while the growth temperature was varied.

The temperature window, in which the VLS growth of GaAs nanowires on Si(111) is possible, can be easily determined by the measured nanowire lengths L of several samples grown between 530°C and 670°C in fig. 4.3a. Below 530°C, no nanowire growth is possible via the VLS mechanism, since no liquid Ga droplets form at the nanowire tip. This can be easily seen in the side view SEM image of a corresponding sample in fig. 4.3b. Apparently, these nanowires grow slowly via a vapor-solid process, while most of the material forms a continuous layer of clusters. In the temperature range between 540°C and 650°C, VLS growth of GaAs nanowires is possible. Here, the nanowire length is nearly temperature independent. This indicates that the axial nanowire growth rate is hardly affected by the temperature, but highly As-limited (compare sections 2.1.8 and 2.2.4). At temperatures higher than 650°C, no nanowires grow, but only Ga droplets are observed (fig. 4.3c). Apparently, at such elevated temperatures, the GaAs crystal is not stable in ultra-high vacuum (UHV). This was confirmed by growing wires at lower temperatures and annealing them at temperatures above 650°C with the result of dissociating nanowires [151].

While the nanowire length hardly varies in the temperature range of VLS growth, the areal nanowire density, depicted in fig. 4.4a, increases almost linearly with growth temperature up to 640°C, and then decreases again. The increase may be either explained by a thermally driven partial desorption, or an annealing effect of the passivating oxide, which results in more pinholes on the surface. The decrease of the areal nanowire density is ascribed to the decrease of the sticking coefficient of Ga on the silicon oxide down to zero at $T_g \geq 640°C$ [152], so less diffusing Ga atoms form less liquid Ga droplets at the

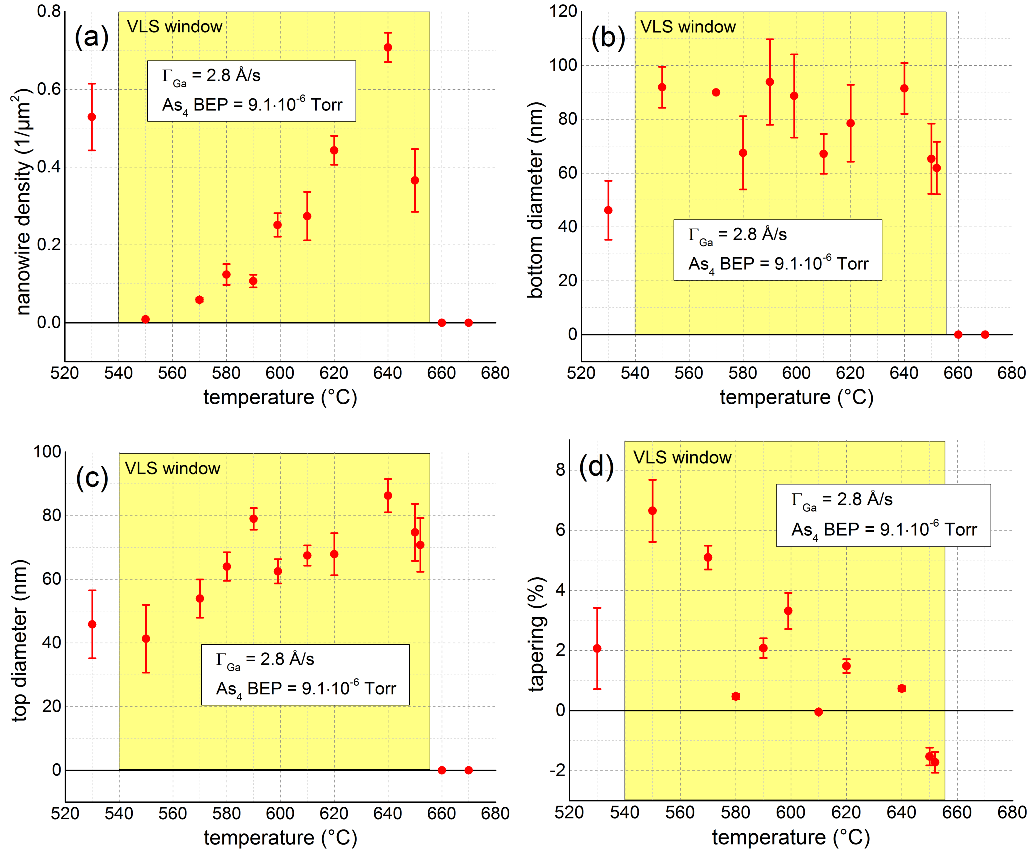

Figure 4.4.: Dependencies of macroscopic GaAs nanowire characteristics on growth temperature. Error bars mark the standard deviation due to the averaging over at least twenty nanowires. (a) The areal nanowire density in the VLS window increases first with temperature to a maximum at 640°C and then decreases again. (b) The diameter at the nanowire bottom is temperature independent, while the top diameter in (c) increases with temperature. (d) The tapering, evaluated from the data in figures 4.3a, 4.4b and 4.4c via $100 \cdot (d_{top} - d_{bottom})/L$, shows a clear trend from positive to negative values for an increase in temperature. This means a transition from a tapered to an inversely tapered nanowire shape. The reasons for these behaviors are stated in the text.

openings in the oxide, where the GaAs nanowire growth proceeds afterwards.

The shape of the nanowires was investigated concerning the diameter at the nanowire top, d_{top}, and the wire bottom, d_{bottom}, and the resulting tapering. The tapering is quantified via the expression $100 \cdot (d_{\text{top}} - d_{\text{bottom}})/L$ to determine the shape of the wires with increasing distance from the substrate. Here, positive and negative values denominate tapered and inversely tapered nanowires, respectively.

The nanowires grown within the VLS window possess a widely distributed bottom diameter between 60 nm and 100 nm (fig. 4.4b). This appears to be independent on the temperature, and probably corresponds to the occasional forming openings in the oxide. The nanowire diameter at the top (fig. 4.4c) increases with temperature. Consequently, the nanowire shape (fig. 4.4d), shifts continuously from tapered to inversely tapered with increasing growth temperature. This behavior can be explained via the increasing Ga adatom diffusion length on the GaAs nanowire side facets with temperature before desorption prevails (compare section 2.1.6). At higher temperatures, more Ga adatoms feed the droplet, resulting in a larger catalyst droplet from which a thicker nanowire precipitates. Instead, at lower temperatures, the droplet size decreases with increasing nanowire length, and thus also the wire diameter.

4.2.2. Dependence on the arsenic pressure

In a second set of samples, the dependence of the macroscopic nanowire characteristics on the As_4 BEP were investigated. Here, the growth temperature was held constant at 600°C. The nanowires were grown using a Ga rate of 2.8 Å/s, while the As_4 BEP was varied between $2.5 \cdot 10^{-6}$ Torr and $15 \cdot 10^{-6}$ Torr.

The dependence of the nanowire length on the As_4 BEP is plotted in fig. 4.5a. The nanowire length increases nearly linearly with the As_4 BEP within the VLS regime, i.e. for As_4 fluxes from $2.5 \cdot 10^{-6}$ Torr to $8.8 \cdot 10^{-6}$ Torr, while for an As_4 BEP of $15 \cdot 10^{-6}$ Torr the growth rate drops again. The linear behavior can be explained with the VLS nucleation mechanism of the nanowires. Since one nucleation event is necessary for the growth of a complete monolayer underneath the droplet, the growth rate is set by the nucleation rate. The nucleation rate is linearly dependent on the concentration of As, and therefore linear in the As_4 BEP (compare section 2.1.8). For an increased As_4 BEP of $15 \cdot 10^{-6}$ Torr the growth rate drops due to a local excess of As atoms compared to Ga atoms. In this regime, the liquid catalyst particle is absent and a facet-driven selective area growth mode with a reduced vertical growth rate of the wires is obtained [146].

The areal nanowire density (fig. 4.5b) seems to increase logarithmic with increasing As_4 BEP over the whole examined range, if we neglect the data at $8.8 \cdot 10^{-6}$ Torr, which might stem from a poor substrate preparation. The logarithmic increase of the nanowire density can be attributed to a reduced diffusion length of the Ga adatoms on the silicon oxide due to an elevated adatom-solid incorporation rate with increasing As_4 BEP. This results in the formation of more GaAs clusters on the substrate, where Ga droplets form atop and subsequently mediate nanowire growth.

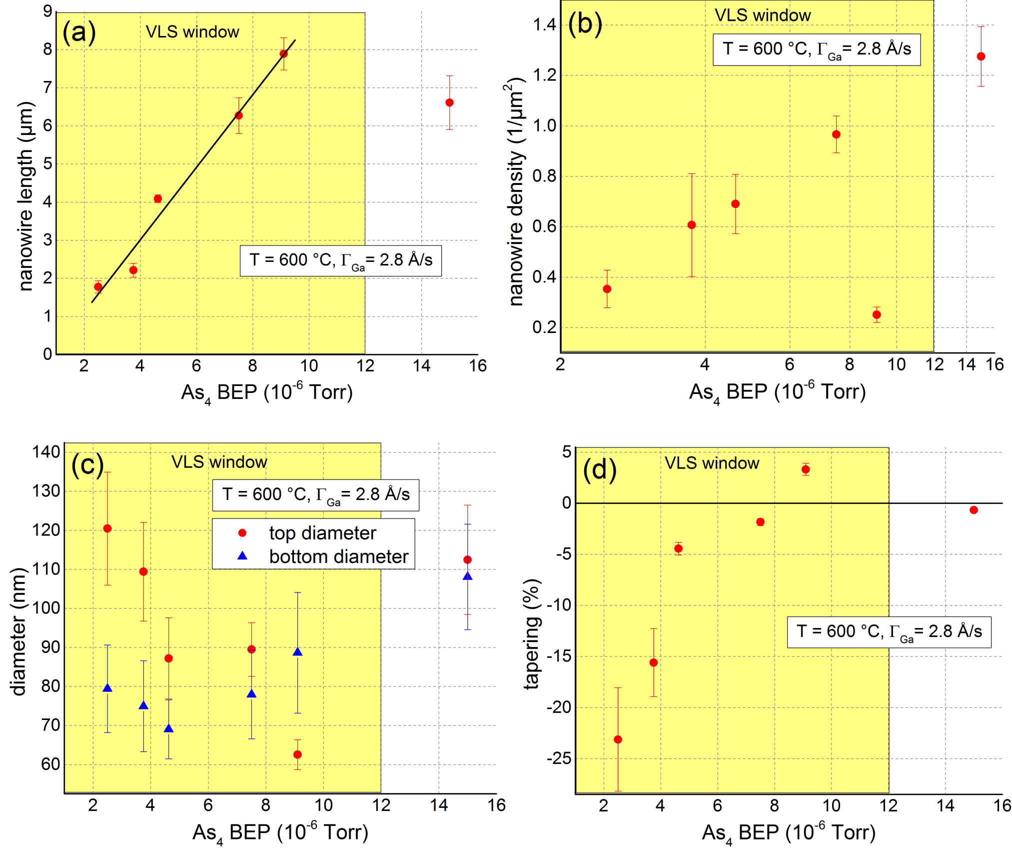

Figure 4.5.: Dependencies of macroscopic nanowire characteristics on the As_4 BEP. The error bars mark the standard deviation due to the averaging over at least twenty nanowires. (a) In the VLS regime, the nanowire length increases linearly with increasing As_4 BEP, while at an As_4 BEP of $15 \cdot 10^{-6}$ Torr the NW length is reduced. (b) Seemingly, the nanowire density increases logarithmic with the As_4 BEP. (c) The nanowire bottom diameter is independent on the As_4 BEP while the top diameter decreases with increasing As_4 BEP in the VLS regime. (d) With increasing As_4 BEP, the nanowire shape changes from heavily inverse tapered to slightly tapered. The reasons for these behaviors are stated in the text.

The decrease of the Ga adatom diffusion length with increasing As_4 BEP may be also identified in the behavior of the nanowire top diameter in fig. 4.5c. The diameter decreases continuously with increasing As_4 BEP due to a reducing droplet size. However, the main reason for the reducing droplet size with increasing As_4 BEP is certainly the faster axial growth rate of the wire (compare fig. 4.5a) depleting the liquid catalyst droplet. The bottom diameter is quite randomly distributed with values from 60 nm to 100 nm, caused by the different sizes of the openings in the oxide. Thus, the shape of the nanowires (fig. 4.5d) changes with increasing As_4 BEP from heavily inversely tapered to slightly tapered. This reflects an As-limited growth regime (Ga excess) at the lower end of the VLS window and a Ga-limited one (As excess) at the upper end.

4.2.3. Dependence on the Ga rate

Next, the dependence of GaAs nanowire growth on the Ga rate was studied. Thereby, the growth temperature and the As_4 BEP were kept fixed for a series of samples at 600°C and $9.1 \cdot 10^{-6}$ Torr, respectively, while the Ga rate was varied from 0.2 Å/s to 2.8 Å/s. The different parameters extracted by SEM are depicted in figs. 4.6.

The nanowire length (fig. 4.6a) is zero for a Ga rate of 0.2 Å/s, and initially increases with the Ga rate. As the axial growth rate is mainly determined by the As_4 BEP, this behavior is explained with the time necessary to form a Ga droplet and the GaAs seed (”incubation time” [153]), which is longer for lower Ga rates than for higher ones. Correspondingly, the effective growth time of the wires is less for lower Ga rates. At 0.2 Å/s, the Ga rate is even too low to form a catalyst droplet. Too few Ga atoms adsorb on the surface droplet before they desorb again or form a GaAs crystal without a liquid phase attached. At 2.8 Å/s, the nanowire length drops again due to an increased radial growth at higher Ga rates (compare fig. 4.6c).

The areal nanowire density decreases in the VLS window with increasing Ga rate (fig. 4.6b). This can be explained by a merging of Ga droplets during incubation time, resulting in the formation of larger Ga droplets on the substrate, which also leads to larger diameters at the nanowire bottoms (compare fig. 4.6c). This behavior suppresses nanowire growth for extremely high Ga rates, and leads to the formation of Ga lakes on the substrate (not shown), which inhibit the growth of nanowires.

The dependencies of the top and bottom diameters on the Ga rate is shown in fig. 4.6c. Both diameters increase with the Ga rate, while the bottom diameter remains in any case larger than the top diameter, leading to a tapered shape of the nanowires. Again, this behavior can be ascribed to the formation of larger initial droplets at higher Ga rates, which leads to the growth of thicker nanowires. Even an increased radial growth at the nanowire side facets during the axial nanowire growth may contribute here, caused by the deposition of more material during the growth with higher Ga rates than for lower Ga rates.

The shape of the nanowires is generally slightly tapered (fig. 4.6d), since the chosen As_4 BEP is relatively high. This leads to a high nanowire growth rate, involving a reduction of the catalyst droplet with increasing nanowire length. We observe a decrease of the

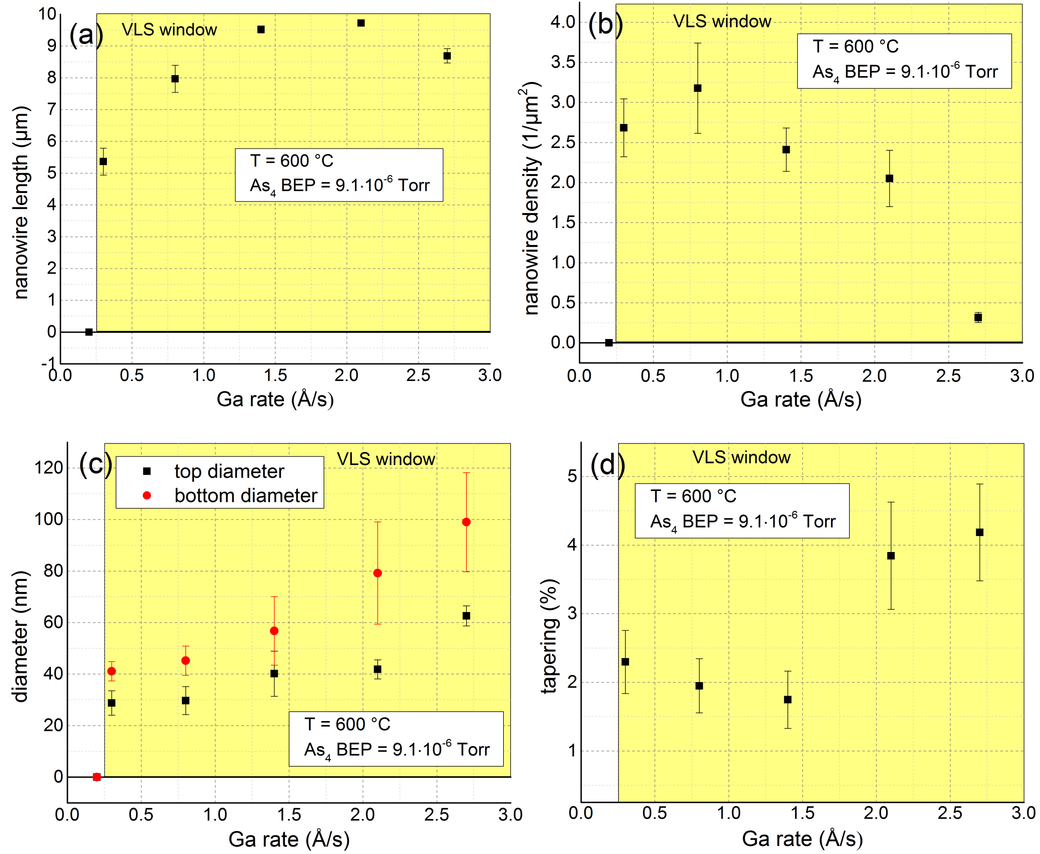

Figure 4.6.: Dependencies of macroscopic nanowire characteristics on the Ga rate. The error bars mark the standard deviation due to the averaging over at least twenty nanowires. (a) The nanowire length first increases with the Ga rate due to a reduced incubation time, peaks and decreases again because of an enhanced radial growth for high Ga rates. (b) The nanowire density decreases with increasing Ga rate, ascribed to the merging of Ga droplets during the initial stages of nanowire growth. (c) The nanowire diameter at the bottom and the top of the nanowire increases with the Ga rate due to larger initial catalyst droplets and an increasing radial growth at elevated Ga rates. (d) All investigated samples show a tapered nanowire shape. The decrease of the tapering with increasing Ga rate due to an higher refilling rate of the Ga droplet (0.3 Å/s to 1.4 Å/s) is reversed when strengthened radial growth takes place (2.1 Å/s and 2.8 Å/s).

nanowire tapering for an elevation of the Ga rate from 0.2 Å/s to 1.4 Å/s, which gets reversed above 1.4 Å/s. Since the Ga rate determines the amount of Ga atoms refilling the droplet and thus the nanowire diameter at the tip, the decrease in tapering from 0.2 Å/s to 1.4 Å/s is reasonable. The increase in tapering at higher Ga rates may be explained by an elevated radial growth at the bottom of the nanowire. Radial growth occurs mainly for high Ga rates, when the diffusion length of the Ga adatoms on the nanowire side facets decreases due to already occupied adatom sites (compare section 2.1.5). Then, the incorporation of the Ga atoms in the GaAs crystal at the wire bottoms is enhanced.

4.2.4. Conclusion

The growth of GaAs nanowires on Si(111) using the self-catalyzed VLS mode is possible within a temperature window of approximately 100°C for various As_4 BEPs and Ga rates. The parameters measured from the grown nanowires can be explained with the growth models introduced in section 2.1.

The axial nanowire growth rate increases linearly with the applied As_4 BEP (fig. 4.5a), since the As concentration in the liquid droplet limits the nucleation of a monolayer. Also, the axial growth rate is nearly independent on the growth temperature and the Ga rate. Therefore, the nanowire length can be steered mainly by the As_4 BEP and the growth time, which is also affected by the incubation time to form the initial GaAs seed. The incubation time depends only on the Ga rate, and is longer for low Ga rates than for high ones.

The areal nanowire density depends on all three investigated parameters, since here the diffusion of the Ga adatoms, the growth of GaAs clusters on the substrate and the surface quality play an important role. The wire density increases with temperature until the sticking coefficient of the Ga adatoms strongly reduces, and also increases with As_4 BEP due to a corresponding decrease of the Ga adatoms diffusion length. An increasing Ga rate reduces the nanowire density due to the merging of Ga droplets during incubation time.

The shape of the nanowires is mainly affected by the As_4 BEP (fig. 4.5d), leading to an inversely tapered shape for low As_4 BEPs and a tapered shape for high As_4 BEPs. The diameter at the nanowire bottom can only be affected by the Ga rate (fig. 4.6c) via the formation of larger catalyzing Ga droplets during the incubation time. However, the diameter towards the nanowire tip is strongly dependent on the axial nanowire growth rate and the Ga adatom diffusion lengths on the nanowire side facets, and therefore can be mainly steered by the As_4 BEP.

Consequently, the deduced dependencies allow the growth of GaAs nanowires on Si(111) with a defined density and shape within a low fluctuation margin on a single sample. However, the growth conditions do not only affect the macroscopic nanowire parameters, but also the nanowire crystal structure. The optimization of the GaAs nanowire crystal structure towards defect-free wurtzite and zinc-blende phases is described in the following section.

4.3. Crystal structure optimization of GaAs nanowires

In this section, the crystal structure optimization of GaAs nanowires is described. This is a necessary step in nanowire growth to obtain phase pure structures, since in GaAs nanowires commonly zinc-blende (ZB) and wurtzite (WZ) crystal structure coexist. However, the growth of nanowires of either ZB or WZ crystal phase, without the introduction of twin planes or stacking faults along an entire wire, was not reported before the start of this work.

The results of former investigations on the crystal structure of GaAs nanowires performed at the University of Regensburg already show the growth of nanowires with exclusively ZB or WZ crystal structure [114]. This means, that the growth of the other crystal structure within one wires was largely suppressed. Nevertheless, most of the wires contained a large amount of stacking faults or twin planes.

The necessary conditions for the growth of phase pure GaAs nanowire growth were already deduced theoretically in section 2.2. In the following, the gained results are summarized.

In order to favor the WZ phase during growth, a liquid catalyst droplet wetting the whole nanowire top facet to its edges, together with a contact angle of approximately 90° is recommended. Then, nucleation occurs predominantly at the edges of the top facet, favoring WZ nuclei. This can be realized most easily, when a growth temperature at the lower end of the VLS window is chosen, and an Au-Ga alloy is used to catalyze nanowire growth.

To attain ZB nanowires, nucleation at the edges of the top facet has to be avoided, and nucleation in center position has to be favored instead. This can be achieved using either small droplets wetting solely the top facet without touching its edges, or using large Ga droplets, whose limits reside fully on the nanowire side facets. Due to these requirements, the kind of the catalyst plays a minor role.

Generally, to maximize the difference in energy necessary for the formation of a monolayer WZ or ZB, a large supersaturation of the liquid is recommended. This means a low growth temperature and a high As concentration in the liquid catalyst, mediated by a high As_4 BEP. Then, a high selectivity for either WZ or ZB crystal structure should be obtained.

The methods used for the crystal structure tuning towards stacking-fault-free WZ nanowires are described in the first part of this section, followed by the results for ZB nanowires. The observed crystalline properties are summarized at the end of section.

4.3.1. Optimizing the wurtzite phase

As recommended by theory, to optimize the WZ crystal structure in GaAs nanowires, we use a Au-Ga droplet as the catalyst. Therefore, instead of Si(111) substrates as in the Ga-catalyzed growth, GaAs(111)B wafers covered with a thin layer of Au were used. Here, at growth temperature, liquid Au-Ga alloys in the form of droplets originate, which catalyze GaAs nanowire growth. The principles of Au-catalyzed nanowire growth, and

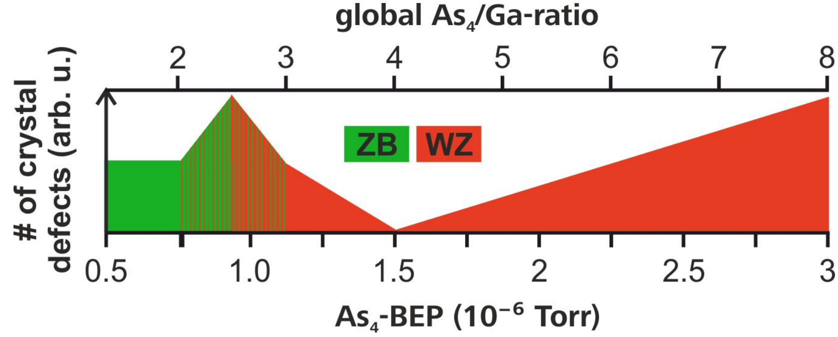

Figure 4.7.: The predominantly occurring crystal structure (green: ZB, red: WZ) and the simultaneously introduced amount of crystal defects (stacking faults (SFs) and twin planes (TPs)) are depicted as a function of the applied As_4 BEP and the respective global As_4/Ga ratio. This sketch summarizes crystal structure determinations of multiple wires from the corresponding samples in TEM: For low As_4 BEPs between $0.5 \cdot 10^{-6}$ Torr and $0.75 \cdot 10^{-6}$ Torr, the amount of TPs in predominantly ZB crystal structure is nearly constant. For slightly elevated As_4 BEPs of $0.75 \cdot 10^{-6}$ Torr to $0.9 \cdot 10^{-6}$ Torr, the TP density increases sharply and even WZ inclusions are observed. At an As_4 BEP of $0.9 \cdot 10^{-6}$ Torr, the main crystal structure changes to WZ, while for a further increase to $1.5 \cdot 10^{-6}$ Torr, the amount of SFs in predominantly WZ wires decreases. Above $1.5 \cdot 10^{-6}$ Torr the main crystal structure remains WZ while the SF density increases again. The overall behavior can be explained with the evolution of the catalyst droplet size and its corresponding contact angle, see text.

the temperature window, in which growth is possible, were already explored by Rudolph [114]. He determined the lowest temperature for VLS growth to be 510°C, which is in the following adopted for the optimization of the WZ crystal structure.

As introduced in section 2.2, the shape of the droplet plays a crucial role in choosing the site where nucleation takes place and determines the crystal structure. For preferential WZ nucleation, a liquid droplet is required, which wets the top facet to its edges and additionally possesses a contact angle β of approximately 90°. To obtain WZ wires without stacking faults along the entire length, this state should not be altered during growth. Thus, a growth regime is searched, where the refilling rate of Ga atoms to the liquid state is equal to the consumption rate from the liquid state, so the shape of the catalyst does not change. This growth regime should result in the formation of untapered wires with pure WZ crystal structure. As elucidated in section 4.2, the nanowire shape and therefore also the droplet shape is mainly affected by the As_4 BEP (this dependency is equivalent for Ga- and Au-catalyzed GaAs nanowire growth).

Thus, to find the regime for the growth of pure WZ wires, the Ga rate was set to the fixed value of 0.4 Å/s throughout this study, while the As_4 BEP was altered from $0.5 \cdot 10^{-6}$ Torr to $3 \cdot 10^{-6}$ Torr. From the different samples, the crystal structure of some wires was determined in TEM. Fig. 4.7 shows the behavior of the predominant crystal structure of these samples in dependence on the As_4 BEP. Additionally, the corresponding amount of introduced crystal defects, i.e. stacking faults and/or twin

planes is schematized.

For low As_4 BEPs between $0.5 \cdot 10^{-6}$ Torr and $0.75 \cdot 10^{-6}$ Torr, the dominant crystal structure is ZB with a constant amount of crystal defects. Here, the nucleation rate is low due to the low As concentration in the droplet, mediated by the low As_4 BEP. This leads to large catalyst droplets with contact angles $\beta \gg 90°$, possibly wetting parts of the nanowire side facets as well. As described in section 2.2.2, these growth conditions favor nucleation in the nanowire center, i.e. ZB crystal structure.

For slightly elevated As_4 BEPs of $0.75 \cdot 10^{-6}$ Torr to $0.9 \cdot 10^{-6}$ Torr, the dominant crystal structure remains ZB, but additionally some small WZ inclusions are detected. These inclusions rise in length and amount for a further increase of the As_4 BEP, until the main crystal structure changes at an As_4 BEP of approximately $0.9 \cdot 10^{-6}$ Torr to WZ. This can be attributed to the elevated As concentration in the droplet, which increases the nucleation rate, and therefore decreases the size of the liquid catalyst. The simultaneous reduction of the contact angle from high values $\beta \gg 90°$ towards 90° results in the decrease of the nucleation barrier at the edges of the top facet with respect to center position, and therefore favors the formation of WZ before ZB.

Above an As_4 BEP of $0.9 \cdot 10^{-6}$ Torr, the increase of the As_4 BEP results in the decrease of the stacking fault density in predominantly WZ nanowires, until an As_4 BEP of $1.5 \cdot 10^{-6}$ Torr is reached. This behavior can be ascribed to the growth rate-related decrease of the contact angle β to 90°. A contact angle of 90° during growth is assumed for this As_4 BEP, since here the amount of stacking faults in the wurtzite crystal is lowest.

Increasing the As_4 BEP beyond $1.5 \cdot 10^{-6}$ Torr leads to an increase in the stacking fault density again, which is ascribed to the decline of the contact angle below 90°. This reduction increases the nucleation barrier at the edges of the top facet again, and therefore decreases the probability to form WZ nuclei. The trend of an increasing stacking fault density in predominantly WZ nanowires is valid until the As_4 BEP reaches $3 \cdot 10^{-6}$ Torr, which was the highest value investigated here. A further elevation of the As_4 BEP should result in the precipitation of predominantly ZB crystal structure above a certain As_4 BEP again, as center nucleation is favored for very low contact angles and for droplets which wet the top facet without touching its edges (compare section 2.2.2).

Nanowire growth at a global As_4/Ga ratio of 4

As mentioned before, TEM measurements of nanowires grown at a Ga rate of 0.4 Å/s and an As_4 BEP of $1.5 \cdot 10^{-6}$ Torr reveal pure wurtzite crystal structure with a low density of stacking faults. This means lots of investigated wires from this sample possess less than ten stacking faults along the entire length of approximately 4.5 µm, or even not a single one. Fig. 4.8a shows a TEM image of a whole wire from the bottom (left) to the top (right). Along the entire wire length of 4.2 µm no stacking fault was detected, which would become apparent as fine line perpendicular to the nanowire axis, compare the subsequent TEM micrographs in figs. 4.9 and 4.10. Figs. 4.8b, 4.8c and 4.8d depict HRTEM images of this wire at the nanowire bottom, center and tip, respectively.

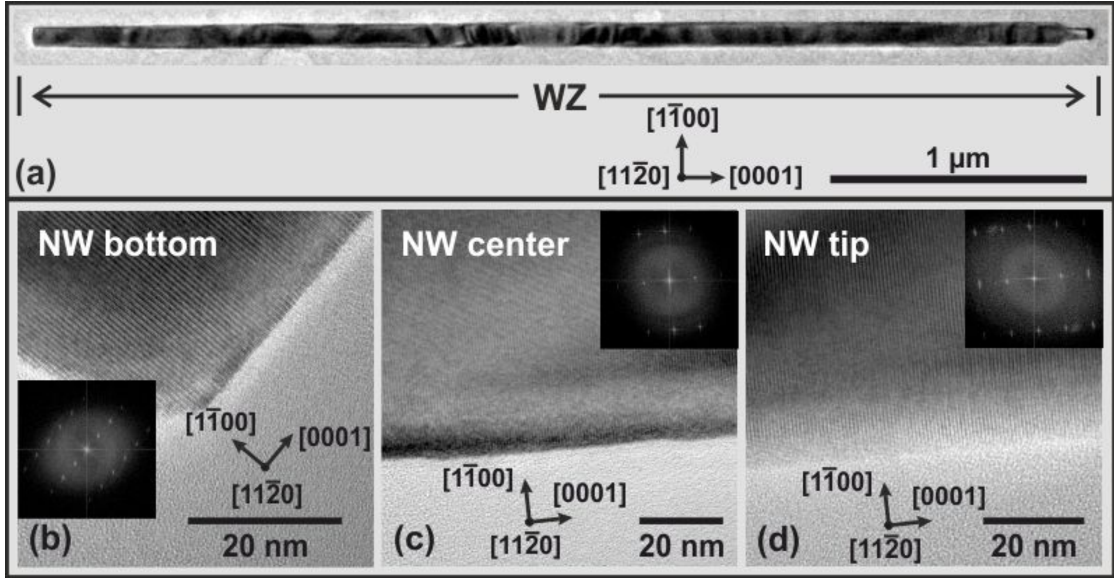

Figure 4.8.: TEM images of a GaAs nanowire grown with a Ga rate of 0.4 Å/s and an As_4 BEP of $1.5 \cdot 10^{-6}$ Torr: (a) Along the whole nanowire length of 4.2 µm no stacking fault is detected. (b)-(d) HRTEM images of the nanowire bottom, center and tip and the corresponding fast fourier transforms reveal exemplarily the phase purity of the crystal. This phase purity is ascribed to the growth from a steady state of the liquid catalyst.

Together with the corresponding fast Fourier transform (FFT), they exemplarily depict the phase purity of the wire.

These results indicate that the nanowire growth originates from a catalyst droplet, which possesses a steady state during the whole growth. The pure crystal structure proves a constant droplet size and a contact angle in the range of 90° during the entire growth. Additionally, as the depletion of the Ga droplet takes place with the constant nanowire growth rate, this means that the droplet refilling with Ga atoms happens at the very same rate, and is constant during the whole growth.

This behavior can be attributed to effects stemming either from the growth temperature or from the nanowire density on the sample. The diffusion equations in section 2.1.7 indicate, that the Ga adatom flux towards the catalyst droplet is generally not constant, but depends highly on the length on the nanowire, and the diffusion lengths on the substrate and the nanowire side facets. Conversely, for the stacking-fault-free WZ wires, the amount of adatoms diffusing to the droplet seems to be independent on the nanowire length, or to be negligibly low. This behavior can be explained either with a strongly reduced diffusion length, most probably induced by the low growth temperature, or within a scenario where diffusion generally plays a minor role, i.e. Ga atoms predominantly reach the droplet directly from the vapor phase. Since the nanowire density of 10 to 20 NW per µm^2 on samples grown with the Au-catalyzed method is rather high, probably most Ga atoms do not adsorb on the substrate or the nanowire

sidewalls but directly on the liquid catalyst, so the latter scenario also seems possible. Most probably, both reasons account for the steady state of the catalyst droplet during growth, and are responsible for the formation of stacking-fault-free wurtzite nanowires.

The growth of WZ GaAs nanowires with a comparable crystalline quality was also achieved for different thicknesses of the Au layer on the GaAs substrate, as well as for the same global As_4/Ga ratios, set by the above mentioned Ga rate and As_4 BEP. This indicates, that the kind of the Au-Ga alloy, which forms on the substrate and catalyzes nanowire growth, is either not of major importance, or independent on the Au layer thickness and has always the same composition. The non-necessity of the usage of distinct Ga and As_4 fluxes to grow SF-free WZ wires, but a fixed As_4/Ga ratio, points to a negligible diffusion of Ga atoms, so a regime with predominantly direct impinging Ga and As atoms from the vapor phase onto the catalyst droplet is found. In this case, the local As/Ga ratio at the position of the forming droplet/wire is solely determined by the global As_4/Ga ratio, and steady state conditions during the whole growth can be achieved.

4.3.2. Optimizing the zinc-blende phase

For the growth of predominantly ZB nanowires, the nucleation at the edge of the nanowire top facet has to be avoided, and nucleation has to take place in center position (compare section 2.2.1). To promote this, two growth regimes are possible. First, the growth from a droplet wetting solely the nanowire top facet but not its edges, leading to a tapered shape of the nanowires. Or second, the growth from a large droplet wetting the nanowire top facet and parts of the side facets. Thereby, the triple phase line (TPL) should reside fully on the side facets, leading to an inverse tapered nanowire shape. Since the growth from a small droplet easily leads to the consumption of the whole droplet, resulting in a vapor-solid growth mode [146], and large droplets are more easily attainable via an As/Ga ratio < 1 at the growth front, the latter regime was chosen for the growth of predominantly ZB nanowires. In the following, the best results obtained in this growth regime using an Au-Ga alloy or pure Ga droplets as catalyst are shown.

Au-catalyzed growth

In the series of samples grown at different As_4 BEP for the optimization of GaAs WZ crystal structure, a range is identified, where ZB crystal structure is favored (compare fig. 4.7). This range resides at low As_4 BEP values or low As_4/Ga ratios, and therefore means the growth from a large catalyst droplet. Due to the reduction of WZ segments and twin plane (TP) density in predominantly ZB wires in the region between $0.9 \cdot 10^{-6}$ Torr and $0.75 \cdot 10^{-6}$ Torr towards a rather constant value, the movement of the TPL onto the nanowire side facets seems completed at an As_4 BEP of $0.75 \cdot 10^{-6}$ Torr. A further reduction of the As_4 BEP results only in an higher degree of inversely tapered nanowires, but not in an improvement of the crystal phase. Exemplarily, the crystal

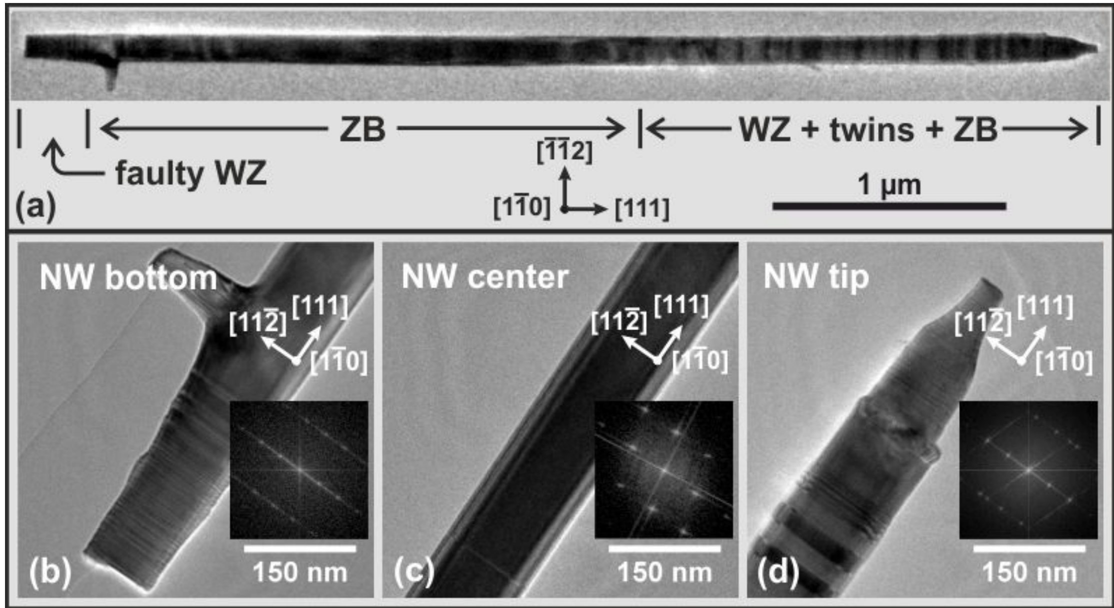

Figure 4.9.: Crystal structure of an Au-catalyzed GaAs nanowire grown at conditions for preferential ZB nucleation: (a) The first 300 nm at the bottom (left) consist of WZ crystal structure with lots of SFs, followed by 2.5 µm nearly TP-free zinc-blende crystal structure with approximately 1 TP per µm. With increasing length, the amount of TPs increases and finally at the tip even small segments of WZ crystal structure are observed. (b) HRTEM at the nanowire bottom: the very first 300 nm consist of WZ crystal structure with lots of SFs. The FFT is taken from this region only. (c) At the nanowire center, long segments of TP-free ZB crystal structure are observed. (d) WZ crystal structure and one stacking sequence of ZB crystal structure is detected at the nanowire tip.

structure along one of those wires is discussed in the following.

Fig. 4.9 shows TEM micrographs of a single nanowire, which was grown at these conditions. Fig. 4.9a depicts the whole wire, whereas figs. 4.9b, 4.9c and 4.9d show magnified sections from the nanowire bottom, center and tip, together with the corresponding FFT.

The very first 300 nm at the nanowire bottom (fig. 4.9a on the left and fig. 4.9b) consist of WZ crystal structure with lots of stacking faults (SFs). The SFs can be easily identified by the fine lines inside the wire perpendicular to the growth axis and the streaky FFT in fig. 4.9b. Thereafter, the nanowire crystal structure transforms to twin-plane (TP)-free ZB (fig. 4.9c). This occurrence can be explained by the initial build-up process of the liquid droplet. After forming the first monolayer(s) of the nanowire and the nanowire side facets, the droplet covers the whole top facet of the GaAs stub, wetting the top facet to its edges. Due to the low amount of Ga atoms forming the droplet in the initial growth phase, the contact angle is relatively low. With increasing nanowire length, the amount of Ga adatoms feeding the droplet initially strongly increases (compare fig. 2.3). This is accompanied by the elevation of the droplet angle from below 90° to much higher

than 90°, while also the TPL moves onto the side facets. During this whole process, the crystal structure changes from predominantly ZB to WZ and back to ZB again. The first transition from ZB to WZ is probably not observed, because this most probably happens during the growth of the first monolayers of the GaAs nanowire, and this region remains on the as-grown substrate when the wires are removed.

Above the faulty WZ segment, the growth of 2.5 µm nearly TP-free ZB crystal structure is monitored (fig. 4.9c), with approximately 1 TP per µm. This segment is dedicated to the now large Ga droplet, with the TPL residing on the side facets only and therefore strongly favoring ZB crystal structure.

Further to the top, the nanowire contains more TPs, and finally even small segments of WZ crystal structure with an increasing density towards the tip (see fig. 4.9a on the right and fig. 4.9d). This behavior is ascribed to a slow consumption of the catalyst droplet and the corresponding motion of the TPL back to the edges of the top facet. Assuming that Ga adatom diffusion takes place on the nanowire sidewalls and the substrate, the amount of Ga adatoms refilling the droplet in dependence on the nanowire length shows a peak behavior (compare fig. 2.3). If the nucleation rate for axial nanowire growth is higher compared to the constant final value of the overall Ga refilling rate of the Ga droplet, above a certain wire length, a creeping consumption of the droplet results. The enhanced dependence on Ga diffusion compared to the growth of SF-free WZ nanowires (section 4.3.1) may be attributed to the decreased As_4 BEP, which increases the diffusion lengths of Ga adatoms via the reduction of adatom-solid transitions.

Ga-catalyzed growth

Using a liquid Ga droplet as the catalyst, the best conditions for the growth of ZB crystal structure were comparable to those for Au-catalyzed growth. At a Ga rate of 0.4 Å/s and an As_4 BEP of $1.0 \cdot 10^{-6}$ Torr, nanowires with predominantly ZB crystal structure were obtained at a growth temperature of 600°C.

In fig. 4.10a a TEM micrograph of an entire wire of the corresponding sample is depicted, whereas fig. 4.10b, 4.10c and 4.10d show different magnified sections of the nanowire bottom, center and tip together with the FFTs.

The crystal structure at the nanowire bottom (left in fig. 4.10a and fig. 4.10b), shows a ZB segment of 3 µm length with a low density of TPs, comparable to the Au-catalyzed grown wires. Here, we detect no WZ phase at the initial stages of nanowire growth (as in the Au-catalyzed case), probably because of a longer incubation time due to the heteroepitaxial growth on a Si(111) substrate. This leads to a large droplet already from the beginning of nanowire growth, favoring ZB crystal structure. Further to the top, the crystal structure changes to faulty ZB and some WZ inclusions (fig. 4.10c). This occurrence is equivalent to the Au-catalyzed wires, caused by a reducing liquid catalyst droplet moving back on the edges of the top facet.

The crystal structure along the last 330 nm of the nanowire behaves different. Here, a pure WZ segment of 300 nm length is detected (fig. 4.10d), followed by 30 nm ZB GaAs, forming the nanowire tip (fig. 4.11). Both occurrences can be attributed to the

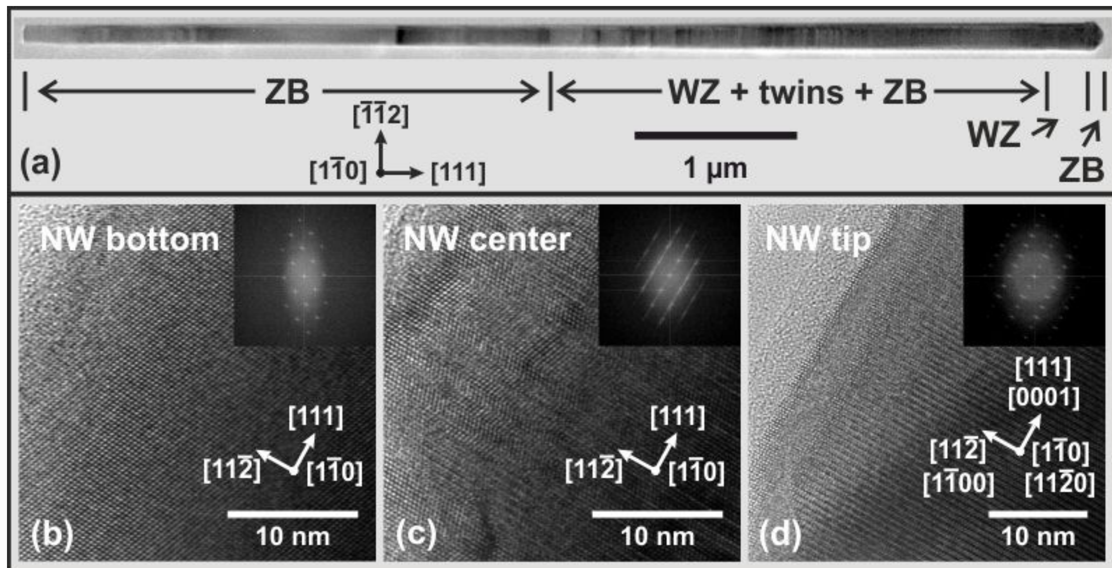

Figure 4.10.: Crystal structure of a Ga-catalyzed GaAs nanowire, grown at conditions for preferential ZB nucleation. (a) The crystal structure at the nanowire bottom (left) is ZB with only 1 TP per µm along 3 µm. Towards the tip, more TPs and even small segments of WZ crystal structure are identified. At the end of the tip, a 300 nm segment of pure WZ without SFs is observed, followed by 30 nm ZB. (b)-(d) HRTEM images and the corresponding FFTs of regions at the nanowire bottom, center and the WZ tip reveal the change in crystal structure along the wire.

complete consumption of the liquid catalyst droplet at the end of nanowire growth, when solely As_4 flux is applied and Ga flux is absent. Apparently, by the reduction of the droplet size, conditions for the growth of SF-free WZ GaAs using pure Ga droplets as catalyst can be also reached, i.e. an contact angle close to 90° with the TPL residing at the edges of the top facet. The occurrence of WZ GaAs in Ga-catalyzed nanowire growth was also monitored by other groups for an reducing droplet size [154, 155]. The very last 30 nm at the nanowire tip reveal the second growth regime, in which ZB predominantly originates: while getting completely consumed, the liquid droplet wets solely the nanowire top facet, but not its edges. Note, that the complete consumption of the catalyst, and correspondingly this pronounced evolution in crystal structure is not accessible in the case of Au-catalyzed growth due to the usage of a foreign catalyst, which stays atop the nanowire.

However, the optimization of ZB crystal structure using the Ga-catalyzed growth mechanism was not as intensively studied as the one using Au-Ga alloy as a catalyst. This means that the optimization of the supersaturation of the liquid with respect to the solid by minimizing of the growth temperature was not performed, which should additionally improve the crystalline quality.

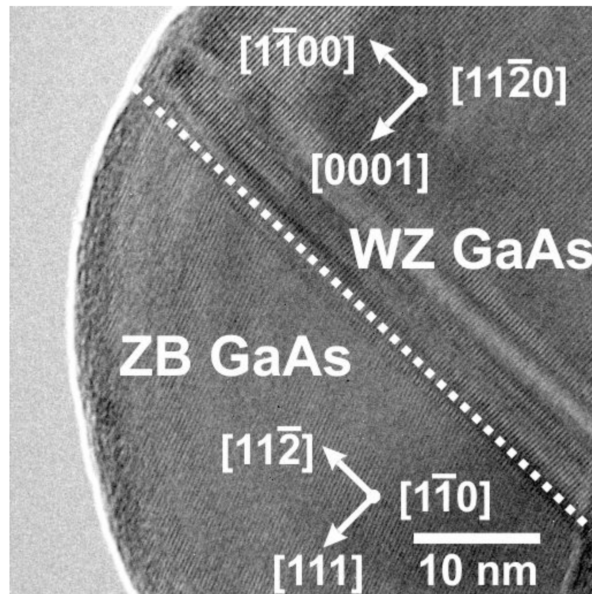

Figure 4.11.: HRTEM of the WZ/ZB transition at the nanowire tip, obtained by the consumption of the Ga catalyst droplet in As_4 flux: When the droplet still wets the edges of the top facet, WZ crystal structure precipitates and the diameter of the wire remains constant. Finally, when the droplet size shrinks further and recedes from the edges of the top facet, the formation of ZB crystal structure is favored.

4.3.3. Conclusion

In this section, the crystal structure of GaAs nanowires was optimized towards SF-free WZ and TP-free ZB segments.

SF-free WZ crystal structure was successfully obtained along entire wires by shifting the nucleation to the TPL at the edge of the side facets in combination with a contact angle close to 90°. This was realized by using an Au-Ga alloy as the catalyst and a low growth temperature to maximize the attainable contact angle before the droplet wets the side facets. To alter the droplet shape, the As_4 BEP was varied, while all other growth parameters were kept constant. The optimum conditions, deduced for completely SF-free growth of WZ GaAs nanowires, are a growth temperature of 510°C, an As_4 BEP of $1.5 \cdot 10^{-6}$ Torr and a Ga rate of 0.4 Å/s.

The growth of nearly TP-free ZB GaAs over large segments of 2-3 µm was obtained using both, the Ga- and Au-catalyzed growth method. This was realized by applying large catalyst droplets, whose TPL fully shifted onto the nanowire sidewalls. In this case, nucleation preferentially takes place in the nanowire center favoring ZB crystal structure. However, this growth regime was only stable for segments at the nanowire bottom of maximal 3 µm length. After that, the catalyst droplet seems to slowly get consumed, introducing TPs and WZ segments more frequently with increasing nanowire length. This behavior was ascribed to the coincident movement of the TPL back to the

edges of the top facet, caused by a lower refilling rate of Ga adatoms with increasing nanowire length.

The crystal structure at the beginning of the nanowire growth apparently depends on the substrate. Due to heteroepitaxy, the initial formation of the GaAs seed on Si(111) happens not before the accumulation of a large droplet with large contact angle, so ZB is the initially forming crystal structure. In case of GaAs(111)B substrates, nanowire growth seems to take place with a less pronounced incubation time. This means growth proceeds initially from a smaller droplet wetting the edges of top facet, so WZ is predominantly formed at the initial stages of nanowire growth.

The crystal structure at the nanowire tip depends on the consumption behavior of the liquid catalyst droplet. This is different for a pure Ga droplet compared to an Au-Ga droplet. Since a Ga droplet can be fully transformed into a GaAs crystal, the crystal structure changes at the wire tip from ZB to WZ and back to ZB again. This behavior is caused by the reducing droplet size and the corresponding evolution of the droplet angle and the wetting area. Using the foreign catalyst Au, the last transformation to ZB seems inhibited, which was ascribed to the remaining Au atop the wire.

The parameters deduced for the optimized growth of WZ and ZB GaAs nanowires are in the following used for the growth of core/shell structures. This is necessary to determine the optical properties of both phases in nanowire geometry, or to obtain phase pure (Ga,Mn)As structures (see chapters 5 and 7).

5. Optical properties of GaAs nanowires

The WZ phase of GaAs is not thermodynamical stable in thin films or bulk crystals, but, due to the high surface to volume ratio, stabilized in nanowires. Since WZ GaAs has a reduced symmetry of the lattice compared to ZB GaAs, a different band structure is expected, but nevertheless remains a direct band gap semiconductor [77] (compare section 2.3.3). Therefore, and since the growth of highly pure WZ GaAs segments in nanowires was successfully developed (section 4.3.1), it should be possible to deduce the optical properties of WZ GaAs easily with photoluminescence (PL) measurements.

In GaAs nanowires non-radiative recombination via surface states dominates, and suppresses radiative recombination. Therefore, to be able to detect the crystal structure relevant electronic transitions optically, the large nanowire surface has to be passivated [80, 82]. Thus, the GaAs wires are covered with an AlGaAs shell. The growth of the shell with MBE, and the determination of optimum shell parameters concerning passivation using PL measurements on single nanowires are evaluated in section 5.1.

Thereafter, a sufficient passivation is used to determine the optical properties of WZ GaAs crystal structure in nanowires, like the excitonic band gap and the polarization of corresponding transition (section 5.2). To exclude effects induced by crystal defects, the PL of the stacking-fault-free WZ nanowire, introduced in section 4.3.1, is analyzed. This study was also published in [156]. For comparison, the optical properties of a nanowire with predominantly ZB crystal structure are evaluated.

Eventually, in section 5.3, the growth and usage of GaAs nanowires for lasing operation in the near infrared regime is shown. This application was recently explored by Saxena et al. [157] and Mayer et al. [158]. Using the large refractive index of the semiconductor and the nanowire geometry, a strong two-dimensional confinement of photonic modes guided along the nanowire axis is enabled, while the nanowire end facets provide optical feedback for the modes. When passivating and designing the wires correctly, lasing operation at room temperature should be obtained.

To perform optical measurements on single nanowires, a micro-photoluminescence (µPL) setup was used. The as-grown wires were removed from the substrate in an ultrasonic bath and dispersed on a Si substrate or a TEM grid. The lying wires were excited above the band gap with different laser diodes, which were focused down in a microscope objective to a spot size of around 1 μm^2. The wavelengths, mode of driving and the power densities of the exciting lasers are depicted for each experiment separately. The PL emitted from the nanowire was collected by the same objective and led to a spectrometer. The measurements were performed in a He cryostat, which enables temperatures between 4 K and room temperature. All µPL experiments were conducted by my colleagues S. Furthmeier and F. Dirnberger.

5.1. Radiative recombination: Enhancing nanowire passivation

When exciting bare GaAs nanowires with laser light, one obtains only very weak emission (compare the black curve in fig. 5.3a). This is ascribed to a predominantly non-radiative recombination mechanism of carriers via surface states, decreasing the radiative recombination in nanowires due to the high surface to volume ratio. To circumvent this problem, in the following the growth of the passivating wider band gap material AlGaAs around the GaAs nanowires is performed (section 5.1.1). Then, an extreme signal increase from optical transitions within the GaAs core in the resulting core/shell structure is expected. Since the AlGaAs shell easily oxidizes in ambient air, a thin layer of GaAs is additionally grown onto the AlGaAs shell, forming a GaAs cap.

Subsequently, to maximize the radiative recombination within the GaAs core, AlGaAs shells with different thicknesses and compositions are grown. The corresponding PL intensity, emitted from single nanowires is compared in sections 5.1.2 and 5.1.3. To do that, single lying wires were excited at 5 K with a 784 nm laser (1.58 eV) driven in continuous wave mode, using a power density of 0.5 kW/cm^2. Due to the 1 μm^2 spot size of the exciting laser, one gets position resolved PL spectra for each wire. To compare the PL spectra from different nanowires, the spectra from the positions with the maximum value in intensity were chosen.

5.1.1. AlGaAs/GaAs shell growth

The radial growth of the AlGaAs/GaAs shell is performed directly after the axial GaAs core growth in MBE. Here, the temperature was decreased to 460°C−480°C to suppress a further axial growth of the nanowire via the VLS mechanism, but was kept as high as possible to reduce the incorporation crystal defects like As anti-sites. Additionally, As_4 BEPs $> 7 \cdot 10^{-6}$ Torr are used, which reduce the diffusion lengths of Al and Ga adatoms by elevated adatom-solid transition rates, so a uniform shell should be gained. The Ga rate used for any shell growth was 0.8 Å/s, while the Al rate remained below 0.45 Å/s to obtain the desired composition of the $Al_xGa_{1-x}As$, which is in any case a direct band gap semiconductor with $x < 38$ % [86]. To yield a radial symmetric shell, the sample was rotated with 7 rpm.

In fig. 5.1a a cross section of a GaAs/AlGaAs/GaAs core/multishell structure is depicted, detected with TEM. The interface between the GaAs areas (dark) and the AlGaAs areas (bright) are atomically flat, compare the HRTEM micrograph of a section of this cross section in fig. 5.1b. The corresponding FFT in fig. 5.1c indicates only one crystal phase, i.e. the AlGaAs and the GaAs shells adopt the crystal structure of the GaAs core.

To evaluate the thickness of the AlGaAs shell in dependence on the deposited 2D AlGaAs layer height, which is the common measure in MBE, four samples with different 2D AlGaAs layer heights deposited onto equivalent GaAs core wires were manufactured. The core wires, grown by the Ga-catalyzed growth mechanism, have a diameter of approximately 45 nm, a length of 7 µm with a density of 1-2 per μm^2, and possess

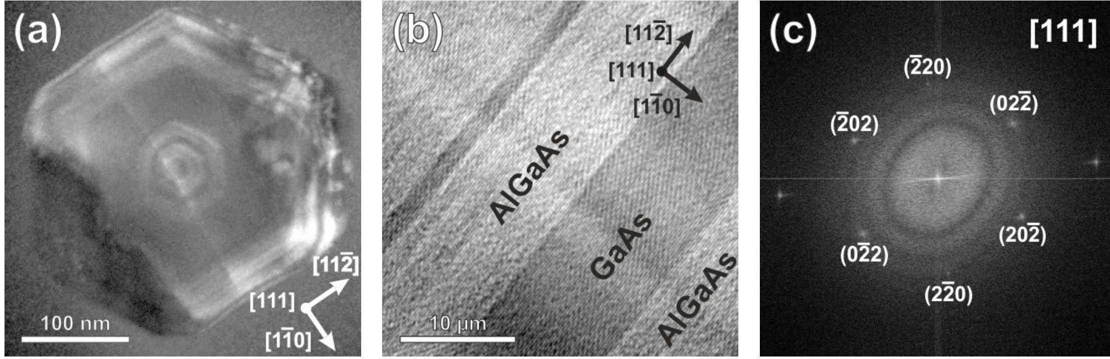

Figure 5.1.: TEM images of GaAs/AlGaAs/GaAs multishell nanowire cross sections: (a) Cross section of a whole wire consisting of 5 AlGaAs (bright) and 6 GaAs (dark) shells. (b) The HRTEM image of a section of (a) reveals atomically sharp AlGaAs/GaAs interfaces. (c) The FFT of the NW cross section indicates only one crystal phase, i.e. the AlGaAs and the GaAs shells adopt the crystal structure of the GaAs core.

predominantly ZB crystal structure. For the shell growth, 2D equivalent $Al_{0.35}Ga_{0.65}As$ layers of 15 nm, 30 nm, 60 nm and 120 nm height, respectively, were deposited, plus 30 nm 2D equivalent GaAs layer height each to prevent the AlGaAs shell from oxidizing.

In fig. 5.2a the averaged nanowire diameters at the wire bottoms and tops are sketched (red and black dots) in dependence on the deposited 2D layers of AlGaAs/GaAs. These parameters were measured by scanning electron microscopy (SEM) for an ensemble of more than twenty wires on each sample. It becomes apparent that, when growing from nearly untapered nanowires, the diameter at the bottom evolves much less pronounced than at the nanowire top. This effect can be ascribed to the shadowing of the molecular fluxes by other nanowires in the vicinity. The shadowing originates due to the inclination angle of the evaporation cells with respect to the substrate normal of 30°, and the above mentioned nanowire density and nanowire lengths. Nevertheless, the shell thickness seems to increase linearly with the amount of deposited material. When fitting the data linearly (dashed lines) one gets the conversion factor between the nominally deposited 2D layer and the shell growth, which is approximately 0.4 for the nanowire top and 0.23 for the bottom. Taking into account shell growth on both sides of the core, this means a factor of approximately 0.2 and 0.12, respectively. This linearized dependence of the shell thickness on the nominal 2D layer growth is sketched in fig. 5.2b. The corresponding AlGaAs shell thicknesses for the four samples are marked by the dots. Here, the evaluated average AlGaAs shell thicknesses are 2.5 nm, 5 nm, 10 nm, and 20 nm.

In the following, these wires are used to determine the AlGaAs thickness-dependent passivation of the GaAs core surfaces. This is done by comparing the intensity of the radiative recombination strength of single core/shell nanowires in µPL.

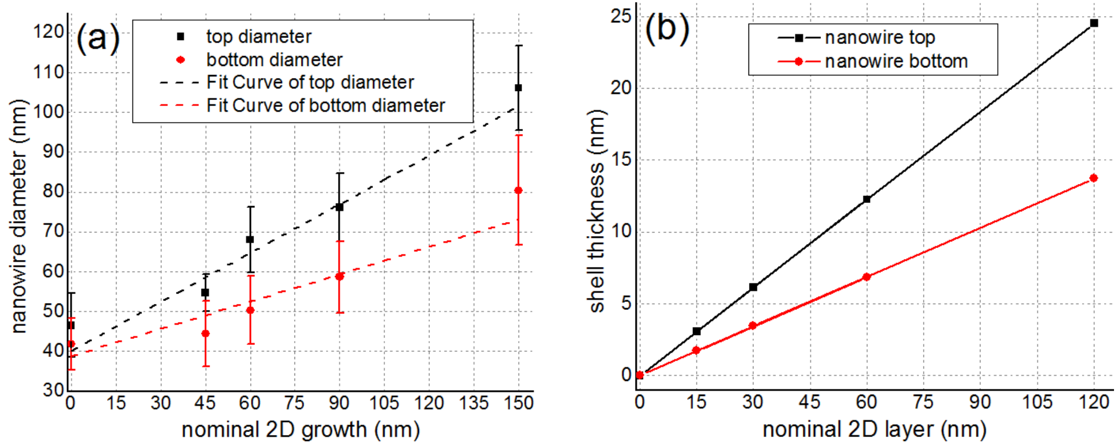

Figure 5.2.: Comparison of shell growth and 2D layer growth: (a) Averaged nanowire diameters of ensembles of at least 20 nanowires in dependence on deposited material in terms of 2D growth. A linear dependence is deduced for the nanowire bottom and the nanowire tip. The conversion factor between shell thickness and 2D layer growth, estimated by the linear dependence, is 0.12 and 0.2 at the nanowire bottom and tip, respectively. (b) Sketch of the resulting linear dependence between AlGaAs shell and 2D layer deposition. Dots: AlGaAs shell thicknesses for the nanowires mentioned in the text.

5.1.2. Radiative recombination strength and AlGaAs shell thickness

Fig. 5.3a shows the intensity distribution of PL spectra, emitted from core/shell nanowires with mean $Al_{0.35}Ga_{0.65}As$ shell thicknesses of 2.5 nm, 5 nm, 10 nm and 20 nm, respectively, as well as a spectrum of a GaAs wire without a shell. For the thinnest shell of 2.5 nm, the radiative recombination of excited carriers is quenched as for bare GaAs nanowires. This may be attributed to an inhomogeneous growth of the barrier with some parts of the GaAs core facets left blank, or a too thin barrier to prevent most of the carriers from tunneling through and relaxing via surface states in the GaAs cap. Apparently, for an average AlGaAs shell thickness of 5 nm, the GaAs core is fully covered and the shell largely inhibits tunneling processes, since here the radiative recombination within the GaAs wire increases by three orders of magnitude. For a further increase of the shell thickness, the intensity of radiative recombination rises due to a reduced probability for tunneling processes.

The peak intensities are detected at an energy of 1.515 eV, which corresponds to the exciton energy of ZB GaAs. This is reasonable, since the main crystal structure of these nanowires is ZB, and, due the excitation by high laser power densities, state filling occurs and consequently most carriers are in an excitonic state. The long tail towards lower energies can be explained by band gap renormalization for highly excited carriers [159].

Surprisingly, the shape of the spectrum changes for the thickest shell investigated. Here, a narrowing of the peak as well as a redshift away from the ZB exciton at 1.515 eV is observed. Since here neither a marked state filling nor a distinct band gap renor-

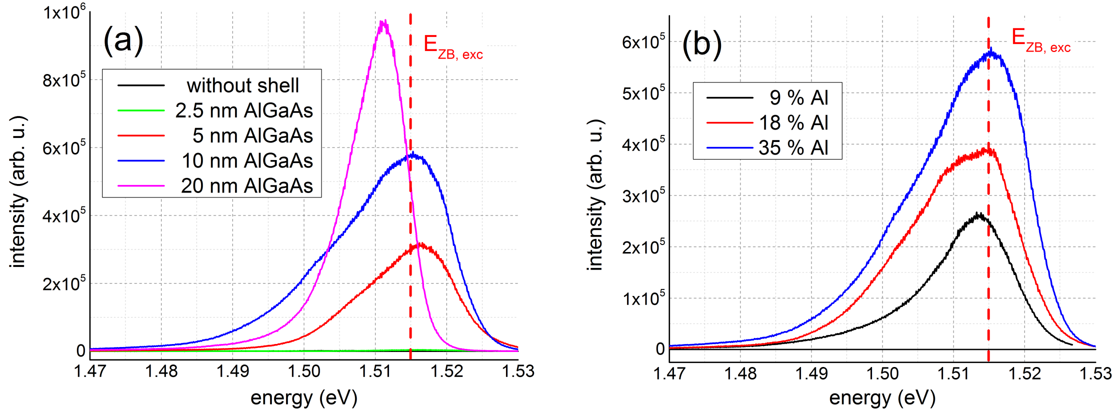

Figure 5.3.: Dependence of the radiative recombination strength in GaAs core nanowires on (a) the $Al_{0.35}Ga_{0.65}As$ shell thickness d and (b) the $Al_xGa_{1-x}As$ shell composition. The peaks at 1.515 eV are ascribed to the ZB exciton due to a predominant ZB crystal structure. (a) While for $d = 2.5$ nm the radiative recombination is as low as for GaAs nanowires without shell, for $d = 5$ nm the intensity rises by three orders of magnitude, indicating a fully covered GaAs core. A further increase of d increases the radiative recombination strength due to a reduced tunneling rate. (b) The passivating behavior improves with increasing Al concentration x due to the simultaneously rising $Al_xGa_{1-x}As$ band gap.

malization is observed, the spectrum has to be explained with an increased number of crystal defects, although the growth conditions for the GaAs cores were throughout the same. These inclusions of the other crystal structure reduce the band gap (compare section 2.3.3).

5.1.3. Radiative recombination strength and AlGaAs shell composition

Since the height of the AlGaAs barrier enclosing the GaAs core strictly depends on the composition of the AlGaAs shell (compare section 2.3.4), a better passivation of the core is expected for larger Al concentrations. Thus, in the following, the dependence of the emitted photoluminescence on the composition of the AlGaAs shell is determined. To do that, equivalent GaAs core wires as introduced in section 5.1.1 were coated with a 10 nm thick $Al_xGa_{1-x}As$ shell containing Al concentrations of $x = 0.09$, $x = 0.17$ and $x = 0.35$, respectively. Here, only shells with $x < 35$ % were produced to avoid the formation of an indirect band gap for $x \geq 38$ % [86].

The intensities of the PL spectra emitted from these wires are compared in fig. 5.3b. Here, we again observe the ZB exciton due to state filling, and the long low energetic tail due to band gap renormalization. The emitted intensity clearly increases with rising Al concentration in the AlGaAs shell, and therefore proves the enhancement of radiative recombination in the GaAs core using an enhanced barrier height of the AlGaAs shell.

5.2. PL: Correlation with nanowire crystal structure

After enhancing the radiative recombination in the GaAs core nanowires in the last section, this section focuses on the dependence of the emitted PL on the crystal structure of the nanowires. Therefore, PL spectra of two single GaAs/AlGaAs/GaAs core/shell nanowires with optimized WZ and ZB crystal structure (compare sections 4.3.1 and 4.3.2), are recorded along their entire length. In both cases, the GaAs core nanowires were passivated with a 10 nm thick $Al_{0.35}Ga_{0.65}As$ shell. Since the polarization of the emitted PL is expected to strongly depend on the crystal structure (section 2.3.3), polarization resolved measurements are conducted as well.

Therefore, the lying wires were cooled down to 5 K and excited by a cw laser operating at 690 nm (1.79 eV). The excitation power density used for spatially and polarization resolved measurements were $5 - 20$ W/cm^2, while the polarization of the exciting laser was chosen to be parallel to the nanowire axis. In this configuration, the absorption in a wire-like structure is maximum [160].

5.2.1. PL: Stacking-fault-free wurtzite GaAs nanowires

In the case of WZ GaAs nanowires, wires from the as-grown substrate were transferred to a TEM grid for a combined PL and TEM study, so PL measurements were already conducted before the crystal structure was determined in TEM. With this, a deterioration of the crystal quality by the high-energetic electron beam exposure was avoided. The photoluminescence stemming from the stacking-fault-free wurtzite nanowire, introduced in section 4.3.1, is presented in the following spatially and polarization resolved, which was also published in [156].

Spatially resolved photoluminescence

Fig. 5.4a shows false color µPL spectra as a function of the position along the 4.2 µm long nanowire. We observe only one peak at 1.518 eV along the whole wire without any shift in energy, which can be attributed to the WZ excitonic ground state, since this wire contains not a single stacking fault. This value corresponds to a slightly elevated excitonic state (3 meV) of WZ GaAs compared to ZB GaAs. An enhanced band gap due to confinement effects can be excluded here, since the wire possesses a uniform diameter of 80 nm. The FWHM of the peak, in fig. 5.4b exemplarily shown for both nanowire ends and the nanowire center, is 4 meV. This value is among the narrowest detected so far for the corresponding transition, and also indicates a very pure crystal structure. With these measurements, the excitonic band gap of WZ GaAs is determined to be 1.518 eV.

Polarization resolved photoluminescence

To measure the emitted PL intensity polarization resolved, a rotatable analyzer was inserted into the emission beam guidance. Since the emitted intensity is also dependent

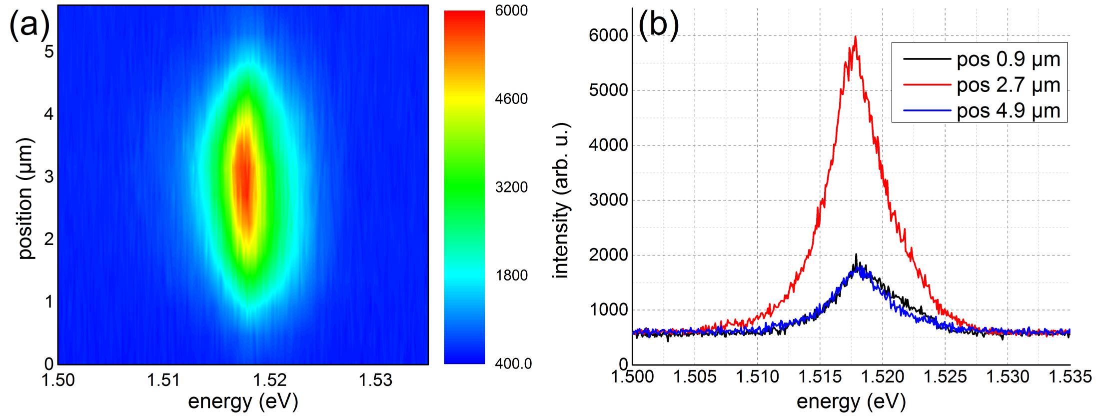

Figure 5.4.: PL spectra of a 4.2 µm long wurtzite nanowire without stacking faults: (a) False color µPL spectra as a function of the position along the nanowire. Emission is only observed at 1.518 eV, indicating the transition energy for free WZ excitons. (b) Single emission spectra, exemplarily shown for the center and both nanowire ends, reveal a full width at half maximum of 4 meV for any position along the wire.

on the position (compare figs. 5.4), the position of the measurement was held fixed, while the analyzer was rotated in 10° steps.

Fig. 5.5a shows a false color plot of PL emission spectra as a function of the angle θ to the nanowire axis. Again, emission resides only at 1.518 eV, attributed to the WZ exciton. The emitted intensity clearly shows a π-periodic behavior in dependence on the angle to the nanowire axis, with maximum values at $\theta = 90°$ and $\theta = -90°$, i.e. perpendicular to the nanowire axis. The angular intensity distribution follows a $\cos^2(\theta - \varphi)$-behavior (see the polar plot fig. 5.5b), with φ being the angle under which the maximum in intensity is detected ($\varphi \approx 89°$, probably due to little misalignment of the analyzer). This indicates emitted light strongly polarized perpendicular to the nanowire axis. The observed degree of linear polarization is determined to be 71 %, i.e. the emission of light polarized along the nanowire axis is not fully suppressed.

Usually, light emitted by a lying nanowire should be polarized parallel to the nanowire axis due to the nanowire aspect ratio and the refractive index mismatch [78]. The observed behavior, which is just vice versa, must therefore be explained by the allowed transitions in the unit cell of the wurtzite crystal structure (see section 2.3.3). The dipole selection rule for the transition from the bottom conduction band to the top valence band allows exclusively emission of light polarized perpendicular to the WZ $\hat{c}$-axis, i.e. perpendicular to the nanowire axis, accounting for the observed polarization. The degree of linear polarization is obviously reduced from 100 % to 71 % due to the additional polarization effect parallel to the nanowire axis, caused by the nanowire aspect ratio and the dielectric mismatch.

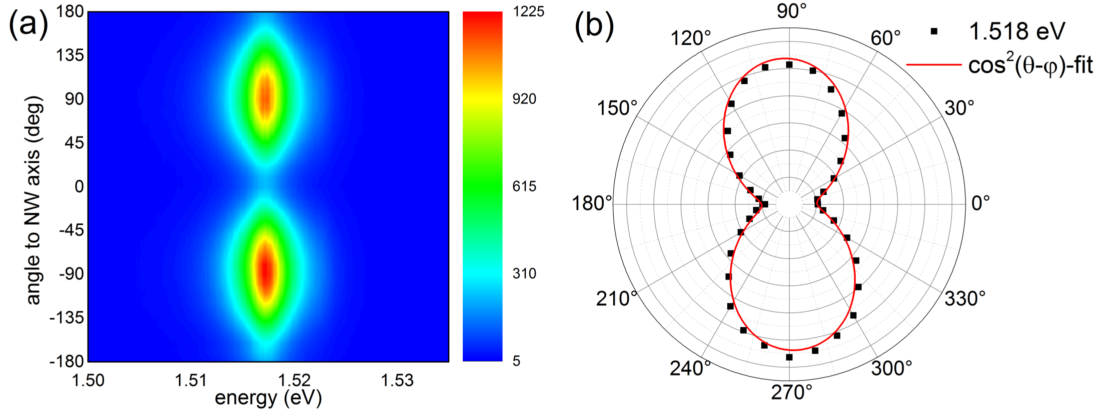

Figure 5.5.: Polarization resolved measurements of a pure wurtzite nanowire without stacking faults: (a) False color plot of PL emission spectra as a function of the angle θ to the nanowire axis. A π-periodic behavior with maxima at angles $\theta = 90°$ and $\theta = -90°$ towards the nanowire axis is revealed. (b) Polar plot of the intensity measured at 1.518 eV. The intensity follows a $\cos^2(\theta - \varphi)$-behavior, with $\varphi = 89°$, indicating emitted light polarized perpendicular to the nanowire axis.

5.2.2. PL: Zinc-blende nanowires

In order to determine the corresponding parameters for nanowires with predominantly ZB crystal structure, a wire grown with the Ga-catalyzed method with optimum parameters for ZB crystal structure (compare section 4.3.2), was examined in µPL. In this case, the combination of PL and TEM measurements on one and the same wire was not developed yet, so the direct comparison between crystal structure and PL is not possible. Here, the qualitative change of the crystal structure with nanowire length, as deduced in section 4.3.2 (fig. 4.10a), will be used to correlate the PL with the crystal structure. First, a spatially resolved recording of the emitted spectrum from the wire is shown, followed by a position invariant polarization resolved measurement.

Spatially resolved photoluminescence

Fig. 5.6a shows a false color intensity plot of the spatially resolved emission spectra along a whole wire in the energy range from 1.47 eV to 1.52 eV, with the bottom of the nanowire located at position 0.5 µm and its tip at 4.5 µm. Along a large part at the nanowire bottom, we detect an emission at 1.51 eV, which transforms near the nanowire tip to a broad emission at 1.48 eV. The signal at 1.51 eV can be attributed to the ZB exciton, since at the nanowire bottom large pure ZB segments exist, whereas the signal at 1.48 eV stems from the multiple twinned part at the nanowire tip [59], where also WZ inclusions appear.

For a deeper insight, single spectra of positions along the nanowire with an interdistance of 0.5 µm are plotted in fig. 5.6b. Here, we observe again the two dominating

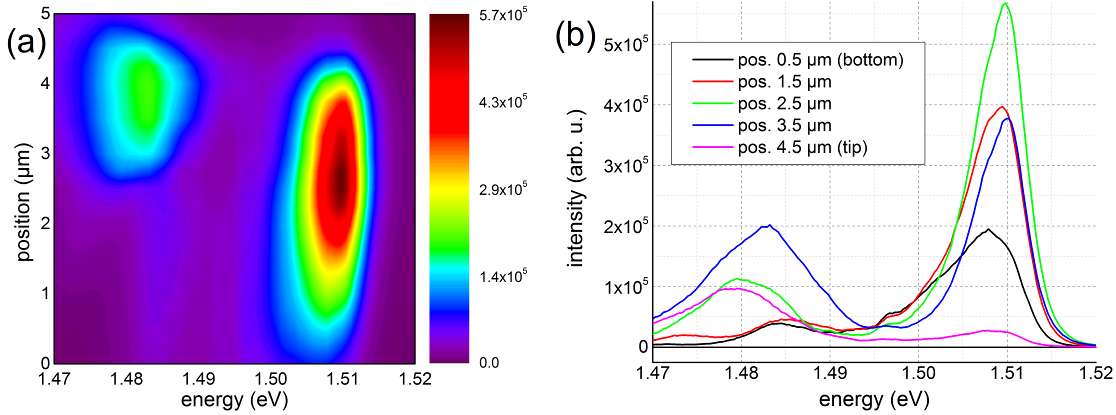

Figure 5.6.: Spatially resolved photoemission of a typical ZB optimized nanowire: (a) False color µPL spectra as a function of the position along the nanowire. The main part of the wire, from the bottom at 0.5 µm to 2.5 µm, emits at 1.51 eV, attributed to the ZB exciton. Towards the nanowire tip at 4.5 µm, redshifted emission at a reduced band gap of 1.48 eV becomes dominant, caused by the introduction of WZ segments. (b) Profiles at certain positions of the spectrum in (a) reveal the evolution of the two peaks. The peak at 1.51 eV increases and blueshifts with increasing distance to the bottom. Exceeding position 2.5 µm, the intensity drops again. For the opposite scanning direction the peak at 1.48 eV shows the same behaviors, which are ascribed to state filling effects.

peaks at 1.51 eV and at 1.48 eV. When scanning from the bottom to position 2.5 µm, the ZB exciton peak at 1.51 eV increases in intensity and blueshifts. This state filling behavior can be explained by an increased amount of excited carriers when moving the exciting laser along the nanowire axis, illuminating at the nanowire edges less nanowire volume than in the nanowire center. For an advanced scanning towards the nanowire tip, the ZB exciton peak reduces in favor of emission at 1.48 eV. This emission can be ascribed to bound excitons at a multiple twinned ZB crystal structure with, possibly, WZ inclusions. These crystal defects account for the separation of electrons and holes in ZB and WZ crystal structure, respectively, and thus cause a reduced band gap (compare section 2.3.3). This peak also shows the effect of state filling when moving the laser spot from the nanowire tip towards the nanowire center, i.e. a blueshift and an increase of the transition strength.

Consequently, the observed PL spectra correlate with the observations made in TEM. A transition from a nearly defect-free ZB crystal structure at the nanowire bottom, to a faulty crystal structure at the nanowire tip is determined.

Polarization resolved photoluminescence

The polarization resolved measurements were performed the same way as for the SF-free WZ wire. To obtain a signal from the defective top part and the pure ZB part at the bottom, the measurement for a 360° rotation of the analyzer position with respect to

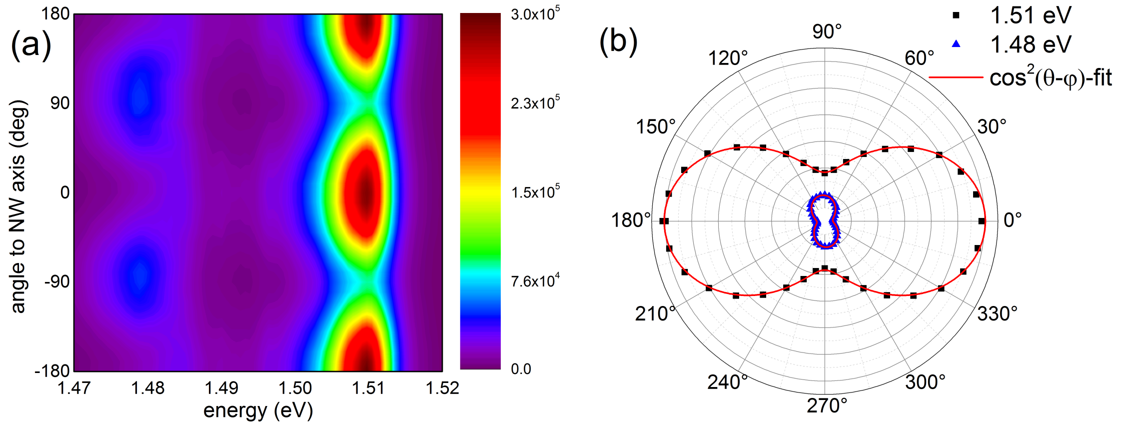

Figure 5.7.: Polarization resolved µPL intensity spectra of a predominantly ZB nanowire: (a) False color plot of the PL emission spectra as a function of the angle θ to the nanowire axis. The peak at 1.51 eV shows a π-periodic behavior of the emitted intensity with maxima at 0° and 180°, while the peak at 1.48 eV possesses a π-periodicity with maxima at 90° and -90°. (c) The polar plots of the intensities for the peaks at 1.51 eV and 1.48 eV show a clear $\cos^2(\theta - \varphi)$-behavior, indicating emitted light polarized parallel ($\varphi = 0°$) and perpendicular to the nanowire axis ($\varphi = 90°$), respectively.

the nanowire axis was performed approximately at position 2.5 µm in figs. 5.6.

The false color plot of the PL emission spectra as a function of the angle θ to the nanowire axis in fig. 5.7a confirms predominant emission at 1.51 eV, and weak emission at 1.48 eV. The intensity at 1.51 eV follows obviously an angular π-dependence with maxima at 0° and 180°, whereas the intensity at 1.48 eV follows a π-dependence with maxima at 90° and $-90°$.

Using a polar plot in fig. 5.7b, a $\cos^2(\theta-\varphi)$-behavior of the intensity can be recognized for both emission energies. This proves that the emission stemming from the bottom part of the nanowire is polarized parallel to the nanowire axis ($\varphi = 0°$), whereas the peak at 1.48 eV emits light polarized perpendicular to the nanowire axis ($\varphi = 90°$).

In ZB GaAs, in contrast to the WZ GaAs crystal structure, the transition from the lowest conduction band to the top valence band is not intrinsically polarized (compare section 2.3.3). The observed polarization parallel to the nanowire axis of the ZB exciton is explained with the nanowire geometry. Wilhelm et al. [78] calculate a strongly enhanced emission polarized parallel to the nanowire axis compared to perpendicular polarized emission, attributed to the high aspect ratio of the nanowire and the large refractive index contrast between GaAs and vacuum.

The observed maxima for polarization perpendicular to the nanowire axis at 1.48 eV is characteristic for WZ GaAs crystal structure (compare sections 2.3.3 and 5.2.1). This energy resides 38 meV below the WZ excitonic state and is explained via the staggered band alignment of WZ/ZB phase transitions, which leads to a separation of electrons and holes towards ZB and WZ phases, respectively. Thus, at WZ/ZB interfaces a less-

ened band gap exists, whose exact value depends on the valence band offset between WZ and ZB GaAs and a possible confinement due to the ZB or WZ segment size along the nanowire axis. The polarization of the emitted luminescence is WZ-like, i.e. polarized perpendicular to the nanowire axis, since these transitions are determined by the symmetry of the topmost WZ valence band.

5.3. GaAs lasing nanowires

Recent publications [157, 158] show the usage of GaAs/AlGaAs/GaAs core/shell nanowires as room temperature lasers, emitting in the near infrared regime. The wires are hereby used both as Fabry-Perot cavity and gain medium. The refractive index mismatch between the nanowire and its surrounding ensures the confinement of the photonic modes inside the nanowire, whereas the nanowire end facets provide optical feedback. The number of guided modes, supported in the nanowire, depends on the nanowire diameter as well as on the surrounding. For nanowires lying on SiO_2, which is in the following used as substrate, the critical diameter for one mode to emerge is 160 nm [157]. Calculations concerning the lowest threshold gain for lasing operation reveal a minimum for nanowire with 330 nm in diameter and a length above 6 µm [157]. The crystal structure of the wire plays a minor role, so the growth of GaAs nanowires was only optimized towards a sufficient quality of the cavity, i.e. a non-tapered wire with the dimensions stated above.

5.3.1. Nanowire growth

Since the axial growth of GaAs nanowires with a diameter of 330 nm is not possible by growing from a catalyst droplet in one run, the growth was split into four separate parts: the axial growth of the GaAs core nanowires with sufficient length, the growth of a GaAs shell until the desired GaAs nanowire diameter was reached, and the growth of a thin passivating AlGaAs shell and a GaAs cap.

To obtain a uniform nanowire shape, the areal nanowire density has to be strongly reduced, so that shadowing effects, which lead to inversely tapered nanowires during shell growth (compare section 5.1.1) are avoided. This was done by applying the Ga-catalyzed growth method on Si(111), using a low Ga rate of 0.33 Å/s and by steering the temperature of the substrate. For the nucleation of sparse distributed GaAs seeds, the temperature was held at 620 °C, which is the highest value for the nucleation of nanowires on Si(111) for the applied Ga rate. Directly after detecting the RHEED spots for nanowire nucleation, the substrate temperature was increased by 10°C to avoid a further nucleation of GaAs seeds on the Si(111) surface, whereas the growth of GaAs nanowires directly on the GaAs stubs is supported. This behavior may be attributed to an elevated amount of energy necessary to form GaAs seeds on a foreign substrate. The energy is in this case provided by a *lowered* growth temperature, increasing the supersaturation of a Ga-As pair in the catalyst droplet. Using this technique, the areal

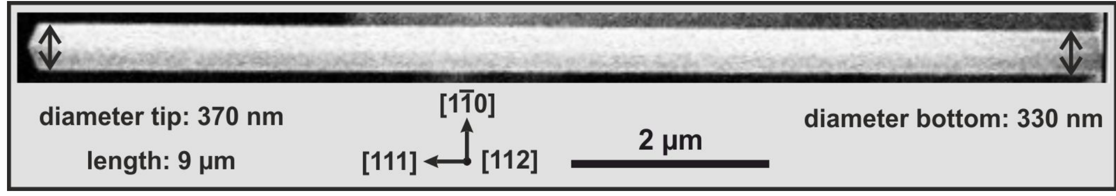

Figure 5.8.: SEM image of a GaAs/$Al_{0.35}Ga_{0.65}As$/GaAs core/shell nanowire used for lasing operation: the nanowires are nearly untapered with an average diameter of 350 nm and a length of 9 µm.

nanowire density was reduced to 1 NW per 50 μm^2, which seemed sufficient for the growth of a uniform shell.

With this method, GaAs core nanowires with a uniform diameter of 30 nm and approximately 10 µm length were produced. Afterwards the GaAs/$Al_{0.35}Ga_{0.65}As$/GaAs shell was grown subsequently at the very same conditions as for the regular shell growth (section 5.1.1). 2D equivalent layers with thicknesses of 800 nm GaAs, 10 nm AlGaAs and 10 nm GaAs were deposited in order to obtain GaAs nanowires with a diameter of 330 nm and a AlGaAs shell plus a GaAs cap with a thickness of 2 nm each. The AlGaAs shell was chosen to be as thin as necessary in order to reduce a possible effect of the Al atoms on the emerging modes in the cavity.

Using these parameters, nearly untapered nanowires of 9 µm length, with diameters of 330 nm at the nanowire bottom and 370 nm at the nanowire tip, were produced. Fig. 5.8 shows exemplarily a scanning electron microscopy image of one of these wires.

5.3.2. PL: Lasing operation

The stimulation of the lying nanowires was performed at 5 K. To do that a pulsed 784 nm laser diode was used, whose polarization was chosen to lie parallel to the nanowire axis. Since these wires possess a predominantly ZB crystal structure, here the maximum in absorption was expected [78]. The laser worked at a repetition rate of 1 MHz with a pulse duration equal to 70 ps, and was focused down to a spot size of 1 μm^2 to excite the nanowires locally. The hereby achieved maximum peak power density of 3 MW/cm^2 was reduced introducing optical density filter into the beam guidance. To find the minimum excitation power density necessary for lasing operation, a power series was measured at one end of the nanowire, since here the decoupling of the laser light from the cavity was expected.

Figs. 5.9a and 5.9b show the intensity of the emitted spectra as a function of the excitation power density. For low excitation power densities < 1.25 MW/cm^2, we observe spontaneous emission with a maximum at 1.505 eV, which broadens with increasing power due to state filling. When exceeding an excitation power of 1.25 MW/cm^2, strong peaks emerge at 1.5012 eV, 1.5025 eV and 1.5035 eV, indicating the amplification of different cavity modes. For a further increase in excitation power, one dominant peak extracts at 1.5012 eV and clearly narrows in FWHM, whereas the other two modes

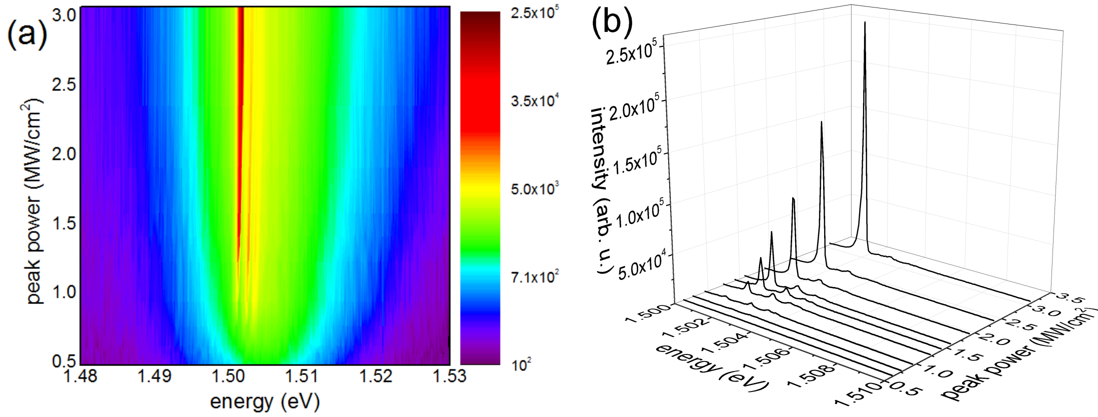

Figure 5.9.: Power dependent photoemission at the tip of a lasing nanowire: (a) False color plot of the PL emission spectra as a function of the peak power excitation density. Increasing the excitation power density from 0.5 MW/cm^2 to 3 MW/cm^2 results in the onset of lasing operation above a threshold level of 1.25 MW/cm^2 at 1.5012 eV after the observation of three Fabry-Perot modes for excitation power densities higher than 0.9 MW/cm^2 (yellow/red lines). (b) The extraction of a single lasing mode can be clearly seen in the PL spectra between 1.50 eV and 1.51 eV for an elevation of the excitation peak power density from 0.5 to 3 MW/cm^2.

remain weak. This behavior is sketched in fig. 5.10a more clearly. For power densities less than 1.25 MW/cm^2, the linear increase in emission intensity (black dots) is low compared to the linear increase at higher power densities. This reveals the typical threshold knee behavior with a threshold level of 1.25 MW/cm^2, verifying the onset of lasing operation. The simultaneous narrowing of the FWHM (blue dots) from 6 nm to 0.1 nm confirms this. The interference pattern, emitted from the nanowire above the threshold value, depicted in fig. 5.10b, looks similar to a pattern produced by two coherent dipole emitters separated by the nanowire length. This observation proves lasing operation, coupled out at both ends of the nanowire cavity.

However, at room temperature (RT), the excitation of these nanowires towards lasing operation was not successful. Here, solely spontaneous emission was detected.

One reason may be reduced optical quantum efficiency, caused by the very thin $Al_{0.35}Ga_{0.65}As$ shell, used to passivate these wires (compare section 5.1.2). A thicker shell would inhibit more carriers from recombining non-radiatively via surface states, but might also affect the origin of the lasing mode(s) in a negative way.

Another reason might be a not sufficient cavity quality, induced by the slight inversely tapered nanowires, which results also in an increase of the lasing threshold value. To overcome this, a further reduction of the nanowire density would be necessary, so the shadowing of the molecular fluxes by nanowires in vicinity is completely absent.

Furthermore, the type of excitation may account for the non-existence of lasing at room temperature. In the experiments described above, only a part of the nanowire was

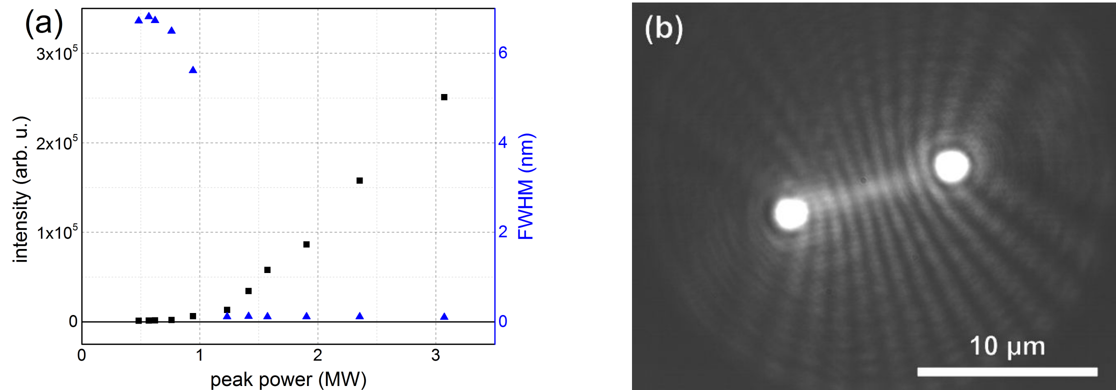

Figure 5.10.: (a) Emitted intensity at 1.5012 eV and FWHM of the corresponding peak in dependence on the excitation power density. The emitted intensity (black squares) shows a knee behavior with increasing power density. The FWHM (blue triangles) narrows correspondingly from 6 nm to 0.1 nm. Both observations prove the onset of lasing operation at 1.25 MW/cm^2. (b) Interference pattern of a nanowire excited with 3 MW/cm^2. The tip and the bottom are the bright spots, which can be considered as two coherent dipole emitters, coupling out the laser light.

excited by the focused pump laser with a spot diameter of 1 µm^2, whereas in [157, 158] RT lasing operation was yielded by pumping the whole nanowire. These groups use an elliptical focus to achieve a high pump power density all along the wire.

All these reasons sum up to a lasing threshold value, which resides apparently beyond a critical energy density, which could not be reached at RT, so finally no lasing operation was obtained.

5.4. Conclusion

In this section, the growth of a passivating AlGaAs/GaAs shell around the GaAs core was introduced in order to reduce non-radiative recombination of carriers at GaAs surface states, and to be able to determine optical transitions within GaAs nanowires. The radiative recombination within the core was maximized using a thick AlGaAs shell with a high Al concentration, to prevent the carriers from tunneling into surface states.

Using this passivation technique, the optical properties of stacking-fault-free WZ GaAs were determined for the first time [156]. The excitonic band gap was estimated to be 1.518 eV, while the FWHM of the corresponding transition was with 4 meV the narrowest observed so far. Polarization resolved measurements revealed light emission from WZ nanowires polarized perpendicular to the nanowire axis. This behavior was explained by the dipole selection rule of the transition from the lowest conduction band to the highest valence band in WZ GaAs crystal structure.

Instead, predominantly ZB nanowires, with the bulk excitonic band gap of 1.515 eV,

emit light polarized parallel to the nanowire axis. This was attributed to a polarization effect occurring due to the elongated shape of the nanowire and the dielectric mismatch between nanowire and surrounding, since here the interband transitions are not polarized in dipole approximation. Note that this polarization effect reduces the degree of linear polarization in WZ wires from 100 % to 71 %.

Thus, PL measurements can be used to determine the GaAs nanowire crystal quality and its kind. Polarization resolved PL measurements determine the predominant crystal structure by parallel or perpendicular polarized emission, while the redshift of the spectrum, caused by WZ/ZB GaAs phase transitions, indicates the crystalline purity.

Furthermore, the growth of GaAs/AlGaAs/GaAs core/shell nanowires applicable for lasing operation in the near infrared was described. Since the wires are thereby used as cavity and gain medium, their shape is crucial for the emergence of lasing modes. Thus, the nanowire growth was optimized for a uniform shell growth by the reduction of the areal nanowire density. However, lasing operation was obtained for cryogenic temperatures only, probably due to the passivation with a relatively thin AlGaAs shell, or due to the spatial limited pumping of the wires, which differs the described experiments from initiation of successful room temperature lasing in literature [157, 158].

6. Spontaneous polarization in WZ GaAs

Spontaneous polarization is a phenomenon occurring in wurtzite crystal structure due to the symmetry breaking of the crystal in [0001] direction. Here, the sp^3 hybridized atoms no longer form a tetrahedron as in the zinc-blende crystal. The attractive or repulsive interaction between the third nearest neighbors deforms the crystal in [0001] direction [63] (compare section 2.3.2). This symmetry breaking leads to the displacement of the centers of positive and negative charges [66], resulting in the formation of "sheets" of alternating charge density σ along the [0001] direction, depicted in the sketch in fig. 6.1a. Especially at the interfaces of heterostructures, spontaneous polarization leads to an accumulation of charges and thus to internal electric fields, that are known to account for the quantum-confined Stark effect [161, 162].

For the very first time, we observed spontaneous polarization experimentally in wurtzite GaAs in nanowires, and determined its polarization strength. This study was published in [164]. To do that, differential phase contrast microscopy (DPC) in a scanning transmission electron microscope (STEM) was used [165], which is a technique to map internal electric fields with a resolution on nanometer scales [166].

In fig. 6.1b, a TEM micrograph of a tip of a GaAs nanowire is shown, which is in the following examined with DPC. The wire was oriented in a $\langle 11\bar{2}0 \rangle \,||\, \langle 1\bar{1}0 \rangle$ zone axis, so the electron beam traverses the wire perpendicular to the [0001] || [111] growth direction, and therefore perpendicular to the expected electric field vectors. The HRTEM image of the yellow marked part is depicted in fig. 6.1c. Due to the consumption of the large catalyst droplet, at the tip of the predominantly ZB nanowire, pure WZ crystal structure and finally ZB crystal structure emerges, before the nanowire diameter reduces towards the droplet. Here, we find two closely related twin stacking faults (white arrow), and a region with mixed crystal structure, each segment only some monolayers thick ("Mix").

Performing DPC-imaging at this wire tip, one obtains a charge distribution map due to the deflection of the incident electron beam by the internal electric fields, displayed in fig. 6.2. The grey scale is a measure for the strength of deflection: dark and bright areas are charged areas, while uncharged areas appear as neutral grey. For clarity, an intensity profile is superimposed. In the pure WZ segment, compare the corresponding HRTEM in fig. 6.1c, we detect alternating electric charges, while in the ZB segments no deflection is observed. Thus, DPC delivers direct evidence for the existence of spontaneous polarization in the WZ phase of GaAs, and its absence in the ZB phase.

Surprisingly, the maximum deflection is not detected in the pure WZ segment, but at WZ/ZB interfaces, indicated in fig. 6.2 by the black arrows. This behavior can be explained by counting the measurement as a convolution of the electron beam and the probed potential landscape. Since the FWHM of the electron beam is larger than the

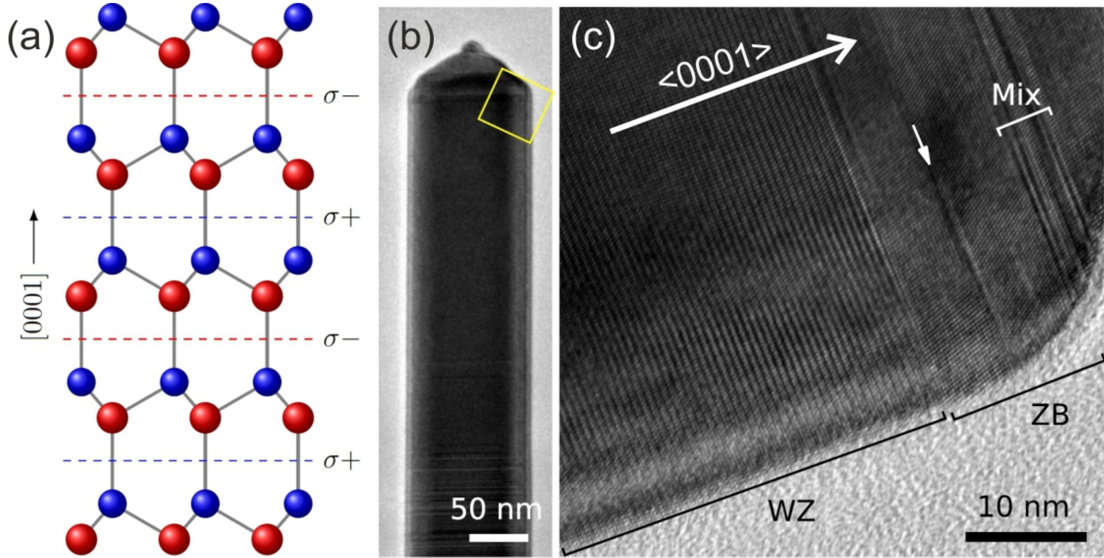

Figure 6.1.: (a) Spontaneous polarization in wurtzite GaAs: due to the symmetry breaking in wurtzite crystal structure, the centers of charge ($\sigma+$ and σ-) are separated along the [0001] direction. Adopted from [163]. (b) Tip of a GaAs nanowire optimized for ZB crystal structure and used for DPC. (c) The HRTEM of the yellow squared region in fig. 6.1b indicates the droplet consumption induced WZ/ZB crystal structure transformation at the nanowire tip. Here, two closely related twin planes (white arrow) and a region with mixed crystal structure (”Mix”) is observed.

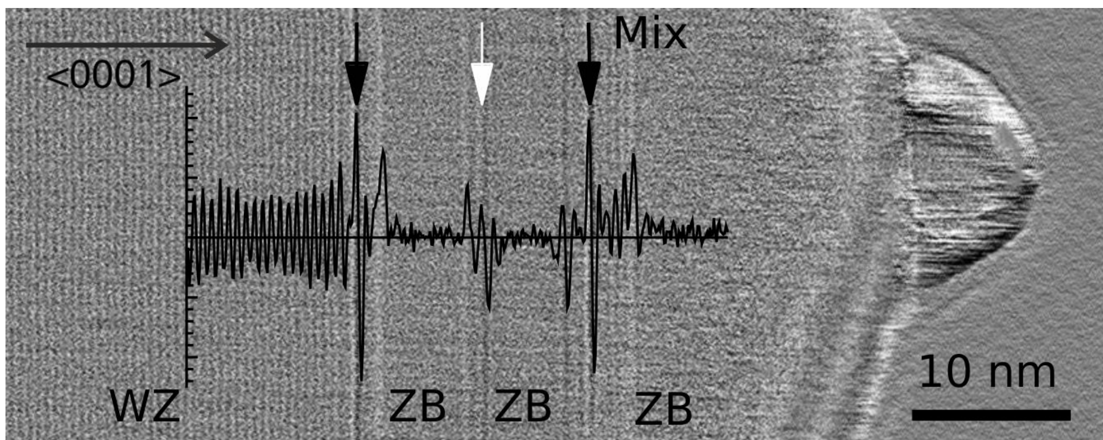

Figure 6.2.: Charge distribution map of the nanowire tip shown in figs. 6.1b and 6.1c with superimposed intensity profile: In pure WZ crystal structure (left) the transmitted electron beam becomes deflected by the electric fields occurring due to spontaneous polarization, whereas in ZB segments (center) no deflection is detected. The maxima of the electric field are observed at ZB/WZ transitions.

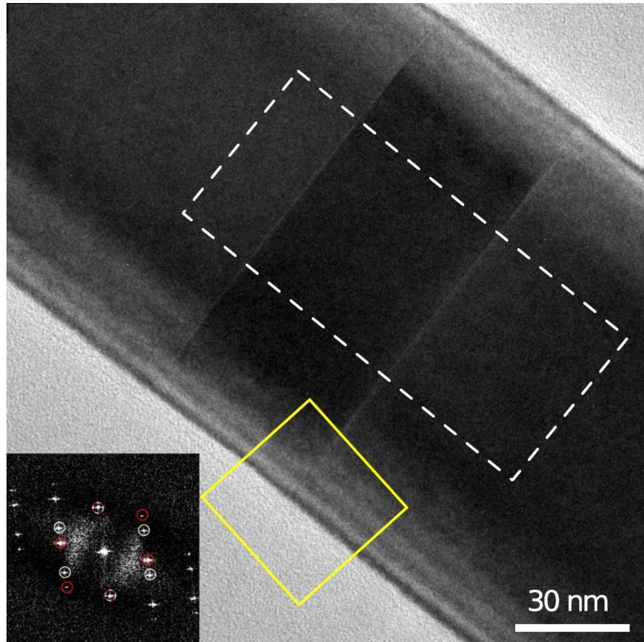

Figure 6.3: TEM overview of the capacitor-like double twin plane structure used for the quantification of the spontaneous polarization in WZ GaAs. The inset shows a diffraction pattern taken from the yellow squared region with the characteristic pattern of twinned ZB GaAs crystal structure.

WZ lattice spacing in [0001] direction, in pure WZ crystal structure several electric fields with opposite direction are probed, and consequently an underestimated deflection is detected. In contrast, in regions with different crystal phases, the measured deflection is strongly affected by the interplay of the electron probe profile and the probed structure. Thus, due to experimental limitations, a direct quantitative access to the spontaneous polarization in WZ GaAs is not possible. However, if the electric field extends over areas larger than the electron beam diameter, the correct values for spontaneous polarization in WZ GaAs should be obtained.

Therefore a structure is needed, which contains a homogenous electric field over several nanometers in length. This structure would be capacitor-like, with the dielectric ZB GaAs - free of polarization effects - embedded between two plates consisting of WZ GaAs. The thickness of the WZ GaAs plates is irrelevant, so twin planes in ZB GaAs, which are the the smallest possible WZ segments and abundant in GaAs nanowires, are sufficient, if they possess a small inter-distance compared to the nanowire diameter.

Consequently, spontaneous polarization in WZ GaAs was quantified using a capacitor-like structure consisting of two twin planes, separated wide apart from each other by the dielectric ZB GaAs. This structure is shown in fig. 6.3. The corresponding charge distribution map, shown in fig. 6.4a, clearly reflects the capacitor-like behavior in this structure. At the crystal phase interfaces, a bright line and a dark line are observed, indicating positive and negative sheet charges. The directions of the electric fields within this structure are shown color coded in fig. 6.4b. At the positions of the twin planes, the sign of the electric field becomes reversed due to the charge separation towards both twin planes.

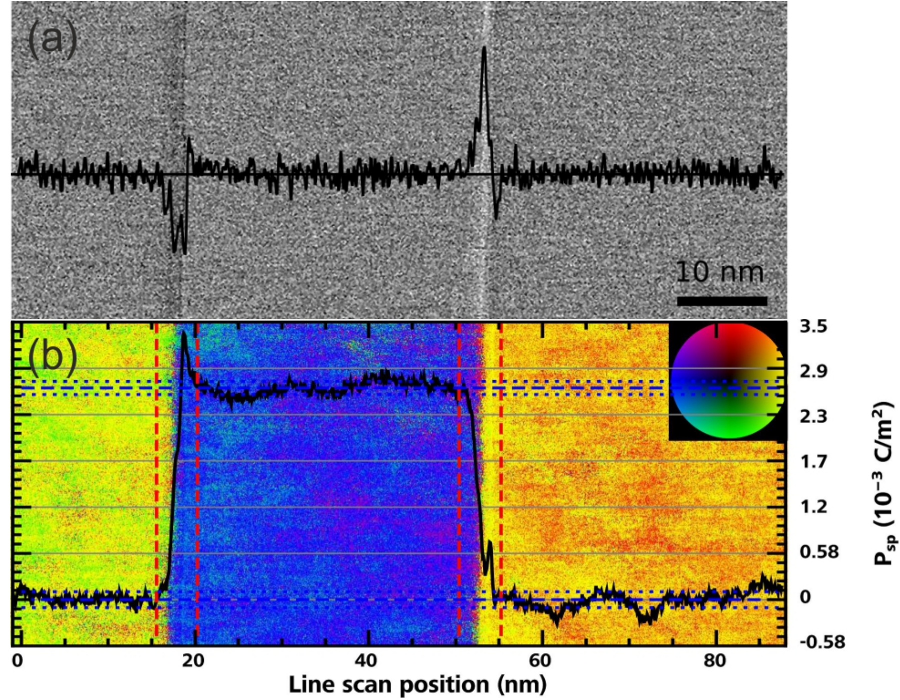

Figure 6.4.: (a) Charge distribution map with superimposed line scan profile of the structure shown in fig. 6.3. Sheet charges are detected at the monolayers of WZ crystal structure. (b) False color plot of the corresponding electric fields: The color indicates the direction of the electric field according to the inset color wheel, and the brightness the field strength. The superimposed curve depicts the averaged electric field along this structure after setting the field outside the twin planes to zero. The spontaneous polarization, evaluated via $P_{\rm sp} = \epsilon_0 \epsilon_{\rm GaAs} |\vec{E}|$ is displayed on the right vertical axis.

After setting the average electric field outside the capacitor-like structure to zero, the absolute value of the spontaneous polarization $P_{\rm sp}$ within the capacitor can be evaluated from the induced electric field strength $|\vec{E}|$ via $P_{\rm sp} = \epsilon_0 \epsilon_{\rm GaAs} |\vec{E}|$. The averaged values of $|\vec{E}|$ and $P_{\rm sp}$ along the structure are shown in the superimposed curve in fig. 6.4b. The change of the electric field strength at the twin planes by (22.9 ± 0.9) MV/m determines the spontaneous polarization of wurtzite GaAs to be $(2.7 \pm 0.6) \cdot 10^{-3}$ C/m^2, which agrees quite well with theoretical calculations [66].

With this, spontaneous polarization in GaAs was observed and its strength quantified for the first time. For a more detailed description of spontaneous polarization in wurtzite structures, and details concerning the measurement process, see [163].

7. GaAs/(Ga,Mn)As core/shell nanowires

The combination of ferromagnetic materials and nanowires may enable the integration of spin-related phenomena in nanoscale objects. In the GaAs system, the diluted magnetic semiconductor (Ga,Mn)As can easily be used for the growth of semiconductor/ferromagnet nanowire heterostructures, since its growth is pseudomorphic, i.e. adopts the crystal structure of the underlying GaAs substrate. The first successful growth of a GaAs/(Ga,Mn)As heterostructure on nanowires was performed by Rudolph et al. [19], who conducted the growth of a (Ga,Mn)As shell after the growth of GaAs core nanowires. Since the (Ga,Mn)As shell adopts the crystal structure of the GaAs core, in nanowires not only the zinc-blende (ZB) (Ga,Mn)As crystal structure is accessible, but also the wurtzite (WZ) (Ga,Mn)As crystal structure.

In this chapter, the differences between the ZB and WZ GaAs/(Ga,Mn)As core/shell nanowires are examined concerning the structural consequences of covering the GaAs core with a (Ga,Mn)As shell, and concerning the magnetic properties of the core/shell systems. To do that, in section 7.1 the (Ga,Mn)As shell thickness dependence along a nanowire is derived. This is non-negligible, since the pseudomorphic growth of the (Ga,Mn)As shell on the GaAs core induces strain in the core/shell system, whose strength depends on the shell thickness, and thus may affect the magnetic anisotropy of (Ga,Mn)As, as observed in thin film growth [117, 118]. Using X-ray diffraction techniques (XRD) and a superconducting quantum interferometry device (SQUID), in section 7.2 the structural differences between core/shell structures with WZ and ZB crystal structure and its bare GaAs cores, as well as the magnetic properties of the WZ and ZB (Ga,Mn)As shells, are determined. Furthermore, the optimization of the (Ga,Mn)As shell growth onto WZ GaAs nanowires is described for three different Mn concentrations in section 7.3. Here, magnetotransport measurements are conducted to compare the magnetic and transport properties.

To ensure a sufficient crystal quality, the parameters optimized in section 4.3 for pure WZ and ZB GaAs nanowire growth, obtained with the Au-catalyzed method, were used for the growth of the GaAs cores. The growth of the (Ga,Mn)As shell with molecular beam epitaxy (MBE) was performed directly after the formation of the GaAs core NWs. Since ferromagnetic (Ga,Mn)As must be grown far from the thermodynamic equilibrium, the growth temperature for the (Ga,Mn)As shell was kept in any case below 220°C. Then, while rotating the sample holder with 7 rpm, Ga, Mn and As were deposited simultaneously on the already existing GaAs nanowires, resulting in the growth of a (Ga,Mn)As shell. The exact conditions for the respective shell growth runs are depicted in each section separately.

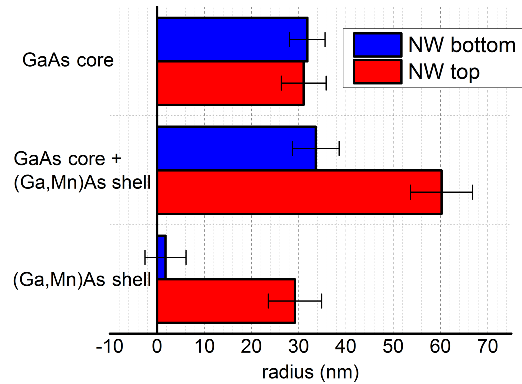

Figure 7.1.: Estimation of the (Ga,Mn)As shell thickness by subtracting the radii of sole GaAs nanowires used as a template from ones overgrown with a (Ga,Mn)As shell. Depositing an equivalent of a 150 nm 2D GaAs layer doped with Mn results in the formation of a (Ga,Mn)As shell of approximately 30 nm at the nanowire tip, whereas at the bottom shell growth is nearly fully suppressed. The error bars mark the standard deviation.

7.1. Strain and (Ga,Mn)As shell thickness

In thin film growth, due to the slightly elevated lattice constant of (Ga,Mn)As with respect to GaAs (see section 3.2.1), (Ga,Mn)As grows in the growth plane strained onto the GaAs substrate. Since no dislocations are observed at the growth interface, strain can be released in growth direction only, leading to an increased inter-atomic distance along the corresponding crystal axis. Hereby, the substrate, which typically has a thickness of some hundred µm, remains completely unaffected when being covered with tens of nanometer (Ga,Mn)As. In (Ga,Mn)As shell growth this may be different, since here the shell thickness is of the order of the core diameter. The strain relief between core and shell may occur here, additionally to the radial (Ga,Mn)As growth direction, along the nanowire axis, resulting in a widening of the core by the shell. This widening was already detected in other pseudomorphic growing core/shell nanowire systems like GaAs/InAs [167] and Ge/Si [168], which have a larger lattice mismatch than GaAs/(Ga,Mn)As. The strength of this widening depends strongly on the shell thickness, and if the shell thickness changes along a single nanowire drastically, the widening should also change along one single nanowire.

Thus in the following, the thickness of the (Ga,Mn)As shell along the nanowire axis is determined. This is done by subtracting the radii of sole GaAs core nanowires from the ones of GaAs/(Ga,Mn)As core/shell nanowires grown with the same core parameters. For this purpose, the untapered WZ optimized GaAs core nanowires with a radius of 30 nm were used. These core nanowires were then covered by a 2D equivalent layer of 150 nm height of GaAs doped with different Mn concentrations from 5 % to 10 %, grown at different temperatures in the range between 190°C and 210°C. To get a sufficient reliability for the mean radii on each sample, the radius at the nanowire top and at the nanowire bottom was estimated from at least twenty nanowires on all those samples. It

turned out, that the mean radii for the core/shell nanowires on all samples are comparable, and were determined to be in average 32 nm at the nanowire bottom and 60 nm at the tip. By subtracting these values from the ones of the untapered core (see fig. 7.1), the thickness of the (Ga,Mn)As shell is evaluated to be in average 30 nm at the nanowire tip and 2 nm at the bottom.

This huge discrepancy of the shell thickness along one nanowire can be again ascribed to the shadowing of the molecular fluxes by the nanowires in vicinity, like in the growth of AlGaAs shells (compare section 5.1.1). The value of 30 nm indicates, that the shell thickness at the tip is comparable to the nanowire radius, so in this region the (Ga,Mn)As crystal volume may even exceed the GaAs crystal volume, especially in the case of the WZ optimized core nanowires. Instead, ZB core nanowires are, due to the chosen growth conditions, inversely tapered and possess a larger radius at the nanowire tip, namely up to more than 55 nm. Thus, WZ core wires should offer less resistance against the force exerted to the crystal by the strained (Ga,Mn)As shell than ZB core wires, resulting in a widening of the GaAs lattice. At the nanowire bottom the situation is rather "thin-film-like", meaning a GaAs core, which dominates the (Ga,Mn)As shell crystal. Therefore, a change of the axial lattice constant of GaAs/(Ga,Mn)As core/shell nanowires due to the coverage of the GaAs core with a (Ga,Mn)As shell, should be rather observable in WZ than in ZB GaAs core/shell nanowires. If one investigates single nanowires, an increase of the axial lattice constant from the nanowire bottom to the top might be monitored.

Thus, in the following section, structural analyzes of the lattice constant along the nanowire axis are performed on GaAs/(Ga,Mn)As core/shell nanowires with predominantly WZ and ZB crystal structure, respectively, using XRD. The magnetic properties of the WZ and ZB (Ga,Mn)As shells are additionally evaluated with SQUID.

7.2. WZ and ZB (Ga,Mn)As shells in comparison

To compare GaAs/(Ga,Mn)As core/shell nanowires of predominantly ZB and WZ crystal structure, GaAs core nanowires of a comparable length were grown using the best parameters for both crystal phases evaluated in section 4.3, and overgrown with an equivalent (Ga,Mn)As shell.

For the growth of a smooth (Ga,Mn)As shell without MnAs precipitates, growth parameters determined by Rudolph [114] were used. The growth of the shell was performed at a temperature of 190°C using a Ga rate of 0.37 Å/s and a Mn rate of 0.02 Å/s, yielding a nominal Mn concentration in the (Ga,Mn)As shell of 5 %. At an As_4/(Ga+Mn) ratio of 1.5, a 2D equivalent layer of GaAs of 150 nm height was deposited, resulting in the in section 7.1 estimated shell thicknesses.

To determine whether the crystal lattice along the nanowire axis is affected, when the GaAs core is covered with a (Ga,Mn)As shell, both types of wires were examined with XRD. To evaluate the magnetic properties of the (Ga,Mn)As shells, SQUID measurements were conducted.

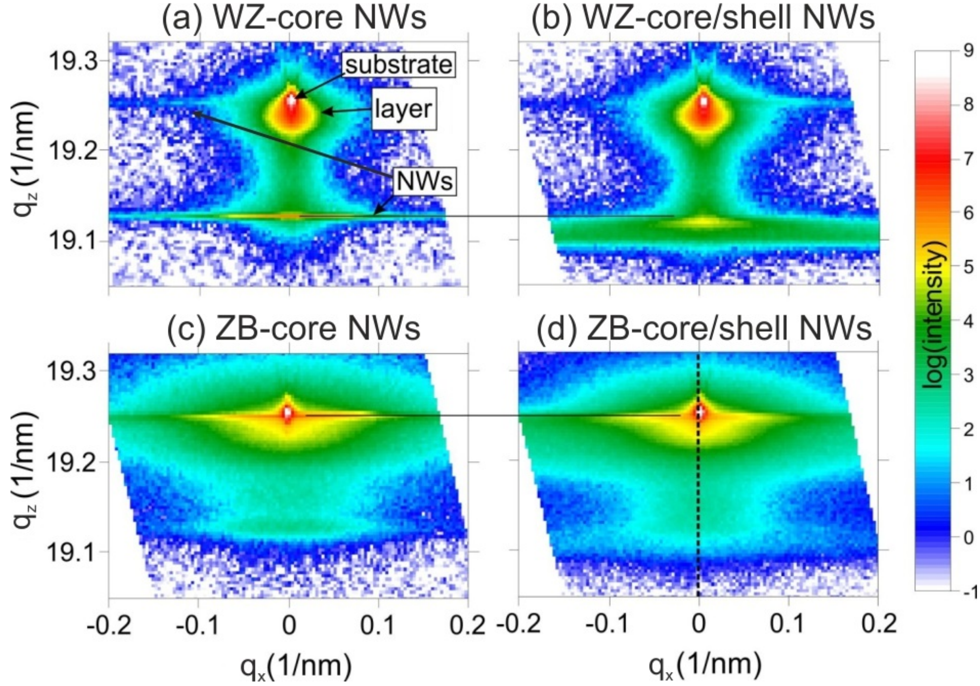

Figure 7.2.: Reciprocal space maps (RSMs) of four as-grown samples with optimized WZ and ZB crystal structure, respectively: (a) and (c) show the RSMs of sole GaAs core nanowires, (b) and (d) RSMs of wires additionally surrounded with a (Ga,Mn)As shell. q_z and q_x depict the projections of the scattered reciprocal space vector along the nanowire axis and parallel to the incoming X-ray beam, respectively.

7.2.1. Lattice relaxation: Reciprocal space mapping

As already pointed out in the previous section, in pseudomorphic growing core/shell structures, with the shells possessing a larger lattice constant than the core, strain relief takes place in radial and axial direction, resulting in a widening of the core nanowire. Since the lattice constant of (Ga,Mn)As is only slightly higher than the one of GaAs, we raise the question whether this is valid also for the system GaAs/(Ga,Mn)As.

To determine the lattice relaxation of the GaAs/(Ga,Mn)As nanowires along the nanowire axis, Θ-2Θ scans were conducted by A. Biermanns at the University of Siegen. Here, constructive interference of an X-ray beam is used to determine the distance of consecutive (111) or (0001) planes in reciprocal space. In fig. 7.2 reciprocal space maps (RSMs) of four as-grown samples, grown on GaAs(111)B substrates, are shown: pure GaAs wires with optimized WZ (fig. 7.2a) and ZB crystal structure (fig. 7.2c), as well as these two wire types covered with a (Ga,Mn)As shell (fig. 7.2b and fig. 7.2d).

In these figures, the intensity of the scattered beam is depicted in dependence of the reciprocal space vector along the nanowire axis, q_z, and along the projection of the incoming X-ray beam onto the sample, q_x. These RSMs are taken in the region of $q_x = 0$, meaning almost no scattering in forward direction, i.e. when Bragg's law

is fulfilled. The distance d of two subsequent GaAs layers in z direction then can be estimated via $d = 2\pi/q_z$, whereas for other crystal directions no statements can be made. For more information about the RSM method, see appendix A.3 .

In all four RSMs, three main features are determined: A very strong dot-like signal is surrounded by an elliptic signal, which is more pronounced in the RSMs of ZB core/shell nanowires than for WZ ones. Additionally, two stripe-like signals, which are broad in q_x-direction, but narrow in q_z-direction, are observed.

The dot-like signal with maximum intensity, labeled "substrate" in fig. 7.2a, is attributed to the substrate. It shows the GaAs(111) substrate reflex at $q_z = 19.256/\text{nm}$, which corresponds to a lattice spacing of 6.526 Å in (111) direction, and coincides well with the corresponding $2/\sqrt{3}$ of the ZB GaAs bulk lattice constant of 5.65 Å.

The elliptic signal in its vicinity, labeled "layer" in fig. 7.2a, probably stems from parasitic growth taking place on the GaAs(111)B substrate in-between the nanowires. This signal is visible in the RSMs with and without shell, and consequently must stem from structures originating during the GaAs core growth. Since the signal extends in q_z-direction, the forming structures apparently possess a slightly different lattice constant in z-direction than the substrate. This is reasonable for structures growing in-between the nanowires, since here growth conditions for a layer-by-layer growth are not necessarily given. When comparing the strength of the "layer" signal for the ZB samples with the WZ ones, we see a more pronounced signal in the ZB case. This occurrence can be explained with the different growth conditions of the core wires: to attain a comparable nanowire length, the overall deposited material is in the ZB case roughly twice as high as in the WZ case, meaning also an elevated structure growth in-between the nanowires on ZB samples. Thus, this elliptic signal can be ascribed to parasitic growth in-between the nanowires.

Finally, two stripe-like signals at $q_z = 19.255/\text{nm}$ and at roughly $q_z = 19.125/\text{nm}$, labeled "NWs" in fig. 7.2a, are visible. The elongation of the signal in q_x-direction means, that Bragg's law is fulfilled for a larger range of q_x-vectors around $q_x = 0$, i.e. for structures on the sample that may be slightly bent. This is the case for the nanowires only, which bend easily due to their high aspect ratio. Thus, a separation of the nanowire signal from the substrate and the layer part is easily possible, when considering the scattered intensity at q_x-values different from zero.

In fig. 7.2a the RSM of solely GaAs core nanowires, grown at WZ optimized conditions, is shown. Here, the main nanowire signal is located at $q_z = 19.125/\text{nm}$, and only slight traces are visible at $q_z = 19.255/\text{nm}$. The signal at $q_z = 19.125/\text{nm}$ corresponds to a lattice constant of 6.571 Å, which is attributed to the WZ lattice spacing along the nanowire axis, i.e. along the [0001] direction, since this value deviates hardly from the literature value of 6.564 Å, determined for 3D WZ GaAs produced by a thermal and pressure treatment [48]. The slight signal at $q_z = 19.255/\text{nm}$, which is close to the substrate peak at $q_z = 19.256/\text{nm}$, is ascribed to a sparse amount of ZB segments in WZ dominated nanowires.

The RSM of GaAs core nanowires, grown at the best conditions for ZB crystal structure nucleation, is depicted in fig. 7.2c. Here, the signal strength dependence is vice versa:

at $q_z = 19.255$/nm the strongest NW signal is detected, whereas at $q_z = 19.125$/nm only a weak one is visible, indicating a dominating ZB crystal structure in the wires over the WZ one.

The RSMs of samples with WZ and ZB GaAs cores, which are additionally covered with a (Ga,Mn)As shell, are shown in figs. 7.2b and 7.2d. In the case of WZ GaAs/(Ga,Mn)As core/shell nanowires (fig. 7.2b), the WZ peak shifts to lower q_z-values and widens, whereas all other characteristics, including the peak attributed to the sparse ZB segments, remain at the same q_z-values. The same phenomenon is observed in the RSM of ZB GaAs/(Ga,Mn)As core/shell nanowires (fig. 7.2d): the q_z-value of the ZB nanowire crystal stays at 19.255/nm, whereas the weak signal from the WZ segments seems to shift to lower q_z-values and to widen.

Considering solely the main crystal structure in each kind of nanowire would confirm the statement made in section 7.1: WZ GaAs core wires, which have a smaller diameter than the ZB ones, get more likely strained along the nanowire axis by the (Ga,Mn)As shell than the ZB wires. The decrease of q_z in the WZ core/shell wires with respect to the WZ core wires can be explained with the tensile strain exerted by the shell on the core. Instead, the coincident widening of the signal can be attributed to the increasing shell thickness towards the wire tip, leading to a hardly affected WZ GaAs lattice constant at the bottom and to at most strained GaAs at the tip. The latter case would then correspond to the lowest q_z-value of the widened signal, $q_z = 19.090$/nm, i.e. $c = 6.583$ Å, meaning a widening of the WZ GaAs lattice in axial direction by 0.18 %. In ZB wires, no detectable tensile strain is mediated by the shell to the core, probably since the GaAs core possesses a too large volume for the shell to exert a sufficient force on the core.

Surprisingly, for both crystal structures, the lattice constant of the less frequent crystal phase does not behave like the main crystal phase. This may be explained by considering where such ZB(WZ) segments are most likely found in WZ(ZB) nanowires. For nanowires with predominantly ZB structure, the WZ segments form at the nanowire tip due to the consumption of the catalyst droplet (compare section 4.3.2). Since the shell thickness is largest at the tip, mostly these WZ segments in the predominantly ZB nanowires will be strained along the nanowire axis by the (Ga,Mn)As shell. This can be monitored in fig. 7.2d by the down shift of the WZ-related q_z-value, whereas the ZB-related one remains at 19.255/nm. In the other case, ZB segments in predominantly WZ wires mostly form at the nanowire bottom in vicinity of the substrate due to the building-up of the liquid catalyst droplet. Since here almost no material adheres during shell growth, the ZB segments in the predominantly WZ wires remain completely unaffected concerning strain, leading in fig. 7.2b to an unchanged q_z-value at 19.255/nm.

7.2.2. Magnetic properties

The magnetic properties of the ZB and WZ GaAs/(Ga,Mn)As core/shell nanowires were extracted from nanowire ensemble measurements in SQUID, conducted by F. Schiller at the chair of Prof. Back. Here, pieces from the same samples were used as for the RSM

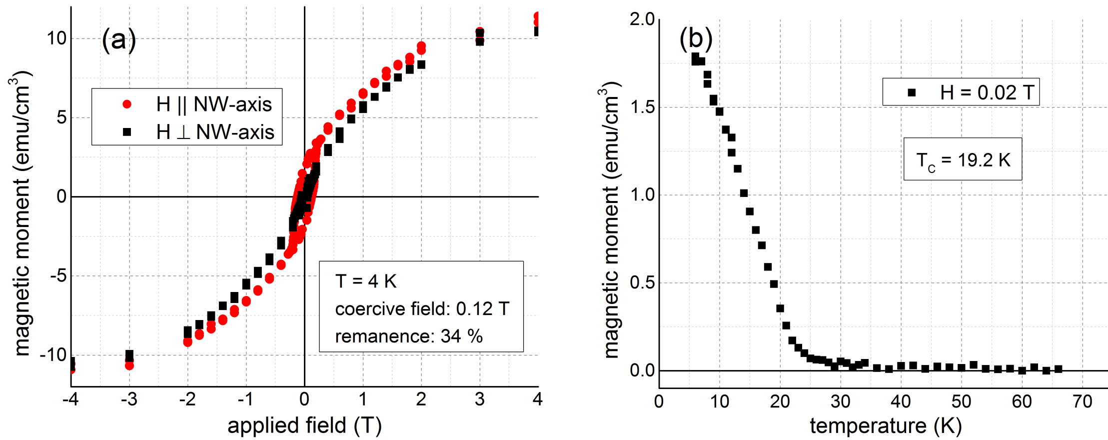

Figure 7.3.: (a) M(H) curves of (Ga,Mn)As shells with predominantly ZB crystal structure, measured at 4 K: In parallel configuration a slight hysteresis is visible, indicating a magnetic easy axis with a remanence of 34 % compared to the value at 4 T and a coercive field strength of 0.12 T. The zero-crossing in perpendicular configuration indicates a magnetic hard axis. (b) The corresponding M(T) curve in parallel configuration reveals ferromagnetism for temperatures below 19.2 K.

measurements. Due to the usage of these as-grown samples, also an eventually growing (Ga,Mn)As layer in-between the nanowires might contribute to the magnetic signal. However, the growth rate of the shell at the nanowire bottom is quite low (compare section 7.1), and this layer growth is negligible. Thus, the recorded ferromagnetic signal is ascribed to the WZ or ZB (Ga,Mn)As shells only.

To compare the magnetic behavior in dependence on the crystal structure, the magnetization was measured in dependence on the applied magnetic field (M(H) curves) at $T = 4$ K. M(H) curves were recorded for magnetic field directions parallel and perpendicular to the nanowire axis, since here the magnetic easy and magnetic hard axes were expected [19]. Additionally, temperature-dependent curves of the magnetization (M(T) curves) were recorded to determine the Curie temperatures of both samples. To do that, a small external magnetic field of 0.02 T was applied along the nanowire axis to align all spins in the same direction. In all below presented curves, the diamagnetism stemming from the GaAs substrate and the GaAs nanowires is already subtracted, so only the magnetic behavior of the (Ga,Mn)As shells is depicted.

In fig. 7.3a, the M(H) curves of core/shell nanowires with predominantly ZB crystal structure are shown. In perpendicular configuration (black), no hysteresis is observed, indicating a magnetic hard axis. In parallel configuration (red), a low marked hysteresis is visible, suggesting a magnetic easy axis. Here, a coercive field of 0.12 T and a remanence of 34 %, compared to the magnetic moment measured at $H = 4$ T, is observed. The M(T) curve of this sample, depicted in fig. 7.3b, reveals a ferromagnetic behavior up to the Curie temperature of 19.2 K, indicated by the turning point of the curve.

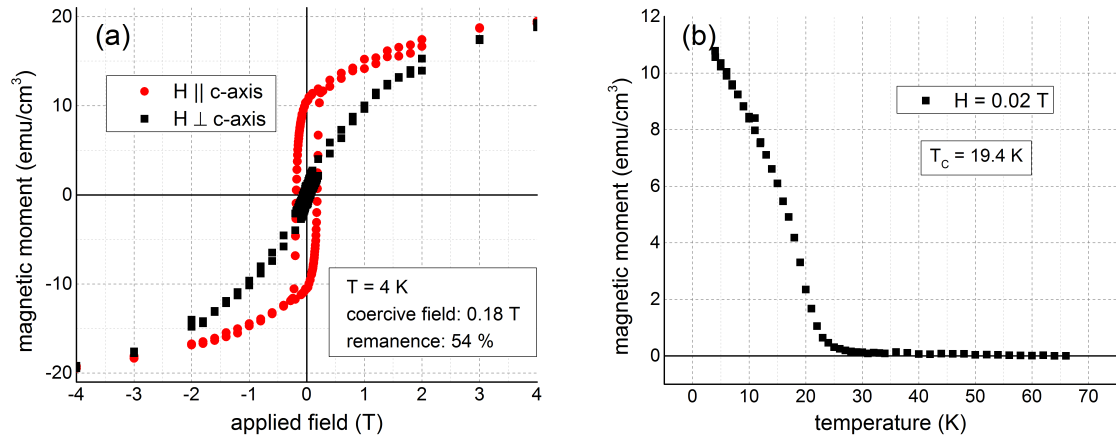

Figure 7.4.: (a) M(H) curves of (Ga,Mn)As shells with predominantly WZ crystal structure, measured at 4 K: A pronounced hysteresis in the parallel configuration is visible (magnetic easy axis), whereas none is observed in perpendicular configuration (magnetic hard axis). The remanence along the magnetic easy axis is 54 % compared to the value at 4 T, while the coercive field is 0.18 T. (b) The corresponding M(T) curve in parallel configuration reveals ferromagnetism for temperatures below 19.4 K.

In the case of predominantly WZ (Ga,Mn)As shells, the magnetic behavior changes slightly (fig. 7.4a). Here, the magnetic easy axis also points along the nanowire, but has a much more pronounced hysteresis than in the ZB case. The remanence and also the coercive field strength of 54 % and 0.18 T, respectively, are higher than for the ZB phase. In perpendicular configuration, i.e. along the magnetic hard axis, no difference to the ZB wires is visible. The Curie temperature of 19.4 K, determined from the M(T) curve in fig. 7.4b is only slightly higher than the one evaluated for wires with ZB crystal structure.

Both crystal structures confirm the uniaxial magnetic behavior estimated by Rudolph et al. [19] with a magnetic easy axis along the nanowire axis and a magnetic hard axis perpendicular the the nanowire axis. Along the magnetic easy axis, both M(H) measurements do not exhibit the typical square hysteresis behavior, but possess a rounded shape for magnetic fields in the range of 1-4 T. Here, the continuously increasing magnetic moment can be attributed to the alignment of anti-ferromagnetic coupling Mn_I [169], or the alignment of non-ferromagnetic interacting domains in general. This is much more pronounced in the ZB case than in the WZ one, quantified via the remanence values of 34 % and 54 %, and therefore indicates an enhanced Mn_{Ga} incorporation in WZ (Ga,Mn)As. The total magnetic moment, which is in WZ (Ga,Mn)As by a factor of two enhanced with respect to ZB (Ga,Mn)As, confirms this. Thus, the finding of an equal Curie temperature for both types of (Ga,Mn)As crystals may be rather unexpected. However, the Curie temperature of (Ga,Mn)As depends in the Zener model besides the density of ferromagnetic coupling Mn atoms also on the hole density and the band structure,

which is completely unknown for WZ (Ga,Mn)As at the semiconductor-metal transition. Thus, many factors, like an enhanced incorporation of impurities or a generally lower hole mobility in WZ (Ga,Mn)As, can account for the equal Curie temperatures of both (Ga,Mn)As phases.

However, the Curie temperature of 19 K observed for both phase is by far lower than the ones obtained in 2D thin film growth of ZB (Ga,Mn)As on comparable crystal faces [115]. This indicates that at least the crystalline quality of the ZB (Ga,Mn)As shell is reduced compared to 2D thin films. As already mentioned by others [113, 114], this observation can be ascribed to the segregation of Mn atoms into stripes along the corners of the side facets, promoting the incorporation of anti-ferromagnetic coupling and hole-compensating Mn interstitials, or an enhanced incorporation of hole-compensating As anti-sites in the (Ga,Mn)As shell. In WZ (Ga,Mn)As shells, even above mentioned crystal structure related effects may decrease the observed Curie temperatures.

7.2.3. Conclusion

The structural and magnetic findings from XRD- and SQUID-measurements on GaAs/-(Ga,Mn)As core/shell nanowires reveal different properties for wires with predominantly WZ and ZB crystal structure.

The coverage of the GaAs core with a (Ga,Mn)As shell leads to an in axial direction tensile strained WZ core, but does not affect the ZB core. This was explained by different volume ratios of core and shell in dependence on the crystal structure. Rather thick ZB cores inhibit the shell from exerting a sufficient force to strain the core, whereas rather thin WZ cores get more easily strained by the (Ga,Mn)As shell.

SQUID measurements reveal an enhanced magnetic moment for WZ (Ga,Mn)As shells compared to ZB shells, and thus an elevated incorporation of ferromagnetic coupling Mn_{Ga}, but a reduced density of Mn_{I} in WZ (Ga,Mn)As. Nevertheless, an equal Curie temperature of 19 K was observed for both (Ga,Mn)As phases. This value is not comparable to the Curie temperatures of 65 K - 75 K, estimated on comparable 2D (Ga,Mn)As thin films, and was explained with the increased introduction of crystal defects during the growth of (Ga,Mn)As shells [113, 114]. The occurrence of a magnetic easy axis along the nanowire and a magnetic hard axis perpendicular to the wire axis for both crystal phases confirms the finding of a uniaxial magnetic anisotropy in GaAs/(Ga,Mn)As core/shell nanowires [19]. Due to the observations in XRD with a fully compressive strained ZB (Ga,Mn)As shell and a slightly relaxed WZ (Ga,Mn)As shell along the wire axis, the magnetic easy axes for ZB and WZ GaAs/(Ga,Mn)As wires can be ascribed to this pseudomorphic growth, as expected previously [19, 20].

To get a further insight of the WZ core/shell system, the growth of WZ (Ga,Mn)As shells around the core was optimized.

7.3. WZ (Ga,Mn)As shells: Different Mn concentrations

Outgoing from the initial growth parameters of the (Ga,Mn)As shells in section 7.2, the growth of the WZ (Ga,Mn)As shell was optimized. This was done to obtain a better crystalline structure, i.e. a reduced incorporation of anti-ferromagnetic coupling and hole-compensating Mn interstitials (Mn_I) and As anti-sites (As_{Ga}), whereas the incorporation of ferromagnetic coupling Mn atoms on Ga sites (Mn_{Ga}) is enhanced. The optimization was performed for three different nominal Mn concentrations by tuning the MBE growth parameters, described in section 7.3.1. Additionally, to improve the crystalline structure of these as-grown wires by removing Mn_I ofter growth, some wires were annealed. To evaluate the respective Curie temperatures and the ferromagnetic state, single as-grown and annealed wires of all three nominal Mn concentrations were characterized in temperature-dependent transport (R(T)) measurements (section 7.3.2). Their magnetic characteristics were determined in magnetotransport (R(H) measurements) (section 7.3.3). The R(T) and R(H) measurements on single wires were conducted by Christian Butschkow in a cryostat at the chair of Prof. Weiss, which enables temperatures down to 1.7 K and external magnetic fields up to 10 T.

7.3.1. Growth

As introduced in section 3.2.1, the quality of the (Ga,Mn)As shell depends, besides the crystalline quality of the substrate, i.e. the GaAs core nanowires, on the growth conditions of the shell. These conditions affect the introduction of impurities in the GaAs host crystal: desired Mn atoms on Ga sites (Mn_{Ga}), but also Mn interstitial defects (Mn_I), As anti-sites (As_{Ga}), and also MnAs clusters.

Generally, an elevation of the growth temperature reduces the incorporation of Mn_I and As_{Ga}, but also increases the possibility to form MnAs precipitates. The precipitation of MnAs at high temperatures is inhibited by applying high As_4 BEPs. However, a high As_4 BEP leads also to an elevated concentration of As_{Ga} defects. Also, a reduction of the nominal Mn concentration c_{Mn} decreases the probability to form of MnAs precipitates and Mn_I, but also reduces the concentration of ferromagnetic coupling Mn_{Ga}.

Due to this non-trivial behaviors, we fixed the As_4/(Ga+Mn) ratio to the relatively low value of 1.5 to optimize the Mn_{Ga} content for three different nominal Mn concentrations in the WZ (Ga,Mn)As shell. To do that, for c_{Mn} of 5 %, 7.5 % and 10 % the maximum growth temperature was sought, which is hereby defined by the temperature above that MnAs cluster formation is observed. This method should result in the introduction of a low concentration of As_{Ga} in the shell (mediated by the low As_4/(Ga+Mn) ratio), whereas for different c_{Mn} the relation of Mn_{Ga} and Mn_I is optimized (by maximizing the growth temperature).

Performing this scheme in steps of 10°C for the three different Mn concentrations yielded a maximum growth temperature of 200°C for each c_{Mn}. This finding indicates that for Mn concentrations between 5 % and 10 % the growth of a smooth (Ga,Mn)As shell is hardly dependent on the Mn flux.

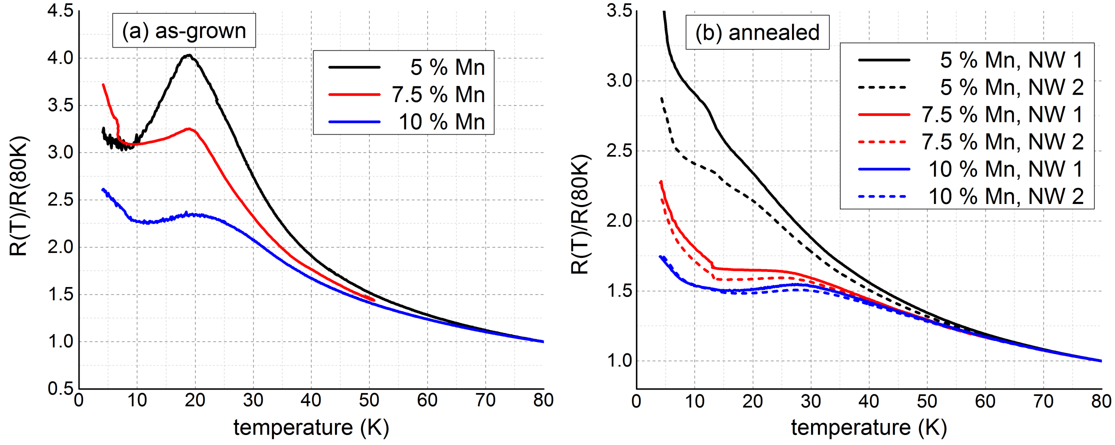

Figure 7.5.: R(T) measurements of single GaAs/(Ga,Mn)As core/shell nanowires nominally doped with 5 %, 7.5 % and 10 % Mn: Both, the as-grown (a) and annealed wires (b), show an increased metallic behavior with an elevated nominal Mn concentration. The Curie temperatures, determined by the turning points below the shoulder behavior in R(T), are summarized in table 7.1. For a better comparability between the wires, the resistance is normalized on R(T=80 K).

In the following, transport and magnetotransport measurements on single core/shell wires are presented, which reveal the Curie temperature and the magnetic anisotropies of the optimized WZ GaAs/(Ga,Mn)As wires.

7.3.2. Curie temperature determination

After removing the wires from the substrate and contacting them with electron-beam lithography, temperature-dependent resistance measurements were conducted. This was done on single as-grown GaAs/(Ga,Mn)As core/shell wires as well as on annealed ones, which rested at 190°C for 9 h in ambient air. The ferromagnetic/non-magnetic state transition was examined with a method following Novak et al. [170]. They ascribe the Curie temperature T_C to an inflection point in the R(T) curve, which appears at a temperature below an occurring shoulder.

The R(T) curves of the as-grown and annealed wires are shown in fig. 7.5a and 7.5b, respectively. For each nominal Mn concentration, one contacted as-grown wire was monitored in the relevant temperature range between 4 K and 80 K, while two annealed wires were investigated. The maximum resistance values of the as-grown wires reside within the order of 10^5 Ω, while the annealed ones possess a resistance maximum one magnitude below, already indicating an enhanced crystal quality after annealing. For a better comparability between the different wires, each resistance curve was normalized on the value measured at 80 K.

All R(T) curves show a more or less pronounced state transition, indicated by the

c_{Mn}	annealed	T_C
5 %	-	17 K
7.5 %	-	17 K
10 %	-	17 K
5 %	✓	19 K
7.5 %	✓	22 K
10 %	✓	25 K

Table 7.1.: Curie temperatures (T_C) deduced from the R(T) curves of single as-grown and annealed WZ GaAs/(Ga,Mn)As core/shell nanowires in figs. 7.5.

shoulder between 20 K and 30 K. Additionally, a reduced increase of the relative resistance is monitored for an increasing c_{Mn}, which points to a shift towards the metallic side of the metal-insulator transition. The Curie temperatures, determined by evaluating the inflection points of the curvatures, are summarized in table 7.1. Surprisingly, all as-grown wires exhibit the same Curie temperatures of 17 K. This value is slightly below 19 K, estimated on the nanowire ensemble with $c_{Mn} = 5$ % by SQUID in section 7.2.2, and also below the 20 K measured on comparable core/shell wires by Rudolph et al. [19]. However, the Curie temperatures lie within the error margin, when comparing values, which were determined with SQUID and R(T) measurements. Values of the Curie temperature, which were obtained by transport exhibit a error margin of ±1 K only [116]. Thus, the measured increase of T_C after annealing to 19 K, 22 K and 25 K for $c_{Mn} = 5$ %, 7.5 % and 10 %, respectively, is reliable.

The occurrence of equal Curie temperatures in the as-grown wires may be ascribed to the equal growth conditions for all (Ga,Mn)As shells, leading to a comparable crystalline quality. Seemingly, this quality does not depend on the nominal Mn concentration. The crystalline quality is slightly improved by annealing, reflected by the increased Curie temperatures of up to 25 K, as Mn_I are the only removable crystal defects in the chose annealing procedure. However, all measured Curie temperatures (as-grown and annealed) are by far lower than the ones observed in 2D (Ga,Mn)As growth on equivalent zinc-blende surfaces [115]. The reduced Curie temperatures are most probably ascribed to an enhanced introduction of crystal defects during WZ (Ga,Mn)As shell growth, although crystal phase-related properties of the WZ (Ga,Mn)As, like a reduced hole mobility, might also forbid comparable values of T_C.

7.3.3. Magnetotransport measurements

For magnetotransport measurements, the same wires were used as for the R(T) measurements. To determine the magnetic anisotropy of the (Ga,Mn)As shell, an external magnetic field was applied in the nanowire plane enclosing different angles with the nanowire axis. Since the magnetic anisotropy was found to be uniaxial, it is sufficient to restrict to these directions only, i.e. parallel and perpendicular to the nanowire axis. In

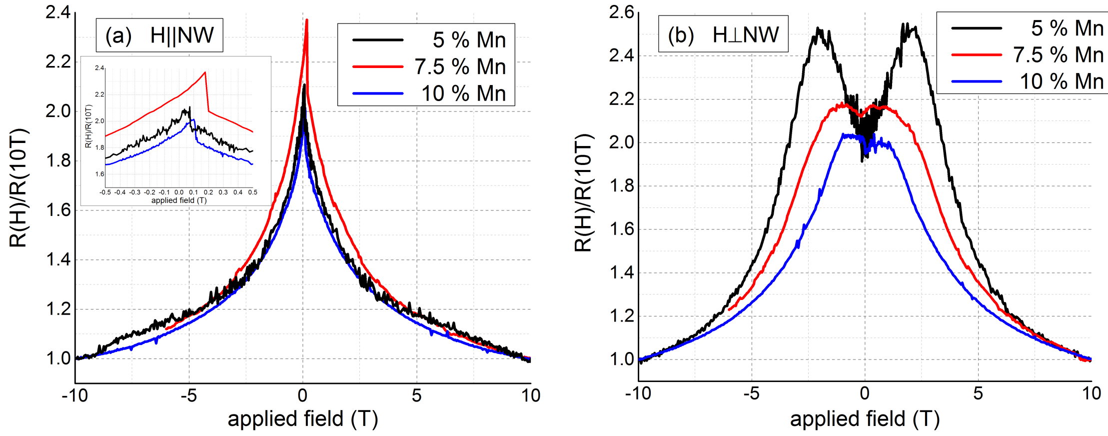

Figure 7.6.: Magnetoresistance curves of single as-grown nanowires with different nominal Mn concentrations for the magnetic field applied (a) parallel and (b) perpendicular to the nanowire axis (the measured resistances are normalized to the values measured at 10 T): (a) A pronounced NMR is observed independent on the Mn concentration, together with a discontinuity at a coercive field strength of 0.07 T − 0.18 T, see inset, indicating a magnetic easy direction. (b) A double peak behavior with a decreasing anisotropy field strength for an increasing Mn concentration reveals a strong NMR behavior along a magnetic hard axis.

figs. 7.6 these R(H) curves are shown for magnetic field sweeps at T = 4 K from −10 T to 10 T, normalized on the values measured at $H = 10$ T. Here, solely measurements on as-grown wires are described.

The behavior of the magnetoresistance (MR), determined in parallel configuration, is depicted in fig. 7.6a. During the sweep of the external magnetic field strength from -10 T to small positive values the MR increases, and then drops instantaneously to a finite value. For a further elevation of the external magnetic field, the MR continuously decreases. Additionally, the relative resistance change in the external magnetic field is independent on c_{Mn}, proving the same physical mechanism in the three wires. For nearly all ranges, the magnetoresistance reduces with an increase of the external field, which can be ascribed to a strong negative magnetoresistance behavior (NMR). The observed magnetoresistances are highest at coercive field strengths of 0.07 T to 0.18 T, and leap for a small elevation of the external magnetic field to a lower value. This instantaneous resistance change is specific for a magnetic easy axis, when the magnetization reverses its sign. Therefore, the magnetoresistance curves depicted in fig. 7.6a are attributed to a dominating NMR behavior along a magnetic easy axis.

The behavior of the magnetoresistance, when the magnetic field is applied perpendicular to the nanowire axis, is depicted in fig. 7.6b. Now, a symmetric and continuous course of the R(H) curves with a double peak behavior is recognizable, decreasing in its characteristic with elevating Mn concentration. In the following, the generally observed behavior of the (Ga,Mn)As shells is described on the basis of the WZ (Ga,Mn)As shell

with 5 % Mn. For large external magnetic fields, the resistance decreases with an increase of the external magnetic field, i.e. a NMR behavior is observed again. Instead, for low magnetic fields between -2 T and 2 T, a double peak is monitored. This occurrence can be explained with a continuously rotation of the magnetization from a parallel alignment with the external magnetic field above the anisotropy field strength of $|H_A| = 2$ T to an alignment along the magnetic easy axis at $H_0 = 0$ T, i.e. parallel to the wire axis. Consequently, the monitored magnetoresistance behavior can be ascribed to a strong NMR behavior along a magnetic hard axis.

However, the anisotropy field strength and the characteristic of the double peak reduces with an increasing Mn concentration in the (Ga,Mn)As shell. The reduction of both features was also detected after annealing (not shown), confirming the findings by Eckrot [127]. As the anisotropy field strength H_A depends strongly on uniaxial anisotropy constant K_U and the saturation magnetization M_S ($H_A = 2K_U/(\mu_0 M_S)$), both properties can account for the observed reduced anisotropy field. The enhancement of the saturation magnetization via an increased nominal Mn concentration or annealing (by removing anti-ferromagnetic coupling Mn interstitials) seems reasonable and therefore can account for the reduced anisotropy field strength. Additionally, in the Zener-model magnetic anisotropies are very sensitive to the relative occupation of the various hole subbands [111]. Therefore, a redistribution of charge carriers due to annealing or an increase of the Mn concentration can lead to reorientations of the magnetic anisotropy, and thus can alter H_A via differently shaped anisotropy constants.

7.3.4. Conclusion

In this section, first the growth of WZ (Ga,Mn)As shells with different c_{Mn} around WZ GaAs core nanowires was optimized. This was done by maximizing the growth temperature at a chosen low As_4/(Ga+Mn) ratio to reduce the introduction of Mn_I and As_{Ga}, while the incorporation of ferromagnetically coupling Mn_{Ga} was enhanced. It turned out, that the optimum growth conditions of T = 200°C for an As_4/(Ga+Mn) ratio of 1.5 are independent of c_{Mn} between concentrations of 5 % and 10 %.

The as-grown Curie temperatures of 17 K, deduced from single wires in R(T) measurements, are comparable to the 19 K estimated in SQUID. Surprisingly, T_C is equivalent for all measured wires and independent on c_{Mn}. After reducing the amount of Mn_I in an annealing step, the Curie temperatures increase at most by 8 K. All these Curie temperatures are far below the ones obtained in thin film growth of (Ga,Mn)As on the equivalent ZB surfaces [115], indicating a low crystalline quality of the WZ shells.

Magnetotransport measurements reveal a dominating negative magnetoresistance behavior in GaAs/(Ga,Mn)As core/shell nanowires, confirming previous studies [20]. In WZ shells, a magnetic easy axis is detected along the nanowire axis, independent of the Mn concentration. Perpendicularly to the wire axis, a magnetic hard axis behavior is observed. The anisotropy field strength decreases for an elevated Mn concentration in the shell and after annealing. This phenomenon stems most probably from a carrier density dependent magnetic anisotropy in WZ (Ga,Mn)As, as found in ZB (Ga,Mn)As [111].

8. MnAs segments in GaAs nanowires

In this chapter a different attempt is made to introduce Mn spins into GaAs nanowires. MnAs, which is a room temperature ferromagnet, can be used besides (Ga,Mn)As as a spin injector or detector in GaAs heterostructures [94, 171]. Therefore, the integration of MnAs in GaAs nanowires would be desirable. This was already realized in the form of MnAs shells on GaAs nanowires, growing MnAs in LT MBE on already existing GaAs nanowires [172, 173]. Opposed to the growth of a continuous shell around the GaAs nanowire, here we focus on the growth of single nanoscale MnAs segments in GaAs nanowires.

It is well known from 2D (Ga,Mn)As layer growth, that when the growth temperature is increased beyond a critical value, Mn dilutes not only in the GaAs lattice, but also precipitates in the form of MnAs nanoscale clusters [18]. Additionally, the growth of GaAs nanowires via the VLS mechanism works only in a temperature range above this value. Thus, on the one hand, the growth of ferromagnetic (Ga,Mn)As nanowires seems not possible [174, 175]. On the other hand, MnAs clusters might originate inside the GaAs nanowires, if one performs the growth of GaAs nanowires under Mn supply.

GaAs nanowire growth under the supply of Mn is examined in section 8.1. On the basis of the obtained results, a method for the epitaxial growth of single ferromagnetic MnAs segments in GaAs nanowires is detected (section 8.2). It is shown that this method can be extended for the subsequent growth of single MnAs clusters, which might be used as spin injection and detection contacts. Finally, a regime for the growth of multiple MnAs nanoclusters onto GaAs nanowires in one run is described.

The nanowires introduced in this chapter were grown with the Ga-catalyzed growth method, using Si(111) wafers covered with a thin layer of native oxide as a substrate. The growth temperature was set to 600°C for all the experiments. The used Mn beam equivalent pressure (BEP) was throughout set to $2 \cdot 10^{-9}$ Torr, which corresponds to a two-dimensional equivalent growth rate of 0.043 Å/s, while the applied Ga rate was 0.4 Å/s to attain a Mn concentration of 7.5 %. An As_4 BEP of $6.5 \cdot 10^{-7}$ Torr was chosen to yield a Ga excess at the growth front, corresponding to a global As_4/(Ga+Mn) ratio of 1.5.

8.1. GaAs:Mn nanowire growth

To test whether either magnetic (Ga,Mn)As or MnAs segments in GaAs nanowires can be obtained, the growth of GaAs nanowires under the supply of Mn is examined. Energy-dispersive X-ray spectroscopy (EDX), micro-photoluminescence (µPL), and transmission

electron microscopy (TEM) measurements reveal the pathways of the Mn atoms, which are discussed using the binary phase diagrams relevant for the respective materials.

The first approach to grow ferromagnetic Mn containing segments in GaAs nanowires was the following: First, a regular GaAs nanowire stub of 300 nm height was grown. During the residual nanowire growth, additionally the Mn cell was opened, intending to form ferromagnetic (Ga,Mn)As or MnAs clusters in the upper part of the wire. The nanowire growth was terminated by closing all cells simultaneously and cooling down to RT, which results in the solidification of the catalyst droplet.

Fig. 8.1a shows a bright field scanning TEM image of a wire grown by this procedure. The overall length of the nanowire is roughly 1.6 µm, equal to GaAs nanowires grown without Mn supply at the very same conditions. Seemingly, the additionally introduced Mn atoms do not inhibit the VLS growth mechanism of the nanowires. Furthermore, the nanowire side facets are well shaped and smooth $\{1\bar{1}0\}$ ones, equivalent to GaAs nanowires grown without Mn supply. This observation suggests that no larger foreign crystal phases exist within the nanowire, which extend to the nanowire side facets and alter the side facet orientation. This statement is confirmed in HRTEM: the crystal structure of the whole wire is determined to be mixed wurtzite (WZ) and zinc-blende (ZB) GaAs (not shown), which rules out the presence of MnAs precipitates or Ga_xMn_y compounds. Solely the solidified catalyst droplet deviates from GaAs nanowires wires grown without Mn supply: Usually, during cooling down, the Ga droplet solidifies in an amorphous sphere, adopting the liquid equilibrium shape. But in fig. 8.1a, the solidified catalyst possesses mainly facets, indicating a crystalline structure, whereas only a small part remains spherical.

To determine the chemical composition of the wire, it was entirely mapped with EDX. The local emerging Kα lines of the elements Ga, As and Mn are depicted in the colored intensity maps of figs. 8.1b, 8.1c and 8.1d, respectively. The wire consists solely of Ga and As up to the catalyst droplet, and is not doped with Mn up to the resolution limit of the EDX, which excludes the growth of a magnetic (Ga,Mn)As crystal [98]. Conversely, a large amount of Mn is found in the solidified catalyst droplet, apparently collected in the liquid Ga during growth. Here, As is almost completely absent.

A different method to prove whether Mn exists in the GaAs wires is to analyze the optical spectrum emitted from the wires. Mn atoms, incorporated at interstitial positions (Mn_I), act as non-radiative recombination centers and therefore quench the PL signal. Instead, Mn atoms at Ga sites (Mn_{Ga}) allow radiative recombination via its acceptor level 113 meV above the valence band edge and lead to an emission line at an energy of 1.41 eV [176]. To detect whether a low amount of Mn atoms exists within GaAs nanowires grown under the supply of Mn, µPL measurements on single nanowires were performed. A typical emission spectrum is shown in fig. 8.2a. We observe a dominant peak at 1.46 eV, attributed to indirect carrier recombination at WZ/ZB GaAs interfaces in the type II band structure, that proves the excellent crystalline quality of a GaAs nanowire without Mn_I. Additionally to this redshifted spectrum away from the GaAs band gap(s), a slight shoulder appears at 1.409 eV, indicating a very low concentration of Mn_{Ga}. The existence of Mn_{Ga} in the wire, whereas Mn_I are absent is explained by

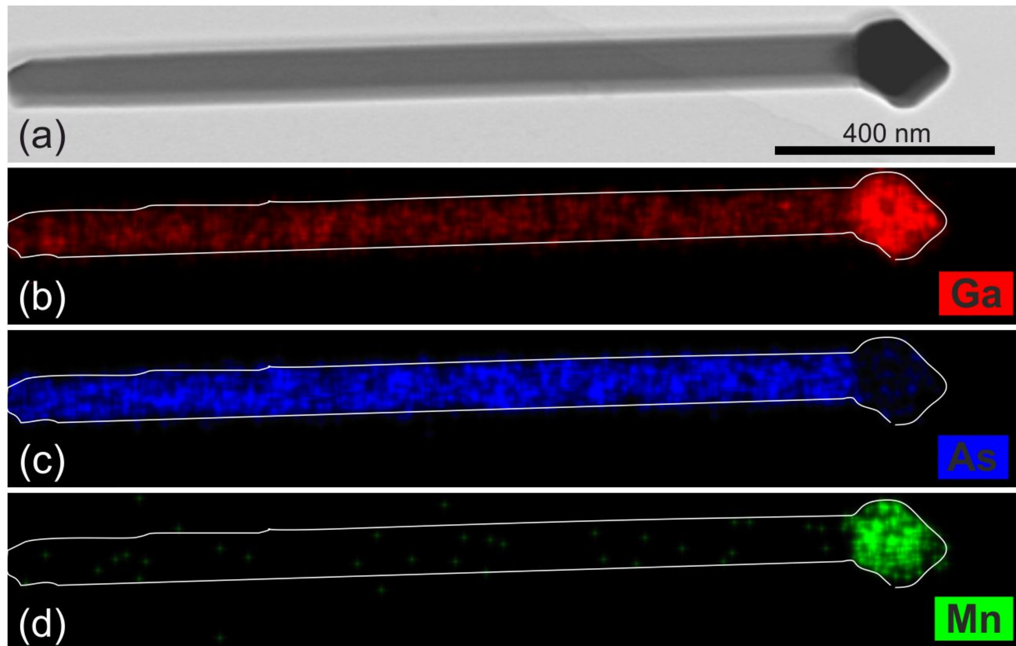

Figure 8.1.: EDX-mapping of a single nanowire grown under the supply of Mn: (a) Bright field STEM image. (b,c,d) Spatial distribution of the elements Ga, As and Mn: Mn is detected in the catalyst at the nanowire tip, while the wire consists only of Ga and As.

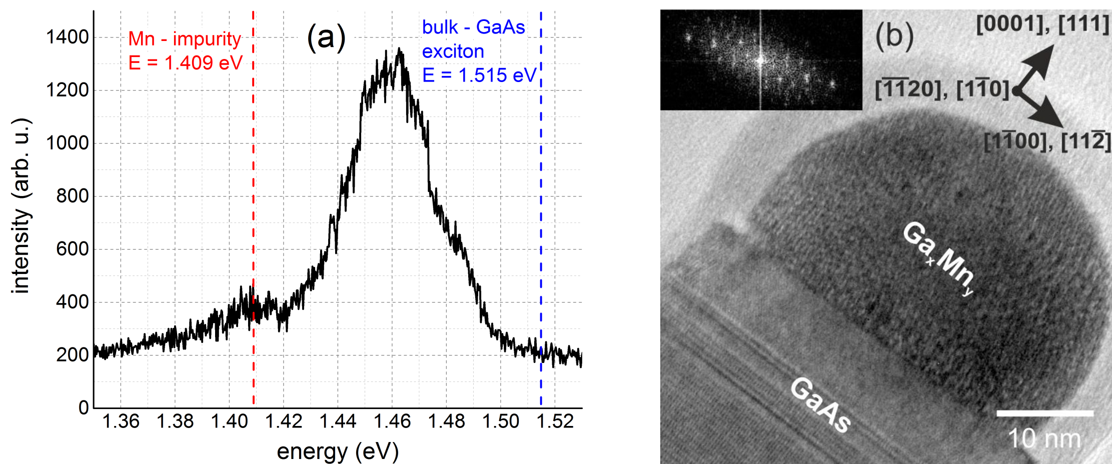

Figure 8.2.: (a) Photoluminescence spectrum of a single nanowire measured at 4 K: Besides the redshifted spectrum stemming from transitions at WZ/ZB interfaces due to the staggered band alignment, a slight shoulder appears at 1.409 eV. This shoulder can be ascribed to isolated Mn atoms residing at Ga sites (b) HRTEM image and the corresponding FFT of a solidified Ga-Mn alloy at the tip of a nanowire: at room temperature, the Ga_xMn_y phase(s) are crystalline.

the low equilibrium solubility of Mn in GaAs, $c_{\mathrm{Mn,GaAs}} < 0.1$ % [98]: at low Mn doping concentrations < 1.5 %, $\mathrm{Mn_{Ga}}$ have a lower formation energy than $\mathrm{Mn_I}$. Similar results were obtained by Sadowski et al. [175, 177] in GaAs nanowires grown at comparable conditions, who determined in PL a Mn doping level of less than 0.01 %.

After cooling down the wires to RT, at the nanowire tips solid $\mathrm{Ga}_x\mathrm{Mn}_y$ phases appear. This can be easily seen in the HRTEM in fig. 8.2b, where a half-sphere of crystalline $\mathrm{Ga}_x\mathrm{Mn}_y$ is epitaxied on the GaAs(111) top facet of the GaAs nanowire underneath. To determine why Mn agglomerates in the liquid Ga catalyst droplet and forms after cooling down to RT different solid $\mathrm{Ga}_x\mathrm{Mn}_y$ phases at the nanowire tips, we consider the corresponding phase diagrams. The states of the liquid droplet during the whole growth would be described by the ternary As-Ga-Mn phase diagram, which is however non-existent. Thus, in the following we neglect As to reduce the problem to the Ga-Mn binary phase diagram (appendix B fig. B.3). This may be justified for two reasons. First, the solubility of As in liquid Ga at growth temperature is generally very low, compare the As-Ga binary phase diagram in appendix B fig. B.1. Second, the collected Mn does not affect the nanowire growth rate and therefore does not alter the solubility of As in the liquid catalyst.

Thus, the Ga-Mn binary phase diagram indicates the phases appearing at the nanowire tip: At the growth temperature of 600°C, the Ga-Mn alloy is entirely liquid for Mn concentrations c_{Mn} up to 10 %. For c_{Mn} between 10 % and 38 %, it is a suspension with $\mathrm{Mn_3Ga_5}$ clusters in liquid Ga with the relative amounts determined by the lever rule. However, for $c_{\mathrm{Mn}} > 38$ %, the Ga-Mn compound solidifies completely. This means that a dissolution of As in liquid Ga, which is the prerequisite for nanowire growth via the VLS mechanism, is assuredly possible up to Mn concentrations of 10 %. For c_{Mn} between 10 % and 38 %, GaAs nanowire growth might proceed as well, in case the $\mathrm{Mn_3Ga_5}$ clusters do not cover the nanowire top facet. At the latest, the complete solidification of the droplet for $c_{\mathrm{Mn}} > 38$ % should terminate nanowire growth.

The solid phases observed at the wire tips in TEM at RT should strongly depend on the composition of the Ga-Mn alloy reached at the end of the nanowire growth: According to the Ga-Mn phase diagram, various intermetallic and ferromagnetic $\mathrm{Mn}_x\mathrm{Ga}_y$ phases are accessible from a Ga-Mn/$\mathrm{Mn_3Ga_5}$ suspension or a pure liquid Ga-Mn alloy. Additionally, due to the peritectic characteristic of the corresponding phase transformations (see appendix B), the duration of the cool-down process should affect the observed $\mathrm{Mn}_x\mathrm{Ga}_y$ phases for a distinct Mn-Ga composition. Thus, for a further insight of the system, the quantification of the elements at the nanowire would be required. However, this evaluation was not possible in EDX, since the element- and TEM-specific Cliff-Lorrimer factors, which are necessary to determine the absolute concentrations of the elements, are affected by large errors and therefore sophisticate the results.

Therefore we investigated, whether the arising liquid Ga-Mn alloy at the nanowire tip can be crystallized well controlled and crystallographic coherent with the GaAs nanowire. Then, the setting of various metallic Ga-Mn polycrystals would be avoided.

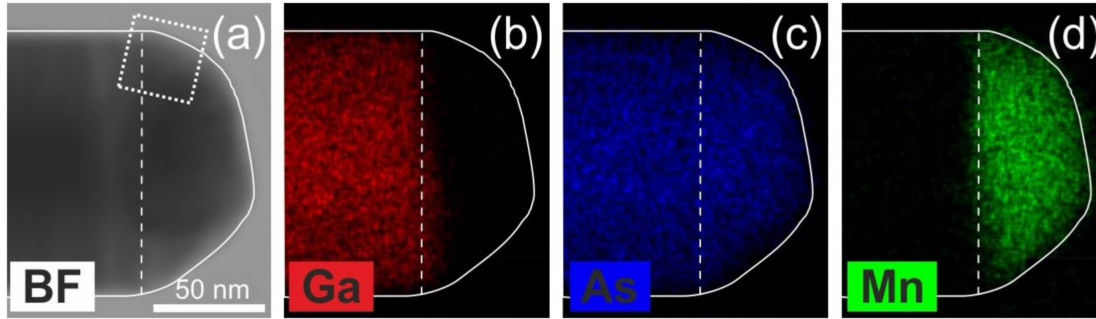

Figure 8.3.: (a) Bright field STEM image, and (b,c,d) EDX maps of the elements Ga, As and Mn of the tip region of a nanowire, grown with Mn supply during nanowire growth and exposed to As flux afterwards: the undoped GaAs nanowire is covered by the elements Mn and As at the end of the tip.

8.2. Ferromagnetic MnAs segments in GaAs nanowires

In this section the growth of ferromagnetic MnAs segments on GaAs nanowires is described. First, single MnAs segments on GaAs nanowires are realized by growing from the in section 8.1 obtained liquid Ga-Mn alloys at the wire tips. The room temperature (RT) ferromagnetism of the MnAs segments is proven by SQUID and RT magnetic force microscopy (MFM), separately. Furthermore, the growth of additional single MnAs nanocluster at the nanowire side facets is shown, as well as conditions for the growth of multiple separate MnAs clusters on GaAs nanowires are revealed.

8.2.1. Growth of single ferromagnetic MnAs segments

Usually, in Ga-catalyzed nanowire growth, by applying solely As_4 flux after the wire growth, the liquid catalyst can be consumed. The droplet then fully transforms into solid GaAs, whereby the crystal structure changes from mainly ZB to WZ and back to ZB again. This change is caused by the shrinking droplet size and the associated reduction of the contact angle (see sections 2.2.2 and 4.3.2). So the question arises what happens if a Ga-Mn alloy at the wire tip, obtained by Mn supply during, or even after the growth of GaAs nanowires (not shown), is exposed to As_4 flux.

Fig. 8.3a shows a bright field STEM image of a nanowire tip, which had been exposed to this procedure. In figs. 8.3b, 8.3c and 8.3d the corresponding EDX maps of the elements Ga, As and Mn are depicted. Obviously, a separation of the elements Ga and Mn is obtained. The end of the tip consists of Mn and As, while the whole nanowire below consists of Ga and As.

The HRTEM image of the dotted area in fig. 8.3a, fig. 8.4, reveals the crystallinity of the Ga-As and Mn-As phases. The crystal structure of the GaAs wire, which is mainly ZB with some twin planes (not shown), transforms in the region near the tip to perfect WZ with the very last nanometers being ZB again, as observed for the consumption of a pure Ga droplet. Obviously, the Ga from the liquid Ga-Mn alloy at the wire tip gets

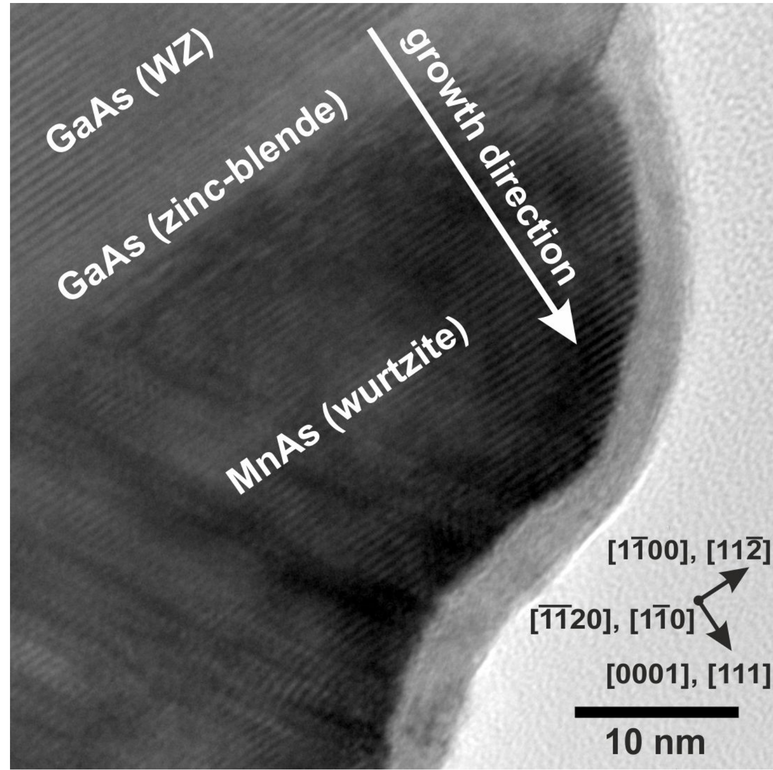

Figure 8.4.: HRTEM image of the dotted area in Fig. 3: At the wire tip the GaAs crystal structure changes from ZB to WZ (not shown) and back to ZB again due to the consumption of Ga from the Ga-Mn alloy. On top, hexagonal MnAs is grown with the epitaxial relations $[\bar{1}\bar{1}20]$MnAs||$[1\bar{1}0]$GaAs, $[1\bar{1}00]$MnAs||$[11\bar{2}]$GaAs and [0001]MnAs||[111]GaAs.

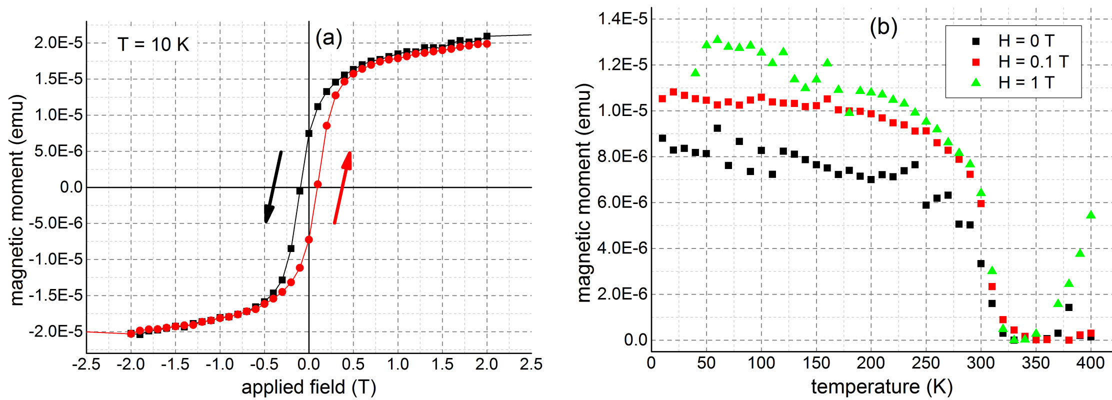

Figure 8.5.: SQUID measurements of an as-grown GaAs nanowire sample with MnAs segments at the wire tips: (a) At 10 K, a hysteresis curve is measured in the magnetic easy plane of MnAs. The coercive field strength is 0.1 T and the remanence 36 %. (b) Temperature-dependent curves of the magnetic moment for different applied magnetic fields reveal ferromagnetism up to the Curie temperature of MnAs of 313 K.

consumed via the VLS mechanism and precipitates as GaAs before a Mn-As compound forms atop the GaAs wire. This Mn-As compound is identified as hexagonal α-MnAs by measuring the distances of the atomic planes. The lattice constants are determined to be $a \approx 3.74$ Å and $c \approx 5.74$ Å, which are close to the literature values of $a =$ 3.725 Å and $c = 5.713$ Å [136]. The observed epitaxial relationships of WZ MnAs grown on ZB GaAs(111) at the wire tip are $[\bar{1}\bar{1}20]$MnAs$||[1\bar{1}0]$GaAs, $[1\bar{1}00]$MnAs$||[11\bar{2}]$GaAs and [0001]MnAs||[111]GaAs, which is consistent with the growth of MnAs thin films on GaAs(111) substrates [133, 171, 178].

The formation of MnAs after the consumption of liquid Ga from the Ga-Mn alloy via the VLS mechanism can be ascribed to the As-rich conditions mediated by the opened As cell. The As-Mn phase diagram (see appendix B fig. B.4) reveals that MnAs is the only stable phase for an excess of As with respect to Mn.

The magnetic properties of the MnAs segments were evaluated in SQUID. Therefore, an as-grown nanowire ensemble was characterized by applying the external magnetic field perpendicularly to the nanowire axis in the magnetic easy plane of MnAs [136, 140].

Fig. 8.5a shows a hysteresis curve measured at 10 K, obtained after subtracting the diamagnetism stemming from the silicon substrate and the GaAs nanowires. The rounded loop is characteristic for the nearly magnetic isotropy in the MnAs(0001) plane [140]. Comparing the measurements to 2D MnAs thin films grown on GaAs(111) grown by Däweritz et al. [140] (see also section 3.3.3), the coercive field strength of 0.1 T and the remanence of 36 % are roughly the same.

Temperature-dependent measurements of the magnetic moment were performed after cooling down the sample to 5 K in an external magnetic field of 7 T. This procedure aligns all spins along one direction in the magnetic easy plane. For applied external magnetic field strengths of 0 T, 0.1 T and 1 T, the magnetic moment of the sample was measured during defrosting (see fig. 8.5b). All curves reveal a transition temperature of 313 K (40°C), which is in excellent agreement with the Curie temperature of MnAs. The remanence of the magnetic moment in the absence of an applied magnetic field (0 T curve) excludes a superparamagnetic behavior of the small MnAs segments and proves ferromagnetism. A contribution to the magnetic signal by MnAs clusters possibly grown on the substrate in-between the wires is ruled out: an as-grown sample with the nanowires removed reveals pure diamagnetism.

To investigate the alignment of magnetic domains within the MnAs segments at the wire tips, RT magnetic force microscopy (MFM) measurements were performed on lying nanowires. Thereby the MFM lift mode was used, allowing to distinguish magnetic forces from van-der-Waals exchange interactions. Reversing the magnetic polarization of the MFM tip (see figs. 8.6a and 8.6b), results in a reversed sign at the nanowire tip, whereas the non-magnetic GaAs part of the nanowire remains unchanged. The ferromagnetic MnAs segment at the nanowire tip shows a pronounced one domain structure with the magnetic poles pointing along one of the $\langle 11\bar{2}0\rangle || \langle 1\bar{1}0\rangle$ directions, since the nanowire lies on one of the $\{1\bar{1}0\}$ side facets.

These findings prove the controlled epitactic growth of single monocrystalline, ferromagnetic, monodomain α-MnAs segments on GaAs nanowires.

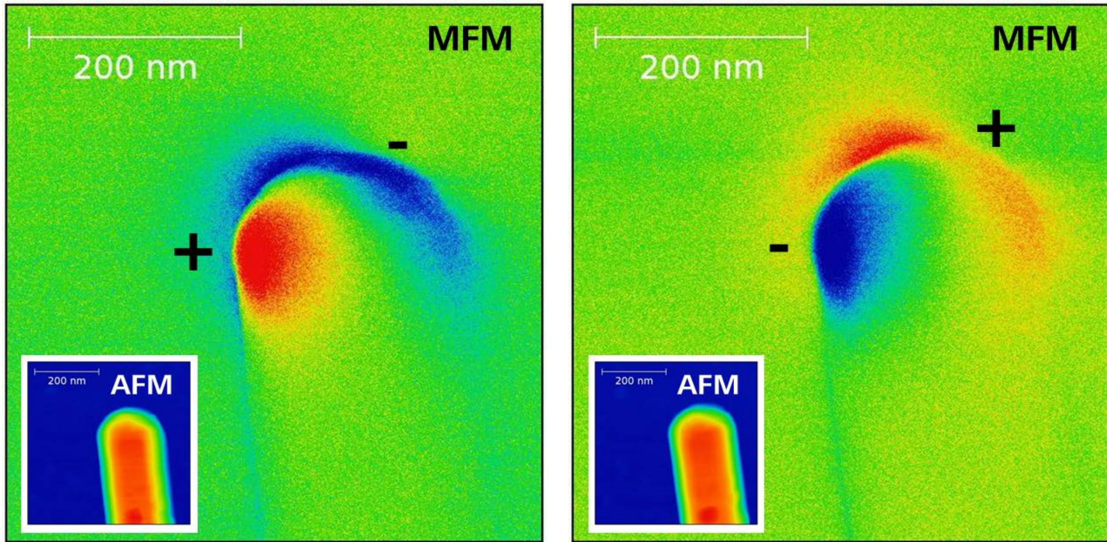

Figure 8.6.: RT MFM measurements on a lying nanowire: (a) The one domain structure of the MnAs segment at the wire tip is obvious, with the magnetic poles labeled as "+" and "-". (b) Reversing the magnetization of the MFM tip results in a reversed sign at the MnAs segment, whereas the GaAs part of the nanowire remains unchanged.

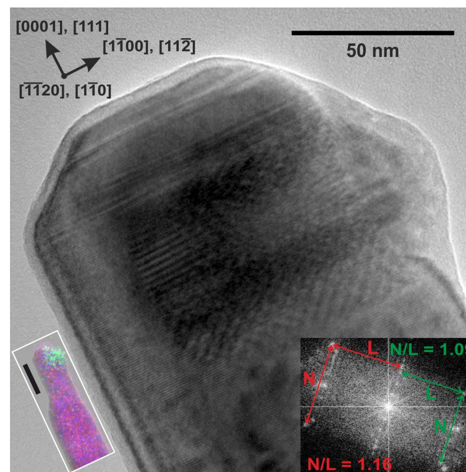

Figure 8.7.: HRTEM image of a nanowire tip. The Ga catalyst droplet was consumed first, followed by the restoration of a Ga droplet at the side facet, Mn deposition and crystallization of the resulting liquid Ga-Mn alloy by applying As_4 flux. The MnAs segment manufactured by this procedure extends in this case from the right side facet to the center side facet, see also the EDX map inset (scale bar = 80 nm), causing a Moire pattern with the subjacent WZ GaAs nanowire part. The FFT of this region evidences the same orientation of the both WZ phases with N/L relations of 1.16 for MnAs and 1.09 for GaAs in [$\bar{1}\bar{1}$20] viewing direction, coinciding with literature [179, 180].

8.2.2. Growth of multiple MnAs segments

To grow multiple MnAs segments usable for the realization of spin injection devices from the ferromagnet MnAs into GaAs, two different approaches were examined. These are the subsequent growth of single MnAs segments, and the growth of multiple MnAs segments in one run.

Subsequent growth of single MnAs segments

The growth of MnAs from a liquid Mn-Ga alloy as shown in section 8.2.1 can be also used to realize additional single nanoscale MnAs segments at the nanowire sidewalls. To do that, after the GaAs wire growth, the catalyzing Ga droplet was consumed in As_4 flux. Applying Ga flux to the wires, while all other beams are shut off, results in the formation of a liquid droplet at the nanowire tip or at the side facets [181]. A subsequent irrigation with Mn, and afterwards with As, leads again to the formation of a Ga-Mn alloy, and finally to ferromagnetic MnAs.

Fig. 8.7 shows a HRTEM image, the corresponding fast fourier transformation (FFT) and the EDX map of a wire tip exposed to this procedure. The hexagonal MnAs crystal ranges from the right side facets to the center (green in the EDX inset). It causes a Moire pattern with the subjacent WZ GaAs crystal, which stems from the consumption process of the catalyzing Ga droplet. The FFT brings out easily the epitaxial relations between both wurtzite phases: [0001]MnAs||[0001]GaAs, [$\bar{1}\bar{1}$20]MnAs||[$\bar{1}\bar{1}$20]GaAs and [1$\bar{1}$00]MnAs||[1$\bar{1}$00]GaAs. These findings coincide with the relations deduced from MnAs shells grown around GaAs core NWs [172].

Growth of multiple MnAs segments in one run

The growth of multiple MnAs segments on GaAs nanowires can be also realized in one growth run. Thereby, Mn and As fluxes are together applied after the growth of GaAs nanowires. To avoid the formation of a homogenous MnAs shell around the GaAs core, which is usually mediated by LT MBE growth, the growth temperature remains in this case comparable to the one used for the axial growth of the nanowires. Then, the formation of single MnAs segments at edges of the nanowire side facets and on the top facets is observed. This can be easily seen in the side view SEM images in figs. 8.8, where the MnAs segments reside spike-like at the wire sidewalls. Obviously, MnAs nucleates preferred at the edges of the side facets, as here strain, which is induced by the different lattice constants of MnAs and GaAs, can be released more easily than directly on the side facets.

The MnAs segment size and its density are strongly dependent on the growth temperature and the As_4 BEP, which both affect the surface diffusion length of the Mn adatoms. To show that exemplarily, GaAs nanowires were grown on two different samples by the same procedure, while the conditions for MnAs segment growth was altered. The amount of deposited MnAs was kept fixed at 19 nm 2D equivalent MnAs, whereas growth temperature and As_4 BEP were varied. The nanowires shown in figs. 8.8a and

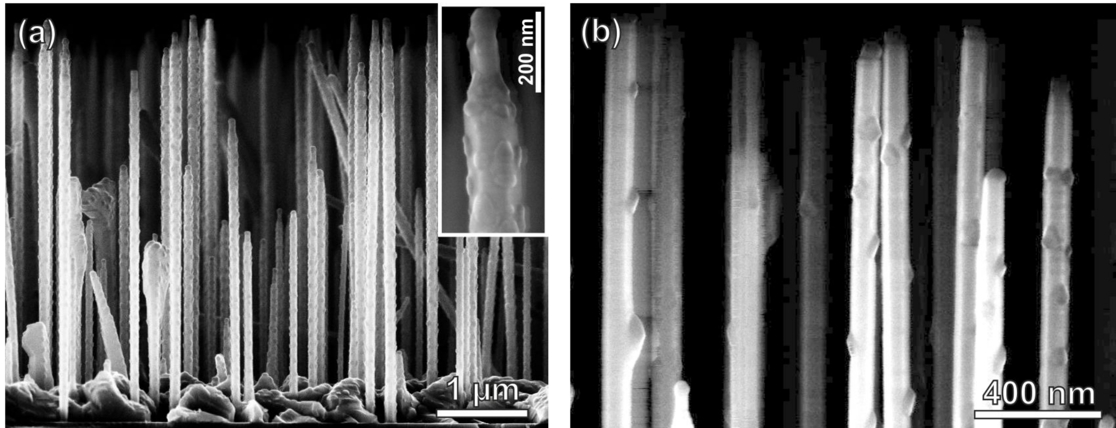

Figure 8.8.: SEM images of GaAs nanowires covered with multiple MnAs nanoclusters on the edges of the side facets and on the top facets. The average nanocluster volume V_{NC} and their mean density ρ_{NC} on the edge of between two side facets can be affected by adjusting the Mn adatom diffusion length via the growth temperature T_g and the As_4/Mn BEP ratio: (a) $T_g = 550$ °C, $As_4/Mn = 1000 \rightarrow V_{NC} \approx 6.8 \cdot 10^3$ nm^3, $\rho_{NC} \approx 10$/µm. (b) $T_g = 600$ °C, $As_4/Mn = 50 \rightarrow V_{NC} \approx 6.5 \cdot 10^4$ nm^3, $\rho_{NC} \approx 1$/µm.

8.8b, were grown at an growth temperature of 550°C and 600°C, respectively, while the As_4/Ga ratio was 1000 and 50, respectively. This change of the growth conditions results in a drop of the MnAs segment density from roughly 10/µm to 1/µm at one edge between two side facets, while the MnAs segment size increases by a factor of 10: the average diameter increases from 44 nm to 83 nm, and the average segment height from 14 nm to 38 nm. Thus, the density and size of the MnAs nanoclusters forming on the edges of the side facets can be steered by choosing suitable growth conditions.

8.3. Conclusion

In this section the pathways of Mn in combination with the Ga-catalyzed growth of GaAs nanowires in MBE were investigated.

First the effect of Mn supply during and after the GaAs wire growth was examined. It turned out, that neither ferromagnetic (Ga,Mn)As nor MnAs is formed in GaAs nanowires, grown at the typical temperatures used for the Ga-catalyzed VLS mechanism. Taking into account the extensive studies on the growth of 2D (Ga,Mn)As, the non-existence of ferromagnetic (Ga,Mn)As in structures grown at temperatures of 600°C is reasonable: the quasi equilibrium conditions reached here allow to incorporate at most the equilibrium Mn concentration in GaAs, which is less than 0.1 %. Surprisingly, MnAs clusters, typically precipitating during the growth of 2D (Ga,Mn)As at elevated temperatures, are not observed when supplying Mn during the GaAs nanowire growth. Instead, a large amount of Mn accumulates in the liquid catalyst droplet. This behavior was

explained by the solubilities of Mn in liquid Ga and solid GaAs at growth temperature. Liquid Ga incorporates at least 10 % Mn whereas GaAs at most 0.1 %. Nearly all supplied Mn atoms may thus dissolve in the liquid. The absence of ferromagnetic MnAs in GaAs nanowires seems therefore directly connected to the usage of the liquid catalyst particle, whereas the absence of ferromagnetic (Ga,Mn)As is simply due to the low solubility of Mn in GaAs.

The forming liquid Ga-Mn alloy at the wire tips was used to grow MnAs epitaxially on top of GaAs nanowires. Exposing the liquid Ga-Mn alloy to As_4 flux results first in the consumption of Ga via the VLS mechanism. When a significant amount of Ga has been consumed from the liquid droplet, the formation of MnAs at the very top of the nanowire is observed. The epitaxial relations between wurtzite α-MnAs and zinc-blende GaAs are $[\bar{1}\bar{1}20]$MnAs$||[1\bar{1}0]$GaAs, $[1\bar{1}00]$MnAs$||[11\bar{2}]$GaAs and [0001]MnAs$||$[111]GaAs. Between α-MnAs and wurtzite GaAs the epitaxial relations are [0001]MnAs$||$[0001]GaAs, $[\bar{1}\bar{1}20]$MnAs$||[\bar{1}\bar{1}20]$GaAs and $[1\bar{1}00]$MnAs$||[1\bar{1}00]$GaAs. The ferromagnetism of multiple α-MnAs segments and their typical Curie temperature of 313 K was confirmed in SQUID, while a monodomain magnetic signature of single segments was observed in RT MFM.

Concluding this study, two different approaches to grow multiple MnAs segments on GaAs nanowires were demonstrated. They might be used for electrical spin injection and detection experiments into GaAs nanowires. It was shown that the subsequent growth of single MnAs segments is possible, as well as the growth of multiple MnAs segments in one run. Here, the MnAs nanocluster size and density can be altered affecting the Mn adatom diffusion length on the GaAs side facets via the growth parameters.

9. Conclusion and Outlook

In this work, first different aspects of GaAs nanowire growth were investigated. The main topics were the integration of controllable GaAs nanowire growth on Si substrates, and the optimization of the GaAs nanowire crystal structures. The latter is a very important step, as in GaAs nanowires the zinc-blende (ZB) and the wurtzite (WZ) phase are accessible, so the physical properties of the WZ GaAs phase can be studied. Additionally, the growth of semiconductor/ferromagnet nanowire heterostructures was performed, which may be used in future spin injection or detection experiments. Here, a shell of (Ga,Mn)As was grown around the GaAs core nanowires, and also nanosize MnAs segments were realized on the GaAs nanowires.

To be able to grow GaAs nanowires with the Ga-catalyzed growth technique on Si(111) in a reproducible manner, the passivating native oxide was prepared by wet chemical etching, so that only vertical nanowire growth was obtained. From these experiments and from site-selective growth of nanowires on fully passivated Si(111) substrates, conclusions for the initial phase of GaAs nanowire growth on Si(111) were drawn. GaAs grows first laterally on bare Si(111) as long as the catalyst droplet is in contact with the substrate. As soon as the catalyst moves fully atop the GaAs crystal, nanowire growth takes place. The specific $\langle 111 \rangle$ growth direction is then set by the GaAs faces wetted by the liquid catalyst. Thus, growth of GaAs nanowires perpendicularly on the substrate can be reached only if no crystal defects occurred during lateral growth, and when the wetted GaAs cluster face is the GaAs(111) top facet. The probability to fulfill these requirements is highest, when only small areas of the substrate surface are free of the passivating oxide, as for example in the case of pinholes in the oxide layer. This regime was reproducibly obtained by reducing the native oxide thickness by wet chemical etching. The rough oxide surface then provides a large amount of pinholes to the underlying substrate, leading to vertical nanowire growth at these sites.

The growth of GaAs nanowires on the optimized Si(111) was also investigated as a function of the growth parameters in terms of the nanowire characteristics, i.e. areal density, length, diameters and shape. It was estimated, that the nanowire length is linearly dependent on the As BEP, as expected from the nucleation limited VLS growth mechanism. The areal nanowire density depends on the substrate temperature, the Ga rate and the As BEP, as diffusion on the substrate plays an important role to initially form the catalyzing Ga droplets. The diameters and the shape of the nanowire depend strongly on the initial droplet size and its evolution during the whole nanowire growth. Thus, the As BEP, which strongly determines the depletion of the droplet via the GaAs nanowire growth, affects mostly the nanowire shape, whereas the initial size of the droplet, i.e. the nanowire diameter at the bottom, increases with the Ga rate.

The shape of the catalyst droplet, as well as its wetting area at the nanowire tip determine the crystal structure of the precipitating GaAs nanowire. Theory predicts that the WZ crystal structure is favored over ZB GaAs when the liquid catalyst droplet wets the nanowire top facet to its edges, and possesses a contact angle of about 90°. By choosing conditions, which enhance the probability to establish a droplet with these requirements, i.e. a low growth temperature and a Au-Ga alloy as the catalyst, the optimum conditions for WZ nucleation were searched. This was done by changing the droplet size and therefore also the contact angle via different As BEPs in MBE growth. Depending on the As BEP, the main crystal structure along the wires as well as the stacking fault density in these wires was estimated in TEM. With this procedure, conditions for the growth of stacking-fault-free WZ GaAs nanowires were identified.

Also, the ZB crystal structure in GaAs nanowires was optimized. To do that, large catalyst droplets, whose edges reside on the side facets of the nanowire only, were used. WZ nucleation was then inhibited, and the growth of large twin-plane-free ZB GaAs segments of 1 µm length was obtained. However, the crystal structure at the nanowire bottom and the nanowire tip is full of stacking faults, leading also to the creation of short WZ segments. These observations are ascribed to the building-up of the liquid droplet at the initial stages of nanowire growth and its consumption at late stages, together with the related changes of wetting area and contact angle. To avoid the introduction of these crystal defects at the extremes of the ZB nanowires, in the future a different growth regime may be established: when using a small droplet catalyst droplet on the nanowire top facet, which does not touch the edges of the top facet, also nucleation of ZB GaAs phase is preferred before the WZ phase. In this case, the building-up and the consumption of the droplet is not associated with the introduction of the WZ phase, as the regime for preferential WZ nucleation is not touched during growth. To realize this regime in MBE, the growth of wires at high As BEPs in the VLS growth mode is recommended, i.e. close to the vapor-solid growth mode (compare fig. 4.5a). Then the growth of twin-plane-free ZB wires should be possible.

To determine the optical properties of GaAs nanowires, the non-radiative recombination paths were passivated. These are strongly present at the GaAs nanowire surfaces, where unsaturated bonds exist. To passivate these bonds, the growth of the wider band gap material AlGaAs around the GaAs core was performed. By optimizing this shell growth to obtain a sufficient barrier thickness and height, the optical quantum efficiency was raised by an order of 10^3 with respect to uncovered GaAs nanowires.

The optical properties of the stacking-fault-free WZ and largely twin-plane-free ZB GaAs nanowires were determined in micro-photoluminescence. The WZ exciton energy was determined to be 1.518 eV, which is 3 meV larger than the ZB counterpart. Additionally, the polarization of the emitted light was investigated. As expected from the selection rules in the WZ crystal phase, at the band edge emission strongly polarized perpendicular to the $\hat{c}$-axis with a degree of linear polarization of 71 % was observed. Instead, in ZB nanowires, the interband transition at the band-edge is unpolarized. However, a shape related effect leads in ZB GaAs nanowires to light emission with a polarization parallel to the nanowire axis. This effect exists also in WZ wires, reducing

the degree of linear polarization from 100 % to the measured 71 %.

To conclude the analysis of optical properties of GaAs nanowires, it was shown that GaAs nanowires can be used as lasers in the near infrared regime. Here, the GaAs nanowire is used both as gain medium and Fabry-Perot resonator. To obtain a low lasing threshold, the nanowire growth was optimized towards untapered nanowires with a diameter larger than 330 nm and a length above 6 µm. By pumping these wires optically, lasing operation was recorded at cryogenic temperatures, once a critical pump power density was exceeded. Instead, at room temperature no lasing operation was obtained, which should indeed be possible [157, 158]. The most probable reasons for this behavior were a too low pump efficiency of the gain medium, and a reduced optical quantum efficiency because of a too thin passivating AlGaAs shell. Very recently, we obtained lasing operation at room temperature, using a thicker AlGaAs shell. Thus, in the presented experiments, non-radiative recombination paths mostly account for the suppression of lasing operation at room temperature.

A prediction for the WZ GaAs crystal structure, which had never been verified experimentally before, is the existence of an intrinsic electric field, called spontaneous polarization. We have visualized this peculiarity for the first time in WZ GaAs, using differential phase contrast spectroscopy in a transmission electron microscope. The strength of spontaneous polarization was not directly determined in pure WZ GaAs, as the electron probe beam is too large to detect this value directly. For a quantitative measurement, a capacitor like structure, with the dielectric ZB GaAs in-between two layers of WZ crystal structure, was used. The estimated strength of the spontaneous polarization in WZ GaAs of $(2.7 \pm 0.6) \cdot 10^{-3}$ C/m^2 agrees well with theoretical predictions [66].

In a final part of this thesis, the integration of ferromagnetic materials with GaAs nanowires was studied. First, the growth of radial GaAs/(Ga,Mn)As nanowire heterostructures with ZB and WZ crystal structure was explored. From these heterostructures, structural and magnetic differences between both crystal phases were evaluated. Due to the pseudomorphic growth of (Ga,Mn)As onto the GaAs nanowire, the larger equilibrium lattice constant of (Ga,Mn)As induces strain into the core/shell system. This strain along the nanowire axis was monitored in X-ray diffraction measurements. A relaxation of the (Ga,Mn)As shell, and coincidentally a tensile straining of the GaAs core along the wire axis, was observed for wires with WZ crystal structure only, but not for ZB ones. This observation was ascribed to the different GaAs core diameters of both nanowire types: the diameter of ZB wires is up to two times larger than the one of WZ wires, so WZ wires get more easily strained by a (Ga,Mn)As shell. The magnetic properties of ZB and WZ (Ga,Mn)As grown under the same conditions reveal a comparable Curie temperature, although the total magnetic moment is two times larger for WZ compared to ZB. This points to an elevated incorporation of ferromagnetically coupling Mn atoms, but also to a reduced coupling strength in WZ (Ga,Mn)As compared to ZB (Ga,Mn)As. Additionally, a uniaxial magnetic anisotropy was detected independent on the core/shell crystal structure. The magnetic easy axis points along the nanowire axis, and the magnetic hard axis is perpendicular to the wire axis. This behavior was

explained by to the strained growth of (Ga,Mn)As along the nanowire axis, as compressively strained (Ga,Mn)As directions promote the formation of a magnetic easy axis in the same direction [117].

To get further insight into the WZ (Ga,Mn)As system, the growth of WZ (Ga,Mn)As shells was optimized for three different Mn concentrations of 5 %, 7.5 % and 10 %. The found growth parameters were equivalent, indicating a low effect of the Mn concentration on shell growth for Mn concentrations between 5 % and 10 %. This observation is reflected in the Curie temperatures of these WZ (Ga,Mn)As shells, estimated from R(T) curves, which are all 17 K, independent on the Mn concentration. After an annealing step (9 h at 190°C), the Curie temperature increases with the nominal doping to 19 K, 22 K and 25 K, respectively. The as-grown and annealed values of the Curie temperature are far below the ones obtained for comparable ZB 2D (Ga,Mn)As thin films (as-grown 75 K, annealed 115 K), indicating a worse crystalline quality in the shell structures. The reduced crystalline quality was explained with the observation of a segregation of Mn atoms into stripe-shaped regions leading to an enhanced incorporation of non-ferromagnetic coupling Mn atoms [113, 114]. Magnetotransport measurements of as-grown wires confirm the uniaxial magnetic anisotropy for WZ (Ga,Mn)As shells, with a magnetic easy axis along the nanowire and a magnetic hard axis perpendicular to the nanowire axis. However, with increasing Mn concentration, the hard axis is less pronounced. This peculiarity was also observed for annealed wires. Thus, it can be speculated that a carrier density dependent anisotropy constant is present in WZ (Ga,Mn)As, just as determined for ZB (Ga,Mn)As [111]. To prove the presence of such a carrier density-dependent phenomenon, SQUID measurements on these samples would be necessary, as well as a method to resolve the favored incorporation sites in (Ga,Mn)As microscopically.

To conclude the thesis, the pathways of Mn atoms in combination with the Ga-catalyzed GaAs nanowire growth were studied. As GaAs nanowire growth proceeds at temperatures, where a quasi-thermodynamical equilibrium is present, no incorporation of Mn in the GaAs nanowire was monitored above the equilibrium solubility of 0.1 %. Also MnAs clusters, which are commonly observed in the growth of (Ga,Mn)As shells at elevated temperatures, did not form. A high concentration of Mn atoms within the liquid catalyst droplet was however measured, which stems from the high solubility of Mn in liquid Ga at the applied conditions. It was shown that from this liquid Ga-Mn alloy the growth of GaAs nanowires is possible, so the VLS mechanism is not inhibited by the solved Mn. Additionally, the liquid Ga-Mn alloy can be used to grow MnAs segments on GaAs nanowires. The performed experiments reveal that MnAs precipitates from the alloy as soon as most of the liquid Ga is transformed to GaAs. The epitactic integration of nanoscale MnAs segments in GaAs nanowires was shown for the ZB and WZ GaAs crystal phase. The ferromagnetic signatures of the MnAs segments at temperatures below its Curie temperature of 40°C were proven in SQUID and with room temperature magnetic force microscopy. Such MnAs segments might be interesting building blocks for future room temperature spin-related nanowire applications.

A. Experimental techniques

In this section the details of the experimental setups used in this work are summarized. In section A.1 the molecular beam epitaxy system used for the growth of the nanowires is presented, including the necessary steps for a reproducible nanowire growth and the in-situ monitoring of the main GaAs nanowire crystal structure. Section A.2 summarizes the techniques to determine the crystal structure, the atomic composition and internal electric fields of the nanowires using transmission electron microscopy. The principles of reciprocal space mapping are described in section A.3, while in section A.4 the functionality of the µPL setup used for the optical excitation of the wires is depicted. The measurements of magnetism in Mn containing GaAs nanowire heterostructures are presented in sections A.5, A.6 and A.7 concerning superconducting quantum interferometry, magnetic force microscopy and magnetotransport. Eventually, the etching procedure for Si(111) substrates covered with native oxide is summarized in section A.8.

A.1. Molecular beam epitaxy (MBE) of GaAs nanowires

The growth of the nanowires was performed in a Veeco Gen II MBE, equipped with typical solid source effusion cells to evaporate Ga, Mn, and Al. For As evaporation a valve cracker cell was used, which enables the growth from As_4 and As_2 molecules. To ensure the growth of pure crystals, ultra-high vacuum conditions were realized in the growth chamber using a cryo pump and an adsorbing, nitrogen-cooled shield.

A.1.1. Cell calibration

The atomic fluxes, evaporated from the cells, are either determined by RHEED, i.e. the growth of a monolayer is monitored, or a beam equivalent pressure (BEP) is measured with an ionization gauge, from which the atomic/molecular flux can be calculated. For Ga and Al, the monolayer growth can be easily deduced during the growth of GaAs or AlAs on a GaAs(001) wafer by monitoring the intensity of the diffracted intensity electron beam, i.e. a growth rate [Å/s] is obtained. For Mn atoms and As_4 molecules, the BEP p_{BEP} was recorded with the ionization gauge. Knowing a cell-related geometrical coefficient α_x and the ionization efficiency η_x of the respective element x relative to nitrogen (N_2), the atomic flux rate Γ_x can be determined via

$$\Gamma_x = \frac{\alpha_x \cdot p_{\mathrm{BEP}_x}}{k_B T \cdot \eta_x} \cdot \sqrt{\frac{8 k_B T_x}{\pi \cdot m_x}}. \tag{A.1}$$

Here, k_B denotes the Boltzmann constant, T the chamber temperature, T_x the temperature of the respective cell and m_x the respective atomic/molecular mass. With this relation the As_4/Ga ratios, as well as the Mn concentration c_{Mn} in (Ga,Mn)As can be estimated. c_{Mn} then reads

$$c_{\mathrm{Mn}} = \beta \cdot \frac{\Gamma_{\mathrm{Mn}}}{\Gamma_{\mathrm{Ga}} + \Gamma_{\mathrm{Mn}}}, \tag{A.2}$$

with the prefactors α_x summarized in $\beta = 1.575$. The desired molecular fluxes were then adjusted by setting the cell temperatures to the corresponding values, or in the case of As_4, choosing the respective opening of the valve.

A.1.2. Nanowire growth

For the growth of GaAs nanowires different substrates were used, depending on the growth variety. For Au-catalyzed growth, $5\mathrm{mm} \cdot 10\mathrm{mm}$ pieces of GaAs(111)B substrates covered with a thin layer of gold ($1 - 10$ Å) were used, while for Ga-catalyzed growth undoped or slightly boron doped ($< 10^{18}\Omega/\mathrm{cm}^3$) $10\mathrm{mm} \cdot 10\mathrm{mm}$ Si(111) wafers were introduced into the growth chamber.

Since the, for Au-catalyzed growth used, GaAs substrates get oxidized in air, after introducing the wafer in the growth chamber an annealing step was performed to desorb the Ga oxide from the substrate surface. Therefore, the substrate temperature was increased beyond 600°C for 10 min. Hereby, an As_4 BEP $> 5 \cdot 10^{-6}$ Torr was applied to prevent a deterioration of the GaAs crystal by the out-diffusion of As atoms. After that, the desired growth temperature was approached, and the wire growth at the specific conditions was started.

Conversely, in Ga-catalyzed growth, the Si oxide is used to passivate the major parts of the surface, and was not desorbed. Here, the growth temperature was directly approached.

A.1.3. Temperature measurement

The temperature of the wafers was measured before the start of the nanowire growth. This was done either with a pyrometer, band edge absorption or black body spectroscopy, depending on the approached temperature range and the wafer configuration on the sample holder. Concerning the different sample holders, see [114].

In the case of GaAs substrates, which were glued to a molybdenum sample holder, that gathers the radiation from the sample heater and mediates the adopted temperature to the GaAs/Au sample and GaAs dummy wafers positioned in vicinity, an Ircon 2000 pyrometer was used in the temperature range above 400°C. This pyrometer measures the emitted radiation between 910 nm and 970 nm wavelength, and estimates the temperature using the emissivity of GaAs and Planck's law. Below 400°C, the temperature of the sample was determined by band edge absorption spectroscopy relating the temperature to the measured GaAs band gap. Here, the GaAs wafers are irradiated by a white light lamp, while the reflected light is collected with an optical fiber. The optical fiber

provides a detection spot of 3 mm in diameter, enabling a spatial resolved temperature measurement. This is of large importance, especially for the growth of (Ga,Mn)As shells, where a reliable temperature can be measured only at a (5mm · 10mm) GaAs wafer glued next to the grown core wires, which deteriorate the temperature measurement due to the temperature gradient along the GaAs wires [182]. For further details about band edge absorption spectroscopy in this MBE system, see [114, 183].

The temperature of the silicon substrates could not be determined with the pyrometer, since here the catchment area is larger than the (10mm · 10mm) Si substrates used for nanowire growth. Thus, the much colder environment would be also taken into account, distorting the temperature measurement. Instead, the temperature above 450°C was determined with black body spectroscopy, using the same optical fiber as in the case of band edge spectroscopy to detect the emitted spectrum from the Si substrate only. Here, the intensity of black body radiation emitted from the Si wafer above the band gap (typically between 1050 nm to 1150 nm wavelength) is compared with the intensity distribution expected from Planck's law.

A.1.4. Reflection high-energy electron diffraction (RHEED)

The main crystal structure of the growing nanowire ensemble can be in-situ determined by RHEED. Usually in RHEED, the from the wafer surface reflected electron beam is detected, to make statements about the surface consistency, e.g. occurring surface reconstructions. In the case of nanowire growth, reflected electron diffraction along certain crystal directions is used to distinguish between wurtzite (WZ) and zinc-blende (ZB) crystal structure.

Since the growth proceeds perpendicular to a {111} plane, due to the nearly parallel incident electron beam, low order diffraction patterns in the GaAs $\langle 11\bar{2}0\rangle \,||\, \langle 1\bar{1}0\rangle$ directions or $\langle 1\bar{1}00\rangle \,||\, \langle 11\bar{2}\rangle$ directions can be detected. WZ and ZB GaAs can be distinguished in $\langle 11\bar{2}0\rangle \,||\, \langle 1\bar{1}0\rangle$ directions only, since the diffraction patterns in $\langle 1\bar{1}00\rangle \,||\, \langle 11\bar{2}\rangle$ directions look quite the same. The electron diffraction patterns for GaAs$\{11\bar{2}0\}$, GaAs$\{1\bar{1}0\}$, GaAs$\{1\bar{1}00\}$ and $\{11\bar{2}\}$ planes are sketched in figs. A.1 [180], and also the corresponding measured RHEED diffraction patters are depicted. The equivalency in figs. A.1a, A.1c and A.1d is obvious. In $\langle 1\bar{1}0\rangle$ directions, the yielded diffraction patterns deviate from the ideal one, since always slight traces of the WZ $\langle 11\bar{2}0\rangle$ diffraction pattern contribute, and additionally the introduction of twin planes leads to a mirroring of the ZB diffraction pattern.

The determined diffraction patterns seem to be restricted to the crystal structure of the actual top parts of the wires, since in the droplet consumption step of ZB wires, see section 4.3.2, the main intensity resides at the WZ diffraction spots. This observation is dedicated to the low angle of approximately 3° between the incident electrons and the substrate plane. Note, that with increasing catalyst droplet size, the diffraction becomes more and more diffusive, until no diffraction pattern can be observed any more.

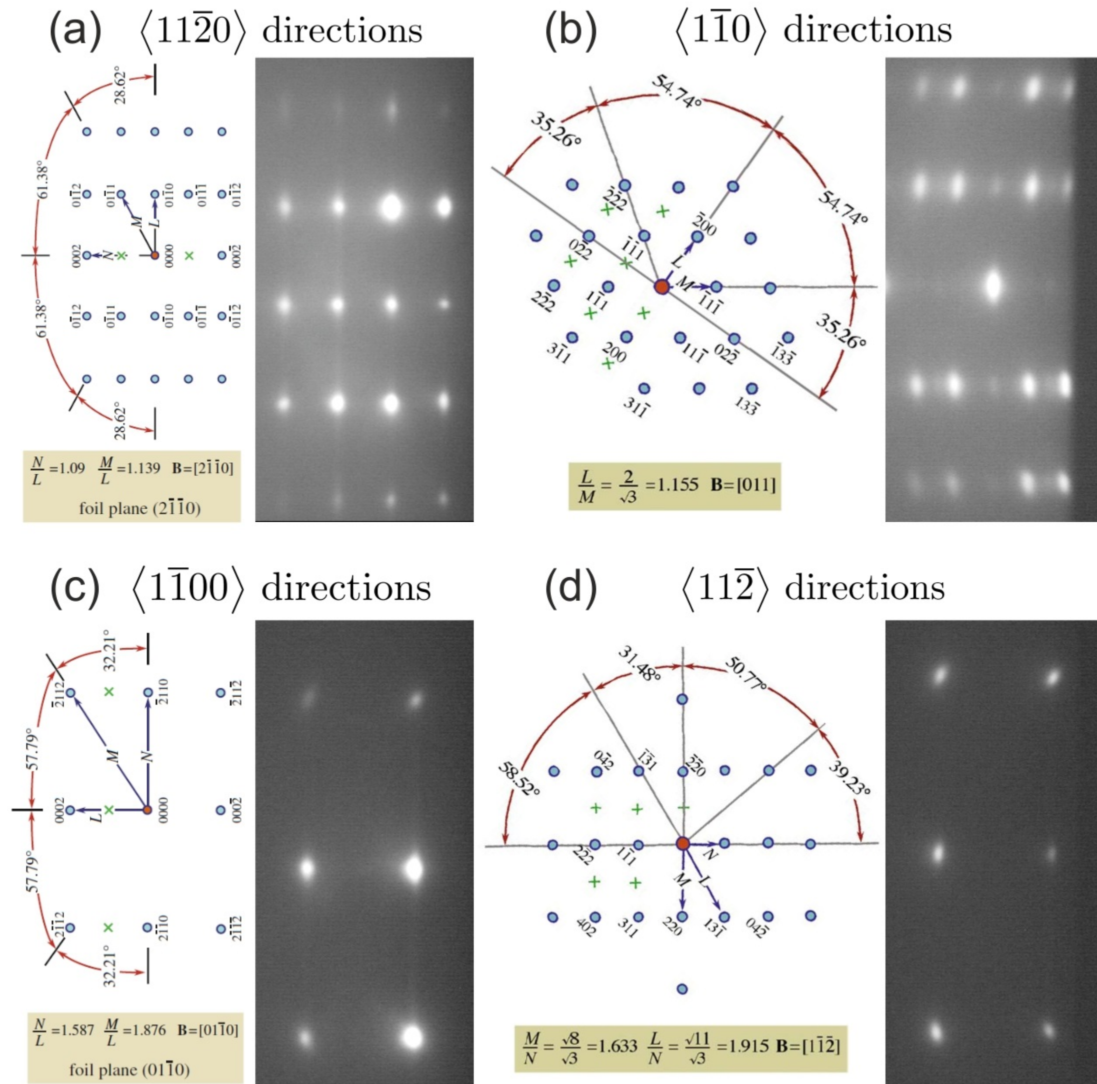

Figure A.1.: Calculated and measured diffraction patterns (DPs) of GaAs planes in vertical viewing directions: (a) DP of a WZ $\{11\bar{2}0\}$ plane in the corresponding $\langle 11\bar{2}0\rangle$ viewing direction. (b) DP of an equivalent ZB $\{1\bar{1}0\}$ plane in the corresponding $\langle 1\bar{1}0\rangle$ viewing direction. (c) DP of a WZ $\{1\bar{1}00\}$ plane in the corresponding $\langle 1\bar{1}00\rangle$ viewing direction. (d) DP of an equivalent ZB $\{11\bar{2}\}$ plane in the corresponding $\langle 11\bar{2}\rangle$ viewing direction.

A.2. Transmission electron microscopy (TEM)

TEM was used to determine the crystalline structure of the via MBE grown nanowires. For TEM measurements the nanowires were transferred to a carbon coated copper TEM grid by simply wiping the grid over the as-grown sample. To distinguish between zinc-blende and wurtzite GaAs crystal structure the nanowires were oriented in a $\langle 11\bar{2}0 \rangle$ zone axis (see the corresponding diffraction patterns in figs. A.1). Also, the epitaxial relations for the growth of MnAs on GaAs nanowires were easily uncovered in TEM. All TEM-related measurements were performed by Benedikt Bauer of the team of Prof. Zweck using a *FEI Tecnai F30* operating at 300 kV, which enables a spatial resolution on sub-Å scales. For a more detailed description of the TEM functionality and the methods, see [163].

A.2.1. Energy-dispersive X-ray spectroscopy (EDX)

To determine the composition of the wires, especially to detect the growth of ferromagnetic (Ga,Mn)As, which is not possible to distinguish from GaAs with solely TEM, EDX measurements were performed in the same TEM using a *Bruker QUANTAX* EDX system with a *XFlash 530* detector. Here, the electrons of the inner shells (K shell) get ionized by the exciting electrons. The energies of the emitted photons, when electrons of the second shell (L shell) fill the unoccupied state, called Kα lines, are detected (see the sketch in fig. A.2a). In fig. A.2b a typical spectrum of a GaAs nanowire is shown, which was grown under Mn supply. Obviously, the Mn Kα line at 5.9 keV is absent, while the Ga Kα line and As Kα line at 9.25 keV and 10.5 keV dominate, and therefore suggest the growth of a GaAs nanowire without a doping of Mn up to the resolution limit of the EDX. For further details, see [163].

A.2.2. Differential phase contrast microscopy (DPC)

DPC in a STEM is a method to determine the strength of magnetic and electric fields, and also charge distributions on sub-Å length scales. In this work, DPC is used to map the internal electric field of WZ GaAs induced by spontaneous polarization. To do that, a ring-shaped detector, which was divided into four segments, was used (fig. A.3c). If no electric field is within the structure, like in ZB GaAs, the four quadrants become illuminated equally and the difference between the intensity detected on the opposing segments is zero (fig. A.3a). When an electric field within the probed volume deflects the electrons, the intensity detected on the quadrants is unequal and the difference between opposing the quadrants becomes non-zero (fig. A.3b), indicating the strength of deflection and the direction. This strength of deflection is proportional to the electric field within the sample and the thickness of the probed volume. A more extensive description of DPC in a STEM, read [185, 166].

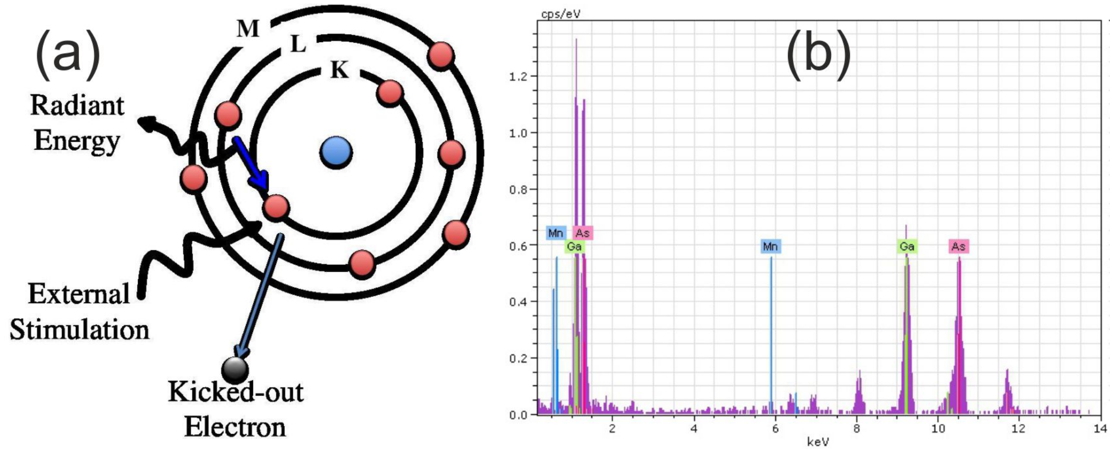

Figure A.2.: (a) Sketch of the principle of EDX: Electrons of the inner atomic shell get excited by external stimulation. The empty state is filled by an electron of the nearest outer shell under the emission of an atomic-specific photon energy. Adopted from [184]. (b) EDX spectrum (violet) of a nanowire grown with Mn supply during growth: the Kα line of Mn at 5.9 keV is absent, while the Ga Kα line and the As Kα line at 9.25 keV and 10.5 keV dominate, indicating an undoped GaAs nanowire.

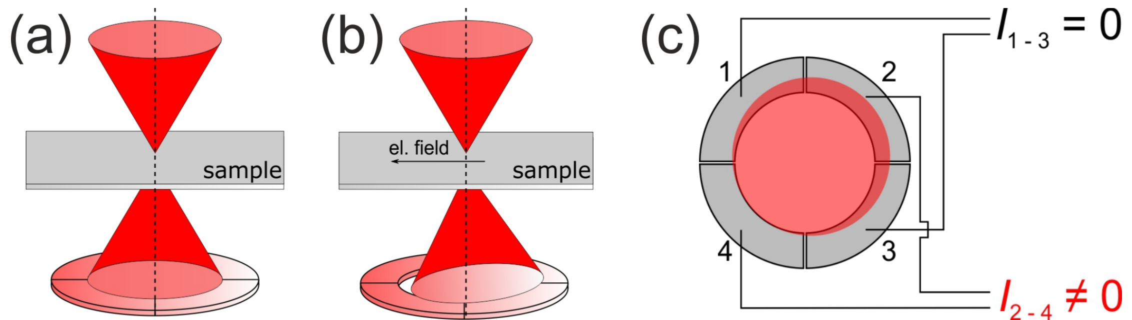

Figure A.3.: Sketches of DPC in a STEM: (a) The vertical to the sample incident electron beam gets deflected by the electric field within the sample. The ring-shaped detector below is separated in four quadrants. (b,c) If an electric field exists within the sample, the diffracted electron distribution is not isotropic any more, and a difference in intensity on opposing sectors is obtained, indicating the strength and direction of the electric field. Adopted from [163].

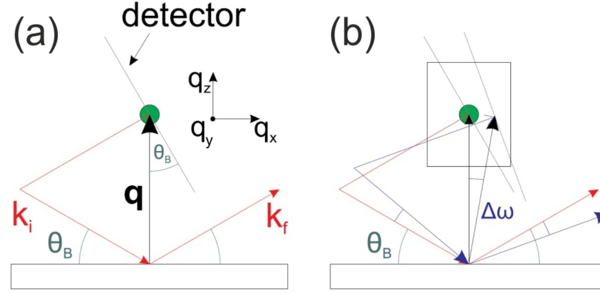

Figure A.4.: Sketch of reciprocal space mapping near symmetric configuration: (a) In symmetric configuration (incidence angle equal scattered angle), the scattering vector $\vec{q} = \vec{k}_f - \vec{k}_i$ is perpendicular to the substrate plane, allowing to monitor constructive interference between crystal planes perpendicular to the substrate surface. (b) By rotating the sample in steps by an angle $\delta\omega$ around the symmetric configuration, a map of diffraction patterns in dependence on the incidence and the scattered angles is recorded, from which the components of the scattering vector, q_x, q_y and q_z, can be calculated.

A.3. Reciprocal space mapping (RSM)

To determine the inter-distances of subsequent atomic planes along the GaAs and GaAs/(Ga,Mn)As core/shell nanowire axes, reciprocal space maps were measured by Andreas Biermanns at the University of Siegen. The experiments were performed using a four circle diffractometer. The samples, mounted on an Euler cradle, were irradiated with the Cu Kα emission line of 1.54056 Å, whose linewidth was narrowed down with a monochromator. In combination with specific analyzer crystals an angular resolution of 0.0001° was yielded.

The RSMs were recorded by performing Θ-2Θ scans in vicinity of the GaAs(111) substrate reflex. In symmetric configuration (fig. A.4a), the scattering vector $\vec{q} = \vec{k}_f - \vec{k}_i$ is vertical to the substrate plane, i.e. Bragg's law can be fulfilled for planes parallel to the substrate surface only. This is the case, when the reciprocal lattice vector, which resides perpendicular to the respective crystal plane, equals the scattering vector (Laue condition). Therefore, in this configuration, the reflex for constructive interference between two subsequent GaAs(111) substrate planes can be found. If the sample is rotated out of the symmetric configuration (fig. A.4b), the Laue condition may be fulfilled for crystal planes, which have an inclination angle towards the substrate. By rotating the sample in small steps $\Delta\omega$ in vicinity of the symmetric configuration, while the incident angle is initially chosen to monitor the GaAs(111) reflex, for each $\Delta\omega$ a diffraction image is recorded, giving a reciprocal space map. Here, the scattered intensity is monitored in dependence of the actual incidence angle for a wide range of scattered angles. From this sets of data all components of the scattering vector q_x, q_y and q_z can be evaluated in reciprocal space, and consequently be attributed to the respective crystal planes. For a more detailed description of X-ray diffraction on GaAs nanowires, read [58].

A.4. Micro-photoluminescence (µPL) spectroscopy

µPL measurements on single GaAs nanowires were performed in a confocal setup in a cryostat, which enables sample temperatures between 4 K and room temperature. By inserting a microscope objective in the beam guidance, the exciting laser light was focused down to a spot of 1 µm in diameter for spatial resolved excitation. The emitted spectrum was collected with the same objective and led to a spectrometer. Polarization resolved measurements were enabled introducing a linear polarizer together with a half-wave plate to be able to adjust the exciting polarization continuously. For analyzing the polarization of the emitted PL, an additional linear polarizer was used. The excitation of the wires was performed with different semiconductor laser diodes above the GaAs band gap, operating in continuous wave (cw) or pulsed mode, depending on the desired excitation power densities. To obtain the characteristic emission related to the GaAs nanowire crystal structure, low power excitation in cw operation was used, avoiding state filling and band gap renormalization effects. In order to yield occupation inversion and lasing-operation from highly excited GaAs nanowires, pulsed laser excitation was chosen. For a more detailed description of the used µPL setup, see [70, 186].

A.5. Superconducting quantum interferometry (SQUID)

Measurements of the magnetic moment of as-grown nanowire ensembles were done in a Quantum Design's Magnetic Property Measurement System, which bases on the functionality of a rf SQUID detector. Moving the magnetic sample back and forth through superconducting detection coils induces an electric supercurrent in the coils. This current is led to a rf SQUID and induces a change in the persistent current flowing in the SQUID, proportional to the change in magnetic flux. Using a Josephson contact, the change in current can be converted into an output voltage, which is proportional to the magnetic moment of the sample. The used device at the chair of Prof. Back is capable to resolve changes of the external magnetic field of 10^{-15} T and allows sample temperatures between 4.2 K and 400 K. For more details about the used SQUID and its measurement methods, see [187].

A.6. Magnetic force microscopy (MFM)

Room temperature magnetic force microscopy measurements were performed with a Veeco Dimension Icon atomic force microscope at the chair of Prof. Weiss. To distinguish between short-ranging van der Waals forces and long-ranging magnetic forces, a ferromagnetic cobalt coated MFM cantilever ("Bruker MESP") was driven in lift-mode. Here, the interaction of probe and sample is first recorded in a AFM contact tapping mode, i.e. mainly van der Waals forces are detected. By tracing the recorded topography in a second scan 50 nm above the sample surface, van der Waals forces, which are proportional to -1/r^6, are drastically reduced. Then, magnetic interactions ($\propto -1/r^3$)

dominate, which also lead to a phase shift of the cantilever oscillation frequency. To depict the magnetic domains of a MnAs segment at a GaAs nanowire tip, the amplitude of this phase shift was plotted in figs. 8.6 in false colors.

A.7. Magnetotransport measurements

To perform magnetotransport measurements on single GaAs/(Ga,Mn)As core/shell nanowires (section 7.3), after nanowire growth, the as-grown wires were first transferred to a SiO_2 covered substrate via ultrasonication and pipetting. Afterwards, single lying wires are contacted with electron beam lithography to be able to measure the resistance in a four terminal configuration. For the details of the contacting procedure and the transfer of the wires, see [127]. The four-terminal magnetotransport measurements were carried out in a cryostat at the chair of Prof. Weiss containing a superconducting coil, which enables monitoring of R(T) and R(H) curves for temperature down to 1.4 K and in external magnetic fields up to 10 T. To be able to align the magnetic field with respect to the nanowire axes, the SiO_2 substrate was mounted on a rotatable holder. For further details about the measurement procedure, see [116].

A.8. Wet chemical etching of Si oxides

To prepare Si(111) wafers, which are covered with a native oxide, for optimum nanowire growth, an etching step was introduced before the growth of the nanowire. Here, a with ultra-pure water diluted ammonium fluoride (NH_4F) mixture containing 1.25 % NH_4F was used. For this mixture, an etching rate of 0.9 nm SiO_2 per second was evaluated previously [145]. The etching of the native oxide was stopped in a bath of ultra-pure water. The silicon substrate is not touched by the etchant, since only SiO_x can be etched by HF-containing mixtures.

B. Binary phase-diagrams

The thermodynamic stable phases occurring in a alloy of two phases at equilibrium conditions are usually summarized in a binary phase diagram. In these diagrams all accessible binary phases from entirely liquid to partially liquid+solid and completely solid are depicted in dependence on its atomic composition and the temperature. In the following, the principles to read a binary phase diagram, and the most common phase transitions are elucidated.

Every binary phase diagram possesses a liquidus line, above which the liquid alloy exists only. This is the top-most line, ranging from the melting point of 100 % of element A to the melting point of 100 % of the element B. For example, in the As-Ga binary phase diagram (fig. B.1), the curve from the Ga melting temperature of 29°C to the melting point of GaAs at 1238°C, which is the only stable solid Ga-As compound, and finally to 818°C for 100 % As. Additionally, one or more solidus lines, depending on the complexity of the binary phase diagram, exist, below which the alloy is completely solid. These are in fig. B.1 the straight lines below either solid GaAs+Ga or GaAs+As are present. In the area between the liquidus and the solidus lines, mixtures of liquid and solid phases exist. Assuming a fixed temperature T and a fixed composition c_0 of the considered system, following the tie line to the next complete solid or liquid phase gives the constituents of the mixture. These constituents possess each the composition given by the respective projection of the intercept to the x-axis (c_l, c_s). The relative amounts f_l and f_s of the constituents are determined by the lever rule. Since the material is found either in the liquid or solid phase, $f_l + f_s = 1$ holds, and additionally the overall composition of both constituents is fixed to c_0, ergo $f_l \cdot c_l + f_s \cdot c_s = c_0$. Then f_s and f_l are set to $f_s = (c_0 - c_l)/(c_s - c_l)$ and $f_l = (c_s - c_0)/(c_s - c_l)$, respectively. Note that the lever rule is not restricted to mixtures of liquid and solid phases only, but also valid for coexisting solid phases.

The most simple phase transition is the one directly from a pure liquid phase to a pure solid one. However, this behavior is rarely seen, for example the forming of stoichiometric GaAs from a liquid of exactly 50 % Ga and 50 % As (compare fig. B.1). If the direct liquid-solid transition from a binary melt to a solid conglomerate is accompanied by the lowering of the melting temperature with respect to the pure phases, this transition is called eutectic. The eutectic point at the local minimum, when the liquidus line meets the solidus line, gives the fixed composition of the eutectic and its melting point. For instance, in the Au-Ga phase diagram (fig. B.2), some eutectic points are observed, one of them enabling to produce a conglomerate of solid Au_7Ga_3 and stoichiometric AuGa directly from a Au-Ga melt with 33.6 % Ga at a melting temperature of 339°C. The knowledge of eutectic points is of technological interest, because here fast proceeding

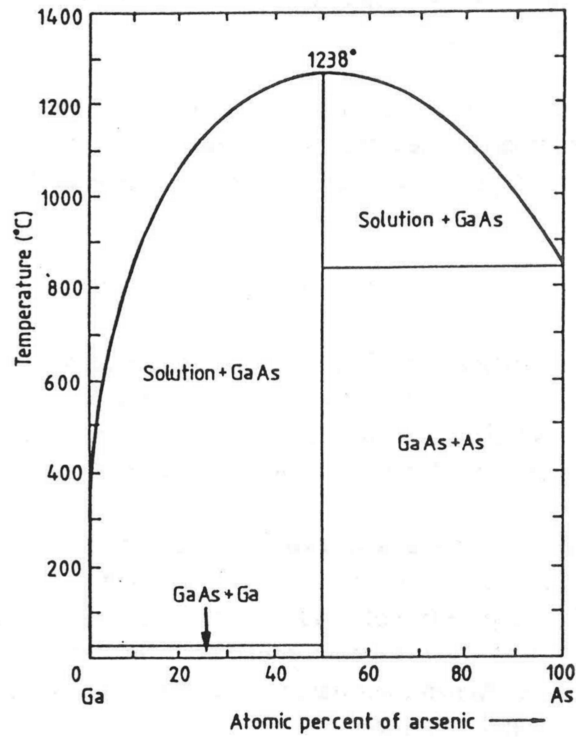

Figure B.1.: Binary As-Ga phase diagram. Adopted from [188].

phase transitions take place at a melting point, which may be crucially below the ones of the pure elements.

Instead, a peritectic phase transition is a very slow proceeding one. Here, clusters of a solid phase α, which are dissolved in the melt, transform during cooling into clusters of another solid phase β. On falling below the transition temperature, which is given by a tie line below the melt+α region, this proceeds by the out-diffusion of one element from the clusters and the corresponding acceptance of the other element in the clusters. At the same time, pure β forms around α, which disturbs the fully transformation of α into β, representing a diffusion barrier for both elements. Thus, during cooling down, usually α particles remain within a shell of β, giving a fingerprint of a peritectic phase transition. The binary Ga-Mn phase diagram (fig. B.3), contains on the Ga-rich side plenty of peritectic reactions. For example, cooling down a suspension of liquid Ga-Mn and $MnGa_4$ with an overall Mn concentration of 10 % below 400°C results in the slow transformation of $MnGa_4$ into $MnGa_6$.

Additionally to the for this work relevant binary phase diagrams in figs. B.1 to B.4, in fig. B.5 a ternary phase diagram of As-Ga-Au is shown. Here, the liquidus surface of the ternary melt is depicted only, sketched by contour lines indicating isotherms. Thus, here the solubility of the three elements in the melt can be extracted only. The liquidus lines from the corresponding binary phase diagrams reside here at the edges of the triangle.

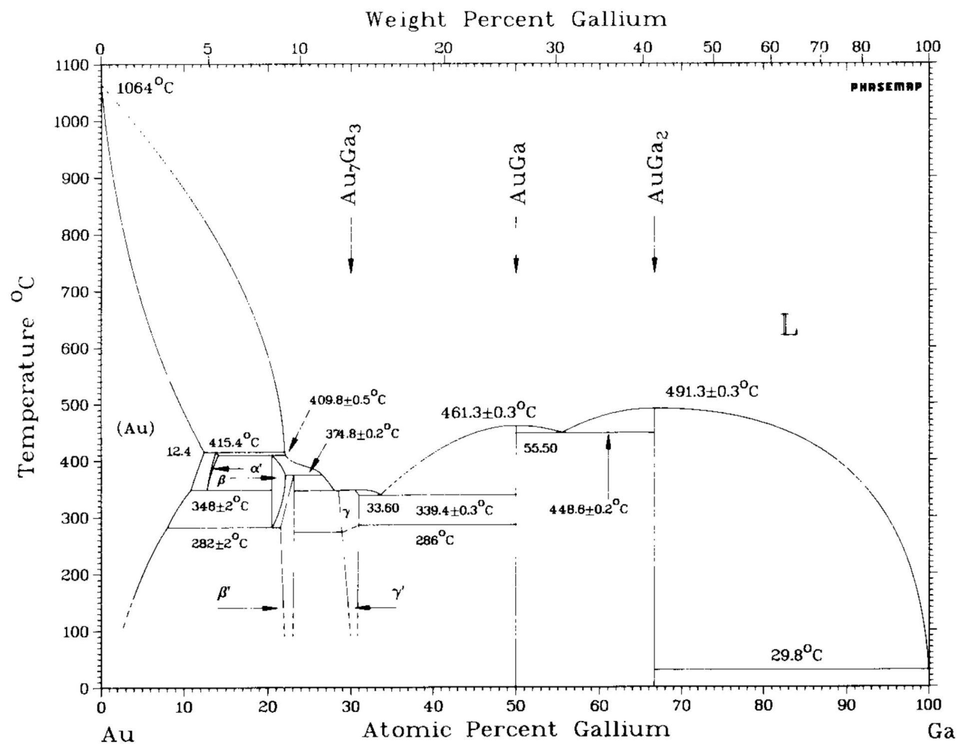

Figure B.2.: Binary Au-Ga phase diagram. Adopted from [189].

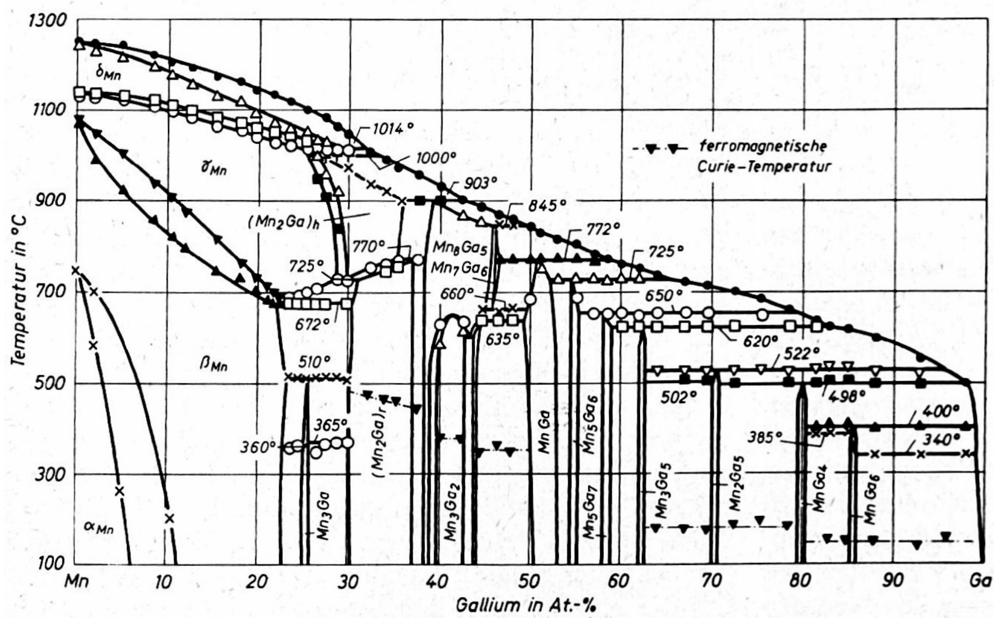

Figure B.3.: Binary Ga-Mn phase diagram. Adopted from [190].

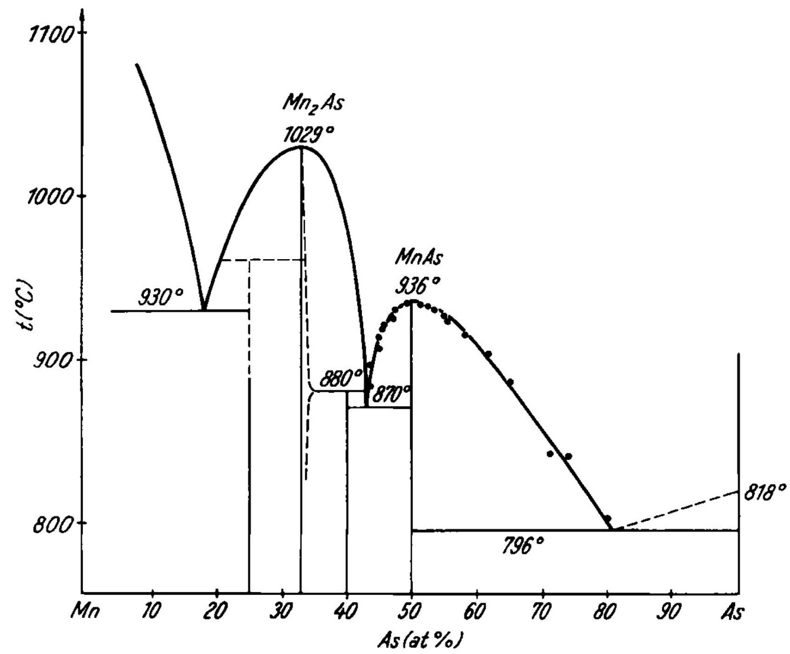

Figure B.4.: Binary As-Mn phase diagram. Adopted from [191].

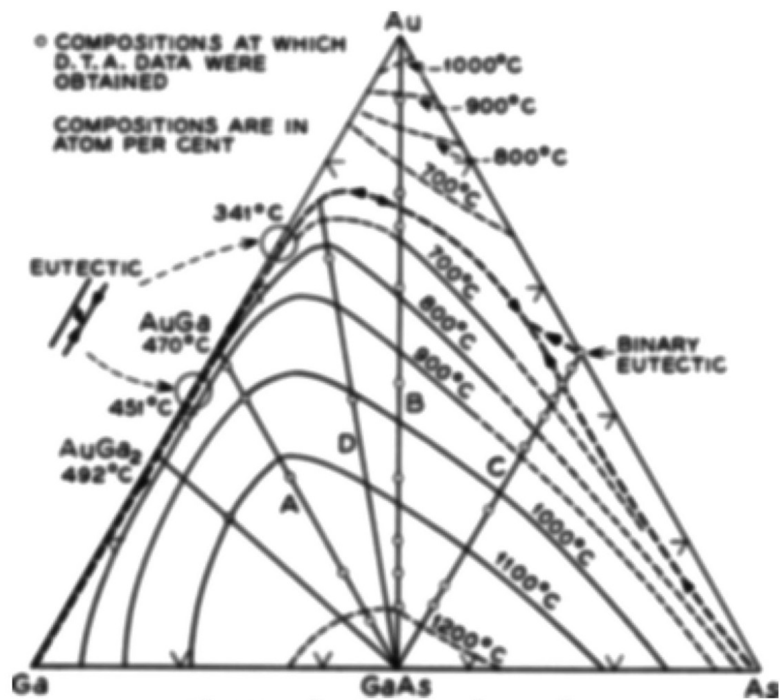

Figure B.5.: Ternary As-Au-Ga phase diagram. Adopted from [192].

C. Publications

Benedikt Bauer, Joachim Hubmann, Matthias Lohr, Elisabeth Reiger, Dominique Bougeard, and Josef Zweck, *Direct detection of spontaneous polarization in wurtzite GaAs nanowires*, Applied Physics Letters **104**, 211902 (2014)

Stephan Furthmeier, Florian Dirnberger, Joachim Hubmann, Benedikt Bauer, Tobias Korn, Christian Schüller, Josef Zweck, Elisabeth Reiger, and Dominique Bougeard, *Long exciton lifetimes in stacking-fault-free wurtzite GaAs nanowires*, Applied Physics Letters **105**, 222109 (2014)

Joachim Hubmann, Benedikt Bauer, Helmut S. Körner, Stephan Furthmeier, Martin Buchner, Günter Bayreuther, Florian Dirnberger, Dieter Schuh, Christian H. Back, Josef Zweck, Elisabeth Reiger and Dominique Bougeard, *Epitaxial Growth of Room-Temperature Ferromagnetic MnAs Segments on GaAs Nanowires via Sequential Crystallization*, Nano Letters, DOI: 10.1021/acs.nanolett.5b03658 (2016)

Joachim Hubmann, Markus Kargl, Andreas Rudolph, Benedikt Bauer, Marcello Soda, Josef Zweck, Dieter Schuh, Werner Wegscheider, Dominique Bougeard and Elisabeth Reiger, *Position controlled growth of GaAs nanowires on Si and GaAs substrates by MBE* (poster), Topical Workshop on MBE-grown Arsenide Nanowires, Berlin (Germany), September 8-9, 2011

Joachim Hubmann, Benedikt Bauer, Christian Butschkow, Stephan Furthmeier, Josef Zweck, Dieter Weiss, Dominique Bougeard and Elisabeth Reiger, *Incorporation of Mn in GaAs-nanowires grown on silicon* (poster), International Workshop on Spin Phenomena in Reduced Dimensions, Regensburg (Germany), September 19-21, 2012

Joachim Hubmann, Benedikt Bauer, Christian Butschkow, Stephan Furthmeier, Dieter Schuh, Josef Zweck, Dieter Weiss, Dominique Bougeard and Elisabeth Reiger, *Incorporation of Mn in GaAs-nanowires grown on silicon* (poster), 7th Nanowire Growth Workshop, Lausanne (Switzerland), June 10-12, 2013

Joachim Hubmann, Stephan Furthmeier, Benedikt Bauer, Andreas Bayer, Elisabeth Reiger, Josef Zweck and Dominique Bougeard, *Polarization phenomena and optical spin orientation in wurtzite GaAs nanowires* (poster), 8th Nanowire Growth Workshop - Nanowires 2014, Eindhoven (Netherlands), 25-29 August, 2014

D. Abbreviations

AFM	atomic force microscopy
BEP	beam equivalent pressure
DPC	differential phase contrast microscopy
EDX	energy-dispersive X-ray spectroscopy
FWHM	full width at half maximum
(LT) MBE	(low temperature) molecular beam epitaxy
MFM	magnetic force microscopy
(µ)PL	(micro)-photoluminescence
(N)MR	(negative) magnetoresistance
MOVPE	metal-organic vapor phase epitaxy
RHEED	reflection high-energy electron diffraction
RSM	reciprocal space map
SEM	scanning electron microscopy
SF	stacking fault
SQUID	superconducting quantum interference device
(HR)(S)TEM	(high resolution)(scanning) transmission electron microscopy
TP	twin plane
TPL	triple phase line
VLS	vapor-liquid-solid growth mechanism
WZ	wurtzite crystal structure
XRD	x-ray diffraction
ZB	zinc-blende crystal structure

Bibliography

[1] P. Yang, R. Yan, and M. Fardy, "Semiconductor nanowire: What's next?," *Nano Letters*, vol. 10, no. 5, pp. 1529–1536, 2010.

[2] Y. Cui, Z. Zhong, D. Wang, W. U. Wang, and C. M. Lieber, "High performance silicon nanowire field effect transistors," *Nano Letters*, vol. 3, no. 2, pp. 149–152, 2003.

[3] K. Tomioka, J. Motohisa, S. Hara, K. Hiruma, and T. Fukui, "GaAs/AlGaAs Core Multishell Nanowire-Based Light-Emitting Diodes on Si," *Nano Letters*, vol. 10, no. 5, pp. 1639–1644, 2010.

[4] M. H. Huang, S. Mao, H. Feick, H. Yan, Y. Wu, H. Kind, E. Weber, R. Russo, and P. Yang, "Room-Temperature Ultraviolet Nanowire Nanolasers," *Science*, vol. 292, no. 5523, pp. 1897–1899, 2001.

[5] R. Yan, D. Gargas, and P. Yang, "Nanowire photonics," *Nature Photonics*, vol. 3, no. 10, pp. 569–576, 2009.

[6] E. Garnett and P. Yang, "Light Trapping in Silicon Nanowire Solar Cells," *Nano Letters*, vol. 10, no. 3, pp. 1082–1087, 2010.

[7] P. V. Radovanovic, C. J. Barrelet, S. Gradečak, F. Qian, and C. M. Lieber, "General Synthesis of Manganese-Doped II-VI and III-V Semiconductor Nanowires," *Nano Letters*, vol. 5, no. 7, pp. 1407–1411, 2005.

[8] S. Plissard, G. Larrieu, X. Wallart, and P. Caroff, "High yield of self-catalyzed GaAs nanowire arrays grown on silicon via gallium droplet positioning," *Nanotechnology*, vol. 22, no. 27, p. 275602, 2011.

[9] B. Bauer, A. Rudolph, M. Soda, A. F. i Morral, J. Zweck, D. Schuh, and E. Reiger, "Position controlled self-catalyzed growth of GaAs nanowires by molecular beam epitaxy," *Nanotechnology*, vol. 21, no. 43, p. 435601, 2010.

[10] S. J. Gibson, J. P. Boulanger, and R. R. LaPierre, "Opportunities and pitfalls in patterned self-catalyzed GaAs nanowire growth on silicon," *Semiconductor Science and Technology*, vol. 28, no. 10, p. 105025, 2013.

[11] A. M. Munshi, D. L. Dheeraj, V. T. Fauske, D. C. Kim, J. Huh, J. F. Reinertsen, L. Ahtapodov, K. D. Lee, B. Heidari, A. T. J. van Helvoort, B. O. Fimland,

and H. Weman, "Position-Controlled Uniform GaAs Nanowires on Silicon using Nanoimprint Lithography," *Nano Letters*, vol. 14, no. 2, pp. 960–966, 2014.

[12] C.-Y. Yeh, Z. W. Lu, S. Froyen, and A. Zunger, "Zinc-blende˘wurtzite polytypism in semiconductors," *Phys. Rev. B*, vol. 46, pp. 10086–10097, 1992.

[13] F. Glas, J.-C. Harmand, and G. Patriarche, "Why Does Wurtzite Form in Nanowires of III-V Zinc Blende Semiconductors?," *Phys. Rev. Lett.*, vol. 99, p. 146101, 2007.

[14] K. A. Dick, P. Caroff, J. Bolinsson, M. E. Messing, J. Johansson, K. Deppert, L. R. Wallenberg, and L. Samuelson, "Control of III–V nanowire crystal structure by growth parameter tuning," *Semiconductor Science and Technology*, vol. 25, no. 2, p. 024009, 2010.

[15] L. J. Lauhon, M. S. Gudiksen, D. Wang, and C. M. Lieber, "Epitaxial core-shell and core-multishell nanowire heterostructures," *Nature*, vol. 420, no. 6911, pp. 57–61, 2002.

[16] Y. N. Guo, J. Zou, M. Paladugu, H. Wang, Q. Gao, H. H. Tan, and C. Jagadish, "Structural characteristics of GaSb/GaAs nanowire heterostructures grown by metal-organic chemical vapor deposition," *Applied Physics Letters*, vol. 89, no. 23, p. 231917, 2006.

[17] P. Caroff, M. E. Messing, B. M. Borg, K. A. Dick, K. Deppert, and L.-E. Wernersson, "InSb heterostructure nanowires: MOVPE growth under extreme lattice mismatch," *Nanotechnology*, vol. 20, no. 49, p. 495606, 2009.

[18] H. Ohno, A. Shen, F. Matsukura, A. Oiwa, A. Endo, S. Katsumoto, and Y. Iye, "(Ga,Mn)As: A new diluted magnetic semiconductor based on GaAs," *Applied Physics Letters*, vol. 69, no. 3, pp. 363–365, 1996.

[19] A. Rudolph, M. Soda, M. Kiessling, T. Wojtowicz, D. Schuh, W. Wegscheider, J. Zweck, C. Back, and E. Reiger, "Ferromagnetic GaAs/GaMnAs Core-Shell Nanowires Grown by Molecular Beam Epitaxy," *Nano Letters*, vol. 9, no. 11, pp. 3860–3866, 2009.

[20] C. Butschkow, E. Reiger, A. Rudolph, S. Geißler, D. Neumaier, M. Soda, D. Schuh, G. Woltersdorf, W. Wegscheider, and D. Weiss, "Origin of negative magnetoresistance of GaAs/(Ga,Mn)As core-shell nanowires," *Phys. Rev. B*, vol. 87, p. 245303, 2013.

[21] L. Chen, S. Yan, P. F. Xu, J. Lu, W. Z. Wang, J. J. Deng, X. Qian, Y. Ji, and J. H. Zhao, "Low-temperature magnetotransport behaviors of heavily Mn-doped (Ga,Mn)As films with high ferromagnetic transition temperature," *Applied Physics Letters*, vol. 95, no. 18, p. 182505, 2009.

[22] S. Hara, “Bottom-Up Formation of Vertical Free-Standing Semiconductor Nanowires Hybridized with Ferromagnetic Nanoclusters,” *Materials Science Forum*, vol. 783-786, pp. 1990–1995, 2014.

[23] R. S. Wagner and W. C. Ellis, “VAPOR-LIQUID-SOLID MECHANISM OF SINGLE CRYSTAL GROWTH,” *Applied Physics Letters*, vol. 4, no. 5, pp. 89–90, 1964.

[24] R. Wagner and W. Ellis, “The Vapor-Liquid-Solid Mechanism of Crystal Growth and Its Application to Silicon,” *TRANSACTIONS OF THE METALLURGICAL SOCIETY OF AIME*, vol. 233, pp. 1053–1064, 1965.

[25] E. Givargizov, “Fundamental aspects of VLS growth,” *Journal of Crystal Growth*, vol. 31, no. 0, pp. 20–30, 1975.

[26] V. G. Dubrovskii and N. V. Sibirev, “Growth rate of a crystal facet of arbitrary size and growth kinetics of vertical nanowires,” *Phys. Rev. E*, vol. 70, p. 031604, 2004.

[27] V. G. Dubrovskii, G. E. Cirlin, I. P. Soshnikov, A. A. Tonkikh, N. V. Sibirev, Y. B. Samsonenko, and V. M. Ustinov, “Diffusion-induced growth of GaAs nanowhiskers during molecular beam epitaxy: Theory and experiment,” *Phys. Rev. B*, vol. 71, p. 205325, 2005.

[28] V. G. Dubrovskii, N. V. Sibirev, G. E. Cirlin, J. C. Harmand, and V. M. Ustinov, “Theoretical analysis of the vapor-liquid-solid mechanism of nanowire growth during molecular beam epitaxy,” *Phys. Rev. E*, vol. 73, p. 021603, 2006.

[29] V. G. Dubrovskii, N. V. Sibirev, J. C. Harmand, and F. Glas, “Growth kinetics and crystal structure of semiconductor nanowires,” *Phys. Rev. B*, vol. 78, p. 235301, 2008.

[30] V. G. Dubrovskii, N. V. Sibirev, G. E. Cirlin, I. P. Soshnikov, W. H. Chen, R. Larde, E. Cadel, P. Pareige, T. Xu, B. Grandidier, J.-P. Nys, D. Stievenard, M. Moewe, L. C. Chuang, and C. Chang-Hasnain, “Gibbs-Thomson and diffusion-induced contributions to the growth rate of Si, InP, and GaAs nanowires,” *Phys. Rev. B*, vol. 79, p. 205316, 2009.

[31] C. Colombo, D. Spirkoska, M. Frimmer, G. Abstreiter, and A. Fontcuberta i Morral, “Ga-assisted catalyst-free growth mechanism of GaAs nanowires by molecular beam epitaxy,” *Phys. Rev. B*, vol. 77, p. 155326, 2008.

[32] G. E. Cirlin, V. G. Dubrovskii, Y. B. Samsonenko, A. D. Bouravleuv, K. Durose, Y. Y. Proskuryakov, B. Mendes, L. Bowen, M. A. Kaliteevski, R. A. Abram, and D. Zeze, “Self-catalyzed, pure zincblende GaAs nanowires grown on Si(111) by molecular beam epitaxy,” *Phys. Rev. B*, vol. 82, p. 035302, 2010.

[33] M. Soda, A. Rudolph, D. Schuh, J. Zweck, D. Bougeard, and E. Reiger, "Transition from Au to pseudo-Ga catalyzed growth mode observed in GaAs nanowires grown by molecular beam epitaxy," *Phys. Rev. B*, vol. 85, p. 245450, 2012.

[34] P. Krogstrup, S. Curiotto, E. Johnson, M. Aagesen, J. Nygård, and D. Chatain, "Impact of the Liquid Phase Shape on the Structure of III-V Nanowires," *Phys. Rev. Lett.*, vol. 106, p. 125505, 2011.

[35] P. Krogstrup, H. I. Jørgensen, E. Johnson, M. H. Madsen, C. B. Sørensen, A. F. i Morral, M. Aagesen, J. Nygård, and F. Glas, "Advances in the theory of III–V nanowire growth dynamics," *Journal of Physics D: Applied Physics*, vol. 46, no. 31, p. 313001, 2013.

[36] B. Mutaftschiev, *The Atomistic Nature of Crystal Growth.* Springer, 2001.

[37] F. Glas, "Chemical potentials for Au-assisted vapor-liquid-solid growth of III-V nanowires," *Journal of Applied Physics*, vol. 108, no. 7, p. 073506, 2010.

[38] H. Eyring, "The Activated Complex in Chemical Reactions," *The Journal of Chemical Physics*, vol. 3, no. 2, pp. 107–115, 1935.

[39] P. Krogstrup, R. Popovitz-Biro, E. Johnson, M. H. Madsen, J. Nygård, and H. Shtrikman, "Structural Phase Control in Self-Catalyzed Growth of GaAs Nanowires on Silicon (111)," *Nano Letters*, vol. 10, no. 11, pp. 4475–4482, 2010.

[40] M. R. Ramdani, J. C. Harmand, F. Glas, G. Patriarche, and L. Travers, "Arsenic Pathways in Self-Catalyzed Growth of GaAs Nanowires," *Crystal Growth & Design*, vol. 13, no. 1, pp. 91–96, 2013.

[41] V. Pankoke, S. Sakong, and P. Kratzer, "Role of sidewall diffusion in GaAs nanowire growth: A first-principles study," *Phys. Rev. B*, vol. 86, p. 085425, 2012.

[42] F. Glas, M. R. Ramdani, G. Patriarche, and J.-C. Harmand, "Predictive modeling of self-catalyzed III-V nanowire growth," *Phys. Rev. B*, vol. 88, p. 195304, 2013.

[43] J. Johansson, C. P. T. Svensson, T. Mårtensson, L. Samuelson, and W. Seifert, "Mass Transport Model for Semiconductor Nanowire Growth," *The Journal of Physical Chemistry B*, vol. 109, no. 28, pp. 13567–13571, 2005.

[44] C.-Y. Wen, J. Tersoff, M. C. Reuter, E. A. Stach, and F. M. Ross, "Step-Flow Kinetics in Nanowire Growth," *Phys. Rev. Lett.*, vol. 105, p. 195502, 2010.

[45] V. G. Dubrovskii, "Self-regulated pulsed nucleation in catalyzed nanowire growth," *Phys. Rev. B*, vol. 87, p. 195426, 2013.

[46] J. Johansson, L. S. Karlsson, C. Patrik T. Svensson, T. Martensson, B. A. Wacaser, K. Deppert, L. Samuelson, and W. Seifert, "Structural properties of $\langle 111 \rangle$B - oriented III-V nanowires," *Nature Materials*, vol. 5, pp. 574–580, 2006.

[47] J. Johansson, J. Bolinsson, M. Ek, P. Caroff, and K. A. Dick, "Combinatorial Approaches to Understanding Polytypism in III–V Nanowires," *ACS Nano*, vol. 6, no. 7, pp. 6142–6149, 2012.

[48] M. I. McMahon and R. J. Nelmes, "Observation of a Wurtzite Form of Gallium Arsenide," *Phys. Rev. Lett.*, vol. 95, p. 215505, 2005.

[49] A. Jenichen, C. Engler, and B. Rauschenbach, "Comparison of wurtzite and zincblende GaAs surfaces as possible nanowire side walls: {DFT} stability calculations," *Surface Science*, vol. 613, no. 0, pp. 74–79, 2013.

[50] A. Jenichen and C. Engler, "Reconstructions and surface facets of the GaAs(112)A and (112)B surfaces: First-principles {DFT} supercell calculations," *Surface Science*, vol. 608, no. 0, pp. 204–211, 2013.

[51] S. Takeuchi and K. Suzuki, "Stacking Fault Energies of Tetrahedrally Coordinated Crystals," *physica status solidi (a)*, vol. 171, no. 1, pp. 99–103, 1999.

[52] F. M. Ross, J. Tersoff, and M. C. Reuter, "Sawtooth Faceting in Silicon Nanowires," *Phys. Rev. Lett.*, vol. 95, p. 146104, 2005.

[53] C. Chatillon and D. Chatain, "Congruent vaporization of GaAs(s) and stability of Ga(l) droplets at the GaAs(s) surface," *Journal of Crystal Growth*, vol. 151, no. 1–2, pp. 91–101, 1995.

[54] S. Hardy, "The surface tension of liquid gallium," *Journal of Crystal Growth*, vol. 71, no. 3, pp. 602 – 606, 1985.

[55] R. Eötvös, "Ueber den Zusammenhang der Oberflächenspannung der Flüssigkeiten mit ihrem Molecularvolumen," *Annalen der Physik*, vol. 263, no. 3, pp. 448–459, 1886.

[56] K. C. Mills and Y. C. Su, "Review of surface tension data for metallic elements and alloys: Part 1 – Pure metals," *International Materials Reviews*, vol. 51, no. 6, pp. 329–351, 2006.

[57] T. Young, "An Essay on the Cohesion of Fluids," *Philosophical Transactions of the Royal Society of London*, vol. 95, pp. 65–87, 1805.

[58] A. Biermanns, "X-ray diffraction from single GaAs nanowires," PhD thesis, Universität Siegen, 2012.

[59] D. Spirkoska, J. Arbiol, A. Gustafsson, S. Conesa-Boj, F. Glas, I. Zardo, M. Heigoldt, M. H. Gass, A. L. Bleloch, S. Estrade, M. Kaniber, J. Rossler, F. Peiro, J. R. Morante, G. Abstreiter, L. Samuelson, and A. Fontcuberta i Morral, "Structural and optical properties of high quality zinc-blende/wurtzite GaAs nanowire heterostructures," *Phys. Rev. B*, vol. 80, p. 245325, 2009.

[60] J. Johansson, B. A. Wacaser, K. A. Dick, and W. Seifert, "Growth related aspects of epitaxial nanowires," *Nanotechnology*, vol. 17, no. 11, p. S355, 2006.

[61] T. Akiyama, K. Sano, K. Nakamura, and T. Ito, "An Empirical Potential Approach to Wurtzite–Zinc-Blende Polytypism in Group III–V Semiconductor Nanowires," *Japanese Journal of Applied Physics*, vol. 45, no. 3L, p. L275, 2006.

[62] R. Leitsmann and F. Bechstedt, "Surface influence on stability and structure of hexagon-shaped III-V semiconductor nanorods," *Journal of Applied Physics*, vol. 102, no. 6, p. 063528, 2007.

[63] T. Ito, T. Akiyama, and K. Nakamura, "Simple Systematization of Structural Stability for $A^{N}B^{8-N}$ Compounds," *Japanese Journal of Applied Physics*, vol. 46, no. 1R, p. 345, 2007.

[64] T. Ito, "Simple Criterion for Wurtzite-Zinc-Blende Polytypism in Semiconductors," *Japanese Journal of Applied Physics*, vol. 37, no. 10B, p. L1217, 1998.

[65] R. T. Sanderson, *Chemical bonds and bond energy.* New York ; London : Academic Press, 1971.

[66] A. Belabbes, J. Furthmüller, and F. Bechstedt, "Relation between spontaneous polarization and crystal field from first principles," *Phys. Rev. B*, vol. 87, p. 035305, 2013.

[67] J. Lähnemann, O. Brandt, U. Jahn, C. Pfüller, C. Roder, P. Dogan, F. Grosse, A. Belabbes, F. Bechstedt, A. Trampert, and L. Geelhaar, "Direct experimental determination of the spontaneous polarization of GaN," *Phys. Rev. B*, vol. 86, p. 081302, 2012.

[68] J. L. Birman, "Some Selection Rules for Band-Band Transitions in Wurtzite Structure," *Phys. Rev.*, vol. 114, pp. 1490–1492, 1959.

[69] J. L. Birman, "Simplified LCAO Method for Zincblende, Wurtzite, and Mixed Crystal Structures," *Phys. Rev.*, vol. 115, pp. 1493–1505, 1959.

[70] F. Dirnberger, "Spin Dynamics in Wurtzite GaAs Nanowires," masters thesis, Universität Regensburg, 2015.

[71] R. Winkler, *Spin-orbit Coupling Effects in Two-Dimensional Electron and Hole Systems.* Springer, 12 2010.

[72] Y. Varshni, "Temperature dependence of the energy gap in semiconductors," *Physica*, vol. 34, no. 1, pp. 149–154, 1967.

[73] M. R. Brozel and G. E. Stillman, eds., *Properties of Gallium Arsenide.* Inspec/Iee, 3 sub ed., 1996.

[74] C.-Y. Yeh, S.-H. Wei, and A. Zunger, "Relationships between the band gaps of the zinc-blende and wurtzite modifications of semiconductors," *Phys. Rev. B*, vol. 50, pp. 2715–2718, 1994.

[75] M. Murayama and T. Nakayama, "Chemical trend of band offsets at wurtzite/zinc-blende heterocrystalline semiconductor interfaces," *Phys. Rev. B*, vol. 49, pp. 4710–4724, 1994.

[76] Z. Zanolli, F. Fuchs, J. Furthmüller, U. von Barth, and F. Bechstedt, "Model GW band structure of InAs and GaAs in the wurtzite phase," *Phys. Rev. B*, vol. 75, p. 245121, 2007.

[77] A. De and C. E. Pryor, "Predicted band structures of III-V semiconductors in the wurtzite phase," *Phys. Rev. B*, vol. 81, p. 155210, 2010.

[78] C. Wilhelm, A. Larrue, X. Dai, D. Migas, and C. Soci, "Anisotropic photonic properties of III-V nanowires in the zinc-blende and wurtzite phase," *Nanoscale*, vol. 4, pp. 1446–1454, 2012.

[79] L. P. Bouckaert, R. Smoluchowski, and E. Wigner, "Theory of Brillouin Zones and Symmetry Properties of Wave Functions in Crystals," *Phys. Rev.*, vol. 50, pp. 58–67, 1936.

[80] O. Demichel, M. Heiss, J. Bleuse, H. Mariette, and A. Fontcuberta i Morral, "Impact of surfaces on the optical properties of GaAs nanowires," *Applied Physics Letters*, vol. 97, no. 20, p. 201907, 2010.

[81] C.-C. Chang, C.-Y. Chi, M. Yao, N. Huang, C.-C. Chen, J. Theiss, A. W. Bushmaker, S. LaLumondiere, T.-W. Yeh, M. L. Povinelli, C. Zhou, P. D. Dapkus, and S. B. Cronin, "Electrical and Optical Characterization of Surface Passivation in GaAs Nanowires," *Nano Letters*, vol. 12, no. 9, pp. 4484–4489, 2012.

[82] N. Jiang, P. Parkinson, Q. Gao, S. Breuer, H. H. Tan, J. Wong-Leung, and C. Jagadish, "Long minority carrier lifetime in Au-catalyzed GaAs/$Al_xGa_{1-x}As$ core-shell nanowires," *Applied Physics Letters*, vol. 101, no. 2, p. 023111, 2012.

[83] R. J. Nelson and R. G. Sobers, "Interfacial recombination velocity in GaAlAs/GaAs heterostructures," *Applied Physics Letters*, vol. 32, no. 11, pp. 761–763, 1978.

[84] D. Rudolph, S. Funk, M. Döblinger, S. Morkötter, S. Hertenberger, L. Schweickert, J. Becker, S. Matich, M. Bichler, D. Spirkoska, I. Zardo, J. J. Finley, G. Abstreiter, and G. Koblmüller, "Spontaneous Alloy Composition Ordering in GaAs-AlGaAs Core–Shell Nanowires," *Nano Letters*, vol. 13, no. 4, pp. 1522–1527, 2013.

[85] W. Yi, V. Narayanamurti, H. Lu, M. A. Scarpulla, A. C. Gossard, Y. Huang, J.-H. Ryou, and R. D. Dupuis, “Bandgap and band offsets determination of semiconductor heterostructures using three-terminal ballistic carrier spectroscopy,” *Applied Physics Letters*, vol. 95, no. 11, p. 112102, 2009.

[86] D. A. Beaton, K. Alberi, B. Fluegel, A. Mascarenhas, and J. L. Reno, “Precise Determination of the Direct–Indirect Band Gap Energy Crossover Composition in $Al_xGa_{1\text{-}x}As$,” *Applied Physics Express*, vol. 6, no. 7, p. 071201, 2013.

[87] L. Pavesi and M. Guzzi, “Photoluminescence of $Al_xGa_{1-x}As$ alloys,” *Journal of Applied Physics*, vol. 75, no. 10, pp. 4779–4842, 1994.

[88] H. J. Zhu, M. Ramsteiner, H. Kostial, M. Wassermeier, H.-P. Schönherr, and K. H. Ploog, “Room-Temperature Spin Injection from Fe into GaAs,” *Phys. Rev. Lett.*, vol. 87, p. 016601, 2001.

[89] A. T. Hanbicki, B. T. Jonker, G. Itskos, G. Kioseoglou, and A. Petrou, “Efficient electrical spin injection from a magnetic metal/tunnel barrier contact into a semiconductor,” *Applied Physics Letters*, vol. 80, no. 7, pp. 1240–1242, 2002.

[90] A. Kawaharazuka, M. Ramsteiner, J. Herfort, H.-P. Schönherr, H. Kostial, and K. H. Ploog, “Spin injection from Fe_3Si into GaAs,” *Applied Physics Letters*, vol. 85, no. 16, pp. 3492–3494, 2004.

[91] A. Sinsarp, T. Manago, F. Takano, and H. Akinaga, “Electrical Spin Injection from Out-of-Plane Magnetized FePt/MgO Tunneling Junction into GaAs at Room Temperature,” *Japanese Journal of Applied Physics*, vol. 46, no. 1L, p. L4, 2007.

[92] B. T. Jonker, Y. D. Park, B. R. Bennett, H. D. Cheong, G. Kioseoglou, and A. Petrou, “Robust electrical spin injection into a semiconductor heterostructure,” *Phys. Rev. B*, vol. 62, pp. 8180–8183, 2000.

[93] Y. Ohno, D. Young, B. a. Beschoten, F. Matsukura, H. Ohno, and D. Awschalom, “Electrical spin injection in a ferromagnetic semiconductor heterostructure,” *Nature*, vol. 402, no. 6763, pp. 790–792, 1999.

[94] M. Ramsteiner, H. Y. Hao, A. Kawaharazuka, H. J. Zhu, M. Kästner, R. Hey, L. Däweritz, H. T. Grahn, and K. H. Ploog, “Electrical spin injection from ferromagnetic MnAs metal layers into GaAs,” *Phys. Rev. B*, vol. 66, p. 081304, 2002.

[95] R. Fiederling, M. Keim, G. a. Reuscher, W. Ossau, G. Schmidt, A. Waag, and L. Molenkamp, “Injection and detection of a spin-polarized current in a light-emitting diode,” *Nature*, vol. 402, no. 6763, pp. 787–790, 1999.

[96] S. Blundell, *Magnetism in Condensed Matter (Oxford Master Series in Physics)*. Oxford University Press, USA, 1 ed., 2001.

[97] T. Jungwirth, K. Y. Wang, J. Mašek, K. W. Edmonds, J. König, J. Sinova, M. Polini, N. A. Goncharuk, A. H. MacDonald, M. Sawicki, A. W. Rushforth, R. P. Campion, L. X. Zhao, C. T. Foxon, and B. L. Gallagher, "Prospects for high temperature ferromagnetism in (Ga,Mn)As semiconductors," *Phys. Rev. B*, vol. 72, p. 165204, 2005.

[98] T. Jungwirth, J. Sinova, J. Mašek, J. Kučera, and A. H. MacDonald, "Theory of ferromagnetic (III,Mn)V semiconductors," *Rev. Mod. Phys.*, vol. 78, pp. 809–864, 2006.

[99] K. M. Yu, W. Walukiewicz, T. Wojtowicz, I. Kuryliszyn, X. Liu, Y. Sasaki, and J. K. Furdyna, "Effect of the location of Mn sites in ferromagnetic $Ga_{1-x}Mn_xAs$ on its Curie temperature," *Phys. Rev. B*, vol. 65, p. 201303, 2002.

[100] A. H. MacDonald, P. Schiffer, and N. Samarth, "Ferromagnetic semiconductors: moving beyond (Ga,Mn)As," *Nature Materials*, vol. 4, pp. 195–202, 2005.

[101] A. Suda and N. Otsuka, "Arsenic flux dependence of incorporation of excess arsenic in molecular beam epitaxy of GaAs at low temperature," *Applied Physics Letters*, vol. 73, no. 11, pp. 1529–1531, 1998.

[102] J. Mašek, J. Kudrnovský, and F. Máca, "Lattice constant in diluted magnetic semiconductors (Ga,Mn)As," *Phys. Rev. B*, vol. 67, p. 153203, 2003.

[103] R. A. Chapman and W. G. Hutchinson, "Photoexcitation and Photoionization of Neutral Manganese Acceptors in Gallium Arsenide," *Phys. Rev. Lett.*, vol. 18, pp. 443–445, 1967.

[104] G. van der Laan, K. W. Edmonds, E. Arenholz, N. R. S. Farley, and B. L. Gallagher, "Valence-state model of strain-dependent Mn $L_{2,3}$ x-ray magnetic circular dichroism from ferromagnetic semiconductors," *Phys. Rev. B*, vol. 81, p. 214422, 2010.

[105] T. Jungwirth, J. Sinova, A. H. MacDonald, B. L. Gallagher, V. Novák, K. W. Edmonds, A. W. Rushforth, R. P. Campion, C. T. Foxon, L. Eaves, E. Olejnik, J. Mašek, S.-R. E. Yang, J. Wunderlich, C. Gould, L. W. Molenkamp, T. Dietl, and H. Ohno, "Character of states near the Fermi level in (Ga,Mn)As: Impurity to valence band crossover," *Phys. Rev. B*, vol. 76, p. 125206, 2007.

[106] T. Dietl, H. Ohno, F. Matsukura, J. Cibert, and D. Ferrand, "Zener model description of ferromagnetism in zinc-blende magnetic semiconductors," *Science*, vol. 287, no. 5455, pp. 1019–1022, 2000.

[107] M. A. Ruderman and C. Kittel, "Indirect Exchange Coupling of Nuclear Magnetic Moments by Conduction Electrons," *Phys. Rev.*, vol. 96, pp. 99–102, 1954.

[108] T. Kasuya, "A Theory of Metallic Ferro- and Antiferromagnetism on Zener's Model," *Progress of Theoretical Physics*, vol. 16, no. 1, pp. 45–57, 1956.

[109] K. Yosida, "Magnetic Properties of Cu-Mn Alloys," *Phys. Rev.*, vol. 106, pp. 893–898, 1957.

[110] T. Dietl, A. Haury, and Y. Merle d'Aubigné, "Free carrier-induced ferromagnetism in structures of diluted magnetic semiconductors," *Phys. Rev. B*, vol. 55, pp. R3347–R3350, 1997.

[111] T. Dietl, H. Ohno, and F. Matsukura, "Hole-mediated ferromagnetism in tetrahedrally coordinated semiconductors," *Phys. Rev. B*, vol. 63, p. 195205, 2001.

[112] X. Yu, H. Wang, D. Pan, J. Zhao, J. Misuraca, S. von Molnár, and P. Xiong, "All Zinc-Blende GaAs/(Ga,Mn)As Core-Shell Nanowires with Ferromagnetic Ordering," *Nano Letters*, vol. 13, no. 4, pp. 1572–1577, 2013.

[113] M. Soda, "Structural and morphological TEM characterization of GaAs based nanowires," PhD thesis, Universität Regensburg, 2012.

[114] A. Rudolph, "MBE Growth of GaAs Nanowires and Nanowire Heterostructures," PhD thesis, Universität Regensburg, 2011.

[115] U. Wurstbauer, M. Sperl, M. Soda, D. Neumaier, D. Schuh, G. Bayreuther, J. Zweck, and W. Wegscheider, "Ferromagnetic GaMnAs grown on (110) faced GaAs," *Applied Physics Letters*, vol. 92, no. 10, p. 102506, 2008.

[116] C. Butschkow, "- title not yet available -," PhD thesis, Universität Regensburg, 2015.

[117] J. Wenisch, C. Gould, L. Ebel, J. Storz, K. Pappert, M. J. Schmidt, C. Kumpf, G. Schmidt, K. Brunner, and L. W. Molenkamp, "Control of Magnetic Anisotropy in (Ga, Mn)As by Lithography-Induced Strain Relaxation," *Phys. Rev. Lett.*, vol. 99, p. 077201, 2007.

[118] J. Wenisch, L. Ebel, C. Gould, G. Schmidt, L. Molenkamp, and K. Brunner, "Epitaxial GaMnAs layers and nanostructures with anisotropy in structural and magnetic properties," *Journal of Crystal Growth*, vol. 301–302, no. 0, pp. 638–641, 2007.

[119] G. Xiang, A. W. Holleitner, B. L. Sheu, F. M. Mendoza, O. Maksimov, M. B. Stone, P. Schiffer, D. D. Awschalom, and N. Samarth, "Magnetoresistance anomalies in (Ga,Mn)As epilayers with perpendicular magnetic anisotropy," *Phys. Rev. B*, vol. 71, p. 241307, 2005.

[120] V. D. Nguyen, C. Naylor, L. Vila, A. Marty, P. Laczkowski, C. Beigné, L. Notin, Z. Ishaque, and J. P. Attané, "Magnon magnetoresistance of NiFe nanowires: Size

dependence and domain wall detection," *Applied Physics Letters*, vol. 99, no. 26, p. 262504, 2011.

[121] K. W. Edmonds, K. Y. Wang, R. P. Campion, A. C. Neumann, N. R. S. Farley, B. L. Gallagher, and C. T. Foxon, "High-Curie-temperature $Ga_{1-x}Mn_xAs$ obtained by resistance-monitored annealing," *Applied Physics Letters*, vol. 81, no. 26, pp. 4991–4993, 2002.

[122] K. W. Edmonds, P. Bogusławski, K. Y. Wang, R. P. Campion, S. N. Novikov, N. R. S. Farley, B. L. Gallagher, C. T. Foxon, M. Sawicki, T. Dietl, M. Buongiorno Nardelli, and J. Bernholc, "Mn Interstitial Diffusion in (Ga, Mn)As," *Phys. Rev. Lett.*, vol. 92, p. 037201, 2004.

[123] M. Malfait, J. Vanacken, V. V. Moshchalkov, W. Van Roy, and G. Borghs, "Enhanced annealing effect in an oxygen atmosphere on $Ga_{1-x}Mn_xAs$," *Applied Physics Letters*, vol. 86, no. 13, p. 132501, 2005.

[124] T. Hayashi, Y. Hashimoto, S. Katsumoto, and Y. Iye, "Effect of low-temperature annealing on transport and magnetism of diluted magnetic semiconductor (Ga,Mn)As," *Applied Physics Letters*, vol. 78, no. 12, pp. 1691–1693, 2001.

[125] M. Adell, L. Ilver, J. Kanski, V. Stanciu, P. Svedlindh, J. Sadowski, J. Z. Domagala, F. Terki, C. Hernandez, and S. Charar, "Postgrowth annealing of (Ga,Mn)As under As capping: An alternative way to increase T_C," *Applied Physics Letters*, vol. 86, no. 11, p. 112501, 2005.

[126] D. E. Bliss, W. Walukiewicz, J. W. Ager, E. E. Haller, K. T. Chan, and S. Tanigawa, "Annealing studies of low-temperature-grown GaAs:Be," *Journal of Applied Physics*, vol. 71, no. 4, pp. 1699–1707, 1992.

[127] A. Eckrot, "Annealing Experiment an GaAs/GaMnAs core-shell Nanodrähten," diploma thesis, Universität Regensburg, 2011.

[128] S. Hilpert and T. Dieckmann, "Über Arsenide. I. (Eisen- und Manganarsenide.)," *Berichte der deutschen chemischen Gesellschaft*, vol. 44, no. 3, pp. 2378–2385, 1911.

[129] K. H. Ploog, "Spin injection in ferromagnet-semiconductor heterostructures at room temperature (invited)," *Journal of Applied Physics*, vol. 91, no. 10, pp. 7256–7260, 2002.

[130] M. Tanaka, "Ferromagnet (MnAs)/III–V semiconductor hybrid structures," *Semiconductor Science and Technology*, vol. 17, no. 4, p. 327, 2002.

[131] K. Takahashi and M. Tanaka, "Magnetotransport properties of MnAs/GaAs/MnAs ferromagnet/semiconductor trilayer heterostructures," *Journal of Applied Physics*, vol. 87, no. 9, pp. 6695–6697, 2000.

[132] L. Däweritz, "Interplay of stress and magnetic properties in epitaxial MnAs films," *Reports on Progress in Physics*, vol. 69, no. 9, p. 2581, 2006.

[133] M. Kästner, L. Däweritz, and K. Ploog, "Surface reconstruction, screw dislocations and anisotropic step flow growth of MnAs on GaAs(111)B substrates," *Surface Science*, vol. 511, no. 1–3, pp. 323–330, 2002.

[134] N. Mattoso, M. Eddrief, J. Varalda, A. Ouerghi, D. Demaille, V. H. Etgens, and Y. Garreau, "Enhancement of critical temperature and phases coexistence mediated by strain in MnAs epilayers grown on GaAs(111)B," *Phys. Rev. B*, vol. 70, p. 115324, 2004.

[135] R. Engel-Herbert, T. Hesjedal, D. M. Schaadt, L. Däweritz, and K. H. Ploog, "Micromagnetic properties of MnAs(0001)/GaAs(111) epitaxial films," *Applied Physics Letters*, vol. 88, no. 5, 2006.

[136] M. Tanaka, J. P. Harbison, M. C. Park, Y. S. Park, T. Shin, and G. M. Rothberg, "Epitaxial orientation and magnetic properties of MnAs thin films grown on (001) GaAs: Template effects," *Applied Physics Letters*, vol. 65, no. 15, pp. 1964–1966, 1994.

[137] L. Däweritz, D. Kolovos-Vellianitis, A. Trampert, C. Herrmann, K.H. Ploog, E. Bauer, A. Locatelli, S. Cherifi, and S. Heun, "Orientation and interface effects on the structural and magnetic properties of MnAs-on-GaAs hybrid structures," *J. Phys. IV France*, vol. 132, pp. 159–162, 2006.

[138] F. Schippan, G. Behme, L. Däweritz, K. H. Ploog, B. Dennis, K.-U. Neumann, and K. R. A. Ziebeck, "Magnetic structure of epitaxially grown MnAs on GaAs(001)," *Journal of Applied Physics*, vol. 88, no. 5, pp. 2766–2770, 2000.

[139] R. W. De Blois and D. S. Rodbell, "Magnetic First-Order Phase Transition in Single-Crystal MnAs," *Phys. Rev.*, vol. 130, pp. 1347–1360, 1963.

[140] L. Däweritz, C. Herrmann, J. Mohanty, T. Hesjedal, K. H. Ploog, E. Bauer, A. Locatelli, S. Cherifi, R. Belkhou, A. Pavlovska, and S. Heun, "Tailoring of the structural and magnetic properties of MnAs films grown on GaAs—Strain and annealing effects," *Journal of Vacuum Science and Technology B*, vol. 23, no. 4, pp. 1759–1768, 2005.

[141] E. Uccelli, J. Arbiol, C. Magen, P. Krogstrup, E. Russo-Averchi, M. Heiss, G. Mugny, F. Morier-Genoud, J. Nygård, J. R. Morante, and A. Fontcuberta i Morral, "Three-Dimensional Multiple-Order Twinning of Self-Catalyzed GaAs Nanowires on Si Substrates," *Nano Letters*, vol. 11, no. 9, pp. 3827–3832, 2011.

[142] F. Matteini, G. Tütüncüoğlu, D. Rüffer, E. Alarcón-Lladó, and A. F. i Morral, "Ga-assisted growth of GaAs nanowires on silicon, comparison of surface SiO_x of different nature," *Journal of Crystal Growth*, vol. 404, no. 0, pp. 246–255, 2014.

[143] S. J. Gibson and R. R. LaPierre, "Model of patterned self-assisted nanowire growth," *Nanotechnology*, vol. 25, no. 41, p. 415304, 2014.

[144] B. Bauer, "Positionskontrolliertes Wachstum von GaAs-Nanodrähten durch Vorstrukturierung der Substrate mittels Elektronenstrahllithographie," diploma thesis, Universität Regensburg, 2010.

[145] J. Hubmann, "GaAs-Nanodrähte: Vorstrukturierung der Substrate und Charakterisierung des Wachstums," diploma thesis, Universität Regensburg, 2012.

[146] D. Rudolph, S. Hertenberger, S. Bolte, W. Paosangthong, D. Spirkoska, M. Döblinger, M. Bichler, J. J. Finley, G. Abstreiter, and G. Koblmüller, "Direct Observation of a Noncatalytic Growth Regime for GaAs Nanowires," *Nano Letters*, vol. 11, no. 9, pp. 3848–3854, 2011.

[147] S. Breuer, M. Hilse, A. Trampert, L. Geelhaar, and H. Riechert, "Vapor-liquid-solid nucleation of GaAs on Si(111): Growth evolution from traces to nanowires," *Phys. Rev. B*, vol. 82, p. 075406, 2010.

[148] S. Breuer, M. Hilse, L. Geelhaar, and H. Riechert, "Nucleation and growth of Au-assisted GaAs nanowires on GaAs(111)B and Si(111) in comparison," *Journal of Crystal Growth*, vol. 323, no. 1, pp. 311 – 314, 2011.

[149] G. Wulff, "Zur Frage der Geschwindigkeit des Wachstums und der Auflösung der Krystallflächen," *Zeitschrift für Krystallographie und Mineralogie*, vol. 34, p. 449–530, 1901.

[150] E. Russo-Averchi, M. Heiss, L. Michelet, P. Krogstrup, J. Nygard, C. Magen, J. R. Morante, E. Uccelli, J. Arbiol, and A. Fontcuberta i Morral, "Suppression of three dimensional twinning for a 100 % yield of vertical GaAs nanowires on silicon," *Nanoscale*, vol. 4, pp. 1486–1490, 2012.

[151] B. Loitsch, D. Rudolph, S. Morkötter, M. Döblinger, G. Grimaldi, L. Hanschke, S. Matich, E. Parzinger, U. Wurstbauer, G. Abstreiter, J. J. Finley, and G. Koblmüller, "Semiconductor Nanowires: Tunable Quantum Confinement in Ultrathin, Optically Active Semiconductor Nanowires Via Reverse-Reaction Growth," *Advanced Materials*, vol. 27, no. 13, p. 2125, 2015.

[152] M. Heiß, E. Riedlberger, D. Spirkoska, M. Bichler, G. Abstreiter, and A. F. i Morral, "Growth mechanisms and optical properties of GaAs-based semiconductor microstructures by selective area epitaxy," *Journal of Crystal Growth*, vol. 310, no. 6, pp. 1049–1056, 2008.

[153] A. Fontcuberta i Morral, C. Colombo, G. Abstreiter, J. Arbiol, and J. R. Morante, "Nucleation mechanism of gallium-assisted molecular beam epitaxy growth of gallium arsenide nanowires," *Applied Physics Letters*, vol. 92, no. 6, p. 063112, 2008.

[154] A. M. Munshi, D. L. Dheeraj, J. Todorovic, A. T. van Helvoort, H. Weman, and B.-O. Fimland, "Crystal phase engineering in self-catalyzed GaAs and GaAs/GaAsSb nanowires grown on Si(111)," *Journal of Crystal Growth*, vol. 372, no. 0, pp. 163–169, 2013.

[155] X. Yu, H. Wang, J. Lu, J. Zhao, J. Misuraca, P. Xiong, and S. von Molnár, "Evidence for Structural Phase Transitions Induced by the Triple Phase Line Shift in Self-Catalyzed GaAs Nanowires," *Nano Letters*, vol. 12, no. 10, pp. 5436–5442, 2012.

[156] S. Furthmeier, F. Dirnberger, J. Hubmann, B. Bauer, T. Korn, C. Schüller, J. Zweck, E. Reiger, and D. Bougeard, "Long exciton lifetimes in stacking-fault-free wurtzite GaAs nanowires," *Applied Physics Letters*, vol. 105, no. 22, p. 222109, 2014.

[157] D. Saxena, S. Mokkapati, P. Parkinson, N. Jiang, Q. Gao, H. H. Tan, and C. Jagadish, "Optically pumped room-temperature GaAs nanowire lasers," *Nat Photon*, vol. 7, pp. 963 – 968, 2013.

[158] B. Mayer, D. Rudolph, J. Schnell, S. Morkötter, J. Winnerl, J. Treu, K. Müller, G. Bracher, G. Abstreiter, G. Koblmüller, and J. J. Finley, "Lasing from individual GaAs-AlGaAs core-shell nanowires up to room temperature," *Nat Commun*, vol. 4, no. 2931, 2013.

[159] L. M. Smith, H. E. Jackson, J. M. Yarrison-Rice, and C. Jagadish, "Insights into single semiconductor nanowire heterostructures using time-resolved photoluminescence," *Semiconductor Science and Technology*, vol. 25, no. 2, p. 024010, 2010.

[160] H. Ruda and A. Shik, "Polarization-sensitive optical phenomena in semiconducting and metallic nanowires," *Phys. Rev. B*, vol. 72, p. 115308, 2005.

[161] S. C. Jain, M. Willander, J. Narayan, and R. V. Overstraeten, "III–nitrides: Growth, characterization, and properties," *Journal of Applied Physics*, vol. 87, no. 3, pp. 965–1006, 2000.

[162] D. A. B. Miller, D. S. Chemla, T. C. Damen, A. C. Gossard, W. Wiegmann, T. H. Wood, and C. A. Burrus, "Band-Edge Electroabsorption in Quantum Well Structures: The Quantum-Confined Stark Effect," *Phys. Rev. Lett.*, vol. 53, pp. 2173–2176, 1984.

[163] B. Bauer, "Transmission Electron Microscopy on GaAs Nanowires - Spontaneous Polarization and MnAs Nanocrystals," PhD thesis, Universität Regensburg, 2015.

[164] B. Bauer, J. Hubmann, M. Lohr, E. Reiger, D. Bougeard, and J. Zweck, "Direct detection of spontaneous polarization in wurtzite GaAs nanowires," *Applied Physics Letters*, vol. 104, no. 21, p. 211902, 2014.

[165] J. Chapman, P. Batson, E. Waddell, and R. Ferrier, “The direct determination of magnetic domain wall profiles by differential phase contrast electron microscopy,” *Ultramicroscopy*, vol. 3, no. 0, pp. 203–214, 1978.

[166] M. Lohr, R. Schregle, M. Jetter, C. Wächter, T. Wunderer, F. Scholz, and J. Zweck, “Differential phase contrast 2.0—Opening new “fields” for an established technique,” *Ultramicroscopy*, vol. 117, no. 0, pp. 7–14, 2012.

[167] K. L. Kavanagh, J. Salfi, I. Savelyev, M. Blumin, and H. E. Ruda, “Transport and strain relaxation in wurtzite InAs–GaAs core-shell heterowires,” *Applied Physics Letters*, vol. 98, no. 15, p. 152103, 2011.

[168] I. A. Goldthorpe, A. F. Marshall, and P. C. McIntyre, “Synthesis and Strain Relaxation of Ge-Core/Si-Shell Nanowire Arrays,” *Nano Letters*, vol. 8, no. 11, pp. 4081–4086, 2008.

[169] K. W. Edmonds, N. R. S. Farley, T. K. Johal, G. van der Laan, R. P. Campion, B. L. Gallagher, and C. T. Foxon, “Ferromagnetic moment and antiferromagnetic coupling in (Ga,Mn)As thin films,” *Phys. Rev. B*, vol. 71, p. 064418, 2005.

[170] V. Novák, K. Olejník, J. Wunderlich, M. Cukr, K. Výborný, A. W. Rushforth, K. W. Edmonds, R. P. Campion, B. L. Gallagher, J. Sinova, and T. Jungwirth, “Curie Point Singularity in the Temperature Derivative of Resistivity in (Ga,Mn)As,” *Phys. Rev. Lett.*, vol. 101, p. 077201, 2008.

[171] M. Tanaka, K. Saito, and T. Nishinaga, “Epitaxial MnAs/GaAs/MnAs trilayer magnetic heterostructures,” *Applied Physics Letters*, vol. 74, no. 1, pp. 64–66, 1999.

[172] N. S. Dellas, J. Liang, B. J. Cooley, N. Samarth, and S. E. Mohney, “Electron microscopy of GaAs/MnAs core/shell nanowires,” *Applied Physics Letters*, vol. 97, no. 7, p. 072505, 2010.

[173] M. Hilse, Y. Takagaki, M. Ramsteiner, J. Herfort, S. Breuer, L. Geelhaar, and H. Riechert, “Strain in GaAs–MnAs core–shell nanowires grown by molecular beam epitaxy,” *Journal of Crystal Growth*, vol. 323, no. 1, pp. 307–310, 2011.

[174] J. Sadowski, P. Dłużewski, S. Kret, E. Janik, E. Łusakowska, J. Kanski, A. Presz, F. Terki, S. Charar, and D. Tang, “GaAs:Mn Nanowires Grown by Molecular Beam Epitaxy of (Ga,Mn)As at MnAs Segregation Conditions,” *Nano Letters*, vol. 7, no. 9, pp. 2724–2728, 2007.

[175] J. Sadowski, A. Siusys, A. Kovacs, T. Kasama, R. E. Dunin-Borkowski, T. Wojciechowski, A. Reszka, and B. Kowalski, “GaAs–MnAs nanowires,” *physica status solidi (b)*, vol. 248, no. 7, pp. 1576–1580, 2011.

[176] M. Poggio, R. C. Myers, N. P. Stern, A. C. Gossard, and D. D. Awschalom, "Structural, electrical, and magneto-optical characterization of paramagnetic GaMnAs quantum wells," *Phys. Rev. B*, vol. 72, p. 235313, 2005.

[177] K. Gas, J. Sadowski, T. Kasama, A. Siusys, W. Zaleszczyk, T. Wojciechowski, J.-F. Morhange, A. Altintas, H. Q. Xu, and W. Szuszkiewicz, "Structural and optical properties of self-catalytic GaAs:Mn nanowires grown by molecular beam epitaxy on silicon substrates," *Nanoscale*, vol. 5, pp. 7410–7418, 2013.

[178] Y. Morishita, K. Iida, J. Abe, and K. Sato, "Substrate-Orientation Dependence on Structure and Magnetic Properties of MnAs Epitaxial Layers," *Japanese Journal of Applied Physics*, vol. 36, no. 8B, p. L1100, 1997.

[179] J. Varalda, A. J. A. de Oliveira, A. Ouerghi, M. Eddrief, M. Marangolo, D. Demaille, V. H. Etgens, N. Mattoso, and D. H. Mosca, "Growth and magnetic properties of MnAs epitaxied on GaAs(111)B," *Journal of Applied Physics*, vol. 100, no. 9, p. 093524, 2006.

[180] D. B. Williams and C. B. Carter, "The transmission electron microscope," in *Transmission Electron Microscopy*, p. 301, Springer US, 1996.

[181] G. Priante, S. Ambrosini, V. G. Dubrovskii, A. Franciosi, and S. Rubini, "Stopping and Resuming at Will the Growth of GaAs Nanowires," *Crystal Growth and Design*, vol. 13, no. 9, pp. 3976–3984, 2013.

[182] F. Glas and J.-C. Harmand, "Calculation of the temperature profile in nanowhiskers growing on a hot substrate," *Phys. Rev. B*, vol. 73, p. 155320, 2006.

[183] M. Utz, "Epitaxie von (Ga,Mn)As," PhD thesis, Universität Regensburg, 2012.

[184] U. of Notre Dame. http://www3.nd.edu/ kamatlab/images/Facilities/edxs.jpg, 2015.

[185] M. Lohr, "Quantitative Bestimmung innerer elektrischer Felder mit Hilfe von Differentieller Phasenkontrastmikroskopie," PhD thesis, Universität Regensburg, 2013.

[186] B. Eßer, "Orts- und zeitaufgelöste Spektroskopie an Halbleiter-Nanodrähten," diploma thesis, Universität Regensburg, 2012.

[187] W. Kipferl, *Spinwellenanregungen in ferromagnetischen ultradünnen epitaktischen Fe-Schichten und Nanostrukturen.* Logos, 2005.

[188] W. Köster and B. Thoma, "Aufbau der Systeme Gallium-Antimon, Gallium-Arsen und Aluminium-Arsen," *Zeitschrift für Metallkunde*, vol. 46, no. 4, pp. 291–293, 1955.

[189] R. P. Elliott and F. A. Shunk, “The Au-Ga (Gold-Gallium) system,” *Bulletin of Alloy Phase Diagrams*, vol. 2, no. 3, pp. 356–358, 1981.

[190] E. Wachtel and K. J. Nier, “Magnetische Untersuchung des Systems Mangan-Gallium im festen und flüssigen Zustand,” *Zeitschrift für Metallkunde*, vol. 56, no. 11, pp. 779–789, 1965.

[191] J. Paitz, “The P-T-x Phase Diagram of the Mn-As System,” *Kristall und Technik*, vol. 7, no. 9, pp. 999–1005, 1972.

[192] M. B. Panish, “Ternary Condensed Phase Systems of Gallium and Arsenic with Group lB Elements,” *Journal of The Electrochemical Society*, vol. 114, no. 5, pp. 516–521, 1967.

Acknowledgments

Abschließend möchte ich mich bei allen bedanken, die zum Gelingen dieser Arbeit beigetragen haben, besonders:

- Prof. Dr. Dominique Bougeard für die Möglichkeit in seiner Arbeitsgruppe zu promovieren und die vielen Diskussionen rund um das Nanodrahtwachstum
- Dr. Elisabeth Reiger für das Engagement in Nanodrahtbereich
- Prof. Dr. Josef Zweck für die freundliche Übernahme des Zweitgutachters
- Dr. Dieter Schuh für die Wartung der MBE und das Einweihen in deren Geheimnisse
- Benedikt Bauer für die unzähligen TEM- und EDX-Aufnahmen, sowie die Diskussionen rund um die verschiedenen Kristallgitter
- Andreas Biermanns für das Anfertigen von RSMs an GaAs und GaAs/(Ga,Mn)As core/shell Nanodrähten
- Fritz Schiller, Helmut Körner für das Bestimmen der Magnetisierung meiner feromagnetischen Proben mittels SQUID
- Stephan Furthmeier, Florian Dirnberger, Benjamin Esser für die vielen Photolumineszenz-Messungen an den Nanodrähten
- Imke Gronwald für das Schleusen und Sortieren der Proben, sowie die Handhabe der unterschiedlichen MBE-Halter
- Peter Müller für die Wartung des Posterdruckers, und das Reinigen der MBE-Halter
- Christian Butschkow für die Magnetotransport-Messungen an einzelnen GaAs/-(Ga,Mn)As core/shell Nanodrähten, und die Diskussionen rund um den DMS (Ga,Mn)As
- Andreas Schützenmeier für den Elan wenn (mal wieder) eine Kammeröffnung anstand und für die Besorgung und Anfertigung von MBE-Haltern oder anderen Ausrüstungsgegenständen
- Mario Bamesreiter und Christian Neumann für das Ausstellen temporärer Passwörter und das Versorgen mit Hard- und Software

- Andreas Rudolph für die Einführung ins Nanodrahtwachstum und das Beibringen sonstiger Kniffe die dafür nötig sind
- Ulla Franzke für die Hilfe und den Durchblick bei diversen Anträgen, Formblätter etc.
- Martin Utz das Einführen ins (Ga,Mn)As-Wachstum
- Helene Plank für das Vermessen der Si Substrate mit FTIR
- Josef Loher und Michael Schmalzbauer dafür, dass Diskussionen rund um den Fußball nicht zu kurz kamen
- meinen Bürokollegen Juliane Lauerer, Andreas Bayer und Stephan Furthmeier für das nette Arbeitsklima
- allen Mitgliedern der AG Bougeard für das tolle Team
- meinen Korrekturlesern Benedikt Bauer, Christian Butschkow, Stephan Furthmeier und Florian Dirnberger dafür, dass durch euch die Arbeit (einigermaßen) lesbar wurde
- meinen Eltern, dafür, dass sie mich immer unterstützt haben